THE UNIVERSITY *of* EDINBURGH

The impact of the radiation balance on snowmelt in a sparse deciduous birch forest

Rachael Heather Turton

A thesis submitted for the degree of Doctor of Philosophy
The University of Edinburgh

December 2016

Declaration

This thesis is an account of research undertaken between January 2008 and December 2016 at the Centre for Ecology and Hydrology, Wallingford and the School of GeoSciences, University of Edinburgh.
Except where explicitly stated, this thesis and the material presented in it is my own work and has not been submitted in whole or part for a degree in any university.
The figures in Chapter 8 were produced in collaboration with Alberto Martinez-de la Torre, a colleague at CEH.

Rachael Heather Turton

December 2016

Acknowledgements

This project was funded by the Centre for Ecology & Hydrology's Biogeochemistry program. This research complements the Arctic Biosphere Atmosphere Coupling at Multiple Scales (ABACUS), a Natural Environment Research Council (NERC) project. The research objectives of ABACUS were to understand the temporal and spatial controls on the exchange of energy, water, and carbon between Arctic terrestrial ecosystems and the atmosphere.

I would like to thank my supervisors Eleanor Blyth and Richard Essery.

I would also like to express my gratitude to all the Abisko research station staff in particular Annika Kristoffersson. In 2009 my fieldwork assistant Pete Walker who was invaluable. Also field assistance from Katie Walker, Laura Comeau, Lorna Street and Paul Stoy.

Helpful comments and assistance from the staff at CEH in particular Doug Clark and Alberto Martinez-de la Torre for his help in running JULES distributed.

Finally I'd like to thank Craig Montgomery, my friends and family for their love and kind words of support and encouragement.

Abstract

The representation of high-latitude surface processes and quantifying surface-climate feedbacks are some of the most serious shortcomings of present day Arctic land surface modelling. The energy balance of seasonally snow-covered sparse deciduous forests at high latitudes is poorly understood and inaccurately represented within hydrological and climate models.

Snow cover plays an important role in wintertime fluxes of energy, water and carbon, controlling the length of the active growing season and hence the overall carbon balance of Arctic ecosystems. Snow cover is non-uniform and spatially variable, as wind redistributes snow from areas of exposed open tundra to sheltered areas within the forest, where a deeper snowpack develops. Low solar zenith angles, coupled with sparse deciduous leafless trees, cast shadows across the snow surface. The spatial distribution of canopy gaps determines the timing of direct radiation which penetrates down through the canopy to the snow surface. The forest canopy also excludes incoming longwave radiation and yet also emits longwave radiation to the snow surface. Consequently the forest canopy plays a key role in the radiation balance of sparse forests.

To improve our knowledge of these complex processes, meteorological and field observations were taken in an area of highly heterogeneous birch *Betula pubescens* ssp. *czerepanovii* forest in Abisko, Sweden during the spring of 2008 and 2009. Detailed measurements of short and longwave radiation above and below the canopy, hemispherical photographs, tree temperatures and snow surveys were conducted to quantify the radiation balance of the sparse deciduous forest.

An array of below canopy pyranometers found the mean canopy transmissivity to be 74 % in 2008 and 76 % in 2009. Hemispherical photographs taken at the pyranometer locations analysed with Gap Light Analyzer (GLA) showed reasonable agreement with a mean canopy transmissivity of 75 % in 2008 and 74 % in 2009. The canopy transmissivity was found to be independent of the diffuse fraction of radiation as the canopy is very sparse.

A series of survey grids and transects were established to scale up from the below canopy pyranometers to the landscape scale. Hemispherical photographs analysed with GLA showed the sparse forest canopy had a mean transmissivity of 78 % and a mean LAI of 0.25, whereas the open tundra had a mean transmissivity of 97 % and a mean LAI of < 0.01. Snow surveys showed

the sparse forest snow depth to vary between 0.34 and 0.55 m, whereas the snow depth in the open tundra varied between 0.12 and 0.18 m.

Observations of canopy temperatures showed a strong influence of incident shortwave radiation warming the tree branches to temperatures up to 15 °C warmer than ambient air temperature on the south facing sides of the trees, and up to 6 °C on the north facing sides of the trees.

To reproduce the observed radiation balance, two canopy models (Homogenous and Clumped) were developed. The Homogeneous canopy model assumes a single tree tile with a uniform sparse canopy. The Clumped canopy model assumes a tree and a grass tile, where the tree tile is permanently in shade from the canopy and the grass tile receives all the incoming radiation. These canopy models identified the need for a parameter that accounts for the spatial and temporal variation of the shaded gaps within the sparse forest.

JULES (Joint UK Land Environment Simulator) is the community land surface model used in the UK Hadley Centre GCM suite. Modifications of the land-surface interactions were included in JULES to represent the shaded gaps within the sparse deciduous forest. New parameterisations were developed for the time-varying sunlit fractions of the gap (f_{lit}), the sky-view fraction (f_v), and the longwave radiation emitted from the canopy (LW_{tree}). These model developments were informed by field observations of the forest canopy and evaluated against the below canopy short and longwave radiation observed data sets. The JULES Shaded gap model output showed a strong positive relationship with the observations of below canopy shortwave and longwave radiation. The JULES Shaded gap model improves the ratio of observed to modelled short and longwave radiation on sunny days compared to the JULES model. The JULES Shaded gap model reduces the time to snow melt by 2 to 4 days compared to the JULES model, making the model output more aligned with in-situ observational data. This shortening of the modelled snow-season directly impacts on the simulated carbon and water balance regionally and has wider relevance at the pan-Arctic scale.

When JULES Shaded Gap was evaluated on the global scale, it improved the modelled snowmass across large areas of sparse forest in northern Canada, Scandinavia and Northern Russia with respect to GlobSnow. The performance of the land surface-snow-vegetation interactions of JULES was improved by using the Shaded gap to model the radiation balance of sparse forests in climate-sensitive Arctic regions. Furthermore these observational data can be used to develop and evaluate high latitude land-surface processes and biogeochemical feedbacks in other earth system models.

Contents

List of Figures

List of Tables

Acronyms

AATSR	Advanced Along Track Scanning Radiometer
AVHRR	Advanced Very High Resolution Radiometer
ALMIP	AMMA Land Surface Model Intercomparison Project
ABACUS	Arctic Biosphere Atmosphere Coupling at Multiple Scales
AMAP	Arctic Monitoring and Assessment Program
AWS	Automatic Weather Station
BERMS	Boreal Ecosystem Research and Monitoring Sites
BOREAS	Boreal Ecosystem-Atmosphere Study
CLASS	Canadian Land Surface Scheme
CLM	Community Land Model
DHSVM	Distributed Hydrology-Soil-Vegetation Model
GLA	Gap Light Analyser
GORT	Geometric-Optical and Radiative Transfer
GOES	Geostationary Operational Environmental Satellites
GCM	General Circulation Models
GHCN	Global Historical Climatology Network
GSWP - 2	Global Soil Wetness Project
IGBP	International Geosphere-Biosphere Program
ILAMB	The International Land Model Benchmarking Project
ISBA	The interactions between soil-biosphere-atmosphere model
JULES	Joint UK Land Environment Simulator
LAI	Leaf Area Index
LAPP	Land Arctic Physical Processes
MERIS	Medium Resolution Imaging Spectrometer Instrument
MOSES	Met Office Surface Exchange Scheme
MSG	Meteosat Second Generation
MODIS	Moderate Resolution Imaging Spectroradiometer
NOHRSC	National Operational Hydrologic Remote Sensing Center
NSIDC	National Snow and Ice Data Center
NERC	Natural Environment Research Council

NESDIS	National Environmental Satellite Data and Information Service
NOAA	National Oceanic and Atmospheric Administration
ORCHIDEE-CAN	Organising Carbon and Hydrology In Dynamic Ecosystems-CANopy model
PAI	Plant Area Index
SAI	Stem Area Index
SCA	Snow Covered Area
SCE	Snow Cover Extent
SNOWMIP	Snow Model Intercomparison Project
SWE	Snow Water Equivalent
SMMR	Scanning Multi-channel Microwave Radiometer
SSM/I	Special Sensor Microwave/Imager
TESSEL	Tiled ECMWF Scheme for Surface Exchanges over Land model
WINTEX	WINTer EXperiment

Chapter 1

Introduction

1.1 Introduction

One of the most serious shortcomings of present day Arctic terrestrial and climate modelling is the representation of high-latitude surface processes and quantifying surface-climate feedbacks [*Kattsov and Källén*, 2005; *Chapin, F. S. III et al.*, 2008; *Weller*, 2000]. The energy balance of seasonally snow-covered sparse deciduous forests at high latitudes is poorly understood and inaccurately represented within hydrological and climate models [*Harding et al.*, 2001]. Snow cover plays an important role in wintertime fluxes of energy, water and carbon [*Dye*, 2002], controlling the length of the active growing season and hence the overall carbon balance of Arctic ecosystems [*Harding et al.*, 2001; *Groisman et al.*, 1994]. Previous studies have primarily focussed on the energy balance of evergreen needleleaf trees [*Chen*, 1996; *Essery et al.*, 2008a; *Essery and Pomeroy*, 2001; *Essery et al.*, 2003, 2009; *Gryning et al.*, 2001; *Hardy et al.*, 2004; *Li et al.*, 1995; *Ni et al.*, 1997; *Ni-Meister and Gao*, 2011; *Pomeroy et al.*, 2009; *Stähli et al.*, 2009].

This thesis presents the results of an investigation into the representation of the radiation balance of a sparse deciduous forest in the land surface model Joint UK Land Environment Simulator (JULES) [*Best et al.*, 2011], part of the Hadley Centre HadGem3 suite of general circulation models, using observations from a sparse birch forest field site in Abisko, Northern Sweden taken in 2008 and 2009.

1.2 Study background

The Arctic forms part of a dynamic system, where the climatology, meteorology, pedology, hydrology and ecology regimes are inexplicably linked. The interactions between these different elements of the Arctic system are important when considering the observed changes and modelled projections for the Arctic climate system.

In 2011 the Arctic Monitoring and Assessment Program (AMAP) reported on the observed changes in Arctic climate including: warmer air temperatures particularly in autumn; reduced snow cover extent, duration and depth; increased precipitation, particularly in winter; retreat of the permafrost and warmer soil temperatures; early break up of lake and river ice; reduced sea ice thickness and depth; retreat of mountain glaciers, and the Greenland ice sheet; and wetland loss and creation from impeding drainage [*AMAP*, 2011; *Serreze et al.*, 2000; *Serreze and Barry*, 2011]. There is considerable uncertainty regarding the feedbacks from some of these changes, which in turn may alter the rate of change. Understanding each of these changes and their associated feedbacks to other elements of the Arctic system generate considerable uncertainty in future climate projections [*AMAP*, 2011].

A major part of the Arctic system is the land surface which experiences seasonal snow cover. The changes in climate depend upon the interactions between the snow and vegetation. Changes in the hydrological regime from increased winter precipitation and earlier snow melt, will affect the ecological functioning of the forest due to the timing and availability of water. Combined with increased air and soil temperatures, these changes may alter the composition of the vegetation, which could in turn alter the interaction of the forests with the atmosphere. Considering the unprecedented level of warming in the Arctic to date, and the potential impacts of future global change it is important that we understand how the land surface processes function in order to better understand how they will respond to global change.

One current weakness in land surface modelling is the representation of these physical processes of snow and vegetation interaction in the high latitudes [*Harding et al.*, 2001; *Sellers et al.*, 1997]. This thesis addresses this issue in land surface modelling of the Arctic.

1.3 Arctic ecosystems

Climate change has been at its most rapid and pronounced in the high latitudes. If temperatures in the Arctic rise at a magnitude predicted by the climate models, the temperature will be the same as those which currently occur in the boreal forest far to the south [*Juday*, 2005]. Definitions of the Arctic have been restricted to areas of treeless tundra, snow and ice in the highest latitudes [*Juday*, 2005]. However, in order to appreciate how the boreal forest will respond to these changes, it is important to study the Arctic at a much broader scale. The *AMAP* [2011] has taken a much broader perspective of the Arctic being inclusive of landscapes and vegetation from the northern forests to the polar deserts [*Huntington and Weller*, 2005], specifically encompassing the boreal forest of the Nordic countries, Canada and Alaska [*Juday*, 2005]. The International Arctic Research Center, at the University of Alaska Fairbanks, has set out to build an integrated

understanding of the Arctic, as a system, with clear and accurate conceptualization of the role of the Arctic in the broader global system.

The Arctic has experienced average temperature increases twice that of the global average rate over the past 100 years [*Trenberth et al.*, 2007]. For the period 1900 to 2003 the land-surface air temperatures of the Arctic (north of 60°N) increased by 0.09 °C per decade according to the Global Historical Climatology Network (GHCN) dataset [*McBean*, 2005]. The warmest six years (2005 to 2010) on record since 1880 [*Serreze and Barry*, 2011] coincided with the measurements taken in this thesis (2008 and 2009), this warmest trend has continued as December 2015 to February 2016 was the warmest winter on record [*Cullather et al.*, 2016]. The latest IPCC projections from CMIP5 models are that it is very likely the Arctic region to continue to warm more rapidly than the global mean temperature [*IPCC*, 2014].

Many areas in the northern hemisphere have seen an overall reduction in the Snow Covered Area (SCA) of nearly 10 % for the period 1972 to 2003 [*Walsh*, 2005; *Serreze et al.*, 2000]. There has been a decline in SCA in North America, however it has been most pronounced in Eurasia due to earlier snow melt [*AMAP*, 2011; *Walsh*, 2005]. There has been a significant reduction in terrestrial Snow Cover Extent (SCE) for May and June, with successive records for the lowest June SCE since 2008 in Eurasia, and for four out of the last five years in North America [*Derksen and Brown*, 2012]. This reduction in SCA is seasonal, which despite winter warming has been most pronounced in spring and summer months [*Trenberth et al.*, 2007; *Walsh*, 2005; *AMAP*, 2011], and it has been shown that temperature has a significant role in this trend [*Trenberth et al.*, 2007]. The reduction in SCA is occurring despite an observed increase in winter precipitation [*Serreze et al.*, 2000]. The mid to high latitudes (55°N to 85°N) saw an increase in precipitation over the 1990 to 1995 period with the largest increase in the winter months, relative to the 1951 to 1980 mean [*Serreze et al.*, 2000]. The updated work of *Peterson and Vose* [1997] also found increased precipitation over the winter months across Europe, however some areas such as Eastern Russia have seen a reduction in winter precipitation [*McBean*, 2005]. There has also been a shift in the maximum monthly SCA from February to January [*Trenberth et al.*, 2007], and there has also been a shift in the timing of the spring melt arriving 9 to 15 days earlier over the period 1972 to 2000 [*Dye*, 2002]. Therefore, if there is an observed reduction in snow cover extent and winter precipitation is increasing not decreasing, the observed changes must be due to changes to the snow melt. CMIP5 model ensembles simulate widespread reduction in the SCE of 7 ± 4 % for RCP2.6 by the end of the 21st century [*Collins et al.*, 2013].

Another reason to study the snowmelt is the growth and distribution of Arctic vegetation which is limited by low air temperatures, low soil temperatures, low soil moisture, low soil nutrient availability and the snow free period (growing season length) [*Press et al.*, 1998]. Hence, small changes in temperature or moisture availability can have a significant effect on the growth and

survival of the vegetation, which could have important feedback on the seasonal snow cover.

The ecological functioning of Arctic ecosystems and the hydrological regime are a dynamic system where snow melt has a positive feedback on the climate via the ecosystem [*Harding and Pomeroy*, 1996; *Callaghan et al.*, 2011a; *Larsen et al.*, 2014]. Arctic ecosystems are sensitive to the duration, structure and depth of snow cover. Snow cover insulates the understorey vegetation from the harsh winter temperatures, ice-crystal blast, wind scouring, desiccation and some deeper snowpacks can prevent the ground from freezing [*Callaghan et al.*, 2011b]. The snow cover cuts out the shortwave radiation reaching down to the underlying vegetation, limiting the photosynthetic activity in the snow covered period. The highly reflective surface of the snow, reflects most of the sun's energy and maintains cool surface and air temperatures [*Harding and Pomeroy*, 1996]. When the snow melts, it is often the most significant contribution to the water balance despite its short duration [*McBean*, 2005]. The timing of the snow melt is crucial to the functioning of Arctic ecosystems as the vegetation must be able to take advantage of the melt water and flush of nutrients, therefore any changes to its arrival and length will have a significant impact on the ecosystem.

Observations of snow cover have shown a reduction in duration, extent and depth. The statistical analysis of multiple data sets provides high confidence that spring northern hemisphere snow cover extent is significantly reduced, and the loss of snowcover increases with latitude [*Vaughan et al.*, 2013]. The presence of snow affects soil temperatures and therefore the rate of soil respiration. Shallow snow packs expose vegetation to cooler temperatures, reduce soil temperatures, particularly in autumn and winter, and release less melt water in spring and summer. This would have a significant impact on the freshwater resources, wetlands and tree survival of Arctic ecosystems [*Larsen et al.*, 2014]. Shallow snowpacks are vulnerable to periods of extreme winter warming, which can expose vegetation to the harsh winter wind and temperatures. When the snow melts it reveals a darker land surface which absorbs more energy, which has a positive feedback on the ground surface and air temperatures. Warmer air temperatures, earlier snowmelt and increased precipitation lead to increased evaporation which may lead to drier land surfaces, and even summer droughts in forests and wetlands [*AMAP*, 2011; *Jiménez Cisneros et al.*, 2014]. Warmer air and soil temperatures lead to the thawing of permafrost, which increases the depth of the soil active layer, and in turn makes the soil more vulnerable to drying out, and releasing its stores of carbon [*Larsen et al.*, 2014; *Vaughan et al.*, 2013].

1.4 Boreal forests

The boreal forest encircles the Earth above 48°N [*Sellers et al.*, 1997], covering over 14.7 million km^2 [*Bonan and Shugart*, 1989]. The present day distribution can be seen in Figure 1.1.

Second in areal extent only to the tropical forest [*Sellers et al.*, 1997], the boreal forest covers 17 % of the terrestrial land surface [*Juday*, 2005; *Bonan et al.*, 1992] and 21 % of the forested land surface [*Whittaker and Likins*, 1975]. It covers over 500,000 km^2 in Fennoscandia alone, of which 47 % is in Sweden [*Esseen et al.*, 1997].

The boreal forest has been defined as a belt of forest which occurs south of the tundra, comprising cool coniferous (spruce, larch, pine, and fir) and broad-leaved species (birch and poplar/aspen) [*Usher*, 2005]. This mosaic pattern of vegetation types is due to the competing interaction of dynamic environmental factors including the climate, solar radiation, soil moisture, soil temperature, permafrost, the forest floor organic layer, nutrient availability, insect outbreaks and wildfires [*Bonan and Shugart*, 1989]. The boreal forests are climatically distinguished by seasonal variability with short, relatively warm and moist summers with low maximum solar elevations contrasting to long, extremely cold and dry winters with very low solar elevation [*Bonan and Shugart*, 1989; *Lieffers et al.*, 1999; *Leblanc et al.*, 2005] which causes the cessation of growth [*Harding and Pomeroy*, 1996]. Boreal forests are particularly sensitive to global warming due to these specific climatic conditions of this ecosystem [*Leblanc et al.*, 2005].

Seasonal snow cover in the boreal forests play an important role on the energy balance, particularly the radiative flux, latent and sensible heat fluxes, and the ground heat flux [*Harding and Pomeroy*, 1996] (see section 1.6). The rough texture and dark surface of the forest canopy intercepts and absorbs a large proportion of solar radiation and radiates heat down to the snowpack [*Juday*, 2005; *Bonan et al.*, 1992]. This contrasts strongly to the smooth, snow covered tundra, which is highly reflective to solar radiation [*Juday*, 2005; *Bonan et al.*, 1992]. The presence of the boreal forest, leads to warmer winter temperatures, than if the trees were not present, as the trees mask the snow [*Bonan et al.*, 1992]. Therefore, if the boreal forest expands into the present day tundra regions due to rising temperatures, the presence of a forest canopy would amplify the warming further [*Bonan et al.*, 1992; *Juday*, 2005; *Thompson et al.*, 2004]. *Betts* [2000] showed the northern latitude forestation would amplify rather than mitigate climate change as it would substantially reduce the surface albedo.

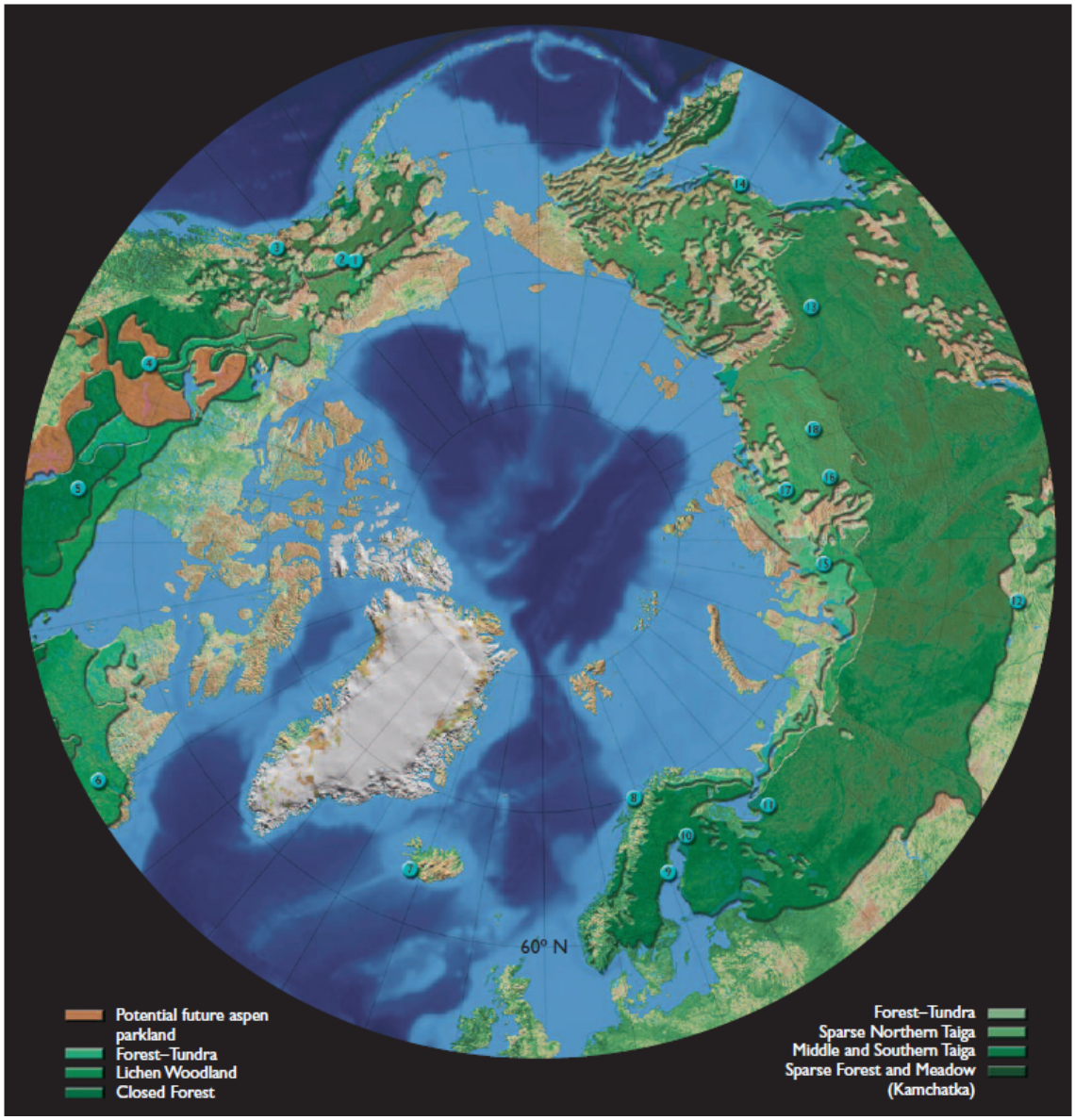

Figure 1.1: Present-day boreal forest distribution, using a simplified formation system representing a gradient of decreasing productivity and species diversity from south to north. Arctic Climate Impact Assessment, Chapter 14, figure 14.1 [*Juday*, 2005].

Boreal forests are an important terrestrial carbon sink and contain large stocks of carbon [*Juday*, 2005], containing approximately 20 % of the global reactive soil carbon [*Juday*, 2005]. At the global scale boreal forests are important in the uptake of atmospheric CO_2 through photosynthesis and the storage of carbon as living and dead plant matter, in boles and soils. The carbon is released much later through decomposition of dead organic matter, live plant and animal respiration and combustion through natural forest fires [*Juday*, 2005]. The capacity of the boreal forest to take up atmospheric CO_2 is impeded by both natural (forest fire and insect outbreak) and anthropogenic disturbance (management of timber) [*Juday*, 2005]. Enhanced temperatures are predicted to

increase the frequency and severity both spatially and temporally of pests and pathogen outbreaks [*Ayers*, 1993; *Juday*, 2005; *Virtanen and Neuvonen*, 1999; *Virtanen et al.*, 1998; *Williams and Liebhold*, 1995]. A warming climate is predicted to increase fire frequency and severity in some parts of the boreal forest [*Rupp et al.*, 2000a, b, 2002; *Turner et al.*, 2003; *Flannigan and Wagner*, 1991], while there may be a decreased fire frequency in others [*Flannigan et al.*, 1998]. There is a need to understand how climate change will affect the carbon cycling in these ecosystems at both the regional and global scale [*Juday*, 2005], as it will provide an improved understanding of the future carbon balance. Although this is outside of the scope of this thesis, these ecosystem disturbances and future climate change scenarios require the land surface model to represent the radiative processes in these sparse forests correctly.

There have been several international projects on the land surface processes of the boreal regions, including Land Arctic Physical Processes (LAPP) and WINTer EXperiment (WINTEX) [*Harding et al.*, 2001] with European field programmes in 1996-1998. The LAPP program was focussed on the exchanges of heat, water and carbon in the active season, whereas WINTEX was aimed at measuring and modelling the processes, specifically the interaction between the snow and the atmosphere in the winter [*Harding et al.*, 2001]. Perhaps the largest has been the Boreal Ecosystem-Atmosphere Study (BOREAS) project focussed on the interaction between the boreal forest biome and the atmosphere, to anticipate the effects of global change, specifically temperature and precipitation [*Sellers et al.*, 1997]. Specifically BOREAS focussed on the exchanges of radiative energy, sensible heat, water, CO_2 and other radiatively active trace gases between the lower atmosphere and the boreal forest [*Sellers et al.*, 1997].

Model projections of boreal forests under warmer climates show a northward advance of the boreal forest into the tundra displacing 11 - 50 % tundra (depending upon location) within 100 years [*Callaghan*, 2005] see Figure 1.2. Figure 1.2 panel a shows the present day vegetation distribution and Figure 1.2 panel d shows the potential vegetation distribution for 2100, which shows a northward advance of the treeline. *Pearson et al.* [2013] projected that at least half the vegetated areas of the Arctic would shift to a different physiognomic class, and there would a 52 % increase in woody cover. Thawing permafrost, warmer air temperatures and early snowmelt will allow tree growth to expand northwards, but only into areas where there is sufficient water [*AMAP*, 2011; *Larsen et al.*, 2014]. Boreal forests are under threat from drought due to warmer air temperatures, reduced winter snow cover and early snow melt leading to less water availability particularly in the summer months. In North America 40 % of the boreal forest treeline is growth limited by temperature induced-drought-stress. As broadleaf species are able to make better use of variable summer rainfall than conifers, changes to the seasonal type of moisture with less snow and more rain favours the broadleaf trees over conifer species [*AMAP*, 2011]. However, in general less carbon is stored in the vegetation of broadleaf (due to autumnal leaf senescence) than coniferous species, which could lead to a positive feedback on the climate [*Juday*, 2005].

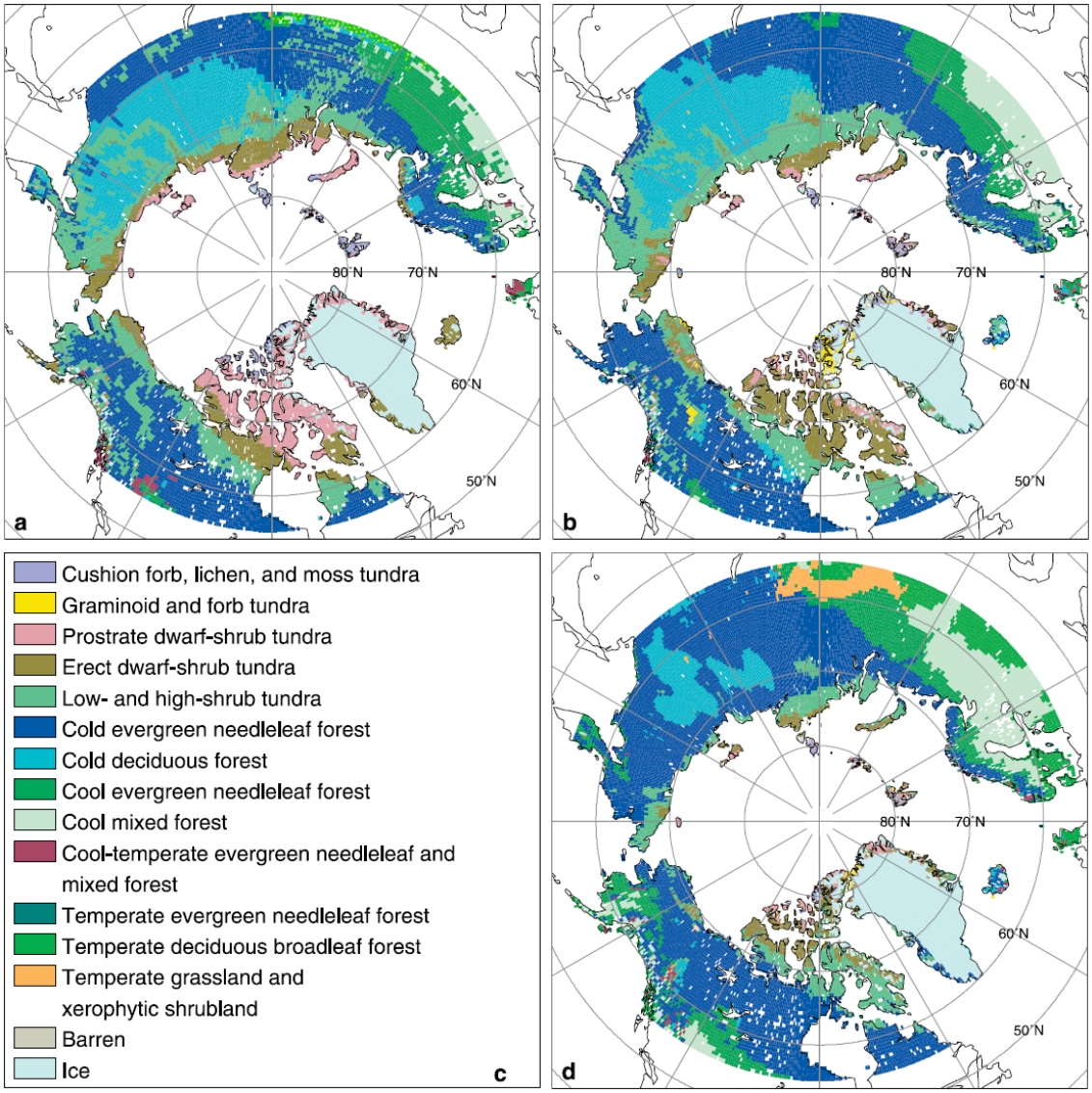

Figure 1.2: Panel a: Present-day potential natural vegetation of the Arctic and neighbouring regions from floristic surveys. Vegetation types 1 to 5 are classified as arctic, whereas types 6 to 8 are classified as boreal forest [*Kaplan et al.*, 2003]. Panel b: Present day vegetation simulated by BIOME4 [*Kaplan et al.*, 2003]. Panel c: Legend. Panel d: Potential vegetation distribution in 2090-2100 as projected by the BIOME4 model driven with output from the HadCMG2SUL model forced with the IS92a emissions scenario [*Kaplan et al.*, 2003].

Therefore even though warmer temperatures would allow the northwards expansion of the boreal forest into the tundra, the boreal forest would also lose ground to the south due to the warmer temperatures speeding up soil moisture evaporation, which in turn would allow low moisture tolerant grasses and trees to expand northwards from the prairies and evergreen forests. Projections of a warmer climate in boreal forests are uncertain on the exact speed of change due to the positive and negative feedbacks of the changing land surface properties on climate, and the complex interactions of vegetation and snow cover. A warmer climate is likely to change the

distribution, structure and species composition of the boreal forest.

1.4.1 Sparse forests

Boreal and mountain forests canopy structure varies widely from dense coniferous to relatively open deciduous and taiga forests [*Essery et al.*, 2008b]. Therefore, there is considerable spatial and temporal variability in the solar radiation interception and transmittance due to the exact forest canopy structure [*Hardy et al.*, 2004]. The size and location of canopy gaps is also highly heterogeneous [*Hardy et al.*, 2004; *Essery et al.*, 2008b] dependent upon the forest species, tree height, density, structure, and the angle of solar incidence which in turn modify the amount of thermal radiation, direct and diffuse shortwave radiation which can penetrate through the canopy [*Hardy et al.*, 2004; *Link et al.*, 2004; *Davis et al.*, 1997]. The amount of these radiation components which are then either absorbed or reflected is dependent on the albedo of the trees, snow and melting snow [*Rowlands et al.*, 2002].

In northern latitudes sparse vegetation with a seasonal snowcover are particularly important, as the vegetation cover shades the snowpack from incoming solar radiation and also enhances the thermal radiation to the sub-canopy surface [*Link et al.*, 2004; *Essery et al.*, 2008b]. This is particularly unusual as a continuous forest canopy would typically only allow minimal shortwave radiation down to an underlying snowpack. The interaction of the forest canopy architecture with the solar radiation provides a considerable energy source, particularly with low solar angles [*Harding et al.*, 2001]. This energy is translated into an upward sensible heat flux, which drives the convective boundary layer [*Gryning et al.*, 2001]. Snow covered canopies can have a large evaporation component, which can exceed the radiation input [*Harding and Pomeroy*, 1996].

As with the boreal forest, sparse forests are vulnerable to fires, land management practices, insect damage and land-use change [*Essery et al.*, 2008b; *Juday*, 2005]. However, they are also susceptible to the northward advance of coniferous boreal forests from the south as the climate warms. However, deciduous trees can make better use of the variable summer rainfall, tolerate lower soil moisture levels, and will tolerate much cooler air temperatures, and therefore could out-compete some coniferous boreal species. However, it is difficult to say whether these deciduous trees are capable of advancing northwards and keeping pace with the rate of modelled projections of increase in temperature. Climate change induced disturbance is the most likely mechanism for the loss of boreal forest [*Juday*, 2005]. Changes in the species composition of the boreal forest would modify the allocation and storage of carbon, particularly as the rates of production and decomposition are higher in deciduous than coniferous forests [*Gower et al.*, 2001], which could have a potential positive feedback on climate.

The present distribution of cold deciduous forest across Russia (larch), and northern Fennoscandia is shown in Figure 1.2 panel a. The sparse birch (*Betula pubescens* ssp. *czerepanovii*) forest of northern Sweden is described as the ecotone between the boreal forest and the tundra of northern Fennoscandia [*Juday*, 2005]. The *B. pubescens* trees are mostly polycormic, comprising of multiple stems produced by basal sprouting, which allows them to maintain contact with the old root system in growth and development [*Tenow et al.*, 2004]. They typically reach 4-6 m in height [*Carlsson et al.*, 1999], see Figure 1.3.

Figure 1.3: A sparse birch forest in northern Sweden.

1.4.2 Measurements of forest canopies

The forest canopy has a direct influence on the radiation penetration, the seasonal snowpack and the understorey vegetation but also on the micro-climate of the forest. There are many different techniques and equipment which have been developed to measure different forest canopy parameters. There are direct light measurements by photometric, radiometric or quantum sensors, and indirect light measurements using visible/infrared scanning systems, terrestrial laser scanners, imaging spectrometry, imaging radar, aerial photography and hemispherical photography (for a review of some of these methods see *Jennings et al.* [1999]). Selecting the most effective methodology is dependent upon the parameter requirements i.e. canopy closure. For a review of the methods available to measure Leaf Area Index (LAI) in vegetation canopies see *Jonckheere et al.* [2004] and for an analysis of the assumptions and limitations of the different

methods see *Weiss et al.* [2004]. Canopy properties such as LAI, canopy cover, gap fraction and sky-view fraction can be obtained indirectly from radiation measurements [*Sicart et al.*, 2004] or quickly and at low cost using hemispherical (fish-eye) photography [*Essery et al.*, 2008b].

LAI is a primary measurement of the forest canopy used in process models for calculating photosynthesis and canopy radiative transfer [*Verseghy et al.*, 1993; *Pomeroy et al.*, 2002; *Ni et al.*, 1997; *Pearson et al.*, 1999]. LAI is defined as half the total leaf surface area per unit ground surface area [*Chen and Black*, 1992, 1991]. Although the term Leaf Area Index (LAI) is used to compare the spring and summer measurements in this thesis it is important to note that the spring time measurements are of the stems of the birch forest (SAI - Stem Area Index), whereas the summer measurements incorporate both the stems and leaves (PAI - Plant Area Index). For consistency this thesis uses the term LAI to describe the canopy area for both spring and summer knowing that the spring canopy is leafless stems or branches.

Hemispherical photography

Hemispherical photography has been used widely [*Anderson*, 1964; *Chen et al.*, 1991, 1997b; *Frazer et al.*, 2001; *Jonckheere et al.*, 2005; *Leblanc et al.*, 2005; *Rhoads et al.*, 2004] as an indirect method to assess canopy structure and therefore the radiation regimes in forests. It requires an upward looking camera and wide angle lens, usually with a viewing angle of 180° to take a photograph of the canopy and its openings in all directions simultaneously [*Hardy et al.*, 2004; *Gonsamo et al.*, 2011]. Digital cameras have removed the need for scanners to digitise the images, which can be quickly viewed on the camera and downloaded to a laptop [*Leblanc et al.*, 2005].

There is a range of commercial and free software available for the analysis of hemispherical photographs including Gap Light Analyser (GLA) [*Frazer et al.*, 1999; *Hardy et al.*, 2004; *Rhoads et al.*, 2004], Hemiview (Delta-T Device, Cambridge, UK) [*Rich et al.*, 1999], CIMES [*Gonsamo et al.*, 2011; *Inoue et al.*, 2011], CAN-EYE [*Weiss and Baret*, 2010] and WinScanopy (Regent Instruments, Quebec, Canada) [*Jarcuska et al.*, 2010; *Macfarlane et al.*, 2007]. One of the main challenges of using hemispherical photography is in the analysis, in particular the thresholding of the images [*Jonckheere et al.*, 2005; *Gonsamo et al.*, 2011]. Thresholding is the optimal selection of brightness value to distinguish between the sky and vegetation [*Jonckheere et al.*, 2005; *Nobis and Hunziker*, 2005] usually performed as a visual comparison of the full colour photograph with black (vegetation) and white (sky) images. Most software packages involve the manual selection of thresholds which can be a source of error as they are subjective [*Englund et al.*, 2000; *Frazer et al.*, 2001; *Jonckheere et al.*, 2005; *Nobis and Hunziker*, 2005]. To remove this subjectivity, automatic thresholding should replace this manual selection process which ensures objectivity,

and repeatability [*Gonsamo et al.*, 2011]. Software such as SideLook [*Nobis*, 2005] have been developed for the automated thresholding of images [*Nobis and Hunziker*, 2005].

1.5 Snow

Snow cover in the high latitudes and altitudes has an important role in both atmospheric and land surface processes [*Sicart et al.*, 2004], in particular the surface energy budget, the hydrological balance and the surface gas exchange [*Lemke et al.*, 2007; *Groisman et al.*, 1994]. The high surface reflectivity or albedo of the snow surface has a strong positive feedback on the climate system, and other weaker feedbacks on moisture storage, latent heat and ground heat flux, and vegetation [*Clark et al.*, 1999]. However, the strength of these feedbacks is dependent upon the depth and age of the snow cover, vegetation cover, vegetation height, the amount of incoming solar radiation and cloud cover [*Lemke et al.*, 2007]. The wide range of model predictions of the snow-albedo feedback mechanisms have been attributed to the masking of snow albedo by forests [*Qu and Hall*, 2014].

Snow cover interacts strongly with vegetation [*Harding and Pomeroy*, 1996], and is particularly sensitive to the structure of the canopy in boreal forests [*Sicart et al.*, 2004]. The work by *Harding and Pomeroy* [1996] found a dramatic difference in the energy balance of an open pine forest canopy and open area (on a frozen lake) while the net downward flux of radiation is positive over the forest canopy, but it is negative over the open area. The high albedo of the snow surface reflects most of the incident solar radiation, whereas vegetation canopies scatter and absorb most of the incoming solar radiation due to the low albedo of the vegetation [*Harding and Pomeroy*, 1996].

1.5.1 Measurements of snow

There are a variety of methodologies available to quantify the depth, water equivalent and areal extent of snowpacks. A range of ground, aircraft and satellite techniques are available for the measurement of precipitation, snowfall, snowpack, or snowmelt and water output parameters, but the specific technique is dependent upon the parameter required.

Precipitation can be measured using a standard storage gauge, a universal gauge and radar, but these are prone to error and impracticalities especially in remote sites and for solid precipitation. Snowfall measurements can be made with a ruler held up against a board set on the surface of the previous snowfall, a universal gauge and radar. Although it is not within the scope of the current research to discuss these measurement techniques in detail, there is a wealth of literature on the

respective problems and inaccuracies of these measurement techniques [*Adam and Lettenmaier*, 2003; *Bowling et al.*, 2003; *Goodison et al.*, 1981, 1998].

In-situ measurements of snowpack properties

The height of a snowpack can be measured by simply inserting a snow stake into the snowpack to the ground surface and reading the depth of the snow on the stake [*Dingman*, 2002; *Goodison et al.*, 1981]. However, for a hydrologist the most important measurement of a snowpack is the Snow Water Equivalent (SWE) [*Dingman*, 2002].

SWE is typically obtained by snow surveys at fixed locations, called snow courses, where a series of measurements are taken at regularly spaced intervals (5 or 6) along a path between 150 to 250 m long, dependent upon the terrain [*Dingman*, 2002; *Pomeroy et al.*, 1995]. At each point a snow tube is inserted into the snowpack to the ground surface, where a depth measurement is taken. It is then pushed further into the soil surface, and twisted to secure a small soil plug which retains the snow inside [*Dingman*, 2002]. The tube is then removed from the snowpack, the soil plug is carefully removed minimising the loss of snow from the sample, and then the tube weighed [*Dingman*, 2002]. The depth of the snowpack and weight of the sample can then be used to calculate the SWE. To encompass a wide range of environmental conditions, snow courses are typically conducted over relatively large spatial scales [*Dingman*, 2002]. Snow courses should be designed such that they include a range of vegetation cover, slope, aspect and elevation, to gain a representative picture of the snowpack in the area of interest [*Dingman*, 2002]. These factors, particularly vegetation cover, contribute to variability in snowpacks [*Pomeroy et al.*, 2002, 1998], and variability associated with vegetation cover will be addressed in this research. Although some work has shown the snow tubes overestimate the water equivalent by up to 10 % [*Goodison et al.*, 1981; *Work et al.*, 1965], they are usually the most accurate measurements of water equivalent [*Dingman*, 2002].

Alternatively snow pits can also be used to assess the depth, density and SWE of a snow pack. As a full profile of the snow pack is exposed, a snow cutter can be inserted into the snowpack to take samples at increasing depths (every 10 cm) through the snowpack, this is weighed and can be used to measure changes in density and SWE within the snowpack.

Remote sensing of snowpack properties

Passive microwave sensors on satellites have the potential to monitor snow cover, snow depth and SWE, unimpeded by cloud cover and winter darkness on a global scale [*Lemke et al.*, 2007]. However, few sensors are available for observational and real-time data measurement of snow covered areas at a regional and continental scale [*Foppa et al.*, 2007]. Polar orbiting optical observation instruments include the Advanced Very High Resolution Radiometer (AVHRR), Moderate Resolution Imaging Spectroradiometer (MODIS), Medium Resolution Imaging Spectrometer Instrument (MERIS), Advanced Along Track Scanning Radiometer (AATSR) and VEGETATION [*Foppa et al.*, 2007; *Maisongrande et al.*, 2004]. There are other Geostationary satellite systems including Geostationary Operational Environmental Satellites (GOES) and Meteosat Second Generation (MSG) which provide high temporal resolution of SCA [*Foppa et al.*, 2007]. However, the premier data set used to evaluate large-scale SCA, which dates from 1966 and is the longest satellite-derived environmental data set of any kind, is the weekly visible wavelength satellite maps of Northern Hemisphere snow cover produced by the US National Oceanic and Atmospheric Administration (NOAA) National Environmental Satellite Data and Information Service (NESDIS) [*Clark et al.*, 1999; *Lemke et al.*, 2007; *Robinson et al.*, 1993].

The National Operational Hydrologic Remote Sensing Center (NOHRSC) and the National Snow and Ice Data Center (NSIDC) publish and distribute snow cover products on a continental to hemispherical scale based on a variety of satellite imagery (for example AVHRR, GOES, MODIS, and Special Sensor Microwave/Imager (SSM/I)) at various spatial resolutions [*Foppa et al.*, 2007]. However, there are problems with homogeneity between the Scanning Multi-channel Microwave Radiometer (SMMR), used from 1978 to 1987, and the SSM/I, used from 1987 to present [*Lemke et al.*, 2007].

GlobSnow [*Takala et al.*, 2011; *Pulliainen*, 2006] was a European Space Agency (ESA) project which delivered northern hemisphere scale snow water equivalent (SWE) for 33 (1979 - 2012) years using data gathered from two different space-borne passive microwave sensors (SMMR and SSM/I) spanning 1979 to 2012 and ground based data [*Pulliainen*, 2006; *Takala et al.*, 2011]. This data-assimilated product can be used to assess modelled snow water equivalent for the northern hemisphere.

Characterisation of the vegetation parameters that influence seasonal dynamics of snow accumulation and ablation are important, and require defining as they partially conceal snow cover from satellite-based remote sensing instruments [*Nolin*, 2004]. A forest canopy can alter the retrieval of optical and microwave satellite data on snow covered areas [*Chang et al.*, 1996; *Klein et al.*, 1998]. Knowing the characteristics of the canopy would allow correction of the remotely sensed

information to obtain information on under-canopy snowpack properties of depth or SWE [*Chang et al.*, 1996; *Nolin*, 2004].

1.6 The energy balance

All mass and energy are conserved. Solar radiation and longwave radiation exchanged between the atmosphere and the earth's surface drive weather and climate [*Bonan*, 2002]. Shortwave radiation from the sun is absorbed by the aerosols, water vapour and clouds in the atmosphere [*King et al.*, 2008]. The re-scattering of this radiation produces diffuse radiation received in all directions [*Bonan*, 2002]. Direct beam radiation from the sun originates from the position of the sun in the sky, calculated from the angle of the sun above the horizon and its location with respect to compass direction [*Bonan*, 2002]. Incident radiation varies with the time of year, time of day, cloudiness, and atmospheric turbidity [*Bonan*, 2002; *King et al.*, 2008]. In the high latitudes of the Arctic the long path of radiation through the atmosphere increases the scattering of radiation. Therefore a greater percentage of diffuse radiation reaches the land surface relative to the percentage of direct beam radiation compared to lower latitudes [*Bonan*, 2002]. The net flux of shortwave radiation (SW_n) (W m^{-2}) is given by the following equation;

$$SW_n = SW_{\downarrow} + SW_{\uparrow} = SW_{\downarrow}(1 - \alpha) \tag{1.1}$$

Where $SW_{\downarrow}$ and $SW_{\uparrow}$ are the downward and upward components of shortwave radiation (W m^{-2}) and α is the albedo.

Longwave radiation is emitted from the sky, particularly atmospheric gases (water vapour and carbon dioxide), land surface, ground, and vegetation [*Bonan*, 2002; *King et al.*, 2008]. Incident longwave radiation is dependent upon the temperature, humidity, and cloudiness due to the strong absorption of infrared radiation by water vapour in the atmosphere [*King et al.*, 2008; *Ohmura*, 2001]. Therefore, the amount of longwave radiation to reach the land surface is particularly dependent upon the conditions in the lowest few hundred meters of the atmosphere [*King et al.*, 2008; *Ohmura*, 2001].

At high latitudes, the amount of longwave radiation can provide similar or higher amounts of energy as the shortwave radiation, due to the low solar elevation and cloud cover resulting from increased atmospheric emissivity [*Sicart et al.*, 2006]. Sparse canopies also increase the incoming longwave radiation to the snow surface in the high latitudes, due to the low solar angles of shortwave radiation. The role of longwave flux in the surface energy budget has therefore been

emphasized with concerns over global warming [*Sicart et al.*, 2006]. All matter warmer than -273.15 °C (0 Kelvin) emits longwave radiation (LW) (W m^{-2}) proportional to the temperature raised to the fourth power, for temperatures in degrees Celsius as follows;

$$LW = \varepsilon\sigma(T + 273.15)^4 \tag{1.2}$$

Where ε is the Emissivity, σ is the Stefan-Boltzmann constant (5.67 x 10^{-8} $\mathrm{Wm^{-2}K^{-4}}$), and T is the absolute temperature of the land surface in Kelvin (K) for the upward radiation component. The emissivity of the land surface varies between 0.9 and 1.0 [*Jin and Liang*, 2006], and approximately 0.96 to 0.99 for a snow covered surface. However, for the atmosphere the emissivity is a function of cloud cover and near surface humidity for partly cloudy skies, or near surface humidity for clear skies [*King et al.*, 2008]. Therefore incoming longwave radiation increases with cloud cover [*King et al.*, 2008] since cloud emissivity increases with cloud cover up to 0.5 for cirrus and 1.0 for dense cloud [*Kimball and Idso*, 1982]).

The warmed land surface loses heat through sensible and latent heat to the atmosphere, and re-radiates energy. Sensible and latent heat fluxes arise from eddies which carry heat and moisture away from the land surface and vary with the topography, vegetation, soils, and landforms [*Bonan*, 2002]. Therefore a simplistic view of the energy balance is as follows;

$$(1 - \alpha)SW_{\downarrow} + LW_{\downarrow} = LW_{\uparrow} + H + LE + G \tag{1.3}$$

Where $(1 - \alpha)SW_{\downarrow}$ is the absorbed shortwave radiation (W m^{-2}), $LW_{\downarrow}$ is the absorbed longwave radiation (W m^{-2}), $LW_{\uparrow}$ is the emitted longwave radiation (W m^{-2}), H is the sensible heat, LE is the latent heat and G is the heat exchange by conduction to the ground [*Bonan*, 2002]. In addition to this, although generally small and not included in the equation above, is the energy flux carried as either sensible or latent heat by precipitation and blowing snow [*King et al.*, 2008]. This thesis is focused on the radiation budgets, which generally account for most of the energy used in snowmelt [*Sicart et al.*, 2006]. Therefore the values of sensible and latent heat, and ground heat exchange are not evaluated here.

1.6.1 Measuring the radiation budget

The radiation budget has a direct influence on the amount of energy available for snowmelt, therefore accurate measurements of the downward and upward components of the short and longwave radiation are essential for accurate modelling of the snow melt and closing the radiation balance

[*Michel et al.*, 2008]. A range of commercial four component net radiometers consisting of two pyranometers ($SW_{\downarrow}$ and $SW_{\uparrow}$) and pyrgeometers ($LW_{\downarrow}$ and $LW_{\uparrow}$) are available. Although few studies have focused on the inter-comparison of these sensors, their assumptions and limitations [*Brotzge and Duchon*, 2000; *Halldin*, 2004; *Michel et al.*, 2008; *Kohsiek et al.*, 2007], generally the more accurate measurements have higher cost, maintenance and power requirements [*Brotzge and Duchon*, 2000]. They are standard micro-meteorology sensors, and providing care is taken in the installation and calibration, sensitivity studies have shown the measurements to be reliable [*Michel et al.*, 2008; *Kohsiek et al.*, 2007].

1.6.2 Previous studies of radiation balance of forests

The best method of establishing the light transmission through a forest canopy is using quantum sensors and data loggers providing information on the temporal variation in light and using multiple sensors to achieve spatial coverage [*Lieffers et al.*, 1999]. There has been research on the thermal and solar radiation regimes of sparse canopies [*Link et al.*, 2004] and discontinuous coniferous forests [*Hardy et al.*, 2004; *Pomeroy et al.*, 2008]. *Hardy et al.* [2004] shows that hemispherical photography and GLA can be used to predict canopy transmissivity to good agreement with quantum sensors for shortwave radiation, *Essery et al.* [2008b] has also used hemispherical photography to inform models of below canopy longwave radiation. Comparisons between radiometer configurations recommend a stationary array with multiple sensors in sparse forests [*Webster et al.*, 2016a].

Radiative transfer models have been developed and compared to study the radiation penetration through complex vegetation canopies [*Nijssen and Lettenmaier*, 1999; *Pinty et al.*, 2001, 2004; *Stähli et al.*, 2009; *Widlowski et al.*, 2007, 2011]. However, these models are difficult to integrate at the global scale into land surface models as they often contain complex physics [*Ni-Meister and Gao*, 2011], therefore there is a need for a simple solution to this complex issue.

1.6.3 Radiative transfer models

There are two main approaches in radiative transfer models "big leaf" and "multi-layered". Big leaf models attenuate radiation according to Beer's law using a light extinction coefficient and compute fluxes of energy, water and CO_2 as one single big leaf scaled to the whole canopy [*Dai et al.*, 2004; *Clark et al.*, 2011]. Big leaf models are computationally efficient [*Dai et al.*, 2004] and have therefore been used extensively in land surface modelling [*Cox et al.*, 1999; *Dai et al.*, 2003; *Dickinson et al.*, 1998; *Sellers et al.*, 1992]. Multi-layered models integrate fluxes of energy, water

and CO_2 over a number of canopy layers (typically 10) based on the two stream approximation of radiation interception from *Sellers* [1985], in which each canopy layer has an incoming and outgoing flux of direct and diffuse radiation [*Clark et al.*, 2011] based on zenith angle and leaf angle distribution. Multi-layered models also include options for light limited photosynthesis and respiration, sunlit and shaded leaves, sun fleck penetration and leaf nitrogen concentrations [*Clark et al.*, 2011; *Dai et al.*, 2004].

1.7 Modelling

Modelled future climate projections for the Arctic include warmer air temperatures, reduced snow covered area especially in autumn and spring, reduced mean snow covered area, and the timing of the spring melt will be earlier. Climate models simulate large changes in temperature in the northern latitudes, due to the strong positive feedback of enhanced temperatures reducing snow cover [*Harding and Pomeroy*, 1996]. Snow cover is particularly sensitive to climate change and variability, for example small changes in temperature could have a strong effect on the surface energy balance (radiative, sensible, latent and ground heat fluxes), phase changes, and the albedo of the snowpack [*Harding and Pomeroy*, 1996; *Lemke et al.*, 2007; *Groisman et al.*, 1994]. It is therefore important to determine what effects these changes in the duration and early melt of the snow cover will have on the radiative balance and overall surface energy budget.

Studies focused on assessing and measuring the properties of forest canopies are often ultimately used to improve a mathematical or computer model of the forest. Previous studies on the energy balance of forested ecosystems have been used in the development of energy balance and hydrological models. A simple model which simulates shaded gap areas has been shown to improve the estimates of shortwave irradiance at the snow surface, compared to models with no gap shading [*Bewley et al.*, 2007].

1.7.1 Land surface models

Land surface models compute the lower boundary conditions of the General Circulation Models (GCM) used in climate prediction. They can also be run off line from the GCM with historic atmospheric driving data and as such are a useful tool for investigating the past response of the land surface to the atmosphere, which can be compared to observations as a quality check of the model. There are many land surface models being developed by academic communities including the Canadian Land Surface Scheme (CLASS) [*Verseghy et al.*, 1993], Community Land Model (CLM) [*Oleson et al.*, 2010], Tiled ECMWF Scheme for Surface Exchanges over Land model (TESSEL) [*Viterbo and Beljaars*, 1995] and JULES [*Best et al.*, 2011; *Clark et al.*, 2011].

The representation of radiative transfer in vegetation canopies and the interactions between snow and vegetation is very simple in land surface models [*Essery et al.*, 2008a; *Harding and Pomeroy*, 1996]. The vegetation canopy is treated as being continuously homogeneous, and an average radiation is calculated [*Essery et al.*, 2008a]. However sparsely vegetated canopies with significant canopy gaps are highly heterogeneous. Some sophisticated land surface models predict radiative fluxes beneath the vegetation canopy, but they have high data input and parameter requirements [*Essery et al.*, 2008b].

JULES: The Joint UK Land Environment Simulator

JULES is a community land surface model and forms the land surface component of the Hadley centre GCMs [*Best et al.*, 2011; *Clark et al.*, 2011; *Blyth et al.*, 2011]. JULES was developed from the Met Office Surface Exchange Scheme (MOSES) [*Cox et al.*, 1999; *Essery et al.*, 2002]. JULES and its predecessor MOSES have been the subject of a number of important research papers on snow cover [*Parajka et al.*, 2010], permafrost [*Dankers et al.*, 2011], runoff [*Gedney et al.*, 2006], benchmarking tests [*Blyth et al.*, 2011], and carbon-cycle feedbacks [*Cox et al.*, 2000]. The JULES model has also been part of several land surface model intercomparison projects including land surface parameterisation schemes PILPS [*Henderson-Sellers et al.*, 1995], solar radiation partitioning in RAMI4PILPS [*Widlowski et al.*, 2011], snow parameterisation in PILPS - Phase 2d [*Slater et al.*, 2001] and SNOWMIP2 [*Essery et al.*, 2009; *Rutter et al.*, 2009] and the Global Soil Wetness Project (GSWP - 2) [*Dirmeyer et al.*, 2006] and AMMA Land Surface Model Intercomparison Project (ALMIP) looking at the land-atmosphere feedbacks over West Africa [*Boone et al.*, 2009].

The meteorological forcing data required to drive JULES are shortwave and longwave radiation, precipitation, wind speed, air temperature, specific humidity and surface pressure [*Best et al.*, 2011]. JULES has a tiled land surface scheme, which allows for heterogeneity at the land surface. The 9 different land surface tile options are bare soil, ice, water, urban and five vegetation covers; a Broadleaf tree (BLT), Needleleaf tree (NLT), C3 grass, C4 grass and Shrub (Figure 7.1).

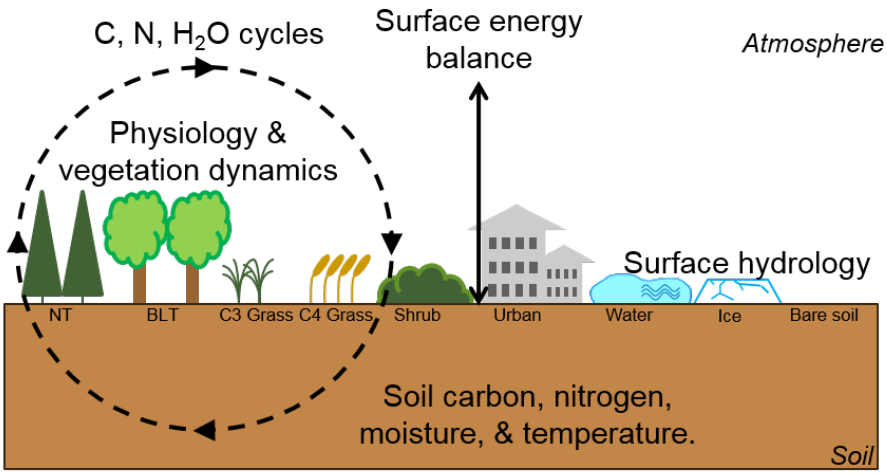

Figure 1.4: Schematic to show a tree, shaded gap and tundra tile in JULES.

JULES uses a two-stream approach for canopy albedo and photosynthesis [*Best et al.*, 2011; *Clark et al.*, 2011], but in the surface energy balance there is no transmission of shortwave radiation through the forest canopy; JULES treats forested ecosystems as though there is a continuous canopy cover (Figure 1.5). At present, the tree canopy in JULES emits longwave radiation from the canopy downwards to the ground (or snow) surface and upwards to the atmosphere based on tile surface temperature and emissivity [*Best et al.*, 2011]. The total longwave radiation (W m^{-2}) to the snow (ground) surface ($LW_{\downarrow\, tot}$) is as follows:

$$LW_{\downarrow\, tot} = v\sigma T_*^4 + (1 - v)LW_{\downarrow} \tag{1.4}$$

Where v is the canopy fractional cover, σ is the Stefan Boltzmann constant, T_* is the tile temperature at 1.5 m above the canopy (Kelvin), and $LW_{\downarrow}$ is the above canopy downward longwave radiation (W m^{-2}) (forcing data). Canopy temperature is calculated using the areal heat capacity C_S (J m^{-2} K^{-1}) as follows:

$$C_S = C_L B_L + C_W B_W \tag{1.5}$$

Where C_L is the specific heat capacity of leaf biomass (J kgC^{-1} K^{-1}), C_W is the specific heat capacity of the woody biomass (J kgC^{-1} K^{-1}), B_L is the leaf biomass (kgC m^{-2}) and B_W is the woody biomass (kgC m^{-2}).

This model of the surface energy balance may be sufficient to represent the energy balance of dense evergreen coniferous forest stands where shortwave radiation penetration to the ground

surface is low, but in sparse discontinuous deciduous forest stands where there are large gaps between the trees, and shortwave radiation penetration to the ground surface is high this may be inadequate. The problem is amplified in sparse forests which also have a seasonal snowcover as the high albedo of the forest understorey reflects much of the solar radiation. However, in the Arctic, the solar elevation is low in early spring and therefore the incidence with the canopy is higher and casts shadows over the snow surface. As the season progresses the solar elevation increases and the forest floor is increasingly illuminated. At present JULES does not take account of the variability in the solar elevation or the gaps between the trees. In the future JULES might be improved through inclusion of the multi-layered two stream approximation to calculate canopy photosynthesis in the radiation balance but this is not currently an option in the model. It is therefore the aim of this thesis to develop a land surface scheme that takes account of this variability in forest structure, and its impact on the radiation balance.

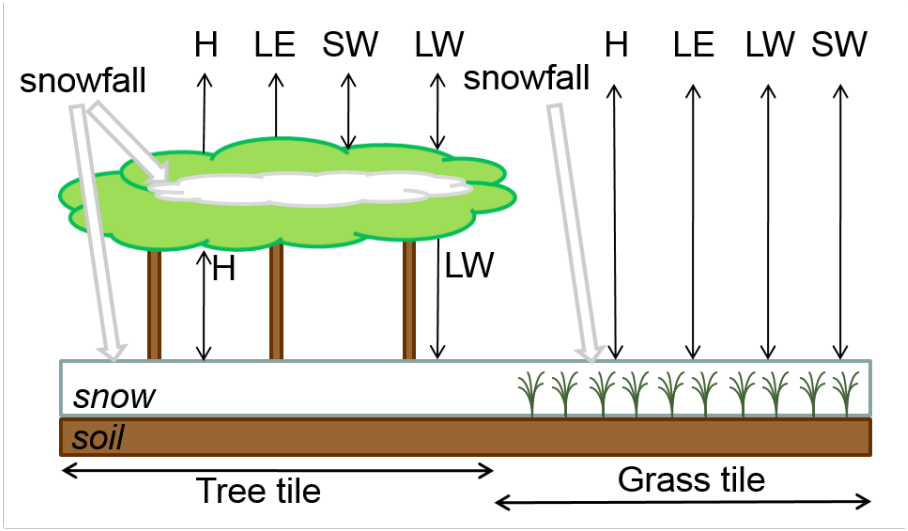

Figure 1.5: Schematic to show the current vegetation tile options for representing the sparse birch forest in JULES; a tree and grass tile.

1.8 Research gaps

Climate change has been at its most pronounced in the high latitudes of the Arctic, which has already experienced enhanced temperatures, reduced snow cover extent and duration. It is important that we understand how current and future climate change will impact on Arctic ecosystems. The boreal forest directly to the south of the Arctic tundra is characterized by limiting environmental and climatic conditions and is particularly sensitive to global warming. Changes in the boreal forest could have strong positive feedbacks on the climate particularly as it contains large stocks of soil carbon which could be released with warmer temperatures and an extended

active growing season. These processes are particularly important in sparse forests where the interaction between the vegetation and seasonal snow cover is strong. Snow cover has a strong influence on the surface energy budget, the hydrological balance and the surface gas exchange. Future projections of snow cover in the northern hemisphere estimate a dramatic reduction in overall snow covered area which would have a strong positive feedback on these processes.

The community land surface model JULES does not currently have a good representation of the surface processes of sparse forests with seasonal snow cover. This research will focus on improving the land surface interactions of the sparse forests with a seasonal snow cover, particularly in the snow melt period using the land surface model JULES.

1.9 Research aims

The overall aim of this thesis is to quantify the radiation balance of the sparse birch forest with a seasonal snowpack. Then, using these measurements to develop a model which accurately represents the energy fluxes in these forests to quantify the impact on the snowmelt. It is not clear which component of the radiation balance is most crucial to modelling these sparse forests, therefore a comprehensive field campaign is required to identify the key processes which the land surface model requires.

The aims outlined here were designed to address the following objectives.

1. Quantify the spatial and temporal properties of a sparse birch forest near Abisko, Sweden, specifically measuring the:
   (a) Canopy properties
   (b) Shortwave radiation distribution
   (c) Longwave radiation
   (d) Snowpack properties
   (e) Meteorological conditions
2. Quantify the effect of a sparse birch canopy on the mass balance of the snowpack.
3. Determine the effect of a sparse birch canopy on the penetration of shortwave and longwave radiation through the canopy to the surface of a snowpack.
4. Evaluate the representation of these processes within a current land surface model.
5. Provide a new scheme for use within climate models to represent these processes.

6. Build and evaluate the new model using measurements taken in the sparse birch forest from spring 2008 and 2009.

1.10 Thesis outline

Chapter 2 outlines the study site and the methodologies employed to collect field data.

Chapter 3 details the fieldwork canopy measurements.

Chapter 4 details the fieldwork radiation measurements.

Chapter 5 details the fieldwork snowpack measurements.

Chapter 6 details the meteorological data.

Chapter 7 details the current representation of these processes in a land surface model and proposes parameterisations of the Shaded Gap tile.

In the final chapter 8, there is a general discussion of the major conclusions and recommendations of the project in relation to the published literature, and a summary of the key findings.

Study site

2.1 Introduction

The purpose of this chapter is to outline the specific measurement techniques employed in a program of field work conducted in two spring seasons in Abisko, northern Sweden, in 2008 and 2009. The primary aim of this study was to determine the variability in the shortwave and longwave radiation which reaches the surface of the snowpack in a sparse birch forest canopy. To achieve this, measurements using pyranometers, hemispherical photography and thermocouples were taken in a sparse deciduous birch forest. In addition, snow surveys were taken to diagnose the impact of the radiation on snowmelt. The measurement plan was limited by both financial resources and time.

The best method for continuously recording the variability in the light environment of a particular site is using quantum sensors [*Lieffers et al.*, 1999]. As discussed in the previous chapter pyranometers have been used extensively to measure shortwave radiation under forest canopies [*Link et al.*, 2004; *Essery et al.*, 2008a; *Hardy et al.*, 2004; *Bewley et al.*, 2007; *Pomeroy et al.*, 2008]. Hemispherical photos have also been used extensively in studies to quantify the forest structure and its influence on the radiation regimes. Hemispherical photography provides useful estimates of the sky view fraction [*Essery et al.*, 2008b; *Hardy et al.*, 2004]. Relative to the cost of the shortwave radiation sensors, measuring the forest with hemispherical photographs enables a much wider area to be assessed cheaply. Snow surveys have been used extensively to measure the properties of snowpacks. In this study the measurements of the snowpack will be used to understand the role of shortwave radiation in snowmelt.

This chapter will outline the fieldwork program designed to quantify the shortwave and longwave radiation from the atmosphere and forest to reach the snow surface. Firstly the shortwave radiation measured by the pyranometer array will be discussed, followed by hemispherical photography, an array of thermocouples and infrared thermometers and finally snow surveys to assess the impact of radiation on the snowmelt. Survey grids and transects will be used to explore the different

aspects of the spatial heterogeneity of the landscape (see Section 2.3.3). Unless stated otherwise the same methods were employed to collect meteorological and hydrological data sets for both field seasons.

2.2 Study site location

Abisko is located in the northern limits of Sweden, in the Lappland Province, situated in the Scandes mountain chain of Scandinavia. It is located 200 km inside the Arctic Circle at 68°32N and 18°83E, on the southern shores of Lake Torneträsk (Figure 2.1). The ABACUS research group established a field site in an area of sparse forest in Abisko, Sweden on the northern flank of Nissunsnuohkki, at 410615.906, 7580681.110 (Easting and Northing UTM) at an elevation of 570 m. There was an established meteorological tower with an array of instruments taking standard meteorological measurements, in addition to many other work packages taking detailed measurements of the soil, fluxes, and canopy characteristics. To make full use of the available meteorological data, it was decided to take field measurements in the vicinity of this established field site.

(a) Fennoscandia (b) Abisko

Figure 2.1: Field site location

The study site is considered to have a sub-Arctic climate, as the proximity to the Atlantic Ocean maintains a warmer climate compared to areas of similar latitude [*Andersson et al.*, 1996]. The mean air temperature in Abisko is 11 °C in July and -11.9 °C in January (30 year means for 1961 to 1990 [*Andersson et al.*, 1996]), but can plunge as low as -20 °C to -40 °C in the extremely harsh winters [*Tenow*, 1996]. The mean annual temperature for 1913 - 2000 was 0.7 °C [*Kohler et al.*, 2006]. It is a relatively dry site with a continental climate, due to the rain shadow effect of the mountains to the west [*Carlsson et al.*, 1999; *Kohler et al.*, 2006]. The mean annual

precipitation at the Abisko Scientific Research Station (ANS) (388 m a.s.l.), is 310 mm (mean for 1913 to 2000 [*Kohler et al.*, 2006]) and the ratio of snow relative to total precipitation is ca. 50 % [*Barnekow*, 1999]. Whereas at Katterjokk, 25 km west of Abisko the mean annual precipitation was 848 mm for 1960 to 1990. The snow season typically starts in October and ends in May, with the maximum monthly snow depth occurring in March, with a mean of 51.5 cm for the period 1913 to 2004 [*Kohler et al.*, 2006].

The site is located in an area of sparse birch *Betula pubescens* ssp. *czerepanovii* forest with an understorey vegetation that was dominated by *Empetrum nigrum* spp. *hermaphroditum*, *Vaccinium uliginosum*, *V. myrtillus* and *V. vitis-idaea*. The trees are polycormic (multiple stems), produced by basal sprouting, allowing contact with the root system during growth and development [*Tenow et al.*, 2004]. The soil was a micro-podzol, with a shallow organic layer [*Hartley et al.*, 2010].

The field work for this study was conducted from March to April in 2008, and from March to June in 2009. The data loggers and sensors were left running from April to June in 2008, however some data sets were not available for this period due to problems with the logging systems.

2.2.1 Ethics statement

The ABACUS research group selected the study site in consultation with the local Sámi community. The site was selected as not to interfere with the reindeer activities, particularly during the breeding season. All the logging systems and sensors were removed from the study site at the end of each field season until the following year, with the exception of the Automatic Weather Station.

2.3 Fieldwork methodologies

The following section outlines the program of fieldwork undertaken for this thesis, the results of which will be presented in Chapters 3 to 6.

2.3.1 Automatic Weather Station

The JULES model requires a continuous set of meteorological forcing data of shortwave radiation, longwave radiation, precipitation, wind speed, air temperature, specific humidity and pressure for each time step. It is possible to force JULES with downscaled climate data or meteorological data from the Abisko ANS meteorological station however, meteorological data from the field site is preferable over both of these options. The ABACUS research group established an Automatic

Weather Station (AWS) on a 6 m tower at the study site in 2006 (Figure 2.2). The AWS had two systems installed, one measuring conditions above the canopy and another measuring conditions within the canopy and at the ground surface. For the purposes of this study the meteorological data from the AWS will be used to force the JULES model from September 2007 to September 2009.

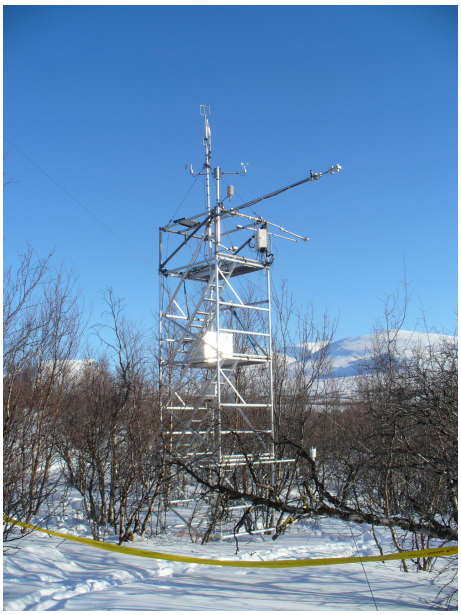

Figure 2.2: Automatic Weather Station (AWS) at the study site.

Above the canopy the meteorological measurements included incoming and outgoing longwave radiation (Four component Net Radiometer, CNR1, Kipp & Zonen, Delft, The Netherlands), incoming and outgoing shortwave radiation (CNR1), incoming direct and diffuse radiation (Sunshine sensor, BF3, Delta-T, Cambridge, UK), temperature, relative humidity, atmospheric pressure, photosynthetic photo flux density (PPFD) (PAR sensor, Skye Instruments, Llandrindod Wells, Wales), wind speed and direction (sonic anemometer, R3, Gill Instruments, Lymington, UK) and sensible heat, latent heat and CO_2 fluxes (Open path IRGA, 7500, Li-Cor Inc., Lincoln, USA).

The within canopy measurement system comprised of a weather transmitter measuring wind speed and direction, precipitation, atmospheric pressure, temperature and relative humidity (WXT510, Vaisala, Helsinki, Finland), incoming longwave radiation to the ground/snow surface (Pyrgeometer, CGR3, Kipp & Zonen, Delft, The Netherlands), soil heat flux, ground/snow surface temperature (IRT 4000; 4GL, Everest Interscience Inc., Tucson, USA), and the temperature of the south-facing side of a birch tree (IRT 4000; 4GL, Everest Interscience Inc., Tucson, USA).

These data were sampled every 10 seconds and the averages of these data were logged every 30 minutes on CR10X data loggers (Campbell Scientific, Logan, Utah), with SM4M storage modules. The data on the storage modules were downloaded by using a SC532 interface (Campbell Scientific, Logan, Utah) to connect the storage modules to a PC using Loggernet software (Campbell Scientific, Logan, Utah).

Quality control of AWS data

The data collected from the automatic weather station (AWS) at the study site is quality controlled by ABACUS work package 4 (CEH Wallingford) and freely available to ABACUS research students. These data are presented and analysed in Chapter 6.2.

2.3.2 Shortwave pyranometer array

Below canopy incoming shortwave radiation was measured using an array of 12 pyranometers (Skye Instruments, Llandrindod Wells, Powys) in spring 2008 and 2009. The pyranometers were distributed within a circular area of 30 m in diameter (limited by cable length from the data logger) across the snow surface. The pyranometers were located under a range of canopy covers to capture the variability in below canopy shortwave radiation in the sparse forest. To capture the variability in the diffuse shortwave radiation the pyranometers were located in areas of very sparse canopy cover through to areas of denser canopy cover, and to capture the variability in direct shortwave radiation the pyranometers were located in areas which were open to the east, south or west. Therefore the pyranometer locations could have similar values of canopy cover but very different direct shortwave radiation regimes.

Calibration 2008

To ensure that each of the pyranometers were measuring the same values they were calibrated against regularly maintained and calibrated pyranometers. The twelve shortwave pyranometers were exposed at the same location as a four component Net radiometer CNR1 (Kipp & Zonen, Delft, The Netherlands) which measures incoming and outgoing shortwave radiation using two thermopile pyranometers with a spectral range from 0.3 to 3μm. The CNR1 at Howberry Field, CEH Wallingford is regularly maintained, calibrated, and often used as the reference instrument for lower performance radiometers. The 12 pyranometers were mounted and levelled to within $\pm$0.02 degrees using an electronic levelling device in the calibration jig (Figure 2.3). The sensors were exposed on days 40 to 42 (9 - 11 February) in 2008 in Howberry Field. Ten minute average

data were logged to a CR10X data logger (Campbell Scientific, Logan, Utah). A linear regression was then performed comparing each pyranometer individually to the CNR1 (Figure 2.4).

Figure 2.3: The pyranometer calibration jig and 12 shortwave radiation pyranometers exposed on Howberry Field, CEH Wallingford for calibration.

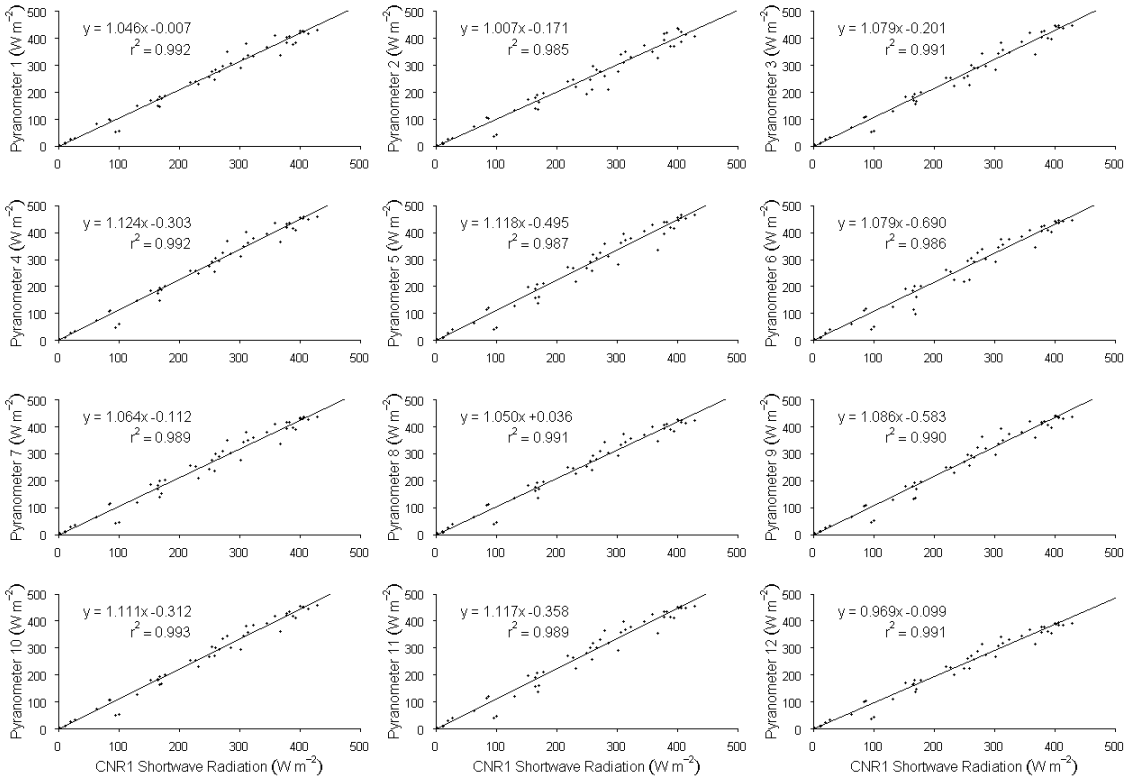

Figure 2.4: Linear regressions of shortwave radiation (W m^{-2}) measured by 12 Skye pyranometers and shortwave radiation (W m^{-2}) measured by a calibrated CNR1 (Kipp & Zonen) on Howberry Field, at CEH Wallingford for days 40 to 42 in 2008.

The shortwave radiation measured by the twelve pyranometers showed a strong positive relationship with the shortwave radiation measured by the CNR1 in Howberry Field, ($r^2 \geqslant 0.985$). The

total incoming shortwave radiation measured from the CNR1 and the observed mean pyranometer (pre-calibration) and the corrected mean pyranometer (post-calibration) shortwave array data are presented in Figure 2.5.

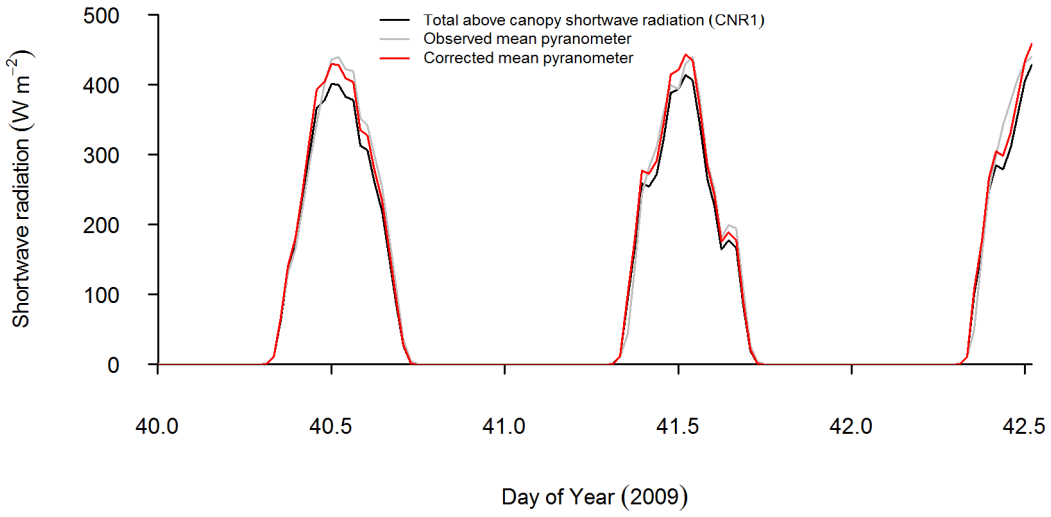

Figure 2.5: Incoming total shortwave radiation (W m^{-2}) measured on Howberry field, CEH Wallingford on the 9 to 11 February 2008 by a CNR1 (black), the observed mean pyranometer (grey) and the corrected mean pyranometer after calibration using the CNR1 (red).

Post calibration the shortwave pyranometer array measurements were more similar to those measurements taken by the CNR1, Figure 2.6 shows the 12 individual pyranometer observations and their corrected values. These corrections were applied to the pyranometer measurements taken in Abisko for 2008 data.

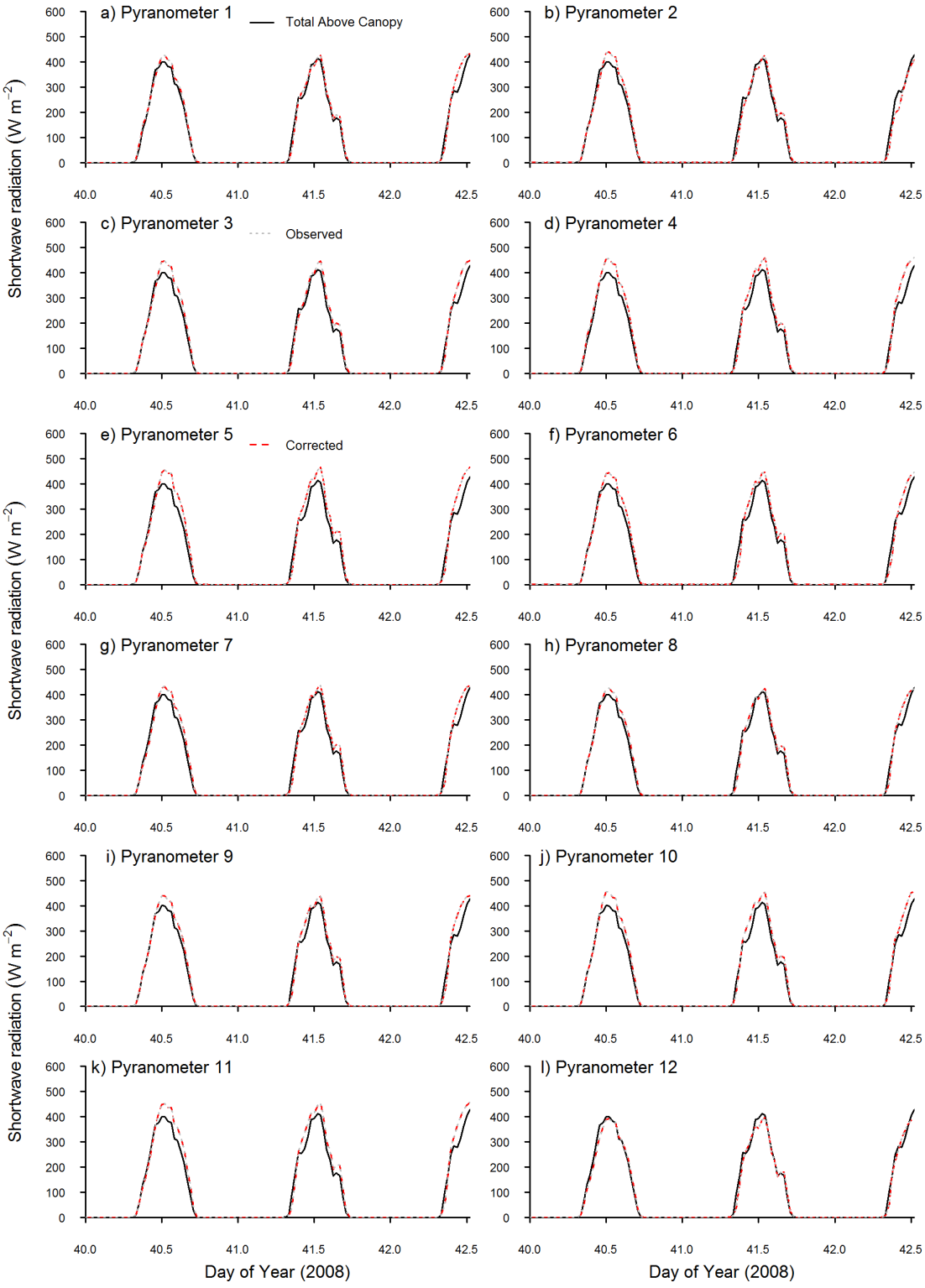

Figure 2.6: Incoming total shortwave radiation (W m^{-2}) measured on Howberry field, CEH Wallingford on the 28 to 31 March 2009 by a CNR1 (black), for the 12 observed pyranometers (grey) and the 12 corrected pyranometers after calibration with the CNR1 (red).

Calibration 2009

The same methods for calibration from 2008 were employed in 2009 for calibration of the pyranometers, except the location, days and instrument. The pyranometers were located in the calibration jig in a large area of open tundra very close to the AWS site on days 86 to 90 (27 March - 31 March). A well maintained CNR1 four component net radiometer positioned above the canopy was used as the reference radiometer. A linear regression was performed comparing each pyranometer individually to the CNR1 (Figure 2.7) and corrections were applied to the pyranometer measurements for 2009 data. Figure 2.8 shows the 12 individual pyranometer observations and their corrected values, while Figure 2.9 shows the mean observed pyranometer and the mean corrected pyranometer.

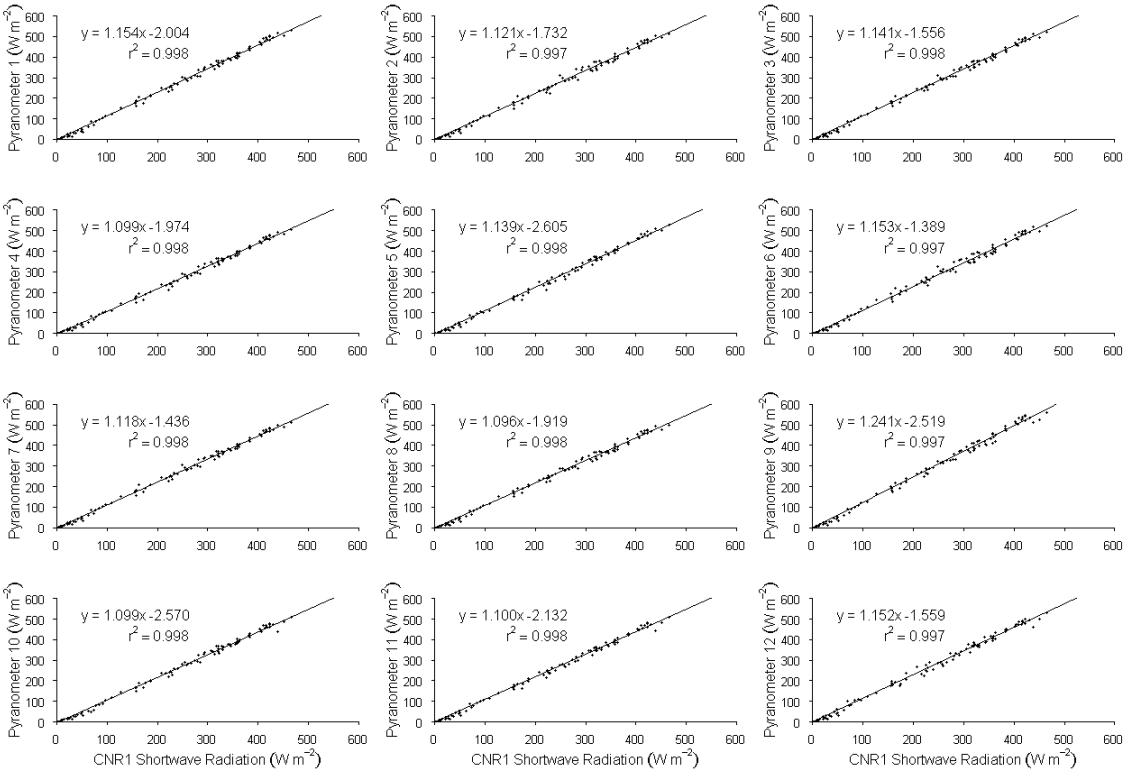

Figure 2.7: Linear regressions of shortwave radiation (W m^{-2}) measured by 12 Skye pyranometers (measured at an open site near the ABACUS birch site) and shortwave radiation (W m^{-2}) measured by a calibrated CNR1 (Kipp & Zonen) (measured at the ABACUS birch site AWS) for days 86 to 90 in 2009.

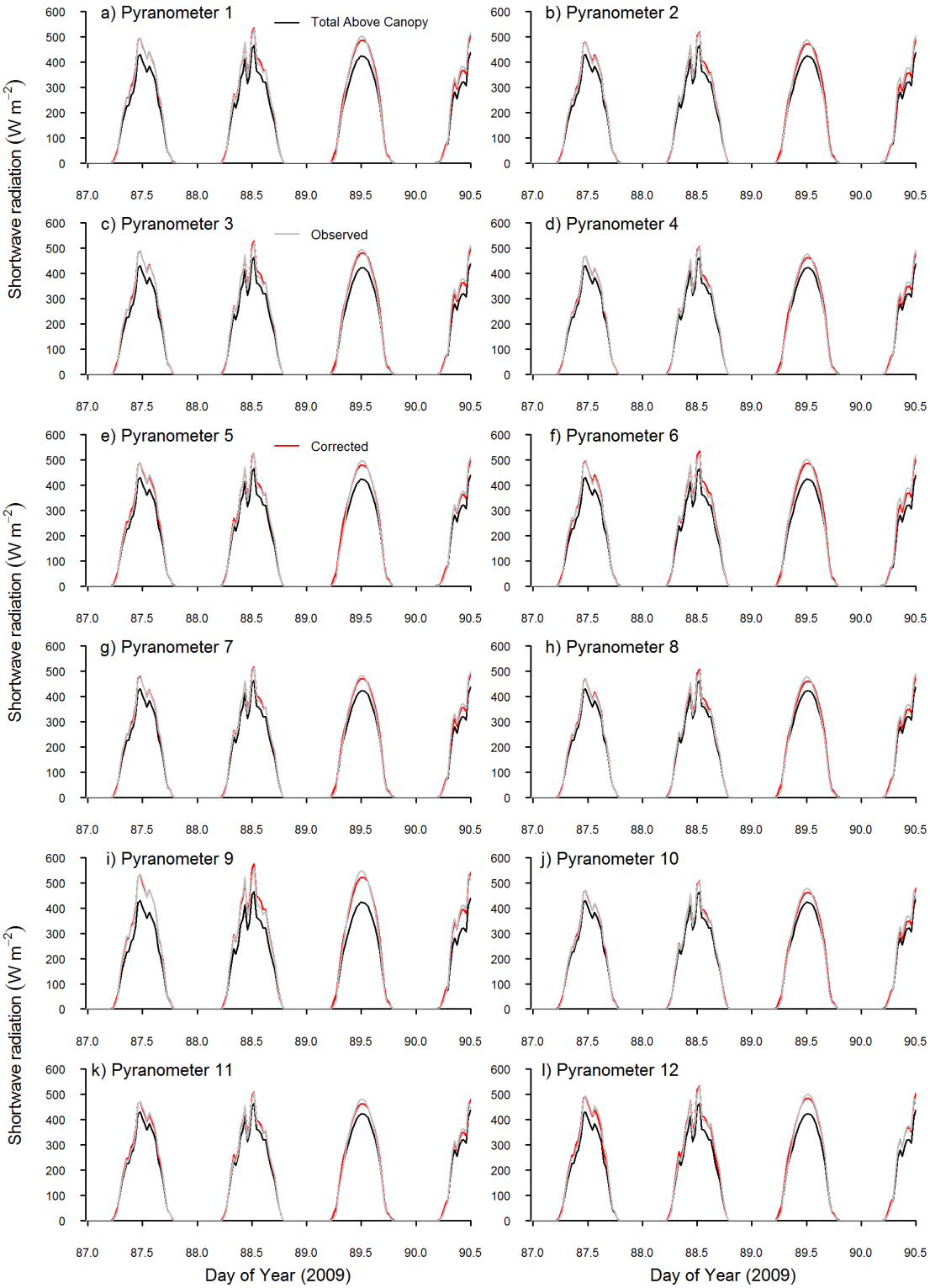

Figure 2.8: Incoming shortwave radiation (W m^{-2}) measured on the ABACUS birch forest tower, on the 28 to 31 March 2009 by a CNR1 the total above canopy shortwave radiation (black), for the 12 observed pyranometers (grey) and the 12 corrected pyranometers after calibration with the CNR1 (red).

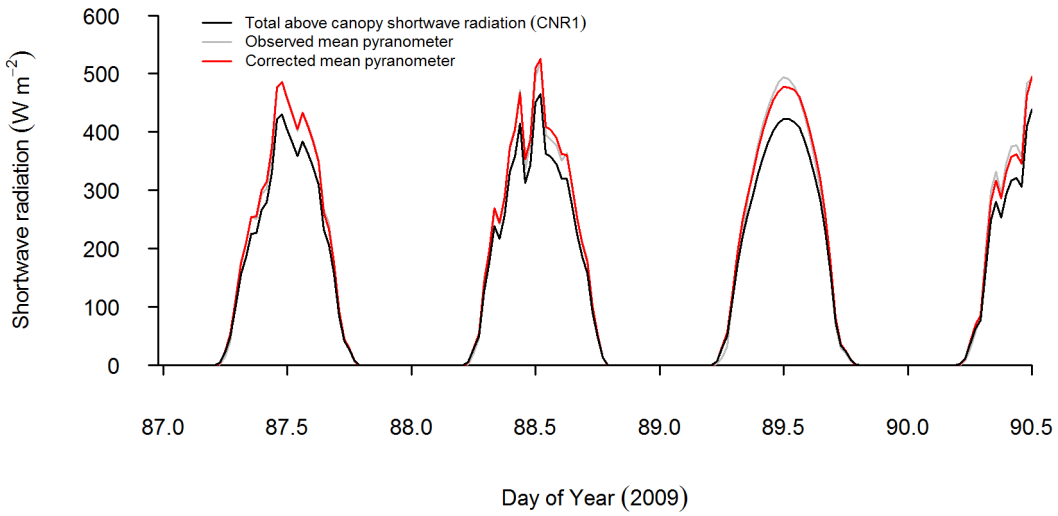

Figure 2.9: Incoming shortwave radiation (W m^{-2}) measured on the ABACUS birch forest tower, on the 28 to 31 March 2009 by a CNR1 the total above canopy shortwave radiation (black), the observed mean pyranometer (grey) and the corrected mean pyranometer after calibration using the CNR1 (red).

Study site deployment

The pyranometers were deployed for the period 29 March to 25 April in 2008 and 31 March to 18 June 2009. The locations of the pyranometers were designed to measure the natural variability in canopy cover, and were located at 12 different locations within a circular area of 30 m in diameter of birch forest, within close proximity to the ABACUS AWS (Automatic Weather Station) (Figure 2.10). This gave 24 unique pyranometer locations for the two years, for a continuous period of 30 days (91 - 121) in 2008 and 80 days (90 - 170) in 2009. The LIDAR data shows the canopy height, which is highly variable within the areas that the pyranometers are sampling.

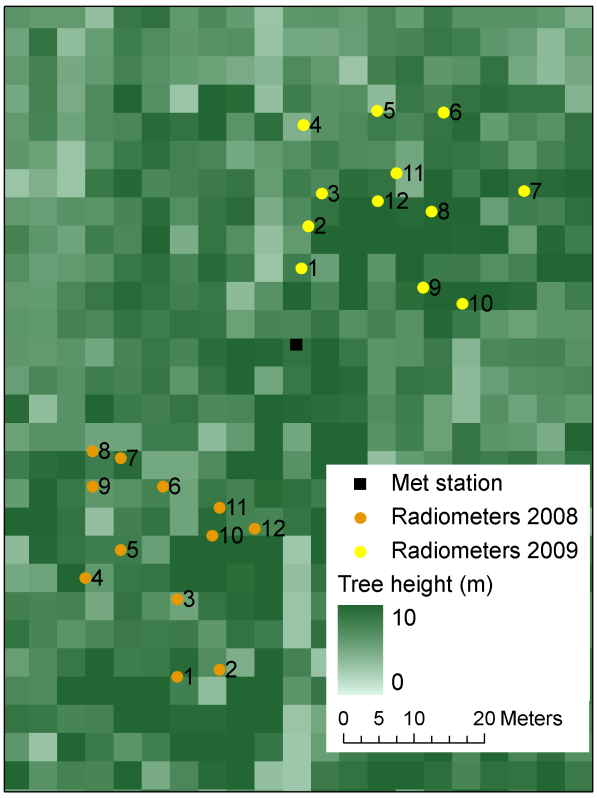

Figure 2.10: Pyranometer locations for 2008 (orange) and 2009 (yellow) with tree height (m) calculated from LIDAR data (Essery pers. comm.) taken in summer 2004.

Sensors were sampled every 10 seconds, and averages were logged every 10 minutes for the period 29th March to 25th April 2008, after which the sensors were sampled every 10 seconds and an average logged every 30 minutes. The pyranometers were located within a levelling device, which was placed on top of a block of wood to provide stability in the snowmelt period (Figure 2.11). The levelling devices consisted of three screws, a bubble level and a small cup which held the pyranometer in place. These were crossed checked using an electronic levelling device to ensure they were level to within $\pm$ 0.02 degrees. The sensors were levelled and cleaned from snow, frost or dew a minimum of twice a day, usually at 11am and 6pm, and at a higher frequency during snowfall events.

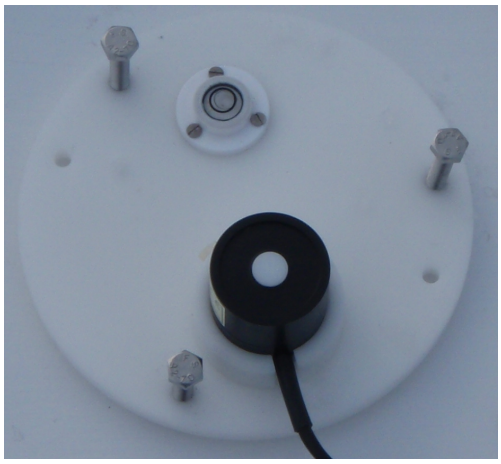

Figure 2.11: Pyranometer held within levelling device and mounted on a wooden base on the snow surface.

Analysis of shortwave pyranometer array

The pyranometer data set were quality controlled to remove any periods of erroneous data. These instances included periods of snow fall or dew on the sensor, or disturbance to the levelling device causing the pyranometer to no longer be level. As the pyranometers were checked twice daily, data were removed from the most recent checked point until the problem was resolved. The high frequency of checking these instruments allowed for only minimal loss of data points.

Once the data were downloaded corrections were applied as calculated in the previous calibration periods from Howberry Field in 2008 and Abisko in 2009.

Whenever possible the sunshine sensor (BF3) was used as an above canopy reference for the direct and diffuse components of incoming shortwave radiation. However, there were periods when the BF3 data were not available and so the CNR1 measuring above canopy total incoming and outgoing shortwave radiation was used. These above canopy data allowed a canopy transmissivity to be calculated based on the measured shortwave radiation. This was compared to an estimate of transmissivity calculated using a hemispherical photograph taken above the pyranometer, and analysed with Gap Light Analyser (GLA) software (Section 2.3.3). GLA can also be used to calculate the percentage canopy cover and LAI for each pyranometer location.

2.3.3 Hemispherical photographs

A camera (Nikon Coolpix 4300) with a fish eye lens (Nikon FC-E8 0.21x) and converter ring (UR-E4), was set up on a tripod approximately 50 cm above the surface of the snow and pyranometer, aligned to magnetic North and levelled (N-S & E-W) to take photos of the forest canopy (Figure 2.12). The camera was set to "Fisheye 1" and an image size of 2272 by 1704 pixels was used. Wherever possible the photographs were taken on uniformly overcast days, to ensure homogeneous light levels across the whole photo. However, this was not possible for all locations.

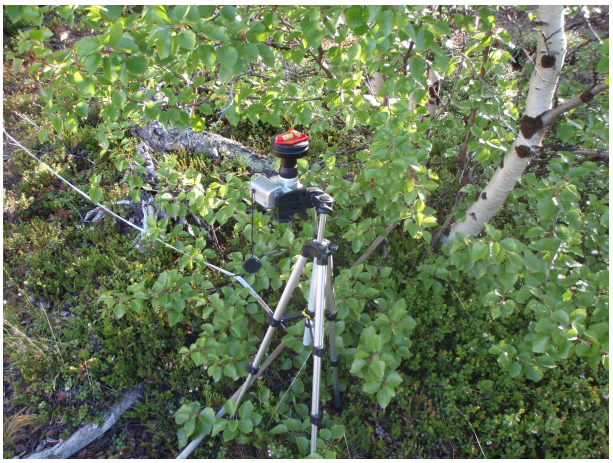

Figure 2.12: Camera with fish eye lens mounted on a tripod with levelling device.

Hemispherical photographs study site deployment

As the pyranometer array is limited to 12 pyranometers, survey grids (30 m by 30 m and 900 m^2) and survey transects (500 m) are used to study the canopy structure across a much wider area (the same as the snow survey grids and transects - see section 2.3.5 and Figures 2.18 and 2.20). Hemispherical photographs were taken at 5 m intervals in survey grids and transects in 2008 and 2009 (Table 2.1).

Table 2.1: Hemispherical photograph survey timetable. Spring refers to photographs taken prior to bud burst and leaf out. *Infra-red thermometers could not be measured in spring due to disturbance to the snowpack.

		Hemispherical Photos		
	Location	Spring	Summer	Autumn
2008	Pyranometers	27 March	8 July	15 October
	Survey Grids	20 - 28 March	7 - 8 July	
		(ABI2, ABI5 & ABI7)	(ABI2, ABI3, ABI5 & ABI7)	
2009	Pyranometers	1 April	20, 23 & 30 May	
			5, 8, 12 & 22 June	
	Survey Grids	16 & 17 May	15 & 21 June	
		(ABI2, ABI3 & ABI5)	(ABI2 & ABI5)	
	Survey Transects	13 - 15 May	15, 16, 21 & 23 June	
	Pryanometer Calibration Jig	1 April		
	Thermocouple Trees	17 May	22 June	
	Infra-red thermometers	*	22 June	

Analysis of hemispherical photographs

The hemispherical photos were analysed using Gap Light Analyser (GLA, version 2, Simon Fraser University, Burnaby, British Columbia, Canada). The software identifies light areas as sky and dark areas as vegetation to calculate a canopy openness, transmissivity and LAI. In GLA canopy openness (%) is defined as the percentage of open sky from beneath the forest canopy, LAI is defined as an effective leaf area index integrated over the zenith angle 0 to 75° [*Welles and Norman*, 1991], and transmissivity (%) is defined as the ratio of the sum of direct and diffuse radiation transmitted by the canopy to the sum of direct and diffuse above canopy incident radiation multiplied by 100. Prior to the analysis some hemispherical photos were digitally altered to account for the sky conditions, tree colour and snow on the ground. These included darkening the white bark of the trees, lightening areas of dark sky and darkening slopes covered in snow. Most of the problems were associated with non-uniform sky conditions, i.e. clouds, the sun or very dark sky.

The settings used during the GLA analysis were fixed for all the photographs. Each photo was configured for the latitude (68° North), longitude (19° East), and elevation of the birch study site (570 m a.s.l.). All the images were registered with an initial and final point in the x (1170 and 1170) and y (80 and 1650), a colour plane selected (typically blue due to the contrast which best

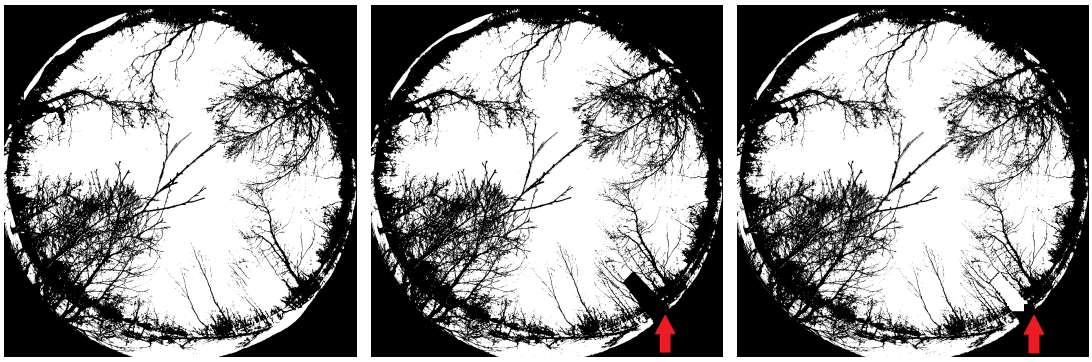

(a) Non-uniform sky with bright sunlight (b) Non-uniform sky with a stake (c) Non-uniform sky with the stake removed

Figure 2.13: Hemispherical photos after GLA analysis for the survey grid ABI5 at 15 m by 15 m. The wooden stake is in the bottom right hand corner of the image indicated by the red arrow.

discriminated between sky and vegetation) and the threshold of brightness was set individually for each photograph. The canopy structure and transmitted gap light were calculated, for the percentage canopy openness, leaf area index (LAI) and percentage transmissivity.

Calibration of GLA analysis of hemispherical photographs

To assess the impact of non-uniform sky conditions during the GLA analysis, bright sunlight in the survey grid ABI5 was blocked from reaching the fish eye lens using a wooden stake. Two photographs were taken; one with the wooden stake blocking the sun directly falling on the lens and a second without the stake with bright sunlight. The images shown in Figure 2.13 show three processed images taken in non-uniform sky, firstly with bright sunlight (Figure 2.13 panel a), secondly the same point with the wooden stake blocking the direct sunlight to the camera lens (Figure 2.13 panel b) and thirdly a post-processed image where the majority of the wooden stake was digitally removed prior to analysis (Figure 2.13 panel c). The sun and wooden stake is located to the south-west, seen in the bottom right-hand corner of the images.

The data shown in Table 2.2 shows the mean LAI, transmissivity and canopy openness for all 49 images taken in ABI5 using the three different sets of images. The results show that the photos analysed with bright sunlight had slightly higher canopy openness and transmissivity, and conversely a slightly lower LAI value. When the photographs containing the stake were analysed, there was a slight increase in the LAI and a decrease in transmissivity and canopy openness as would be expected when the stake was removed. When the photographs were post-processed (replaced the stake as sky) the values for the transmissivity and LAI were as calculated in the sunlight conditions (method a), and the canopy openness was approximately half way between the two values (methods a and b). In all cases the standard error of the mean was larger than

the difference measured between the three techniques and therefore there was no significant difference analysing images with sunlight or using a stake in bright sunlight conditions or post-processing the images to remove the stake. Therefore the post-processing of hemispherical photos to deal with non-uniform sky conditions was not required as it made limited difference to the results.

Table 2.2: Transmissivity (%), LAI and canopy openness calculated for the survey grid ABI5 in 2008 in non-uniform sky conditions with bright sunlight, non-uniform sky with a stake and non-uniform sky with the stake removed in post processing. The mean, standard deviation and standard error of the mean are shown.

		ABI5 survey grid		
		Non-uniform sky with bright sunlight	Non-uniform sky with a stake	Non-uniform sky with the stake removed
Transmissivity (%)	$\bar{x}$	80.96	79.65	80.71
	σ	10.49	10.19	10.29
	$\sigma_{\bar{x}}$	1.50	1.47	1.49
LAI	$\bar{x}$	0.23	0.24	0.23
	σ	0.16	0.16	0.16
	$\sigma_{\bar{x}}$	0.02	0.02	0.02
Canopy openness (%)	$\bar{x}$	73.07	71.82	72.81
	σ	10.14	9.87	10.00
	$\sigma_{\bar{x}}$	1.45	1.42	1.44

2.3.4 Longwave radiation measurement systems

The temperature of the snow surface, ground surface and birch trees were measured using an array of infrared thermometers and thermocouples. These instruments were arranged to measure the effects of variable canopy cover on the balance of longwave radiation between the birch forest and the snow surface (forest floor).

Calibration of infrared thermometers and thermocouples

Four infrared thermometers (Exergen) were connected to a Campbell data logger (CR1000) which was directly connected to a PC using Loggernet software (Campbell Scientific). The four

thermometers were mounted within an environmental chamber in which the temperature was set to known values of approximately -20 °C, -10 °C, 0 °C, 10 °C and 20 °C. For each of the temperatures the readings of the infrared thermometers were noted to calibrate the readings (Figure 2.14).

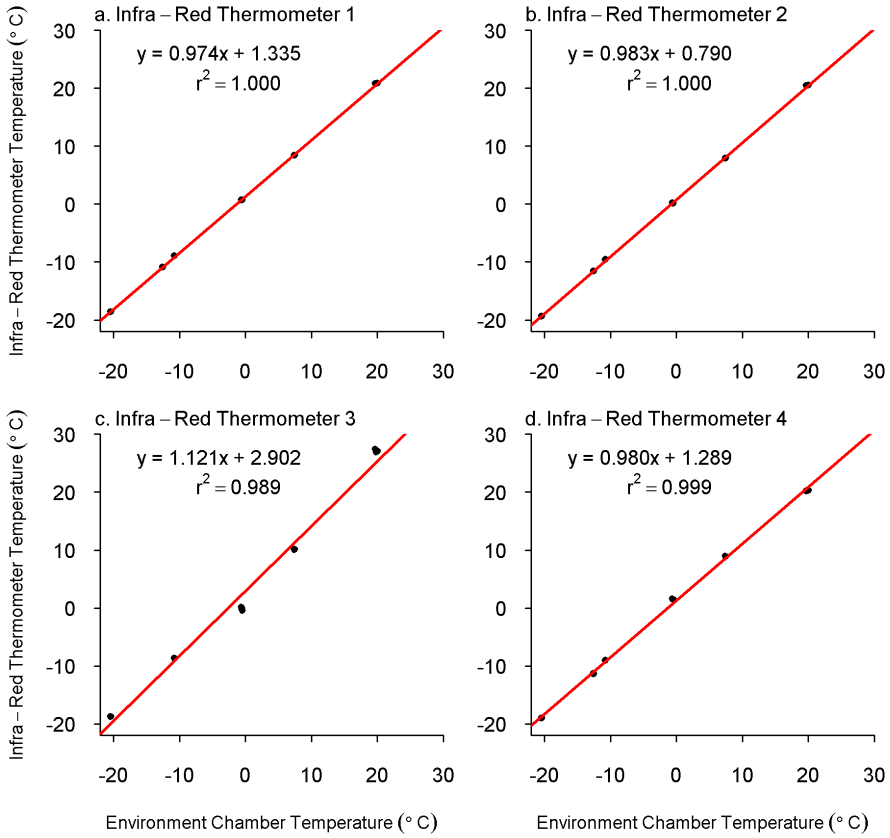

Figure 2.14: Linear regression of four infrared thermometers temperature (°C) against a controlled environment chamber temperature (°C).

The 20 thermocouples (type k) were calibrated in the laboratory as it was not possible to test them in the environment chamber. During the calibration period temperature varied between 18 °C and 21 °C over a 3.5 hour period. All of the thermocouples were regressed against thermocouple 5, except thermocouple 5 which was regressed with thermocouple 3. Thermocouple 5 measured closest to the mean observed temperature for all 20 thermocouples, and therefore to minimise errors in calibration was selected as the "known" temperature. Thermocouple 3 measured the second closest to the mean observed temperature and was therefore selected for the regression of thermocouple 5 (thermocouple 5 has the lowest multiplier with respect to the other 19 regressions but the r^2 was 0.928). The linear regressions (Figure 2.15) were used to calibrate the measurements.

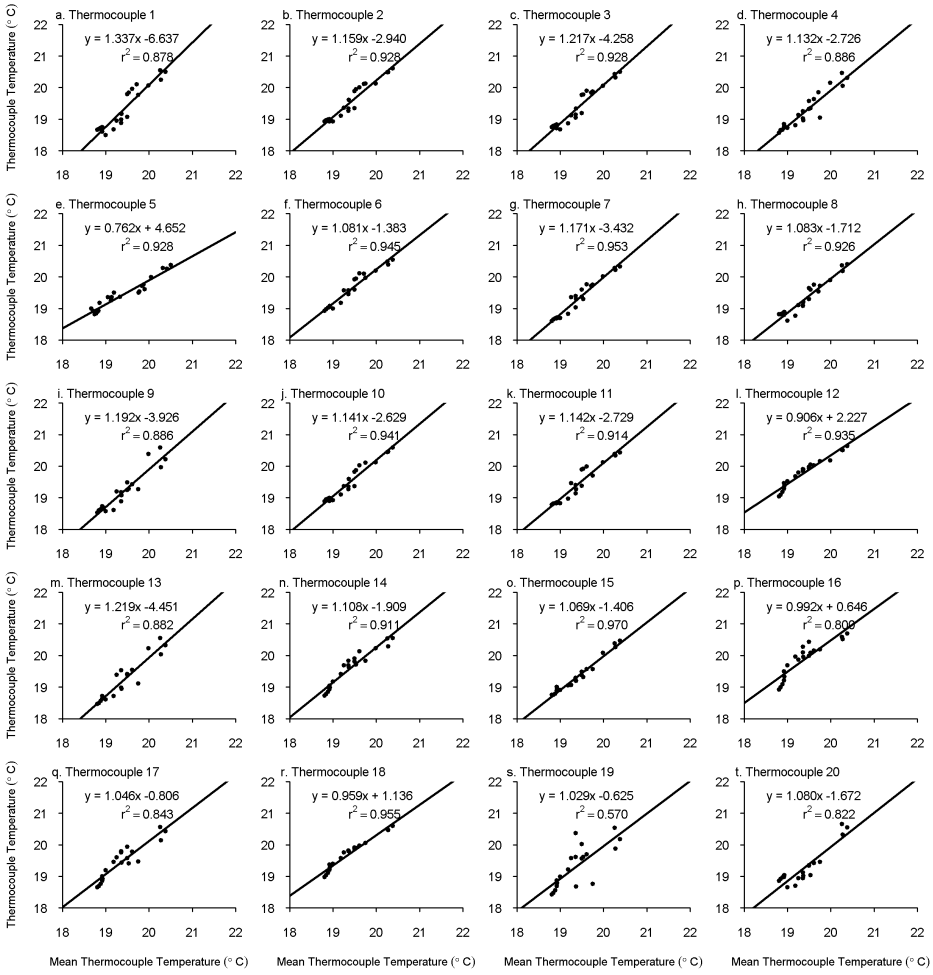

Figure 2.15: Linear regression of 20 thermocouples temperature (°C) against laboratory temperature (°C).

Thermocouple system study site deployment

The sensors installed on the thermocouple system included four infrared thermometers, twelve thermocouples, and a frost gauge which consisted of four thermocouples. The data were logged on a CR1000 (Campbell Scientific) data logger, and data stored to a compact flash card. The data was downloaded by connecting the compact flash card to a PC and downloading the data through Loggernet (Campbell Scientific Software).

Sensor locations in 2008

The thermocouple system was located in an area close to the radiometers (closest to radiometer 5), where there was an area of open snow, a monocormic tree and a polycormic tree. The surface temperature was recorded using three infrared thermometers, one measuring the temperature of the snow surface (Figure 2.16a - located on the tripod leg closest to camera), and two measuring areas of the forest floor which were snow free near the polycormic trees (2 and 3 in Figure 2.16b).

(a) An infrared thermometer measuring snow surface temperature, and frost gauge measuring snowpack temperatures.

(b) The thermocouple system: showing the south facing side of the thermocouple monocormic tree (1), and two polycormic trees, south facing (2) and east facing (3).

Figure 2.16: Snowpack and tree temperature measurement systems in 2008.

To measure the temperatures within the snowpack a thermocouple (type t) array was inserted into the snowpack (Figure 2.16a). Temperatures were recorded at 5 cm, 8 cm, 14 cm and 23 cm above the soil surface, fixed within a frost gauge (A piece of equipment designed by Colin Lloyd, CEH Wallingford), supported by a tripod. These data were logged on to a CR1000 (Campbell Scientific) data logger, and stored on a compact flash card. These data were downloaded by connecting the compact flash card to a PC and downloading data through Loggernet (Campbell Scientific Software).

The surface temperature of the west-facing side of a birch tree was recorded using an infrared thermometer.

An array of thermocouples (type k) were installed to measure the temperature of the trees at 1.5 m

(above the ground surface). Four thermocouples were installed in the cardinal compass points of three trees; a monocormic tree, and two branches of a polycormic tree facing south and east see Figure 2.16b. A small slit was cut into the outer bark of the tree and the thermocouples were inserted underneath the bark. The thermocouples were checked twice daily to ensure that they were held in position, and data were marked erroneous if the thermocouple had not been in position. To minimise solar load on the thermocouple wires the four wires for each branch were held to the north facing sides of the branch using cable ties.

Sensor locations in 2009

The thermocouple system was located in an area close to the radiometers (closest to radiometer 12), where there were several areas of open snow, a monocormic tree and a large polycormic tree. The ground surface temperature was recorded using three infrared thermometers installed above areas of snow cover within the birch forest see Figure 2.17a.

(a) Infrared thermometer measuring temperature of the snow surface.

(b) Infrared thermometer measuring temperature of the southern side of a monocormic tree.

Figure 2.17: Snowpack and tree temperature measurement in 2009.

The surface temperature of the trees were recorded using one infrared thermometer and an array of 20 thermocouples. The infrared thermometer measured the southern side of a monocormic tree (Figure 2.17b). The thermocouples were inserted into 5 branches from one polycormic tree, a central, north, east, south, and west facing branch. Four thermocouples were inserted into the four cardinal compass points of each branch.

2.3.5 Snow surveys

Spring 2008

To assess the impact of the radiation balance on the snowpack properties and snowmelt a series of snow surveys were established. It was not possible to take these measurements at the pyranometer locations due to disturbance of the snow. The snow surveys were selected to encompass the variability in the canopy cover. Therefore snow surveys were conducted in 30 m by 30 m (900 m^2) plots, of which four were within the birch forest (ABI2, ABI3, ABI5, and ABI7) close to the pyranometers and one plot was beyond the birch forest in an area of open tundra (ABI11) (Figure 2.18).

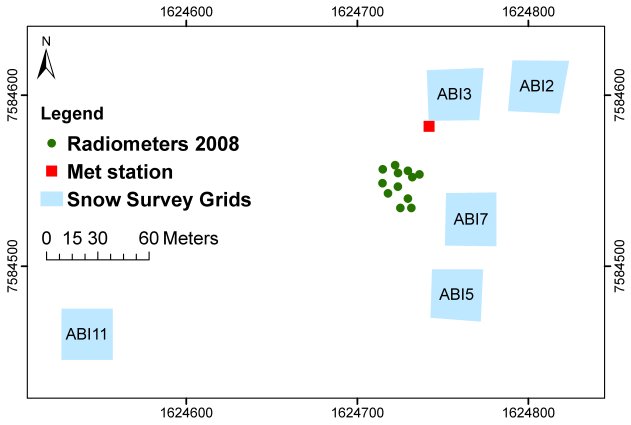

Figure 2.18: Study site showing the five snow survey grids used in 2008.

The depth and density of the snowpack were measured in each of the snow survey plots. Each plot was surveyed once in each of five time periods in the spring season (1st surveys were conducted: 18 - 31 March; 2nd surveys: 4 - 10 April; 3rd surveys: 10 - 15 April; 4th surveys: 20 - 21 April; and 5th surveys: 23 - 24 April). Snow depth probes were inserted into the snowpack to measure the depth of the snow on regular grids within each plot. Snow density measurements were taken in the four corners immediately outside of the plots, to prevent disturbance to the plot for future measurements. In spring 2008 snow density measurements were taken by digging snowpits (Figure 2.19a) and using a snow cutter to take samples of the snowpack (Figure 2.19b).

The first snow survey conducted in plot ABI3 was measured on a grid 2 m by 2 m, which gave 256 measurements of snow depth. This data set was used to calculate the most efficient sampling strategy for the remaining snow surveys (see Chapter 5.3.1). The remaining initial snow surveys (ABI2, ABI5, ABI7, ABI11) were conducted on a grid 5 m by 5 m (n = 49) and then repeat surveys were conducted every 5 m on transects spaced 10 m apart (n = 28).

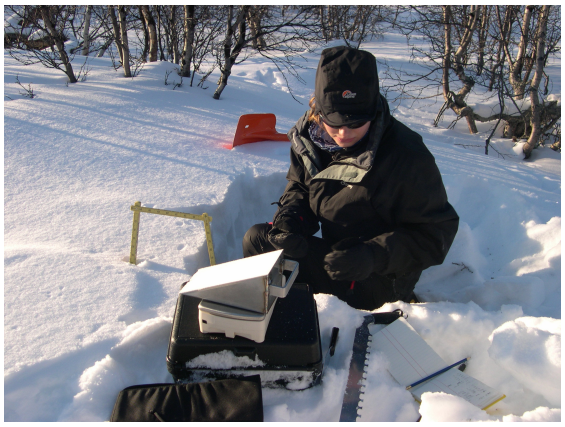

(a) Measurements being taken in a snow pit

(b) Weighing a snow sample taken using a snow cutter.

Figure 2.19: Snow sampling

Spring 2009

The gridded snow surveys from 2008 were repeated in 2009 for the grids ABI2 and ABI5. It was not possible to repeat the other grids due to constraints on time, sensor locations and access. Snow surveys were also conducted on four transects radiating out from the ABACUS AWS for up to 500 m (Figure 2.20). The snow depth measurements were taken every 5 m and snow density and SWE measurements were taken every 25 m along the transects. Density measurements were taken using a snow tube (Figure 2.21a) (Metric Prairie Snow Sampler, Geo Scientific Ltd., Vancouver, Canada). The tube negated the need for digging snow pits, and therefore allowed more frequent density measurements than in 2008. When the snow depth was too shallow for the snow tube, a shorter tube was used (Figure 2.21b).

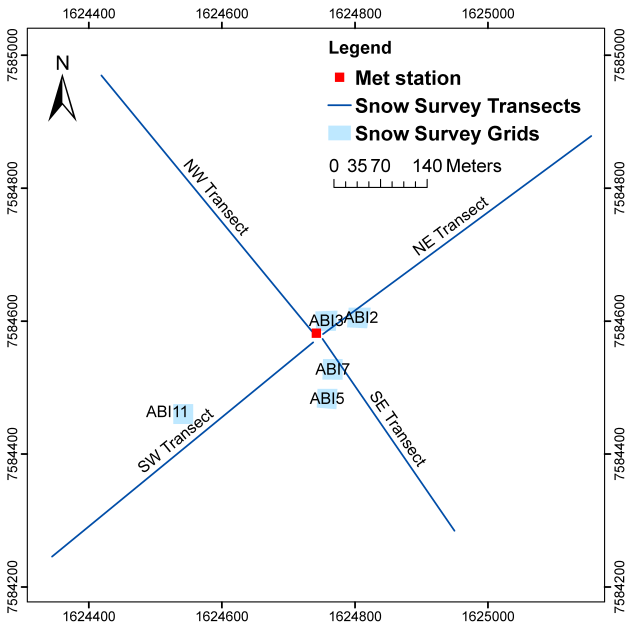

Figure 2.20: Study site showing the two snow survey grids (ABI2 and ABI5) and the four snow survey transects used in 2009. Note survey grids ABI3, ABI7 and ABI11 used in 2008 are shown as reference. Pyranometers were located within ABI3 in 2009, they are not shown due to large scale of map.

(a) Snow tube (b) Small snow tube

Figure 2.21: Snow tubes for measuring snow density

Continuous measurements

Snow depth was measured continuously in spring 2009 using a SR50 (Sonic Ranging Sensor - Campbell Scientific, Logan, Utah) directly west of the AWS (Figure 2.22). The snow depth was measured every 10 seconds and an average logged every minute.

Figure 2.22: A Sonic Ranging Sensor (SR50) measuring snow depth.

Analysis of snow surveys

During the snow surveys extreme care was taken with all samples to ensure minimal error to the weight of the snow tubes and snow cutter.

For the snow survey grids the depth, density and SWE measurements were averaged across the whole grid giving one value. Whereas in the snow survey transects the density measurements were taken every 25 m (providing 21 regular sampling points per transect except SE transect where there were 17 in 350 m). This was primarily due to the snow pit measurements being more time consuming than the snow tube measurements. The weight of the snow samples, with the depth of snow sample and sampling device volume were used to calculate the SWE and snow density.

2.4 Summary

The field site measurements detailed in this chapter have an important role in both model parameterisations and validation. Table 2.3 shows a summary of the tree canopy, radiation and snow measurements in both 2008 and 2009, the days when the measurements are available, and their purpose with respect to the JULES model. Table 2.4 shows a summary of the meteorological variables measured, how they were gap filled and the dates when they are available.

Table 2.3: Summary of canopy, radiation and snow measurements taken in 2008 and 2009, their location, timing and purpose with respect to the JULES model.

Measurement	2008	2009	Purpose
Hemispherical photos - Pyranometers	12 Spring, summer & autumn	12 Spring, & weekly through leaf out	Model parameters LAI & Sky view fraction
Hemispherical photos - Survey grids	Spring: ABI2, ABI5, & ABI7 Summer: ABI2, ABI3, ABI5, & ABI7	Spring: ABI2, ABI3 & ABI5 Summer: ABI2 & ABI5	Model parameters LAI & Sky view fraction
Hemispherical photos - Survey transects	Not available	NE 500 m, SE 350 m, SW 500 m, NW 500 m	Model parameters LAI & Sky view fraction
Longwave radiation - Below canopy	Day 103 - 116. Day 160 - 202	Not available	Model validation
Tree temperature	Day 96 - 181	Day 94 - 169	Explore viable below canopy Longwave radiation
Shortwave radiation - Below canopy	Day 94 - 96, 100 - 104, 106 - 116	Day 91 - 108, 110 - 169	Model validation
Longwave radiation - Below canopy	Day 103 - 116, 160 - 202	Not available	Model validation
Diffuse & total radiation - Above canopy	Day 94 - 115, 285 - 365	Day 1 - 12, 143 - 243	Model parameterisation - diff_frac_const
Snow surveys Grids (Depth, density & SWE)	Day 78 - 115 ABI2, ABI3, ABI5, ABI7, ABI11	Day 110 - 140 ABI2, ABI5	Model validation - SWE
Snow surveys Transects (Depth, density & SWE)	Not available	Day 86 - 139 NE, SW & NW 500 m, SE 350 m from the AWS through birch forest	Model validation - SWE
Continuous snow depth - SR50	Not available	Day 93 - 123	Model validation - Timing of snowmelt
Snow surface temperature	Day 96 - 125	Day 105 - 129	Model validation - Melt out date & T_*
Snowpack temperature	Day 96 - 120	Not available	Model validation - Melt out date & snow depth

Table 2.4: Summary of 30 minute meteorological measurements taken from 1 September 2007 to 1 September 2009 (35088 timesteps - 731 days) to force the JULES model.

Measurement	Adjustment
Shortwave radiation	ABACUS data gap filled with ANS data
Longwave radiation	ABACUS data, gap filled with ANS and Micromet data
Air temperature	ABACUS data
Relative humidity	ABACUS data
Wind speed	ABACUS data
Air pressure	ABACUS data gap filled with ANS data
Precipitation	ANS data - Micromet adjusted and under catch adjusted

Chapter 3

Fieldwork results: Canopy measurements

3.1 Introduction

This chapter will outline the results of the fieldwork program that quantified the canopy properties that impact the radiation balance. The canopy plays an important role in the radiative balance of these sparse forests, by cutting out the downward shortwave and longwave radiation penetration to the surface of the snow, but also acting as a source of longwave radiation down to the snowpack.

One of the primary objectives of this study was to determine the amount of shortwave radiation which penetrates down through the sparse forest canopies to the surface of the snowpack below. Therefore, quantitative and qualitative measurements of the forest canopy were required in order to assess the impact of the canopy on the shortwave radiation balance. To achieve this a series of hemispherical photograph surveys were undertaken designed to capture the spatial variability of the forest canopy during the spring and through the bud-burst into summer. Secondly to quantify the impact of the tree canopy on the below canopy longwave radiation budget, a series of tree temperature (thermocouple) measurements were taken. Thirdly, a longwave radiation pyrgeometer was installed below the canopy on the snow surface. In conjunction with the above canopy measurements of incoming longwave radiation these measurements can be used to investigate how the canopy alters the longwave radiation balance.

3.2 Methodology

The study site was selected for its representation of a sparse deciduous canopy in the Arctic. The methodology for the work presented in this chapter is outlined in Chapter 2. Unless stated otherwise the same methods were employed to collect the data sets for both field seasons.

3.3 Hemispherical photographs

Hemispherical photographs were used to quantify the transmissivity, canopy openness and LAI for a range of survey points. Hemispherical photographs were taken starting at the individual scale of the pyranometers, then expanding to the plot scale of the 30 m by 30 m (900 m^2) birch forest survey grids (every 5 m) and then finally covering the landscape scale of the four transects (every 5 m up to 500 m).

In 2008 hemispherical photos were taken for the 12 pyranometer locations and in the forested survey plots ABI2, ABI5, ABI7. In 2009 hemispherical photos were taken for the 12 pyranometer locations (different to the 12 of 2008); and in the forested plots ABI2, ABI3 and ABI5. Of these ABI2 and ABI5 were repeated in the summer, and the four transects were taken in both spring and summer.

Although the term Leaf Area Index (LAI) is used to compare the spring and summer measurements here it is important to note that the spring time measurements are of the stems of the birch forest (SAI - Stem Area Index), whereas the summer measurements incorporate both the stems and leaves (PAI - Plant Area Index). For consistency this study uses the term LAI to describe the canopy area for both spring and summer recognising that the spring canopy is leafless stems or branches.

In GLA canopy openness (%) is defined as the percentage of open sky seen from beneath the forest canopy, LAI is defined as an effective leaf area index integrated over the zenith angle 0 to 75° [*Welles and Norman*, 1991], and transmissivity (%) is defined as the ratio of the sum of direct and diffuse radiation transmitted by the canopy to the sum of direct and diffuse above canopy incident radiation multiplied by 100. These will be referred to as canopy openness, LAI and transmissivity.

3.3.1 Pyranometers

The hemispherical photographs taken at the 12 pyranometer locations are shown in Figure 3.1 for 2008 and in Figure 3.2 for 2009. Table 3.1 shows the canopy openness, LAI and transmissivity calculated for each of the 12 pyranometers using Gap Light Analyser (GLA) software for both years.

(a) Pyranometer 1 (b) Pyranometer 2 (c) Pyranometer 3

(d) Pyranometer 4 (e) Pyranometer 5 (f) Pyranometer 6

(g) Pyranometer 7 (h) Pyranometer 8 (i) Pyranometer 9

(j) Pyranometer 10 (k) Pyranometer 11 (l) Pyranometer 12

Figure 3.1: Hemispherical photographs for the pyranometers in 2008

(a) Pyranometer 1 (b) Pyranometer 2 (c) Pyranometer 3

(d) Pyranometer 4 (e) Pyranometer 5 (f) Pyranometer 6

(g) Pyranometer 7 (h) Pyranometer 8 (i) Pyranometer 9

(j) Pyranometer 10 (k) Pyranometer 11 (l) Pyranometer 12

Figure 3.2: Hemispherical photographs for the pyranometers in 2009

Figures 3.1 and 3.2 show that the pyranometers in 2008 and 2009 were distributed under variable canopy cover. These included very open canopies like pyranometer 1 in 2008 (Figure 3.1 panel a.) with a transmissivity of 86.76 % (Table 3.1), and pyranometer 9 (Figure 3.1 panel i.) with a transmissivity of 88.47 %. In 2009 pyranometer 4 (Figure 3.2 panel d.) had a transmissivity of 85.37 %, and pyranometer 7 (Figure 3.2 panel g.) had a transmissivity of 83.05 % (Table 3.1). There were also pyranometers distributed under denser canopy cover such as pyranometer 3 in 2008, which had a transmissivity of 66.23 %, and pyranometer 8 in 2009, which had a transmissivity of 65.75 %.

Overall the pyranometers show there is considerable variability in the canopy cover, but the mean of the canopy openness, LAI and transmissivity were similar for both years.

Table 3.1: Canopy openness (%), LAI and transmissivity (%) calculated for the pyranometers in 2008 and 2009. The mean, standard deviation and standard error of the mean are shown for spring 2008 and 2009.

	Pyranometers					
	2008			2009		
	Canopy openness (%)	LAI	Transmissivity (%)	Canopy openness (%)	LAI	Transmissivity (%)
Pyranometer 1	70.81	0.16	86.76	56.95	0.36	72.12
Pyranometer 2	51.84	0.49	64.73	61.37	0.30	72.65
Pyranometer 3	55.14	0.42	66.23	58.22	0.39	69.96
Pyranometer 4	78.79	0.08	89.36	73.58	0.12	85.37
Pyranometer 5	60.20	0.39	71.45	66.83	0.24	73.71
Pyranometer 6	58.80	0.40	68.89	68.62	0.22	79.39
Pyranometer 7	58.15	0.39	67.19	68.49	0.16	83.05
Pyranometer 8	65.13	0.29	78.36	57.38	0.44	65.75
Pyranometer 9	78.57	0.08	88.47	55.46	0.53	70.18
Pyranometer 10	63.77	0.25	74.30	65.21	0.34	77.48
Pyranometer 11	58.89	0.36	70.90	59.93	0.36	72.15
Pyranometer 12	56.68	0.38	71.18	58.23	0.38	64.18
$\bar{x}$	63.07	0.31	74.82	62.52	0.32	73.83
σ	8.79	0.14	8.85	5.82	0.12	6.44
$\sigma_{\bar{x}}$	2.54	0.04	2.56	1.68	0.03	1.86

3.3.2 Survey grids

Hemispherical photographs were taken for each of the birch forest survey grids. An example of the 49 photographs for the survey grid ABI2 is shown in Figure 3.3. These data show that over a 30 m by 30 m (900 m^2) area there was considerable variation in the canopy cover. The mean canopy openness was 74.5 %, the LAI was 0.18, and the transmissivity was 83.45 % (Table 3.2). The ABI2 survey grid had the highest transmissivity and the lowest LAI of all of the survey grids in 2008 and 2009. The canopy cover of the ABI2 survey grid in 2008 was also more open (74.5 %) than the canopy cover where the pyranometers were located in 2008 (63.1 %).

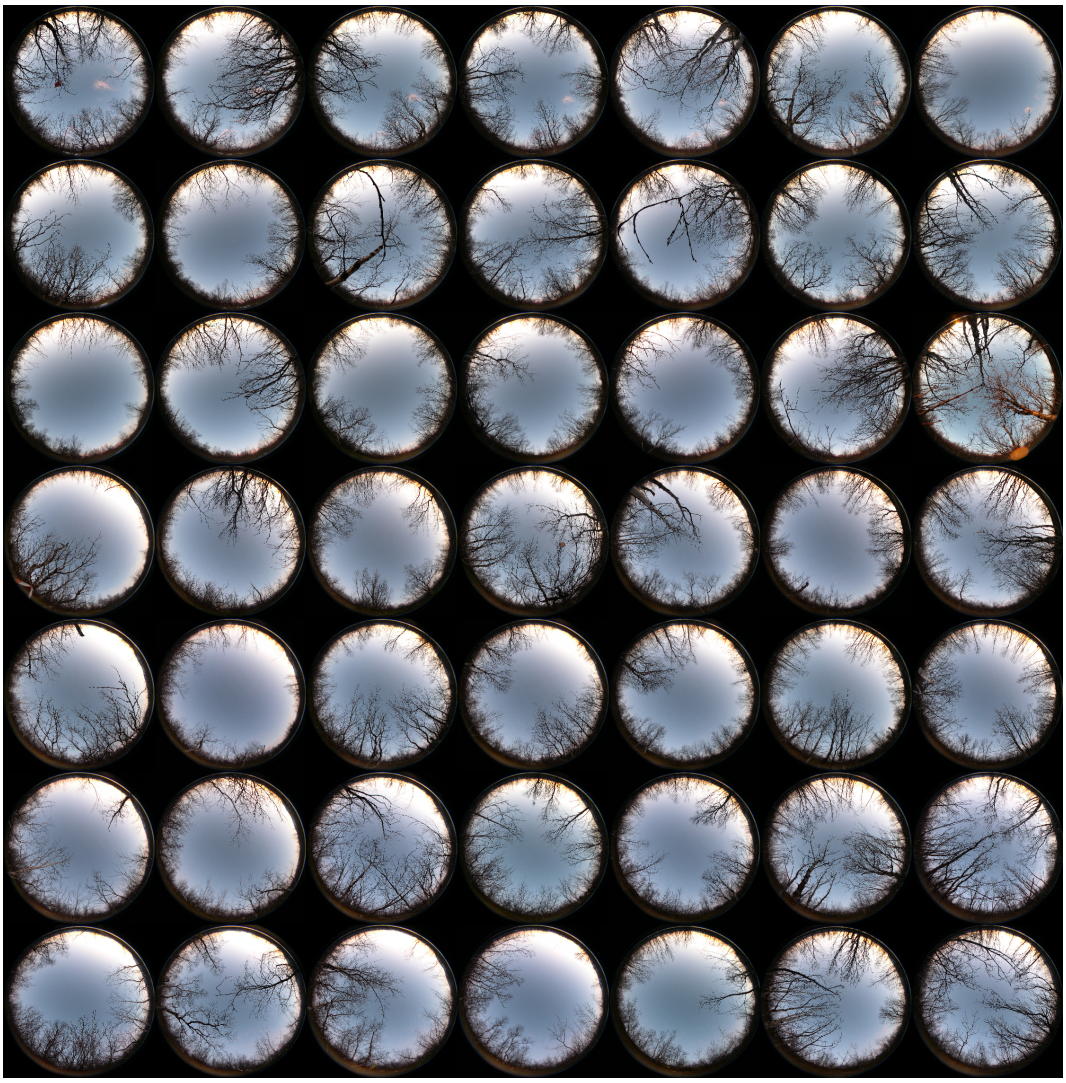

Figure 3.3: Hemispherical photos for snow survey grid ABI2 in spring 2008.

Table 3.2: Canopy openness (%), LAI and transmissivity (%) calculated for the survey grids. The mean, standard deviation and standard error of the mean are shown for spring and summer in 2008 and 2009 (n = 49 for all grids, except ABI2 in spring 2008 where n = 42). Table 2.1 shows the dates of hemispherical photographs.

			Survey Grids							
			Spring				Summer			
			ABI2	ABI3	ABI5	ABI7	ABI2	ABI3	ABI5	ABI7
Canopy openness (%)	2008	$\bar{x}$	74.50		73.07	71.53	42.52	37.04	36.58	34.51
		σ	5.91		10.14	7.36	10.50	13.88	12.32	11.84
		$\sigma_{\bar{x}}$	0.91		1.45	1.05	1.50	1.98	1.76	1.69
	2009	$\bar{x}$	66.66	60.35	57.26		45.89		40.51	
		σ	6.09	9.22	7.90		8.36		7.77	
		$\sigma_{\bar{x}}$	0.87	1.32	1.13		1.19		1.11	
LAI	2008	$\bar{x}$	0.18		0.23	0.22	0.75	0.98	0.95	1.04
		σ	0.10		0.16	0.12	0.30	0.40	0.38	0.41
		$\sigma_{\bar{x}}$	0.02		0.02	0.02	0.04	0.06	0.05	0.06
	2009	$\bar{x}$	0.23	0.36	0.38		0.64		0.80	
		σ	0.11	0.16	0.16		0.21		0.22	
		$\sigma_{\bar{x}}$	0.02	0.02	0.02		0.03		0.03	
Transmissivity (%)	2008	$\bar{x}$	83.43		80.96	81.67	52.34	46.99	44.09	46.03
		σ	6.78		10.49	8.13	12.95	15.52	13.73	15.81
		$\sigma_{\bar{x}}$	1.05		1.50	1.16	1.85	2.22	1.96	2.26
	2009	$\bar{x}$	76.95	70.16	66.00		55.89		48.66	
		σ	8.32	10.82	9.18		10.74		8.42	
		$\sigma_{\bar{x}}$	1.19	1.55	1.31		1.53		1.20	

Table 3.2 shows the canopy openness, LAI and transmissivity calculated for the four survey grids measured in spring and summer for 2008 and 2009. The canopy openness for the survey grids in spring 2008 were 74.5 %, 73.07 % and 71.53 % for ABI2, ABI5 and ABI7 respectively. There was considerable change in the spring time canopy openness when comparing ABI2 and ABI5 in 2008 to those of 2009, as the canopy openness decreased to 66.66 % in ABI2 and decreased in ABI5 from 73.07 % to 57.26 %. The transmissivity decreased from 83.43 % in 2008 to 76.95 % in 2009 for ABI2, and also from 80.96 % in 2008 to 66.00 % in 2009 for ABI5. There was a corresponding increase in LAI for ABI2 from 0.18 in 2008 to 0.23 in 2009 and for ABI5 from 0.23 in 2008 to 0.38 in 2009.

Survey grid ABI7 was only measured in 2008 and ABI3 was only measured in 2009, therefore it is difficult to make assumptions on the variability in the spring measurements between years. However, the measurements of transmissivity, LAI and canopy openness in ABI7 were very similar to the measurements of ABI5, and the measurements in ABI3 were an intermediate between ABI2 and ABI5 in 2009. In the summer of 2009, ABI3 had a canopy openness and a transmissivity which was an intermediate between ABI2 and ABI5, but a LAI higher than both survey grids at 0.98. ABI7 was not an intermediate between ABI2 and ABI5 for summer 2009, as it had the largest LAI at 1.04, and the lowest canopy cover at 34.51 % but the transmissivity was 46.03 % which was an intermediate between ABI2 and ABI5.

The summer measurements of canopy openness and transmissivity were lower than the spring measurements for all grids in both years, while the measurements of LAI were higher in the summer. Even in the very sparse canopy of survey grid ABI2, there is a considerable decrease in canopy openness from 74.5 % to 42.52 % in 2008 and from 66.66 % to 45.89 % in 2009, whilst the LAI increased from 0.18 to 0.75 in 2008 and from 0.23 to 0.64 in 2009.

Survey grids - Summary for spring

Table 3.3 shows the mean, standard deviation and standard error of the canopy openness, LAI and transmissivity across all of the 287 survey grids points for 2008 and 2009. The survey grids had a mean canopy openness of 67.05 %, a mean LAI of 0.27 and a mean transmissivity of 76.36 %. There was an increase in LAI from 0.21 in 2008 to 0.32 in 2009, and a corresponding decrease in canopy openness from 72.96 % to 61.42 % and transmissivity from 81.95 % to 71.04 %.

Table 3.3: Canopy openness (%), LAI and transmissivity (%) calculated for the survey grids in spring. The mean, standard deviation and standard error of the mean are shown for 2008, 2009 and all data.

		Grids - Spring		
		2008	2009	All data
	n	140	147	287
Canopy openness (%)	$\bar{x}$	72.96	61.42	67.05
	σ	8.12	8.72	10.21
	$\sigma_{\bar{x}}$	0.69	0.72	0.60
LAI	$\bar{x}$	0.21	0.32	0.27
	σ	0.13	0.16	0.16
	$\sigma_{\bar{x}}$	0.011	0.013	0.0092
Transmissivity (%)	$\bar{x}$	81.95	71.04	76.36
	σ	8.69	10.46	11.06
	$\sigma_{\bar{x}}$	0.73	0.86	0.65

3.3.3 Survey transects

Spring

Hemispherical Photographs were taken every 5 m along four survey transects in spring 2009, and analysed with GLA (Figure 3.4). The mean, standard deviation and standard error of the mean for the canopy openness, LAI and transmissivity for each transect is shown in Table 3.4.

Table 3.4: Canopy openness (%), LAI and transmissivity (%) calculated for the survey transects. The mean, standard deviation and standard error of the mean are shown for spring and summer in 2009.

			Transects							
			Spring				Summer			
			NE	SE	SW	NW	NE	SE	SW	NW
		n	101	71	100	101	101	71	100	101
Canopy openness (%)	2009	$\bar{x}$	68.65	70.30	80.16	69.95	50.79	58.63	76.40	60.01
		σ	8.82	9.57	11.69	9.30	11.99	15.66	20.27	15.35
		$\sigma_{\bar{x}}$	0.88	1.14	1.17	0.93	1.19	1.86	2.03	1.53
LAI	2009	$\bar{x}$	0.23	0.17	0.08	0.19	0.54	0.41	0.19	0.38
		σ	0.13	0.14	0.14	0.13	0.27	0.30	0.34	0.29
		$\sigma_{\bar{x}}$	0.01	0.02	0.01	0.01	0.03	0.04	0.03	0.03
Transmissivity (%)	2009	$\bar{x}$	79.14	82.48	91.09	81.28	61.63	69.53	86.62	72.50
		σ	9.14	11.10	10.99	9.85	13.94	18.71	19.93	16.15
		$\sigma_{\bar{x}}$	0.91	1.32	1.10	0.98	1.39	2.22	1.99	1.61

Figure 3.4 panel a shows the north-east transect which was 500 m of continuous birch forest which had a mean canopy openness of 68.65 % (varying between 47.14 % and 89.4 %), a mean LAI of 0.22 (varying between 0.01 and 0.66), and a mean transmissivity of 79.14 % (varying between 50.53 % and 97.7 %). As the only transect which was continuous birch forest the values were consistent with the areas of birch forest for the other three transects.

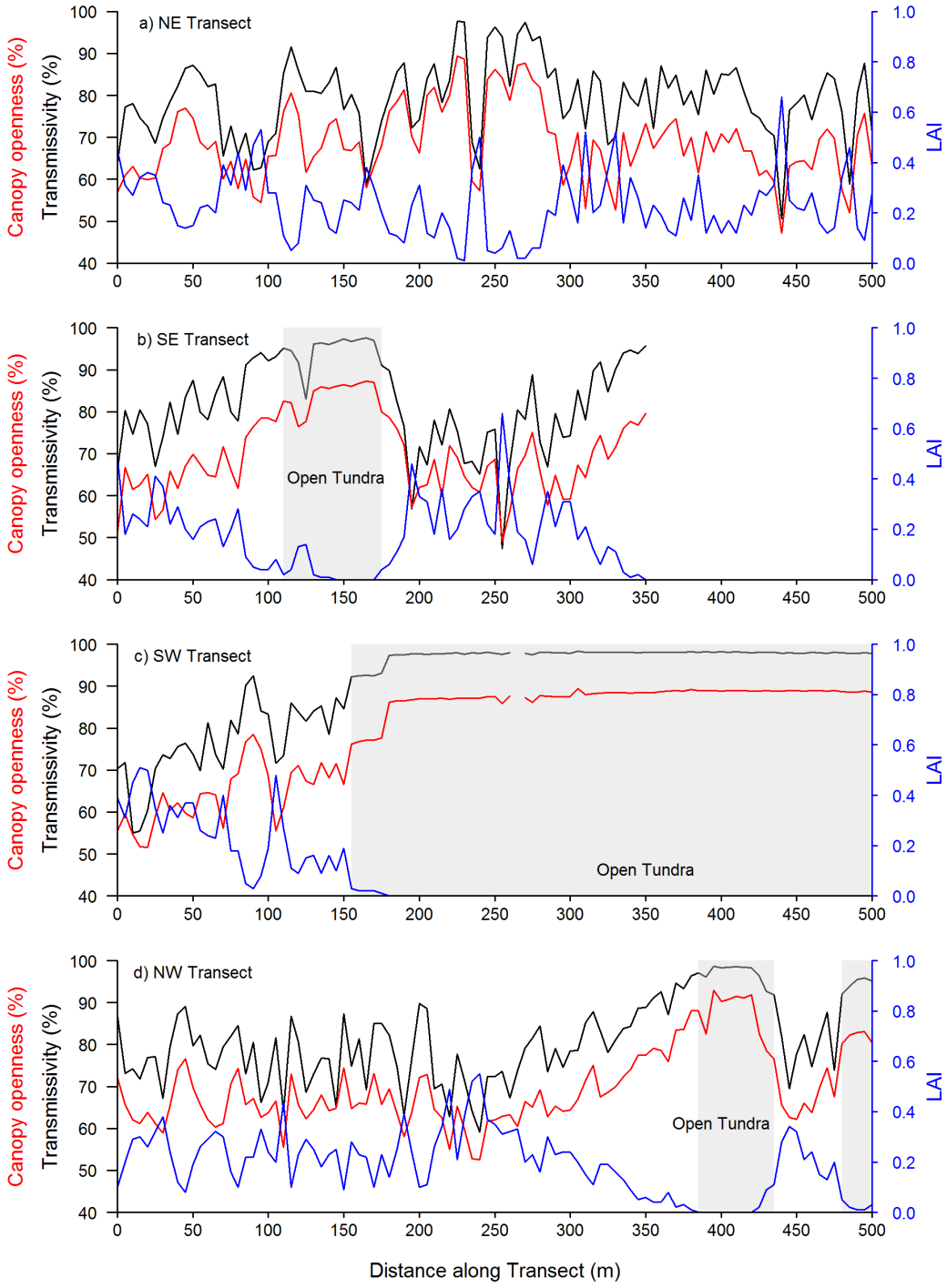

Figure 3.4: Canopy openness (%), transmissivity (%) and LAI for the survey transects in spring 2009. Shaded areas represent areas of Open Tundra.

Figure 3.4 panel b shows the south-east transect where there was an area of open tundra between 110 m and 175 m. Areas of open tundra were defined during fieldwork campaign as large (over 20 m to avoid including canopy gaps within the forest) areas with few sparse trees, with tundra

and wetland vegetation, and often including small lakes. The open tundra had a mean canopy openness of 83.93 % (varying between 76.5 % and 87.27 %). This was much higher than even the very sparse survey grid of ABI2 which had the highest canopy openness at 74.5 %. The areas of birch forest had a mean canopy openness of 66.94 % (varying between 49.1 % and 79.6 %). The area of open tundra had a mean LAI of 0.02 (varying between 0.0 and 0.14) whereas the birch forest had a mean LAI of 0.21 (varying between 0 and 0.66). The area of open tundra had a mean transmissivity of 94.77 % (varying between 83.04 % and 97.59 %) whereas the birch forest had a mean transmissivity of 79.46 % (varying between 47.34 % and 95.72 %).

Figure 3.4 panel c shows the south-west transect where there was an area of open tundra from 155 m to 500 m. This had a mean canopy openness of 87.31 % (varying between 76.18 % and 89.39 %), which was more sparse than the area of open tundra in the south-east transect. The area of birch forest had a mean canopy openness of 64.24 % (varying between 51.56 % and 78.47 %). The area of open tundra had a mean LAI of 0.001 (varying between 0 and 0.03) whereas the birch forest had a mean LAI of 0.25 (varying between 0.03 and 0.51). The area of open tundra had a mean transmissivity of 97.55 % (varying between 92.21 % and 98.29 %) whereas the birch forest had a mean transmissivity of 76.68 % (varying between 55.02 % and 92.48 %).

Figure 3.4 panel d shows the north-west transect with two areas of open tundra from 385 m to 435 m and from 480 m to 500 m, which had a mean canopy openness of 85.35 % (varying between 62.11 % and 93.01 %). The areas of birch forest had a mean canopy openness of 67.05 % (varying between 52.58 % and 88.06 %). The area of open tundra had a mean LAI of 0.02 (varying between 0 and 0.34) whereas the birch forest had a mean LAI of 0.22 (varying between 0.01 and 0.55). The area of open tundra had a mean transmissivity of 96.05 % (varying between 69.45 % and 98.64 %) whereas the birch forest had a mean transmissivity of 78.49 % (varying between 59.13 % and 96.41 %).

There is an increase in the values of canopy openness and transmissivity, while there is a corresponding decline in LAI, as areas of sparse forest transition into areas of open tundra (see 50 m to 110 m along the south-east transect Figure 3.4 panel b, and 250 m to 380 m along the north-west transect Figure 3.4 panel d).

Survey transects - Summary for spring

Table 3.5 shows the mean, standard deviation and standard error of the canopy openness, LAI and transmissivity across all of the 373 survey points. The survey transects had a mean canopy openness of 72.40 %, a mean LAI of 0.17 and a mean transmissivity of 83.56 %.

Table 3.5: Canopy openness (%), LAI and transmissivity (%) calculated for the survey transects. The mean, standard deviation and standard error of the mean are shown for spring in 2009.

			Transects - Spring				
			All Data	All Forest	All Tundra	First 75 m	$>$ 75 m Forest
		n	373	274	99	64	210
Canopy openness (%)	2009	$\bar{x}$	72.40	67.30	86.52	63.69	68.40
		σ	10.97	7.77	3.77	5.94	7.94
		$\sigma_{\bar{x}}$	0.57	0.47	0.38	0.74	0.55
LAI	2009	$\bar{x}$	0.17	0.23	0.0086	0.28	0.21
		σ	0.14	0.13	0.025	0.10	0.13
		$\sigma_{\bar{x}}$	0.0075	0.0076	0.0025	0.012	0.0090
Transmissivity (%)	2009	$\bar{x}$	83.56	78.73	96.92	76.23	79.50
		σ	11.23	9.04	2.32	7.45	9.35
		$\sigma_{\bar{x}}$	0.58	0.55	0.23	0.93	0.65

Included within three of the transects were areas of open tundra, specifically in transects SE, SW and NW (Figure 3.4). When the 99 survey points classed as tundra were excluded from analysis there were 274 points classed as birch forest. The areas of birch forest had a mean canopy openness of 67.30 %, a mean LAI of 0.23, and a mean transmissivity of 78.73 % (Table 3.5). The remaining 99 survey points classed as open tundra had a mean canopy openness of 86.52 %, a mean LAI of 0.008, and a mean transmissivity of 96.92 % (Table 3.5). The areas classed as open tundra show little variation, with respect to the values for the birch forest which show considerable variability in the values of canopy openness, LAI and transmissivity. The areas of open tundra have a very high transmissivity and canopy openness and a very low LAI with respect to the areas of sparse forest, therefore they are significantly different from each other (Welch t-test, $t > 27$, $df > 324$, $p < 0.01$).

To assess if there were distinct areas within the birch forest the first 75 m of all four transects were assessed separately to the remaining birch forest survey points. This area was centered around the AWS meteorological tower and three of the survey grids ABI2, ABI3 and ABI7. The mean canopy openness was 63.69 %, the mean LAI was 0.28, and the mean transmissivity was 76.23 % see Table 3.5. The values for the first 75 m of forest were not normally distributed and could not be tested for significant difference (Shapiro-Wilk n = 16, $p > 0.06$). However, Table 3.5 shows the values for the first 75 M of forest are within the standard deviation of the means for the 274 birch forest survey points (canopy openness σ 7.77, LAI σ 0.12, transmissivity σ 9.03). Therefore,

within the birch forest there is considerable variability in the values of canopy openness, LAI and transmissivity, and crucially the measurements taken within the central 75 m of the AWS meteorological tower are representative of the wider area of birch forest.

Summer

Figure 3.5 shows the GLA analysis for the survey transects in summer 2009. The mean, standard deviation and standard error of the canopy openness, LAI and transmissivity for all four transects are shown in Table 3.4.

Figure 3.5 panel a shows the north-east transect which had a mean canopy openness of 50.79 % (varying between 28.77 % and 76.85 %), a mean LAI of 0.53 (varying between 0.05 and 1.21), and a mean transmissivity of 61.62 % (varying between 30.52 % and 93.17 %). As the only transect which was continuous birch forest the values were consistent with the areas of birch forest for the remaining three transects.

Figure 3.5 panel b shows the south-east transect. The open tundra had a mean canopy openness of 78.74 % (varying between 36.59 % and 84.93 %). The areas of birch forest had a mean canopy openness of 53.68 % (varying between 36.59 % and 84.34 %). The area of open tundra had a mean LAI of 0.06 (varying between 0.0 and 0.33) whereas the birch forest had a mean LAI of 0.49 (varying between 0 and 0.92). The area of open tundra had a mean transmissivity of 91.70 % (varying between 65.13 % and 96.82 %) whereas the birch forest had a mean transmissivity of 64.08 % (varying between 38.44 % and 97.78 %).

Figure 3.5 panel c shows the south-west transect. The open tundra had a mean canopy openness of 88.80 % (varying between 84.65 % and 90.13 %). The areas of birch forest had a mean canopy openness of 48.78 % (varying between 26.3 % and 73.28 %). The area of open tundra had a mean LAI of 0.0005 (varying between 0 and 0.02) whereas the birch forest had a mean LAI of 0.60 (varying between 0.13 and 1.2). The area of open tundra had a mean transmissivity of 98.53 % (varying between 97.1 % and 98.84 %) whereas the birch forest had a mean transmissivity of 60.08 % (varying between 24.95 % and 86.72 %).

Figure 3.5 panel d shows the north-west transect. The open tundra had a mean canopy openness of 77.90 % (varying between 30.74 % and 93.01 %). The areas of birch forest had a mean canopy openness of 55.70 % (varying between 29.93 % and 85.84 %). The area of open tundra had a mean LAI of 0.13 (varying between 0 and 1.11) whereas the birch forest had a mean LAI of 0.44 (varying between 0.01 and 1.21). The area of open tundra had a mean transmissivity of 88.56 %

(varying between 30.52 % and 98.84 %) whereas the birch forest had a mean transmissivity of 68.16 % (varying between 36.6 % and 98.02 %).

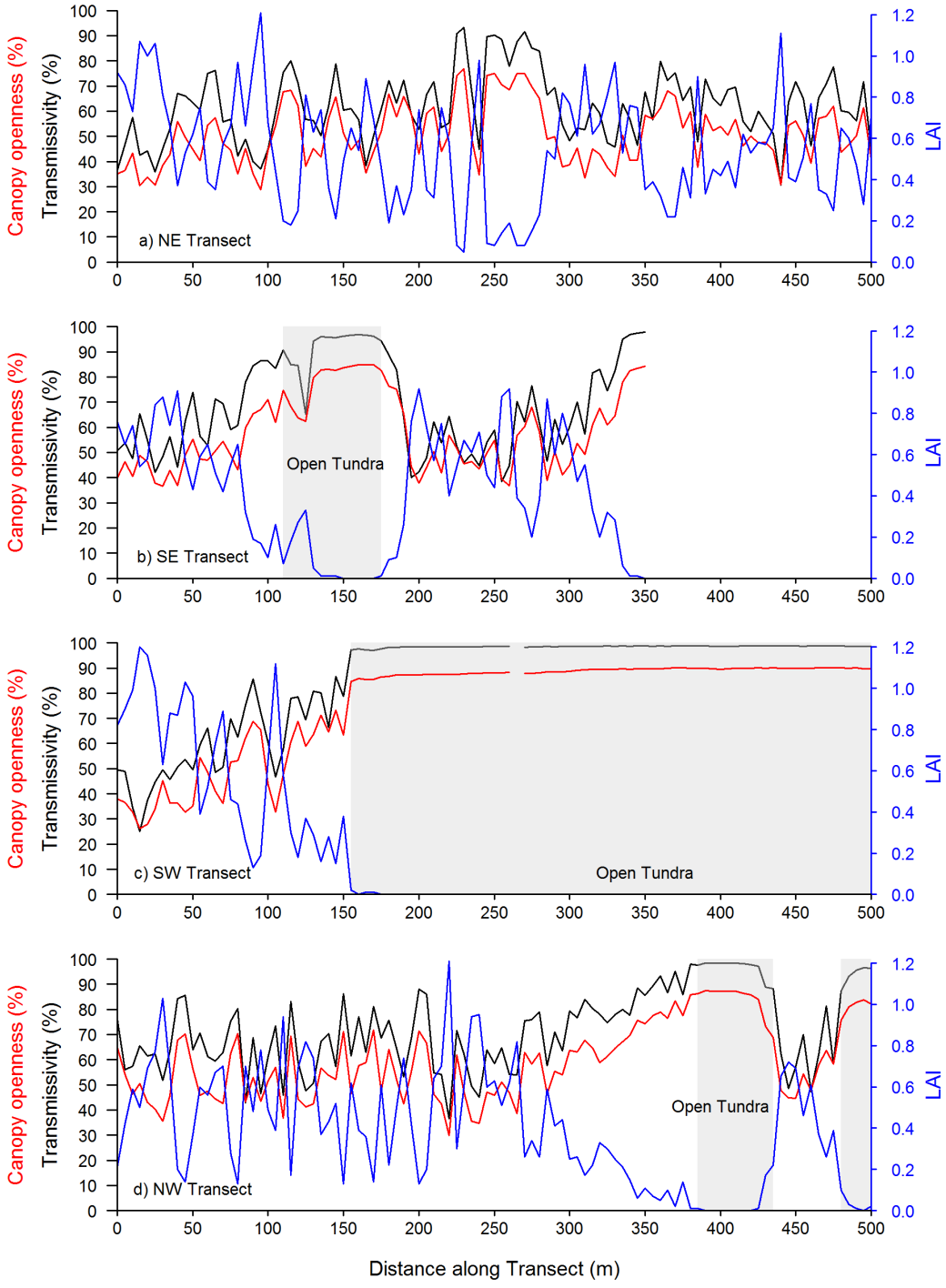

Figure 3.5: Canopy openness (%), transmissivity (%) and LAI for the survey transects in summer 2009. Shaded areas represent areas of Open Tundra.

Across all four transects there were 373 survey points which had a mean canopy openness of 61.46 %, a mean LAI of 0.38 and a mean transmissivity of 72.57 %. There were 274 points classed as birch forest, of which the mean canopy openness was 52.69 %, the mean LAI was 0.51, and the mean transmissivity was 64.00 %. The remaining 99 survey points were classed as open tundra which had a mean canopy openness of 86.43 %, a mean LAI of 0.016, and a mean transmissivity of 97.09 %.

Overall the spring birch forest values were significantly different to the summer values. The canopy openness declined by 15 % (T test, t = 16, $p < 0.001$), the LAI increased by 0.28 (T test, t = 15, $p < 0.001$), and the transmissivity declined by 14 % (T test, t = 14, $p < 0.001$). There was no significant difference in the open tundra values for spring and summer (all T tests, $t < 1.1$, $p > 0.23$). The increasing LAI and decreasing canopy transmissivity clearly show the change in canopy state.

3.3.4 Pyranometer assessment

Collating data from the hemispherical surveys grids (n = 287, these contain 91 repeats from ABI2 (n = 42) and ABI5 (n = 49)) and transects (n = 274), the 12 pyranometer locations in 2008 and 2009 were assessed for their representation of the wider birch forest. Figure 3.6 shows the cumulative distribution of canopy openness, Figure 3.7 shows the cumulative distribution of LAI and Figure 3.8 shows the cumulative distribution of transmissivity, which indicate the pyranometer locations captured over 75 % of the variability in the canopy openness, over 85 % of the variability in LAI and over 70 % of the variability in transmissivity. Therefore the 24 pyranometer locations and the shortwave radiation measurements taken can be used as representative of the wider birch forest.

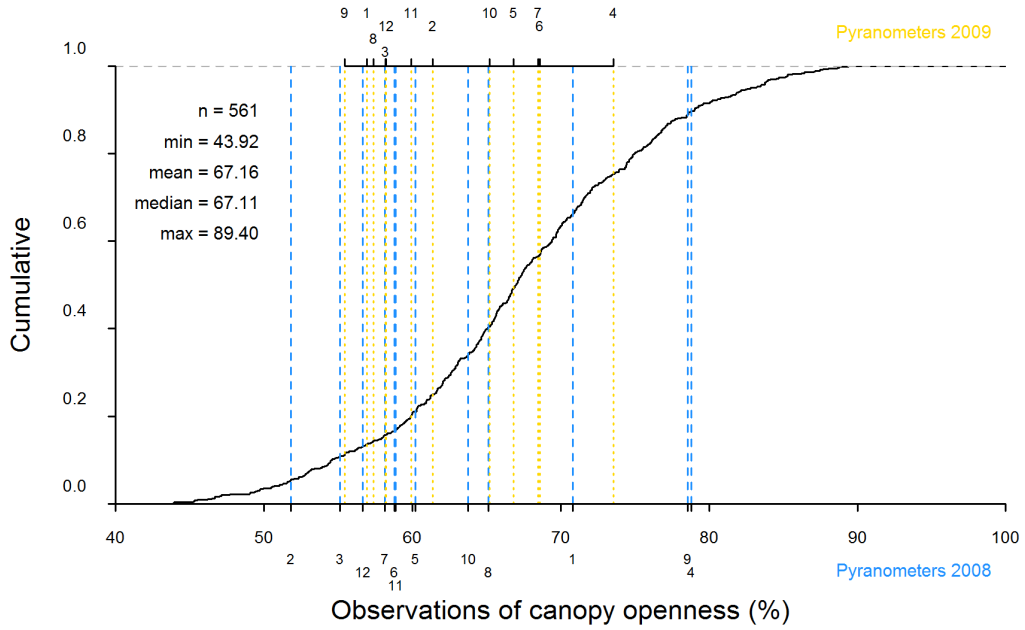

Figure 3.6: Cumulative distribution of the observed canopy openness (%) for spring 2008 and 2009. Individual pyranometers are labelled for 2008 (blue) and 2009 (yellow).

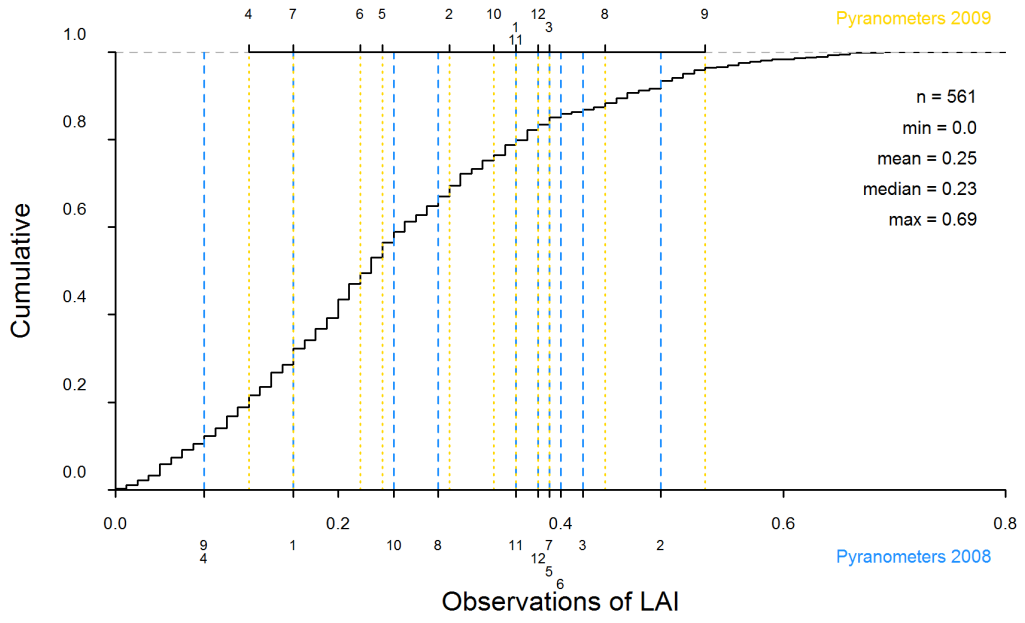

Figure 3.7: Cumulative distribution of the observed LAI for spring 2008 and 2009. Individual pyranometers are labelled for 2008 (blue) and 2009 (yellow).

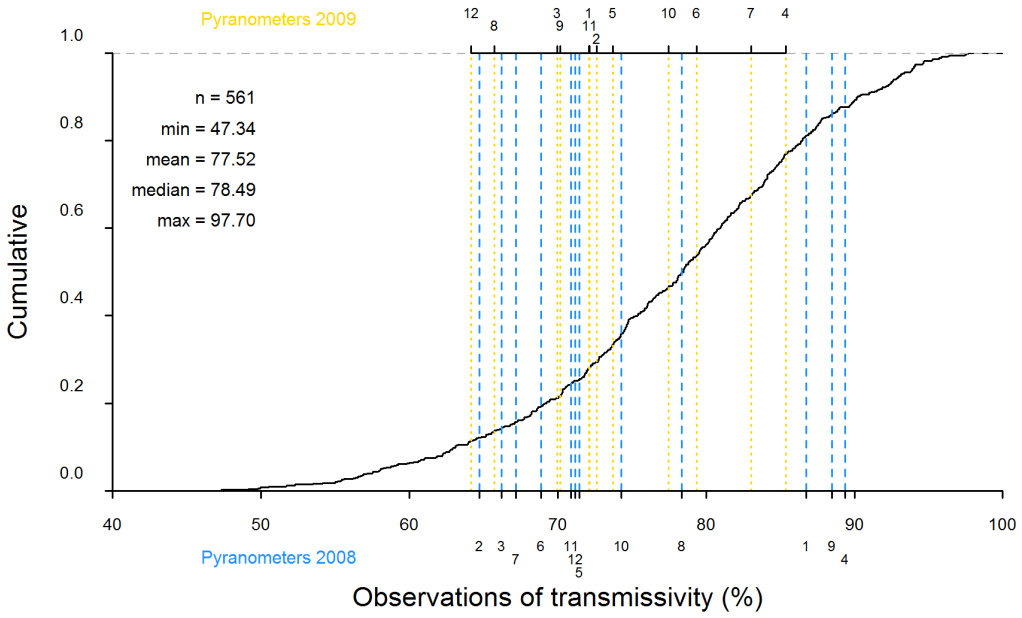

Figure 3.8: Cumulative distribution of the observed transmissivity (%) for spring 2008 and 2009. Individual pyranometers are labelled for 2008 (blue) and 2009 (yellow).

3.4 Canopy temperatures

In 2008 tree temperatures were measured for a period of 86 days from day 96 (6 April) to day 182 (30 June). The tree temperature data shown are averages of three branches, one measured in a monocormic tree, and two in the branches of a polycormic tree. Figure 3.9 shows the average tree temperature recorded for the four cardinal compass points of the three branches and the air temperature recorded at the AWS.

Sunny and cloudy days were defined by the radiation data presented in chapter 4 Figure 4.2 to 4.4. Sunny days were defined by a smooth bell shaped curve in the above canopy total shortwave radiation, and cloudy days were defined by equal above canopy total and diffuse shortwave radiation measurements (Figure 4.8 and 4.9).

The data (Figure 3.9) shows a clear daily warming trend, which is most pronounced on the sunny days such as days 101 to 103. Firstly the east, then the south, and lastly the west facing branches all warm up to temperatures above the other three sides of the branch and the ambient air temperature. Cloudy days (96, 100, and 109) demonstrated the smallest increase and variability in branch temperatures. The peak in daily branch temperature was usually seen on either the south or west facing branches. Therefore branch temperature only exceed the ambient air temperature during the day when there was either direct or diffuse shortwave radiation. Branch temperatures were higher on sunny days as there was over 600 W m^{-2} of direct radiation, relative to 200 W m^{-2} of diffuse radiation on cloudy days (Figure 4.8 and 4.9). This shows the influence of the direct beam shortwave radiation on the sparse canopy at the low solar elevation.

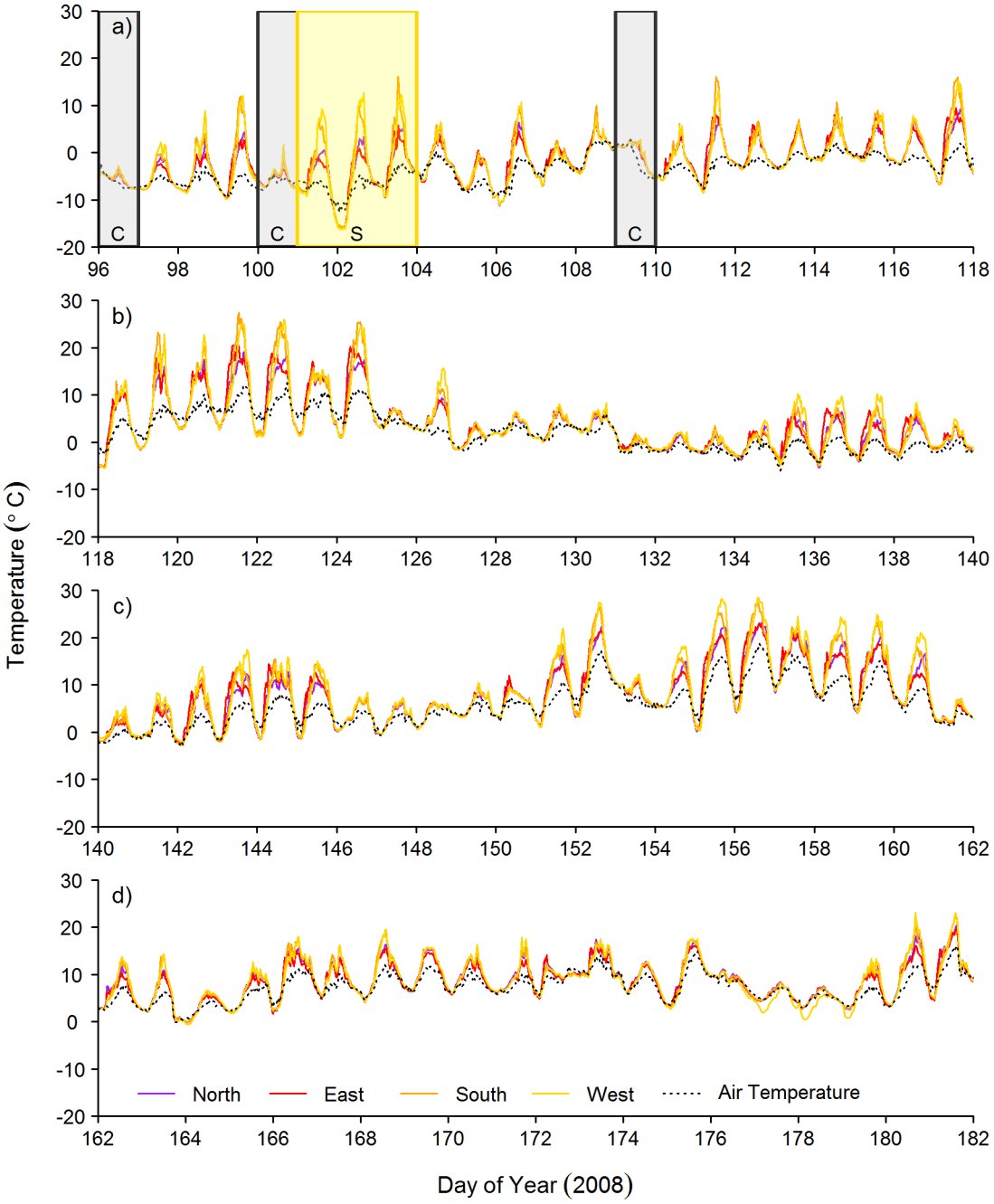

Figure 3.9: Average thermocouple tree temperatures for north (purple), east (red), south (orange) and west (yellow) facing sides of two polycormic branches and one monocormic branch in spring 2008 from day 96 (6 April) to day 182 (30 June). Air temperature is shown from the AWS (black dotted). Shaded areas and letters indicate cloudy (C - grey) and sunny (S - yellow) days.

During the period from day 96 to 118 (Figure 3.9 panel a) the mean tree branch temperature was -1.88 °C while the mean ambient air temperature for the same period was -3.84 °C, showing that there is warming of the forest above that of the ambient air temperature. The mean branch

temperatures during the period from day 96 to 118 for the north, east, south and west facing branches were -2.17 °C, -2.05 °C, -1.56 °C, and -1.76 °C, showing that the south and west facing branches were typically above the mean tree temperature, while the north and east facing branches are typically below mean tree temperature. During the period from day 118 to 140 (Figure 3.9 panel b) the mean branch temperature was 4.06 °C, whereas the ambient air temperature was 2.12 °C. During the period from day 140 to 163 (Figure 3.9 panel c) the mean branch temperature was 8.18 °C, whereas the air temperature was 5.89 °C. During the period from day 162 to day 182 (Figure 3.9 panel d) the mean branch temperature was 8.60 °C, whereas the air temperature was 7.24 °C, which was the smallest difference between the air and tree temperatures.

The average branch temperatures for one sunny day (day 101) and one cloudy day (day 96) are shown in Figure 3.10. The air temperature is warmer than the tree temperatures at the start and end of both of the days. During the day the tree temperatures are warmer than the ambient air temperature, even on the cloudy day. This is a clear indication that the shortwave radiation warms up the tree canopy as all four sides of the branches were warmer than the ambient air temperature after the sun has risen. At dawn there is an increase and at dusk a decrease in all four branch temperatures, with little difference between the temperatures of the four sides of the branch at these times. The heat capacity of the tree branches is relatively small as once the sun sets, the tree temperatures drop back to ambient air temperature or cooler relatively quickly.

There is a clear trend in the branch facing the direct sunlight warming up to the highest temperature on the sunny day. As the solar position changes through the day so do the peaks in branch temperature, starting with the east facing branch in the morning, followed by the south facing branch at midday, and then the west facing branch in the afternoon, with peaks in temperature of -1.03 °C, 7.30 °C and 9.21 °C respectively. The peak in branch temperature on the west facing branch of 9.21 °C is over 15 °C warmer than the ambient air temperature of -6.37 °C. Even the north facing side of the branch, which would not receive any direct shortwave radiation reaches a peak in temperature at the end of the day of 0.51 °C. When compared to the ambient air temperature of -5.70 °C, it can be clearly seen that the shortwave radiation must be warming the whole branch, not just the surface of the branch.

On the cloudy day, there is no difference in the branch temperature for the three branches as each branch shows a similar warming trend throughout the day. This is consistent with the lack of direct shortwave radiation on the branch surface, as there is less warming of the tree, therefore the temperature of the individual branches on the cloudy day is independent of the position of the sun. Each of the mean daily branch temperatures are very similar at -5.68 °C, -5.88 °C, -5.75 °C and -5.52 °C for the north, east, south and west facing branches respectively. The warmest temperature was recorded for the west facing branch of -2.85 °C just after midday, which was over 3 °C warmer than the air temperature of -6.18 °C.

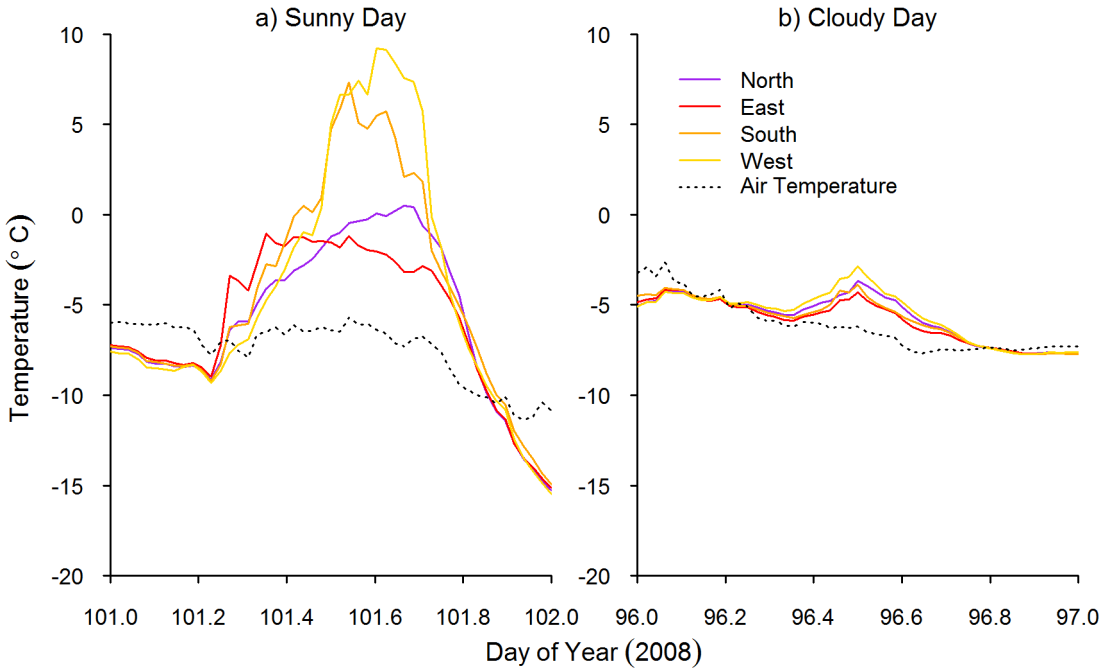

Figure 3.10: Average tree temperatures for the north (purple), east (red), south (orange) and west (yellow) facing sides on a sunny (day 101) and cloudy (day 96) day in 2008. The corresponding radiation data is shown in Figure 4.8 panels a and b.

In 2009 tree temperatures were measured for a period of 76 days from 4 April (day 94) to 19 June 2009 (day 170) (Figure 3.11). The tree temperature data are the average of five polycormic branches of the same polycormic tree.

Figure 3.11 shows the average tree temperature recorded for the four cardinal compass points of the five branches and the air temperature recorded at the AWS. There is a clear daily warming trend in the data, which is most pronounced on the sunny days such as days 94 to 98 and days 134 to 140. Firstly the east, then the south, and lastly the west facing branches all warm up higher than the other three sides of the branch. The cloudiest days (107, 116, 133, 147, 154, 165 and 166) demonstrated the smallest increase and smallest variability in branch temperatures. The air temperature was warmer than the tree temperatures showing that this relationship is very dependent upon direct radiation illumination of the branches. As in 2008, the peak in daily branch temperatures was usually seen on either the south or west facing branches, and the branch temperatures fell below the ambient air temperature during the evenings.

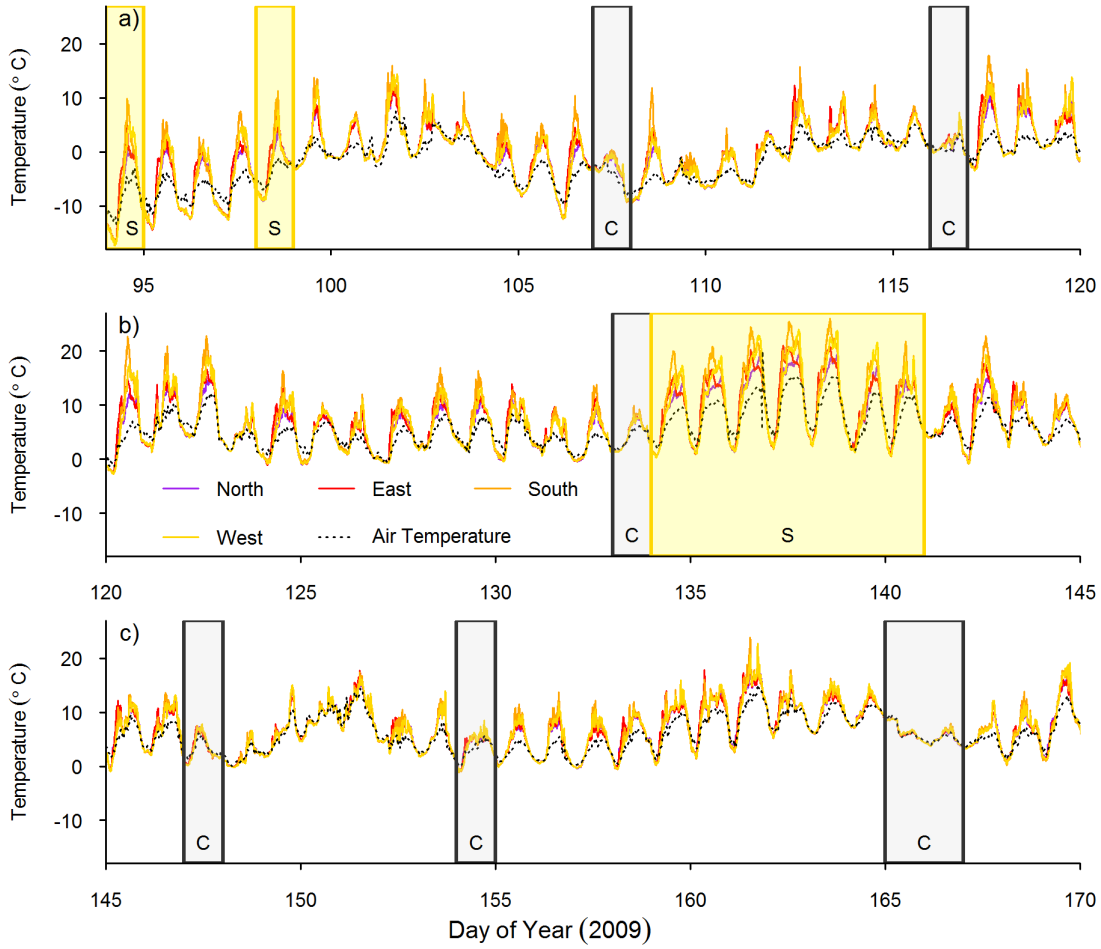

Figure 3.11: Average thermocouple tree temperatures for north (purple), east (red), south (orange) and west (yellow) facing sides of five polycormic branches in spring 2009 from day 94 (4 April) to 170 (19 June). Shaded areas and letters indicate cloudy (C - grey) and sunny (S - yellow) days.

During the period day 94 to 119 (Figure 3.11 panel a) the mean tree branch temperature was -0.44 °C while the mean ambient air temperature for the same period was -1.79 °C, showing that there is warming of the forest canopy above that of the ambient air temperatures. The mean branch temperatures during the period 94 to 119 for the north, east, south and west facing branches were -0.69 °C, -0.34 °C, -0.15 °C, and -0.57 °C, showing that the south facing branches were typically warmer than mean tree temperature, while the north facing branches were typically cooler than mean tree temperature. During the period day 120 to 144 (Figure 3.11 panel b) the mean branch temperature was 7.28 °C, whereas the air temperature was 5.74 °C. During the period day 145 to 169 (Figure 3.11 panel c) the mean branch temperature was 6.85 °C, whereas the air temperature was 5.91 °C.

The average branch temperatures for one sunny day (day 94) and one cloudy day (day 165) in

2009 are shown in Figure 3.12. The air temperature was warmer than the tree temperatures at the start and end of both of the days, and on the cloudy day the air temperature was always warmer than the tree temperatures. On the sunny day, as the solar position changes so do the peaks in branch temperature, starting with the east facing branch in the morning, followed by the south facing branch at midday, and then the west facing branch in the afternoon. There is a clear trend in warming starting with the east facing branch, followed by the south facing branch, and then the west facing branch with peaks in temperature of 5.17 °C, 9.87 °C, and 5.14 °C respectively. The peak in branch temperature on the south facing branch of 9.87 °C at 1.40 pm is over 14 °C warmer than the air temperature of -4.53 °C at 1.30 pm. Even the north facing side of the branches, which would not receive direct shortwave radiation from the sun, reaches a peak in temperature at the middle of the day of 0.41 °C at 1.40 pm. On the cloudy day, as there is no direct shortwave radiation, each branch temperature is independent of the solar position. There is no difference between branch temperatures, and they follow changes in the ambient air temperature. Each of the mean daily branch temperatures are very similar at 6.74 °C, 6.63 °C, 6.71 °C and 6.82 °C for the north, east, south and west facing branches respectively, while the daily mean air temperature was 6.73 °C. These data clearly show that the direct shortwave radiation warms the branches of the trees.

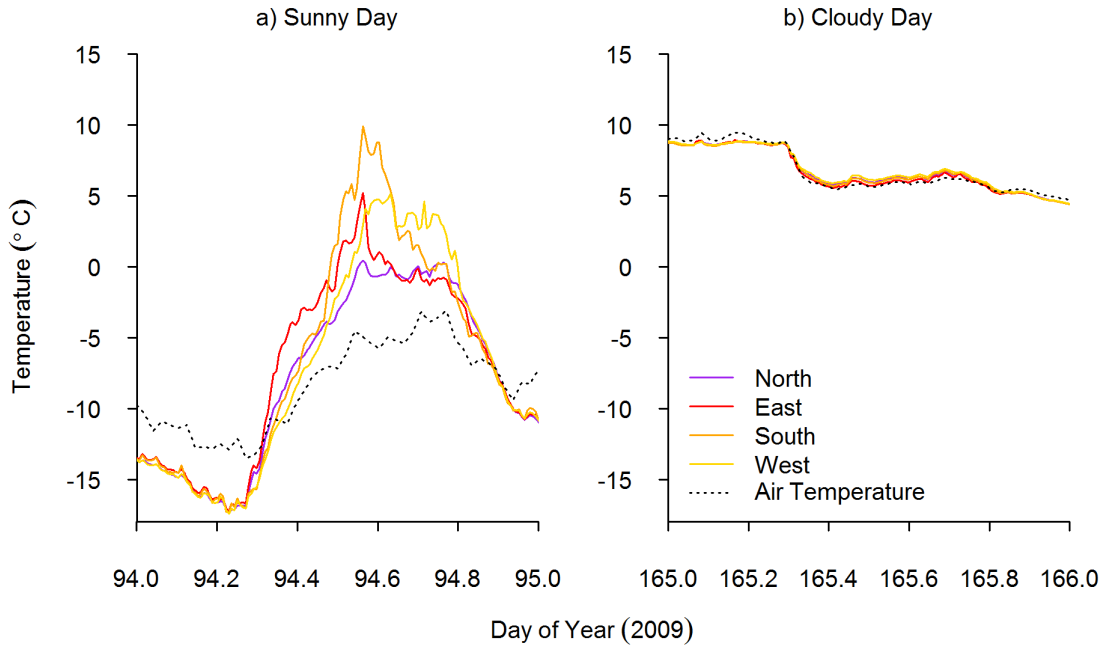

Figure 3.12: Average tree temperatures for the north (purple), east (red), south (orange) and west (yellow) facing sides of five polycormic branches on a sunny (94 - 4 April) and cloudy (165 - 14 June) day in spring 2009. The corresponding radiation data is shown in Figure 4.9 panels a and d.

The increase in temperature for the north facing branches indicates that whole branch warming

occurs, rather than just an increase in the surface branch temperature. The north facing branches had daily increases of up to 10-15 °C warmer than the air temperature, despite not receiving any direct shortwave radiation on the surface. The north facing branches were on average 2 °C warmer than the ambient air temperature over a 20 day period despite dropping below air temperature at night.

3.5 Longwave radiation from the tree canopy

It is possible to calculate the contribution of longwave radiation from the forest down to the snowpack, using the measurements of tree temperature. We can assume that the trees emit longwave radiation according to their temperature as follows:

$$Tree_{LW} = LAI\varepsilon\sigma(T + 273.15)^4 \tag{3.1}$$

Where $Tree_{LW}$ is a calculated longwave radiation (W m^{-2}) from the tree canopy, LAI is the leaf area index (0.23 see All Forest LAI for survey transects in Table 3.5), ε is the Emissivity, σ is the Stefan Boltzmann constant and T is the surface temperature (°C). The $Tree_{LW}$ provides a rough estimate of the canopy contribution to the longwave radiation budget. This can then be used with a fraction of the incoming longwave radiation to estimate below canopy longwave radiation as follows:

$$LW_{bc} = Tree_{LW} + v_f LW_{\downarrow} \tag{3.2}$$

Where LW_{bc} is calculated below canopy longwave radiation (W m^{-2}), v_f is a sky view fraction (0.8 rounded up from All Forest transmissivity (78.73 %) for survey transects in Table 3.5), and $LW_{\downarrow}$ is the incoming longwave radiation (W m^{-2}). The following figures use the measured tree temperatures to calculate $Tree_{LW}$ shown by the black lines in Figures 3.13, 3.14 and 3.15. These estimated values of $Tree_{LW}$ are then used to calculate a below canopy longwave radiation (LW_{bc}) which is shown by the purple lines in Figures 3.13, 3.14 and 3.15.

Figure 3.13 shows the above canopy incoming longwave radiation and the $Tree_{LW}$ calculated using the mean tree temperatures for spring and summer in 2008. For the measurement period day 96 to day 182 the mean below canopy longwave radiation was 314.62 W m^{-2}, the mean above canopy longwave radiation was 281.01 W m^{-2}, and the mean $Tree_{LW}$ longwave radiation was 76.40 W m^{-2}. Therefore the total $Tree_{LW}$ longwave radiation averaged 27 % of the total incoming longwave radiation, over the whole measurement period (day 96 - day 182).

As the below canopy longwave radiation was not available for the full measurement period in 2008, and the early spring period is of particular interest to this study. Figure 3.14 shows the spring period for day 103 to day 117, where the mean above canopy longwave radiation was 264 W m^{-2}, the mean below canopy longwave radiation was 281 W m^{-2} and the $Tree_{LW}$ longwave radiation was 70 W m^{-2}. In contrast over the period day 160 to 182 the mean above canopy longwave radiation was 310 W m^{-2}, the mean below canopy longwave radiation was 335 W m^{-2} and mean the $Tree_{LW}$ longwave radiation was 80 W m^{-2} (Figure 3.13 panel c).

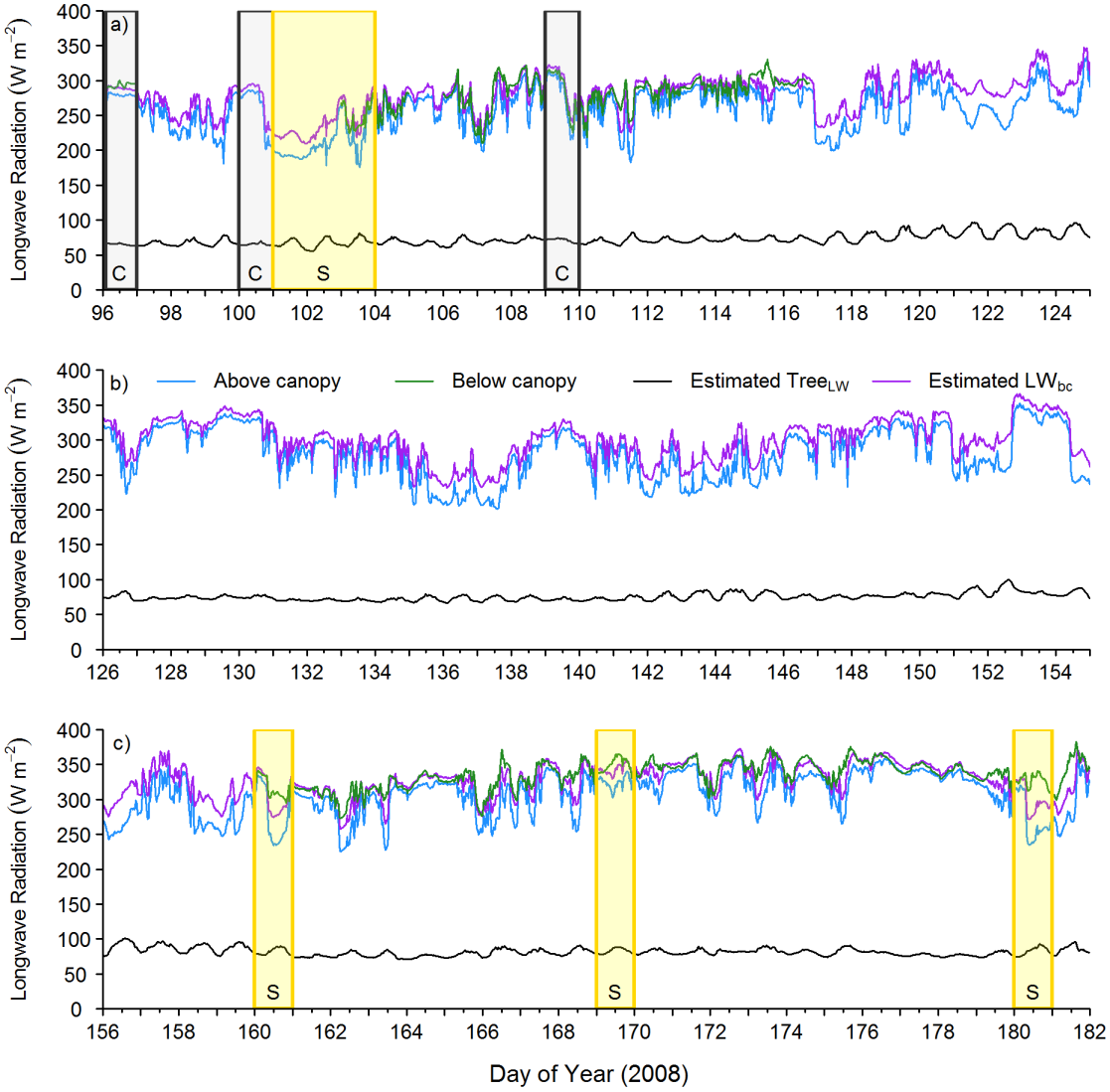

Figure 3.13: The above canopy, below canopy, $Tree_{LW}$ and LW_{bc} longwave radiation in 2008 for days 96 to 182. Below canopy longwave radiation measurements were not available for the whole 2008 period, data were measured on days 96 and 103 to 116 in spring, and days 160 to 182 in summer. Shaded areas and letters indicate cloudy (C - grey) and sunny (S - yellow) days.

The below canopy longwave radiation has a diurnal cycle, increasing as the tree temperature increases. On sunny days (Figure 3.15 and Figure 3.13) when there is a decrease in the incoming above canopy longwave, the observed below canopy radiation does not decrease and in some cases actually increases. What this means is that the decrease in incoming longwave radiation from the sky is balanced by an increase in longwave radiation from the tree canopy. Therefore increasing below canopy longwave radiation when there is a decrease in incoming sky longwave radiation provides the clearest indication that the sparse birch forest is radiating longwave energy to the surface of the snow.

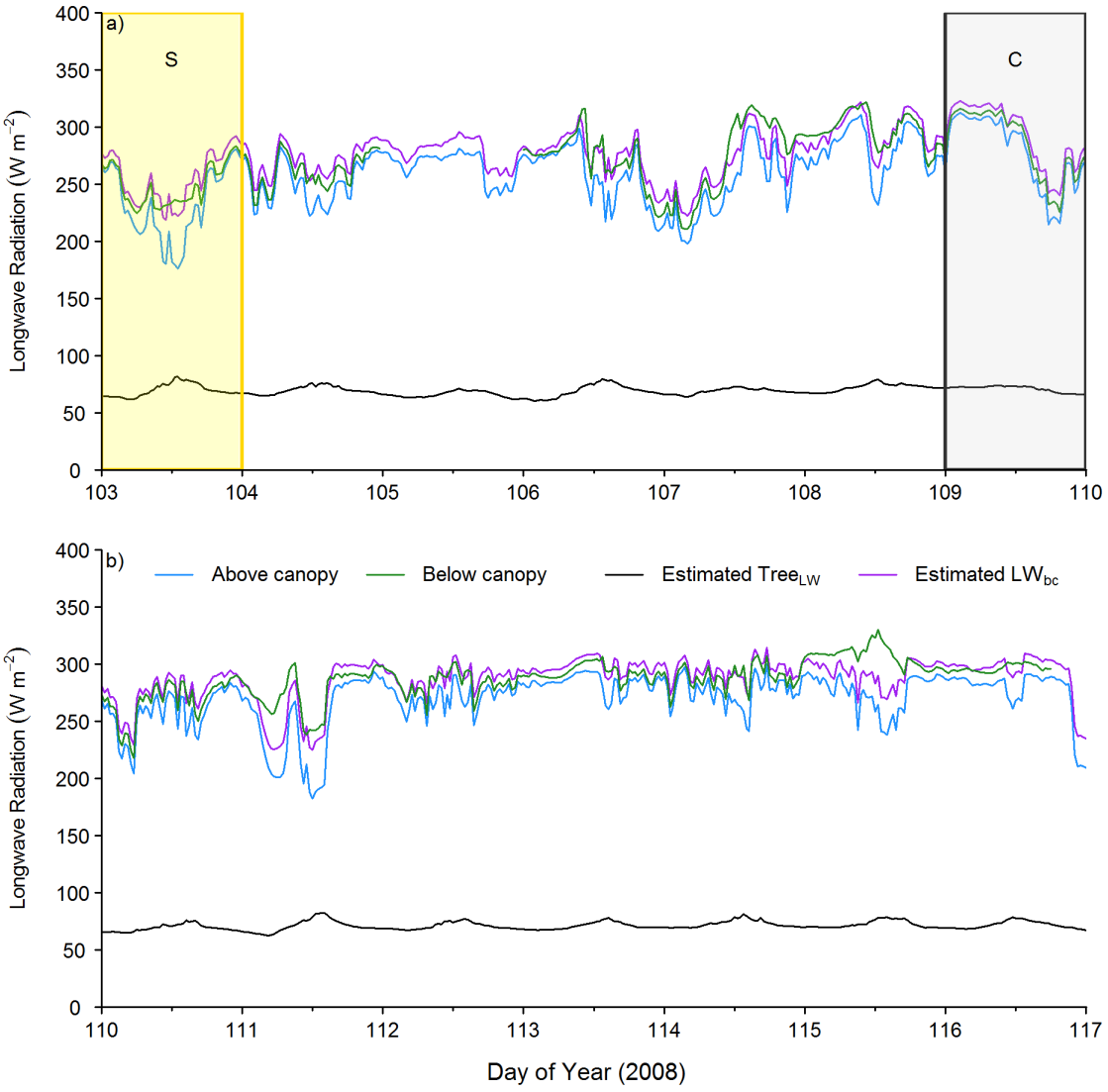

Figure 3.14: The above canopy, below canopy, $Tree_{LW}$ and LW_{bc} longwave radiation in 2008 for days 103 to 117. Shaded areas and letters indicate cloudy (C - grey) and sunny (S - yellow) days.

The longwave radiation for a sunny day and a cloudy day in 2008 are shown in Figure 3.15.

On the sunny day 103 (Figure 3.15 panel a) the mean above canopy longwave radiation was 232.61 W m^{-2}, while the mean $Tree_{LW}$ longwave radiation was 69.70 W m^{-2} which peaked in the afternoon at 81.53 W m^{-2}. The mean below canopy longwave radiation was 249.45 W m^{-2} which peaked at 283.08 W m^{-2} in the evening. The mean $Tree_{LW}$ longwave radiation was 30 % of the total above canopy longwave radiation component.

On the cloudy day 109 (Figure 3.15 panel b) the mean above canopy longwave radiation was 277.71 W m^{-2}, the mean below canopy radiation was 285.55 W m^{-2}, and the mean $Tree_{LW}$ longwave radiation was 74.10 W m^{-2}. The mean $Tree_{LW}$ longwave radiation represented 27 % of the total above canopy radiation.

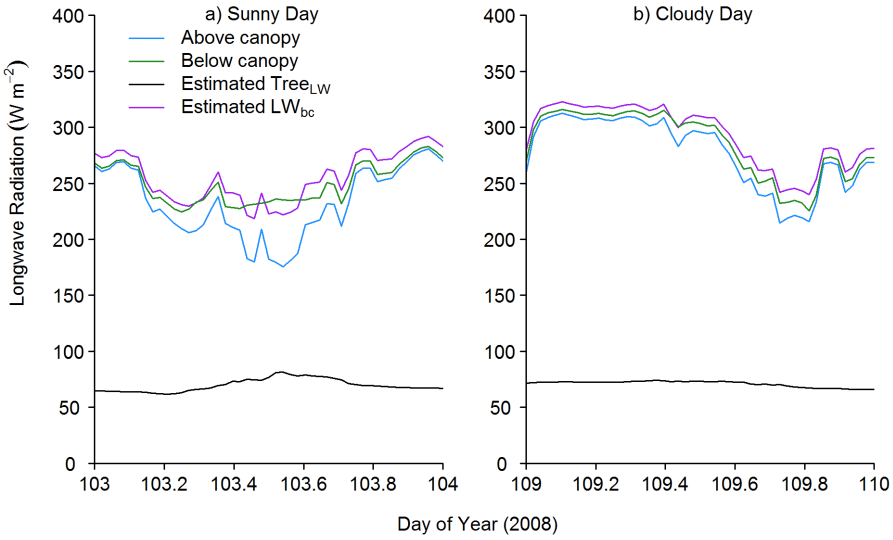

Figure 3.15: The above canopy, below canopy, $Tree_{LW}$ and LW_{bc} longwave radiation for a sunny and cloudy day in 2008.

The cloudy day shows very little variability in the components of longwave radiation, whereas the sunny day has a considerable increase in the below canopy longwave radiation. It is likely that the extra 17 W m^{-2} and 8 W m^{-2} measured below the canopy on the sunny and cloudy days respectively were from the surrounding vegetation.

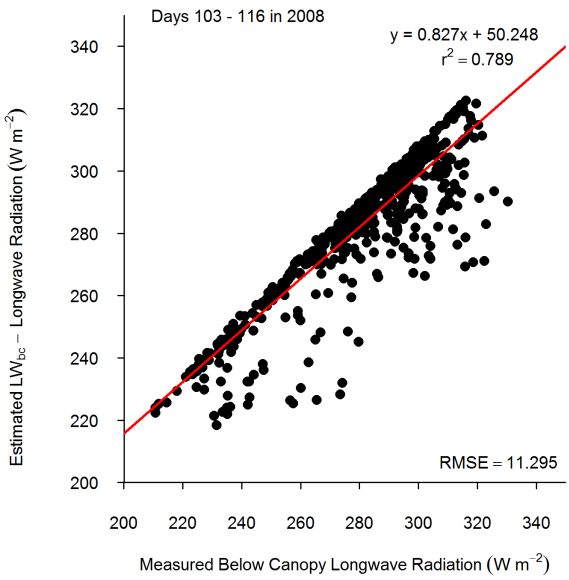

Figure 3.16: Linear regression of estimated LW_{bc} longwave radiation and observed below canopy longwave radiation for days 103 to 116 in 2008.

Figure 3.16 shows a linear regression for the observations of below canopy longwave radiation and the estimated $Tree_{LW}$ longwave radiation for days 103 to 166 in 2008. As the figure shows there is a reasonable agreement between the below canopy measured and estimated $Tree_{LW}$ longwave radiation.

3.6 Discussion

3.6.1 Hemispherical photos

This study has gathered hemispherical photos across the sparse forest in Abisko in spring and summer for two consecutive years, 2008 and 2009. These photographs were analysed for the canopy openness, transmissivity and LAI. The hemispherical photographs taken in 2008 and 2009 show reasonable agreement, but there was significant canopy variability for the survey grids repeated in 2009 compared to 2008. Therefore, the canopy cover for the same sites in consecutive years varies, but this is within the range of canopy variability observed across the whole forest.

The hemispherical photographs taken in the survey transects were useful in determining the canopy characteristics for the areas of sparse forest, and how they contrast to areas of open tundra. It was difficult to determine the exact point where the forest ends and the tundra begins, but these survey transects show that the two areas have distinctive characteristics.

The hemispherical photos show that for the survey grids and transects there is substantial variability in canopy openness, LAI and transmissivity within the sparse forest. Even though the forest appears sparse there are areas of high and low canopy cover and density (due to canopy clumping). The 691 (Pyranometers n =24, Grids n = 294, Transects n = 374) spring hemispherical photographs account for this canopy variability, and can therefore be used to reliably determine the parameters for JULES. To model these sparse forests JULES requires an LAI of the tree canopy, which is used to determine the light extinction through the canopy. The values of LAI calculated by GLA for the field site will be used directly in the JULES model to quantify the transmissivity of the canopy.

By combining hemispherical photographs at the sensor scale of the pyranometers, and scaling up across the landscape to 900 m^2 survey grids in 2008, and to 500 m transects in 2009, these measurements encompass the variability within the forest of LAI and transmissivity (sky view fraction) for the spring leafless period. They allow the expansion of what is a relatively small spatial data set (12 pyranometer measurements) to a much larger area. The LAI and transmissivity (sky view fraction) parameters are of significant importance in land surface modelling of sparse forests, as they can be used to determine the shortwave radiation penetration through the canopy. By capturing the landscape scale variability in canopy transmissivity and LAI, it is possible to determine the values of these model parameters with confidence.

The mean transmissivity for all of the hemispherical photos taken showed that the pyranometers

were representative of the wider landscape scale of birch forest. The birch forest had a very low LAI of 0.25 and very high transmissivity of 77.52 %. These indicate that the forest in Abisko is very open and sparse. *Stähli et al.* [2009] found that a coniferous sub-alpine forest in Switzerland had a transmissivity of less than 15 %. This was consistent with *Pomeroy and Dion* [1996] who measured canopy transmissivity in a jack pine forest at 10 %. *Pomeroy et al.* [2008] measured transmissivity in a spruce forest between 20 to 56 % while *Ellis and Pomeroy* [2007] measured transmissivity in a pine forest between 9 to 36 % (dependent upon slope and aspect) but these coniferous forest had very dense canopy cover. The few studies which have focused on deciduous forests have reported canopy transmissivity to be as high as 35 % but this was in a 60 year old aspen forest with a uniform canopy height of 21 m [*Hardy et al.*, 1997b]. This value is very low compared the 78 % canopy transmissivity measured in Abisko, but is attributed to the very sparse discontinuous canopy of 6 m in height. In a study of surface energy fluxes in canopy models, *Flerchinger et al.* [2012] measured a spring pre-leaf out LAI of 0.45 in an aspen grove, which is more similar to the canopy characteristics of Abisko birch forest which had an LAI of 0.25.

Canopy transmissivity and LAI could have been measured using alternative methods such as LiDAR [*Moeser et al.*, 2014, 2015] or instrumentation such as an LAI-2000 [*Chen et al.*, 1991; *Chen*, 1996; *Chen et al.*, 1997a] but hemispherical photography has been shown to provide quick, accurate and permanent records of the canopy cover and LAI [*Chen et al.*, 1997b; *Rhoads et al.*, 2004; *Garriques et al.*, 2008]. The main challenge in collecting these data was the lack of uniform sky conditions. To reduce the direct solar radiation incidence on the camera lens, hemispherical photographs were taken in late evenings and early mornings (6 pm to 6 am) when the sun elevation was at its lowest. There are several software packages available for the analysis of hemispherical photographs [*Rich et al.*, 1999; *Jarcuska et al.*, 2010; *Weiss and Baret*, 2010], but GLA has been shown to be reliable and was free to use [*Frazer et al.*, 1999; *Hardy et al.*, 2004; *Rhoads et al.*, 2004].

3.6.2 Canopy temperatures and estimated longwave radiation

The above canopy longwave radiation is the most significant contribution to the longwave radiation balance. There were very few perfectly uniform sunny and cloudy days during the measurement period at Abisko, but overall the diffuse radiation was very high. It can be assumed that there was some cloud cover on most days.

The longwave radiation measured above the sparse birch forest canopy was lower than the longwave radiation measured beneath the canopy. Therefore, the warming of the trees within the sparse forests should not be neglected in the overall energy balance within the model. The trees were shown to contribute up to an additional 17 W m^{-2} on a sunny day and up to an additional 8 W m^{-2} on a cloudy day. *Bonan et al.* [1992] found the presence of the boreal forest increases winter and summer air temperatures relative to low level tundra vegetation or bare ground.

Although this study was limited as there was only one sensor for below canopy longwave radiation, it is still possible to draw conclusions on how the sparse forest impacts the below canopy longwave radiation balance, though it cannot be determined how this varies spatially. As the main limitation for the below canopy longwave radiation observations was the lack of spatial variability, in hindsight it would have been worthwhile considering placing the sensor on a moving track. Although there would have been significant challenges for power and installation of this type of system at the field site, aside from additional sensors it would be the most effective way to gather information on the variability of below canopy longwave radiation.

As the trees represent an important part of the longwave radiation budget, tree canopy temperatures were used to effectively model the longwave radiation from the tree canopy ($\mathrm{Tree_{LW}}$) and the below canopy longwave radiation balance ($\mathrm{LW_{bc}}$). Even though there was only one measurement of below canopy longwave radiation available for a short period in 2008, the tree temperature data allowed analysis throughout the 2008 and 2009 field campaign. These calculations are useful for estimating the $\mathrm{Tree_{LW}}$ but the $\mathrm{Tree_{LW}}$ parameter is difficult to reproduce within the JULES model, nevertheless the principle developed here can be applied to JULES.

The collection of canopy temperature data was challenging. Whilst thermocouples are an established instrument for measuring temperature in field studies [*Unwin and Corbet*, 1991] and were cheap and relatively easy to install, they required regular maintenance. The canopy temperature data set was used to evaluate our model of $\mathrm{Tree_{LW}}$. This method of using in-situ temperature observations to calculate longwave radiation is established [*Essery et al.*, 2008b], although caution should be applied when using air temperatures as a proxy for canopy temperature [*Webster et al.*, 2016b]. Modelling below canopy longwave radiation has received much less attention than shortwave radiation [*Essery et al.*, 2008b], but studies have shown its importance in seasonally snow covered boreal forests [*Sicart et al.*, 2006; *Pomeroy et al.*, 2006; *Essery et al.*, 2008b; *Pomeroy et al.*, 2009; *Ellis et al.*, 2010, 2011].

3.7 Summary

The tree canopy measurements detailed in this chapter have an important role in both model parameterisations and validation. Table 2.3 in Chapter 2 on page 50 shows a summary of the tree canopy measurements in both 2008 and 2009, the days when the measurements are available, and their purpose with respect to the JULES model.

Fieldwork results: Radiation measurements

4.1 Introduction

One of the primary objectives of this study was to determine the amount of shortwave radiation which penetrates down through the sparse forest canopies to the surface of the snowpack below. To achieve this a series of quantitative measurements using pyranometers, and multi-component radiometers were taken in a sparse deciduous birch forest. The measurement plan was designed to capture the spatial variability of the forest canopy during the spring and through the bud-burst into summer, with the resources available.

Pyranometers and multi-component radiometers have been used extensively to measure the shortwave and longwave radiation under forest canopies. Providing care is taken in the installation and calibration of the radiometers, the measurements have been shown to be reliable [*Michel et al.*, 2008; *Kohsiek et al.*, 2007].

Pyranometer arrays have been used to successfully measure below canopy radiation regimes [*Hardy et al.*, 1997a, 1998; *Melloh et al.*, 2002]. Measurements of shortwave radiation using pyranometers have also been used in the development and validation of canopy radiation transfer schemes [*Ni et al.*, 1997; *Hardy et al.*, 1997a; *Pearson et al.*, 1999; *Hardy et al.*, 2004; *Pinty et al.*, 2001, 2004; *Essery et al.*, 2008a; *Widlowski et al.*, 2011]. The longwave radiation is measured using pyrgeometers above and less frequently below the canopy to measure the thermal fluxes which enhance snowmelt.

This chapter will outline the fieldwork program designed to quantify the shortwave radiation penetration down thorough sparse canopies to a seasonal snowpack. Firstly the shortwave radiation measured by the pyranometer array will be discussed, and then the use of thermocouples

to assess the contribution of longwave radiation. Unless stated otherwise the same methods were employed to collect meteorological sets for both field seasons.

4.2 Methodology

The study site was selected for its representation of a sparse deciduous canopy in the Arctic, see section in the previous Chapter 2.2. The methodologies for the work presented in this chapter are outlined in Chapter 2.

4.3 Radiation measurements

In 2008 the below canopy pyranometers measured shortwave radiation data for a period of 30 days (day 91 - 121). In 2009 the below canopy pyranometers measured shortwave radiation data for a period of 79 days (day 90 - 169). The data for 2009 are split in presentation by the availability of above canopy total and diffuse shortwave radiation, as the above canopy incoming total and diffuse radiation measurements (Sunshine sensor, BF3, Delta-T, Cambridge, UK) were not available until day 143 (23 May).

There were no measurements of below canopy longwave radiation throughout the 2009 field season and the below canopy longwave radiation is only available for days 94, 103 to 104 and 106 to 117 in 2008.

4.3.1 Calibration: CNR1 and BF3

In order to compare measurements of below canopy shortwave radiation with the above canopy measurements of incoming shortwave radiation from the CNR1 and BF3, a calibration of the two measurements was required. A regression conducted between the measurements of above canopy total shortwave radiation measured by the BF3 and above canopy total shortwave radiation measured by a CNR1 using data for the period day 143 (23 May) to day 170 (19 June) is shown in Figure 4.1. The regression shows that the two measurements are consistent. Data from the BF3 were used in preference over the CNR1 data as it provides both direct and diffuse above canopy shortwave radiation. Days 143 to 170 in 2009 (Figures 4.4 and 4.7) use the BF3 measurements, while days 90 to 142 (Figures 4.3 and 4.6) use the CNR1 above canopy total shortwave radiation.

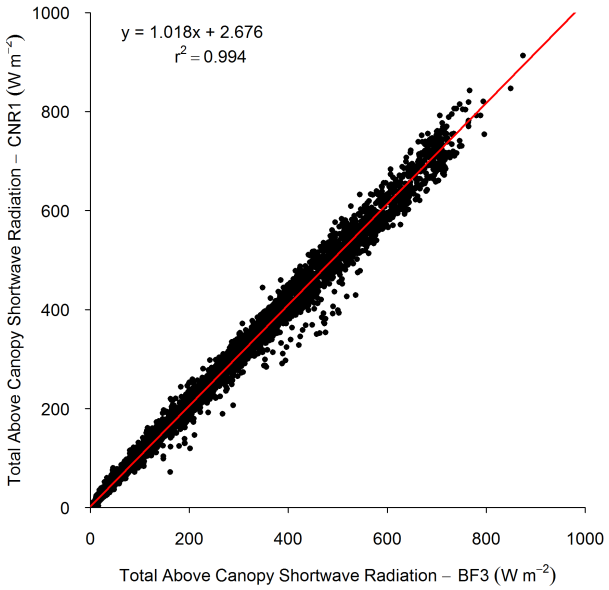

Figure 4.1: Linear regression of total above canopy shortwave radiation (W m^{-2}) measured by the CNR1 and total above canopy shortwave radiation (W m^{-2}) measured by the BF3 for the period 143 (23 May) to day 169 (18 June) in 2009.

4.3.2 Diurnal variability

2008

Figure 4.2 shows the period day 94 to 116 in 2008 for the shortwave radiation below canopy, longwave radiation above and below the canopy, and diffuse and total shortwave radiation above the canopy. The gap in the data set from day 97 to 100 and 105 was due to snowfall which buried the sensors.

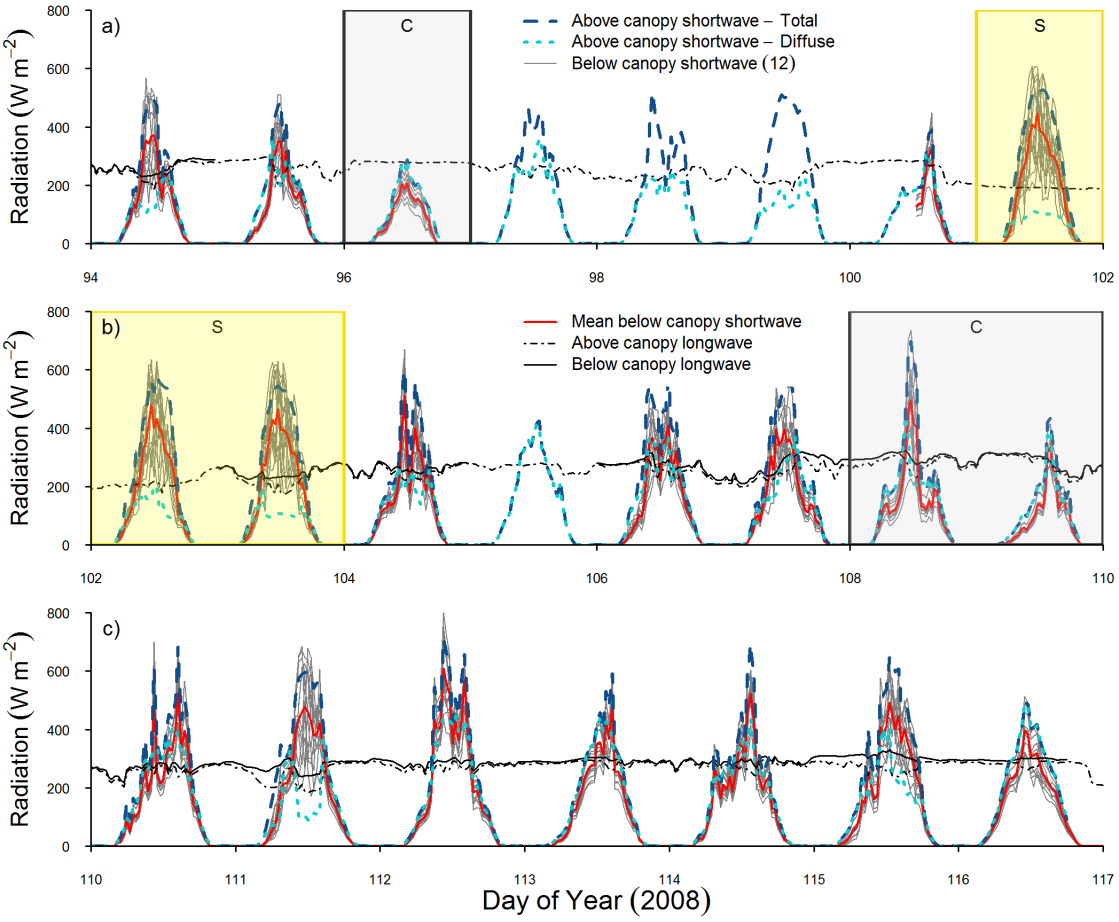

Figure 4.2: Shortwave (total and diffuse) and longwave radiation above and below the birch canopy from day 94 (3 April) to 116 (25 April) in 2008. Twelve observations of below canopy shortwave radiation (grey) and mean below canopy shortwave radiation (red). Missing data on days 97 to 100, and 105 was due to heavy snowfall. Shaded areas and letters show cloudy (C - grey) and sunny (S - yellow) days.

For the majority of days in 2008 there were bright sunny conditions with some cloud cover, characterised by sharp increases and decreases in the above canopy total radiation, measured on days 104, 106, 110, and 114 (Figure 4.2). There were a few sunny days in 2008, defined by a smooth bell shaped curve in the above canopy total radiation, measured on days 101, 102 and 103. There were also a few cloudy days, defined by similar measurements in the above canopy total and diffuse radiation, measured on days 96, 108 and 109.

The below canopy shortwave radiation shows little variation in the early morning and late afternoon, specifically when the radiation is less than 200 W m^{-2}. However, there is considerable variability in the pyranometer measurements of below canopy radiation during the middle of the day, when pyranometers separated by just a few meters can measure as much as 600 W m^{-2}

and as little as 200 W m^{-2}. What these measurements show is that when the solar elevation is low (early mornings and late afternoons), the shortwave radiation which is able to penetrate the forest canopy down to the pyranometers is relatively consistent spatially. This may be due to overcast conditions in the early mornings, as measurements of diffuse and direct radiation were very similar, except for day 111, where there is some variation in the below canopy shortwave radiation in the early morning. When the solar elevation is higher during the middle of the day, the shortwave radiation penetration is much more variable, due to the canopy shading the snow surface.

The measured below canopy shortwave radiation was higher than the total above canopy shortwave radiation, most likely due to sun flecks, or reflected shortwave radiation from the vegetation canopy. This was seen in the calibration data where the pyranometers measured higher shortwave radiance than the four component radiometer (CNR1) in both 2008 and 2009 (Figures 2.4 to 2.9).

2009

For the period day 90 to 142 in 2009 the shortwave radiation below canopy, longwave radiation above the canopy, and total shortwave radiation above the canopy are shown in Figure 4.3. The gap in the data sets from day 89 to 90 was due to calibration and the gap from day 109 to 110 was due to a period of snowfall which buried the sensors. There were no measurements of below canopy longwave radiation in 2009 as the sensor was broken.

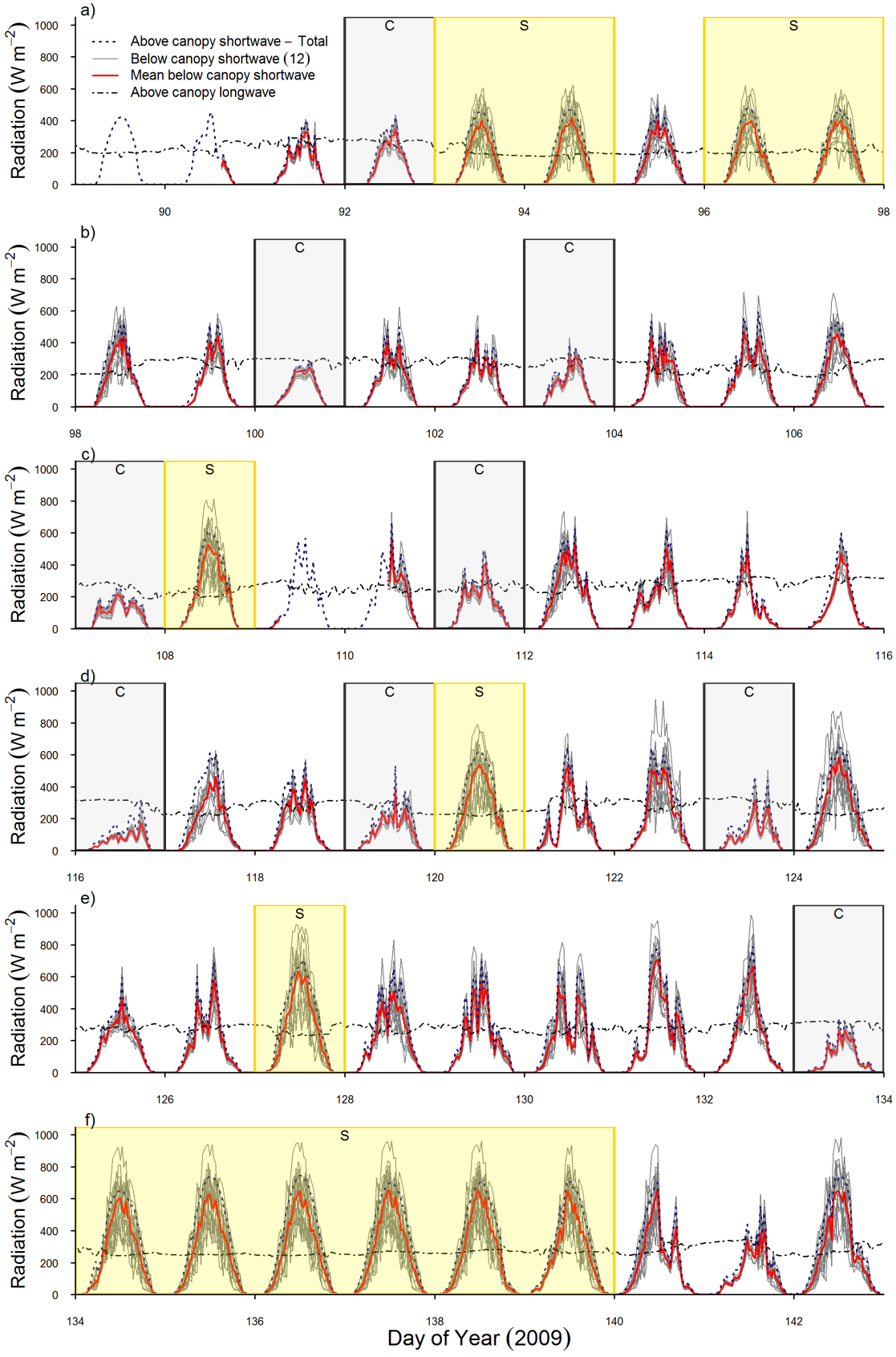

Figure 4.3: Shortwave (total) and longwave radiation above and below the birch canopy from day 91 (1 April) to day 142 (22 May) in 2009. Twelve observations of below canopy shortwave radiation (grey) and mean below canopy shortwave radiation (red). Missing data on days 89, 90, 109, and 110 was due to calibration and snowfall. Shaded areas and letters show cloudy (C - grey) and sunny (S - yellow) days.

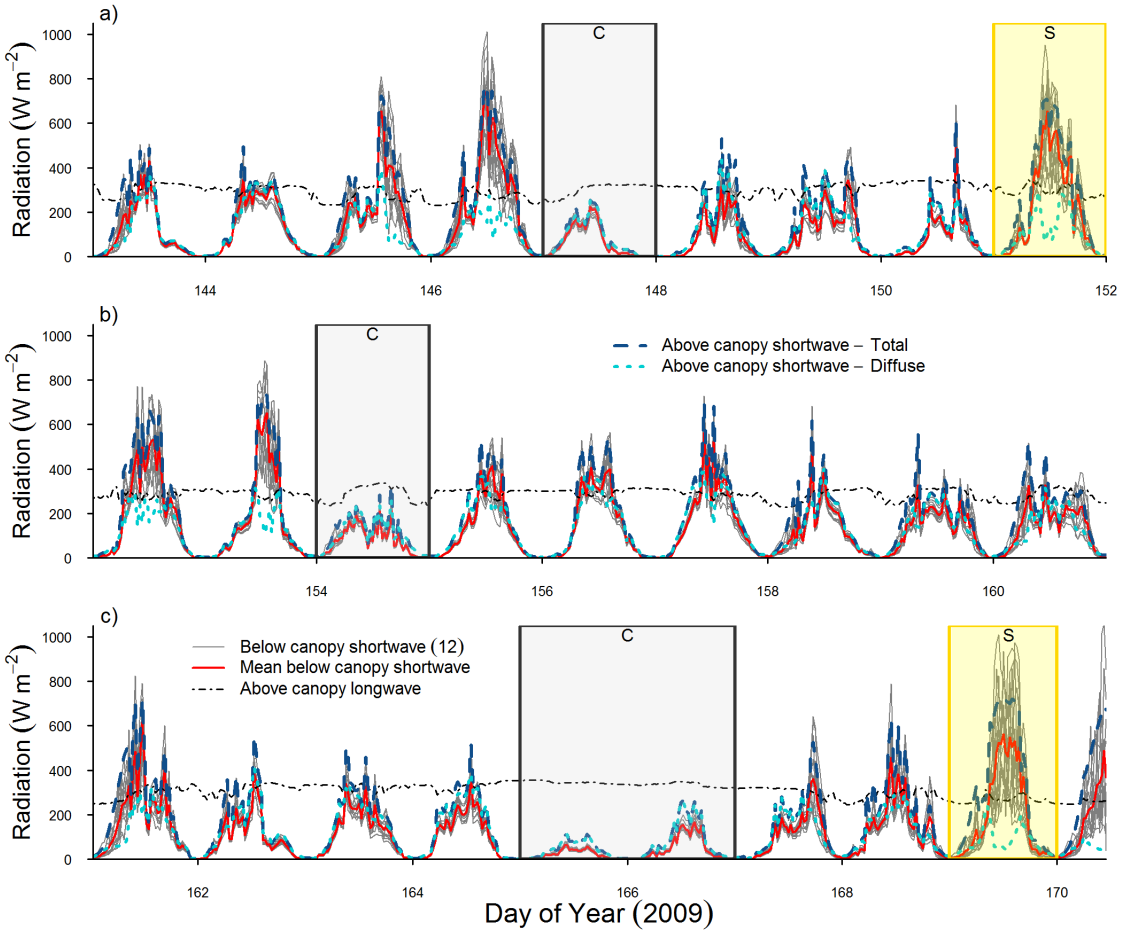

Figure 4.4: Shortwave (total and diffuse) and longwave radiation above and below the birch canopy from day 143 (23 May) to day 170 (19 June) in 2009. Twelve observations of below canopy shortwave radiation (grey) and mean below canopy shortwave radiation (red). Shaded areas and letters show cloudy (C - grey) and sunny (S - yellow) days.

Overall the conditions were dominated by bright sunny days with some cloud cover, characterised by sharp increases and decreases in the above canopy total radiation, like days 102, 104, 105, 112, 113 and 121. There were several sunny days in 2009, defined by a smooth bell shaped curve in the above canopy total radiation, like days 93, 94, 96, 97, 108, 120, 127 and 134 to 139, although most had some short periods of cloud cover. There were also a few cloudy days, defined by similar measurements in the above canopy total and diffuse radiation, like days 92, 100, 103, 107, 111, 116, 119, 123 and 133, although most had short periods of bright sunny conditions. Of these non-uniform overcast days, which had brief periods of bright and sunny conditions in 2009, specifically days 100, 107, 116, 133, 147 and 166, the daily mean for the total above canopy shortwave radiation was less than 99 W m^{-2}, while the daily mean for the below canopy shortwave radiation was less than 77 W m^{-2}.

For the period day 143 to 169 in 2009 Figure 4.4 shows the shortwave radiation below canopy, longwave radiation above and below the canopy, and diffuse and total shortwave radiation above the canopy. For day 143 to 169, the conditions were dominated by bright cloudy days with some sunny periods, characterised by sharp increases and decreases in the above canopy total radiation, like days 102, 104, 105, 112, 113 and 121. There were no perfectly uniform sunny days over this period, the most uniform conditions were on day 151 and 169, although they both had periods of cloud cover. There were many cloudy days, defined by similar measurements in the above canopy total and diffuse radiation, like days 147, 154, 165 and 166.

Similar to the 2008 data, the below canopy shortwave radiation shows little variation in the early morning and late afternoon, specifically when the radiation is less than 200 W m^{-2}, except for the sunny days. However, there is considerable variability in the pyranometer measurements of below canopy radiation around midday, where one pyranometer can be measuring as much as 600 to 800 W m^{-2} and another just a few meters away measuring as little as 200 W m^{-2}. What these measurements show is that when the solar elevation is low (early mornings and late afternoons), the shortwave radiation which is able to penetrate the forest canopy down to the pyranometers is relatively consistent spatially during overcast conditions. However, when the conditions are sunny the variability in shortwave radiation penetration even in the early mornings and late afternoons is considerably variable spatially see days 98, 101, 117, 120 and 124. This variability in the early mornings and late afternoons is small when compared to the variability during the middle of the day when the solar elevation is higher. This is due to the canopy shading the snow surface, and plays an important role in the overall radiative balance in these sparse forests.

4.3.3 Daily variability

2008

The data shown in Figure 4.5 shows the daily variability as boxplots for the above and below canopy shortwave and longwave radiation.

The lowest daily mean above canopy total radiation was 76 W m^{-2} on day 96, and the highest daily mean above canopy total radiation was 197 W m^{-2} on day 111 and 115. The lowest daily mean above canopy diffuse radiation was 48 W m^{-2} on day 101, and the highest daily mean above canopy diffuse radiation was 153 W m^{-2} on day 112. The cloudiest days were 96, 108 and 109 where the mean daily total above canopy radiation was within 10 W m^{-2} of the daily mean above canopy diffuse radiation. Whereas, on the sunniest days 101, 102, and 103, the above canopy total radiation was between 113 to 138 W m^{-2} higher than the diffuse above canopy radiation.

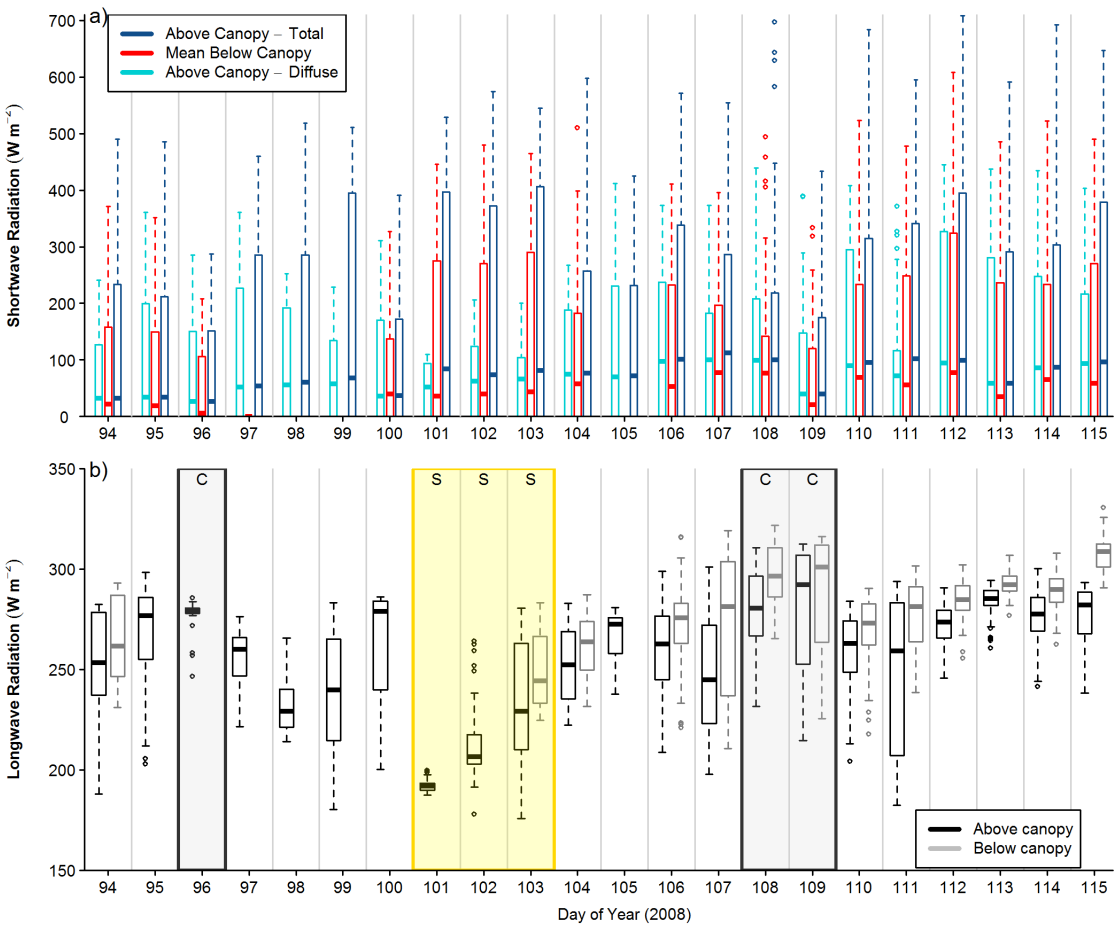

Figure 4.5: Shortwave (total and diffuse) and longwave radiation above and below the birch canopy from day 94 (3 April) to day 116 (25 April) in 2008. The central bar of the boxplots show the median values, the upper and lower edges of the box are the 25 % and 75 % percentiles, the whiskers show the minimum and maximum values, and in the case of outliers 1.5 times the interquartile range of the data. Shaded areas and letters indicate cloudy (C - grey) and sunny (S - yellow) days.

The lowest daily mean below canopy shortwave radiation was 53 W m^{-2} on day 96, and the highest daily mean below canopy shortwave radiation was 156 W m^{-2} on day 112. Therefore, there was considerable daily variability over the measurement period in the shortwave radiation measured below the canopy.

The lowest daily mean longwave radiation above the canopy was 192 W m^{-2} on day 101, and the highest daily mean longwave radiation above the canopy was 295 W m^{-2} on day 91. The lowest daily mean longwave radiation below the canopy was 248 W m^{-2} on day 103, and the highest daily mean longwave radiation below the canopy was 307 W m^{-2} on day 115.

2009

As with the previous graphs for 2009, the data for the measurement period in 2009 are split by the availability of diffuse above canopy shortwave radiation, therefore days 90 to 142 are shown in Figure 4.6 and days 143 to 170 are shown in Figure 4.7 when the above canopy shortwave diffuse component data were available.

The lowest daily mean above canopy total shortwave radiation on day 165 was 41 W m^{-2} which was a very cloudy day, and the highest daily mean above canopy total shortwave radiation was 304 W m^{-2} on day 169 which was a very sunny day. The lowest daily mean above canopy diffuse shortwave radiation on day 165 was 41 W m^{-2}, this was the same as the above canopy total shortwave radiation, as it was a cloudy day. The highest daily mean above canopy diffuse shortwave radiation was 166 W m^{-2} measured on day 157, most likely due to the presence of clouds throughout the day which were not fully masking the sky, due to variable cloud type and altitude.

The lowest daily mean below canopy shortwave radiation was 20 W m^{-2} on day 165, followed closely by 48 W m^{-2} on day 116, and 166. The highest daily mean below canopy shortwave radiation was 233 W m^{-2} on day 137 and the daily mean below canopy shortwave radiation exceeded 200 W m^{-2} on days 127, 134 to 139, 142, 146 and 151.

The lowest daily mean above canopy longwave radiation was 186 W m^{-2} on day 94, and the highest daily mean above canopy longwave radiation was 345 W m^{-2} on day 165.

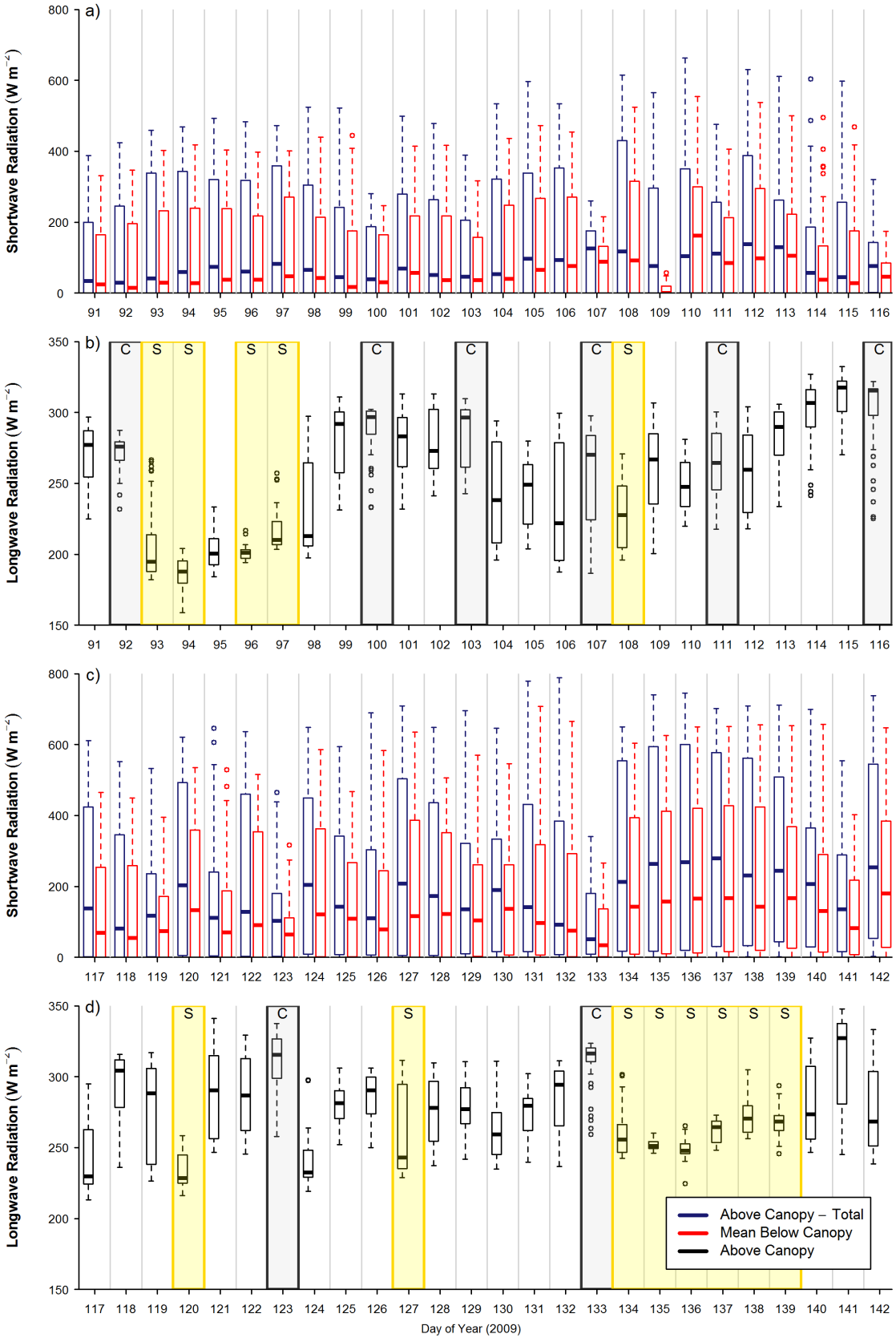

Figure 4.6: Shortwave (total and diffuse) and longwave radiation above and below the birch canopy from day 91 (1 April) to day 142 (23 May) in 2009. The central bar of the box show the median value, the upper and lower edges of the box are the 25 % and 75 % percentiles, the whiskers show the minimum and maximum values, and the outliers are 1.5 times the interquartile range of the data. Shaded areas and letters indicate cloudy (C - grey) and sunny (S - yellow) days.

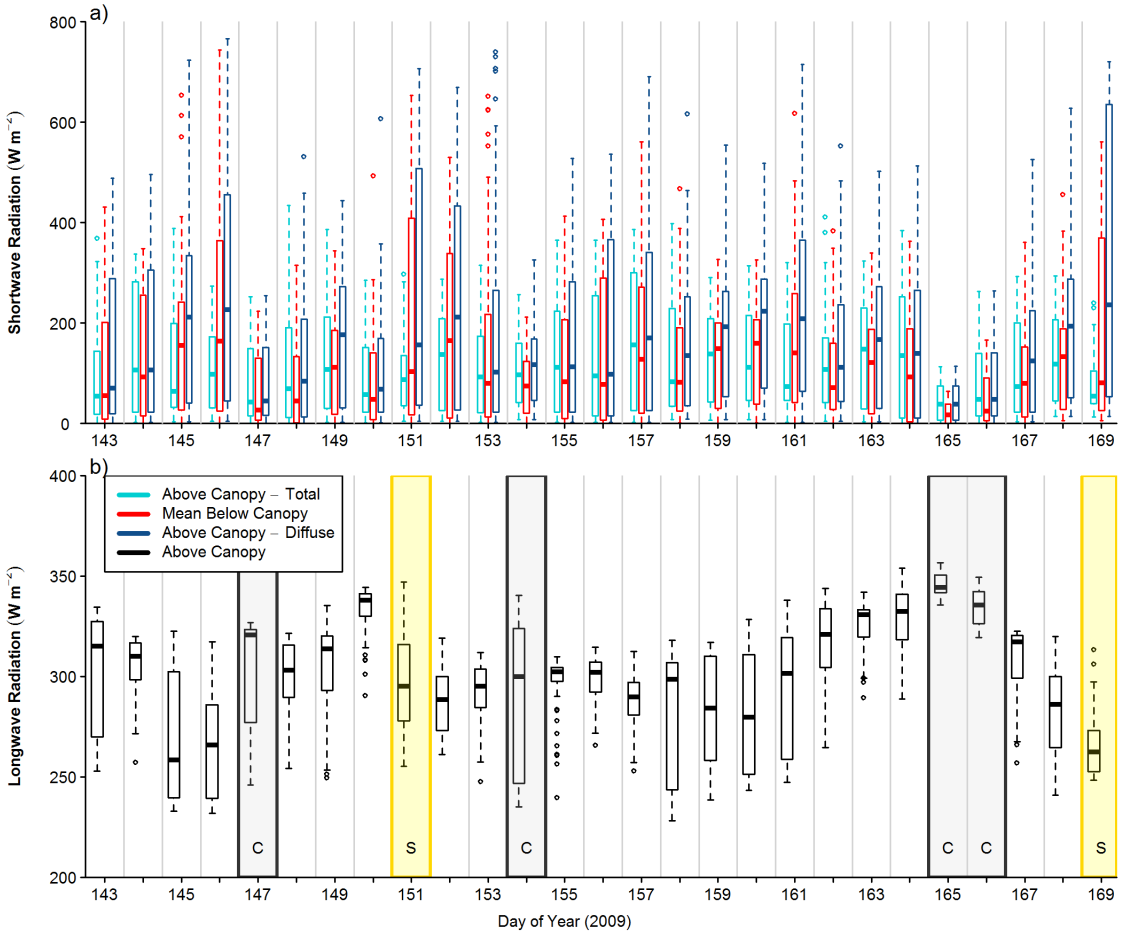

Figure 4.7: Shortwave (total and diffuse) and longwave radiation above and below the birch canopy from day 143 (23 May) to day 170 (19 June) in 2009. The central bar of the boxplots show the median values, the upper and lower edges of the box are the 25 % and 75 % percentiles, the whiskers show the minimum and maximum values, and in the case of outliers 1.5 times the interquartile range of the data. Shaded areas and letters indicate cloudy (C - grey) and sunny (S - yellow) days.

4.3.4 Periodic variability over 3 to 4 weeks

Table 4.1 shows the periodic means for each of the above and below canopy shortwave and longwave radiation measurements. The data in Table 4.1 for 2009 is divided into three periods, day 91 to 116 in order to compare with the data in 2008, day 117 to 142 and day 143 to 169 when the above canopy diffuse shortwave radiation is available.

Table 4.1: Periodic mean radiation measurements (W m^{-2}) for day 94 to 115 in 2008, day 91 to 116, day 117 to 142, and day 143 to 169 in 2009. The above canopy total shortwave radiation (SW_{total}), the above canopy diffuse shortwave radiation ($SW_{diffuse}$), the below canopy shortwave radiation (SW_{bc}), the above canopy longwave radiation (LW_{ac}) and the below canopy longwave radiation (LW_{bc}).

		Daily Mean Radiation Measurements				
	Period	SW_{total}	$SW_{diffuse}$	SW_{bc}	LW_{ac}	LW_{bc}
2008	94 - 115	153.50	100.69	112.65	255.34	278.34
2009	91 - 116	143.02	-	112.35	255.13	-
	117 - 142	226.06	-	170.10	273.65	-
	143 - 169	175.55	115.37	126.73	299.26	-

In 2008 the mean above canopy total radiation from day 94 to 115 was 153 W m^{-2}, the mean above canopy diffuse radiation was 101 W m^{-2}, and the mean daily below canopy shortwave radiation was 113 W m^{-2}. In 2009, the mean above canopy total radiation from day 91 to 116 was 143 W m^{-2}, there was no measurements of above canopy diffuse radiation, but the mean daily below canopy shortwave radiation was 112 W m^{-2}, which was almost identical for days 94 to 115 in 2008. Therefore the measurements of mean above and below canopy shortwave radiation were very similar for both years.

For days 117 to 142 in 2009, the mean above canopy total shortwave radiation was 226 W m^{-2} and the mean below canopy shortwave radiation was 170 W m^{-2}. The mean above canopy total shortwave radiation was 176 W m^{-2} from day 143 to 169, the mean above canopy diffuse shortwave radiation was 115 W m^{-2}, and the mean below canopy shortwave radiation was 127 W m^{-2}. Therefore, shortwave radiation above the canopy was highest for the period day 117 to 142 in 2009, when the highest below canopy shortwave radiation measurements were also at their highest.

For the period day 94 to 115 in 2008 the mean daily above canopy longwave radiation was 255 W m^{-2}, whereas the average daily below canopy longwave radiation was 278 W m^{-2}, indicating

an additional mean daily contribution of 26 W m^{-2} of longwave radiation from the forest canopy. In 2009 the mean daily above canopy longwave radiation for the period day 91 to 116 was 255 W m^{-2}, it was slightly higher for the period 117 to 142 at 274 W m^{-2}, and the largest mean was for the period day 143 to 169 at 299 W m^{-2}. There were no measurements of the longwave radiation below the canopy in 2009. Despite this the mean above canopy longwave radiation were the same for both early 2008 and 2009.

4.3.5 Uniform sunny and cloudy days

The variability of incoming shortwave radiation below the canopy is highlighted by separating out sunny and cloudy days, although there were very few perfectly uniform sunny and cloudy days. Uniform sunny days were defined by a smooth bell shaped curve in the above canopy shortwave radiation (direct or total), whereas cloudy days were defined by generally low level of radiation with equal measurements of total and diffuse above canopy shortwave radiation. Two sunny and two cloudy days from each year are shown in Figure 4.8 and Figure 4.9 and the data are presented in Table 4.2.

2008

In 2008 day 101 was a sunny day, as the above canopy total shortwave radiation is a smooth bell shaped curve. On Day 101 the daily mean above canopy total shortwave radiation was 184 W m^{-2} (Table 4.2) with a maximum of 529 W m^{-2}, whereas, the daily mean above canopy diffuse shortwave radiation was 48 W m^{-2} with a maximum of 109 W m^{-2}. The daily mean below canopy shortwave radiation was 127 W m^{-2} with a peak of 445 W m^{-2}. The daily mean above canopy longwave radiation was 193 W m^{-2} however, the absence of the below canopy longwave radiation data makes it difficult to draw conclusions.

Day 103 was also a sunny day. The daily mean above canopy total shortwave radiation was 182 W m^{-2} (Table 4.2) with a maximum of 545 W m^{-2}, whereas, the daily mean above canopy diffuse shortwave radiation was 57 W m^{-2} with a maximum of 200 W m^{-2}. The daily mean below canopy shortwave radiation was 130 W m^{-2} with a peak of 464 W m^{-2}. The daily mean above canopy longwave radiation was 233 W m^{-2} however, the below canopy longwave radiation data was even higher at 249 W m^{-2}.

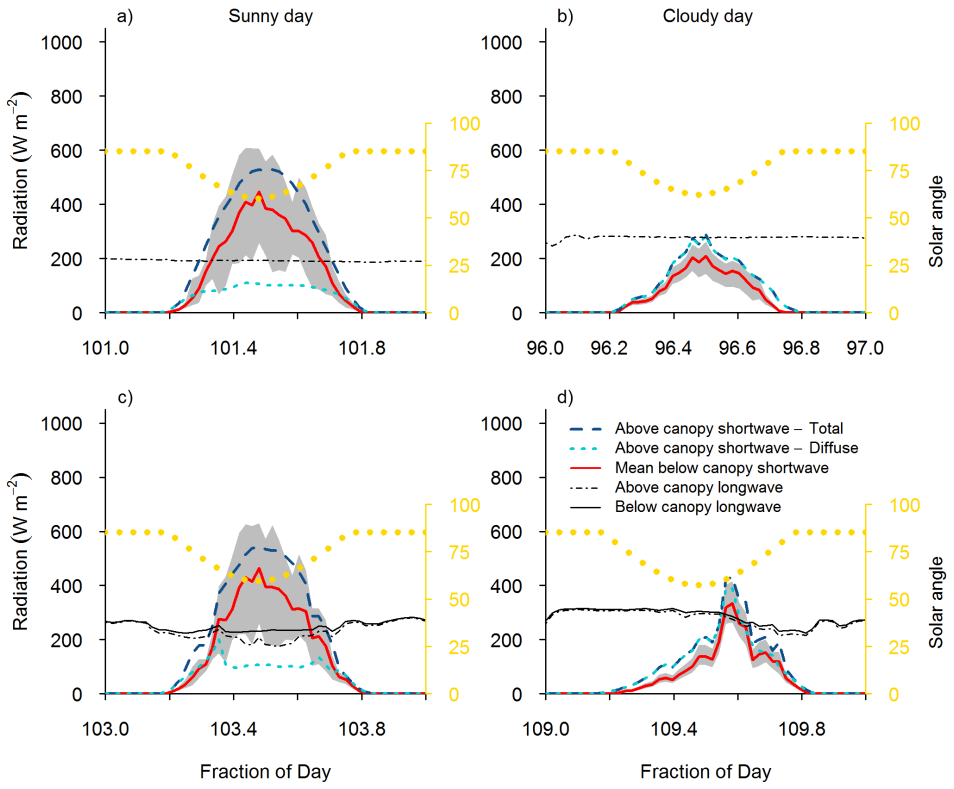

Figure 4.8: Shortwave radiation on two sunny days and two cloudy days in 2008, with the above canopy total (dark blue long dash line) and diffuse radiation (light blue dotted line). The above canopy (dot dashed black line) and below canopy longwave radiation (solid black line) are shown where available. The light grey area shows the range of below canopy shortwave radiation measurements and the mean below canopy shortwave radiation is shown in red. Yellow dots show the solar angle (from the vertical).

Day 96 was a cloudy day, characterised by equal total and diffuse above canopy shortwave radiation. The daily mean above canopy total shortwave radiation was 75 W m^{-2} (Table 4.2) with a maximum of 287 W m^{-2}, while the daily mean above canopy diffuse shortwave radiation was also 75 W m^{-2} with a maximum value of 285 W m^{-2}, confirming that day 96 was an overcast day. The daily mean below canopy shortwave radiation was 53 W m^{-2} with a maximum of 208 W m^{-2}. The daily mean above canopy longwave radiation was 278 W m^{-2} however, below canopy longwave radiation data were not available for a comparison.

Day 109 was also a cloudy day, although there were slightly clearer and brighter conditions during the middle of the day and in the afternoon. The daily mean above canopy total shortwave radiation was 93 W m^{-2} (Table 4.2) with a maximum of 433 W m^{-2}, whereas, the daily mean above canopy diffuse shortwave radiation was 83 W m^{-2} with a maximum value of 389 W m^{-2} which is very similar to that of the total, but indicating some periods of broken cloud with brighter conditions.

The daily mean below canopy shortwave radiation on the cloudy days was 63 W m^{-2} with a maximum of 334 W m^{-2}. The daily mean above canopy longwave radiation was 278 W m^{-2} and the below canopy longwave radiation was even higher at 286 W m^{-2}.

2009

In 2009 day 94 was a sunny day, as the above canopy total shortwave radiation was a smooth bell shaped curve. The daily mean above canopy total shortwave radiation was 157 W m^{-2} (Table 4.2) with a maximum of 468 W m^{-2}. The daily mean below canopy shortwave radiation was 115 W m^{-2} with a peak of 417 W m^{-2}. The daily mean above canopy longwave radiation was 187 W m^{-2} however, the absence of the below canopy longwave radiation data makes it difficult to draw conclusions.

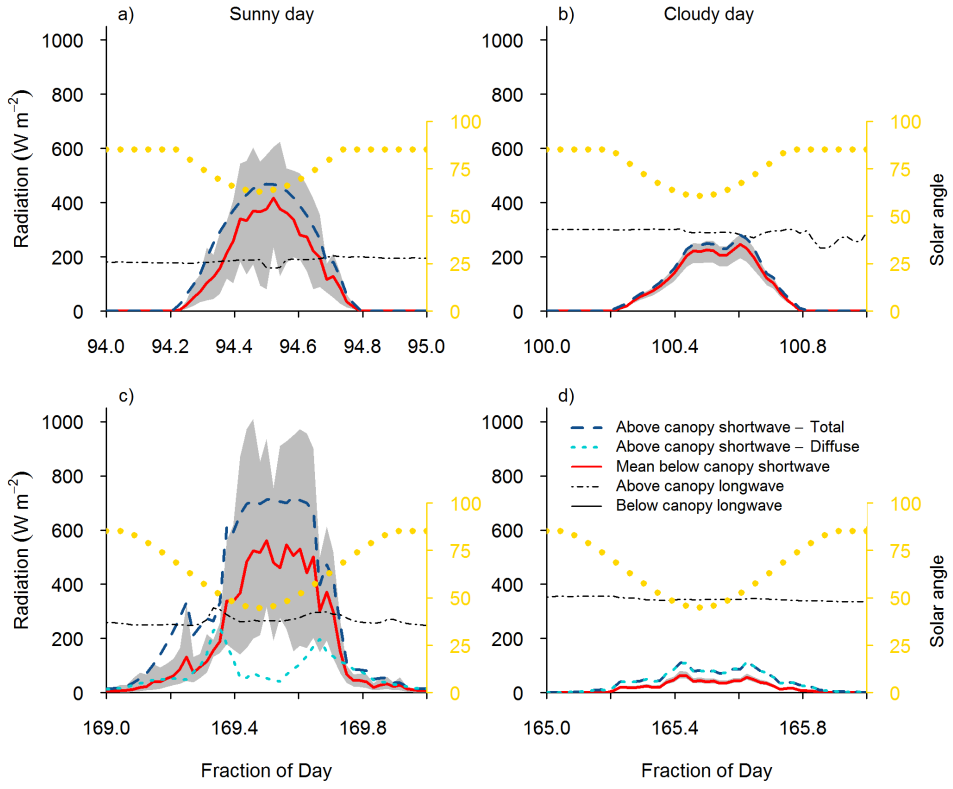

Figure 4.9: Shortwave radiation on two sunny days and two cloudy days in 2009, with the above canopy total (dark blue long dash line) and diffuse radiation (light blue dotted line). The above canopy (dot dashed black line) and below canopy longwave radiation (solid black line) are shown where available. The light grey area shows the range of below canopy shortwave radiation measurements and the mean below canopy shortwave radiation is shown in red. Yellow dots show the solar angle (from the vertical).

Day 169 was also a sunny day, but with overcast conditions in both the morning and afternoon. The daily mean above canopy total shortwave radiation was 298 W m^{-2} (Table 4.2) with a maximum of 720 W m^{-2}, whereas the daily mean above canopy diffuse shortwave radiation was 76 W m^{-2} with a maximum of 240 W m^{-2}. The daily mean below canopy shortwave radiation was 188 W m^{-2} with a peak of 561 W m^{-2}. The daily mean above canopy longwave radiation was 266 W m^{-2}.

Day 100 was a cloudy day, characterised by equal total and diffuse above canopy shortwave radiation. The daily mean above canopy total shortwave radiation was 87 W m^{-2} (Table 4.2) with a maximum of 281 W m^{-2}. The daily mean below canopy shortwave radiation was 76 W m^{-2} with a maximum of 246 W m^{-2}. The daily mean above canopy longwave radiation was 289 W m^{-2}.

Day 165 was also a cloudy day. The daily mean above canopy total shortwave radiation was 41 W m^{-2} (Table 4.2) with a maximum of 114 W m^{-2}. The daily mean above canopy diffuse shortwave radiation was also 41 W m^{-2} with a maximum value of 113 W m^{-2} which is very similar to that of the total, confirming it was an overcast day. The daily mean below canopy shortwave radiation was 20 W m^{-2} with a maximum of 65 W m^{-2}. The daily mean above canopy longwave radiation was 345 W m^{-2}.

Table 4.2: Daily mean radiation measurements (W m^{-2}) for sunny and cloudy days. The above canopy total shortwave radiation (SW_{total}), the above canopy diffuse shortwave radiation ($SW_{diffuse}$), the below canopy shortwave radiation (SW_{bc}), the above canopy longwave radiation (LW_{ac}) and the below canopy longwave radiation (LW_{bc}).

			Daily Mean Radiation Measurements				
		Day No.	SW_{total}	$SW_{diffuse}$	SW_{bc}	LW_{ac}	LW_{bc}
Sunny Days	2008	101	183.79	47.91	126.98	192.62	-
		103	181.77	57.07	130.43	232.61	249.45
	2009	94	156.62	-	115.23	186.71	-
		169	298.36	75.54	188.08	266.20	-
Cloudy Days	2008	96	75.44	74.87	52.53	277.76	-
		109	93.24	83.01	62.75	277.71	285.55
	2009	100	86.59	-	75.57	288.83	-
		165	41.11	40.97	19.65	345.48	-

4.4 Forest canopy transmissivity

Measurements of the above canopy shortwave radiation and the below canopy shortwave radiation have been used to calculate a forest canopy transmissivity for each of the 12 pyranometer locations. As there was not a continuous period of direct above canopy shortwave radiation from the BF3 sensor, analyses were conducted using the total above canopy shortwave radiation (CNR1), as the two measurements were found to be consistent (Figure 4.1) in the previous section. The daily mean transmissivities were used to calculate mean canopy transmissivity for each pyranometer location in 2008 and 2009 (Table 4.3). Table 4.3 shows that the forest canopy transmissivity varied between 57.48 % (pyranometer location 12) and 90.37 % (pyranometer location 9) in 2008 and between 60.68 % (pyranometer location 11) and 87.24 % (pyranometer location 7) in 2009.

Table 4.3: Forest canopy transmissivity (%) data for the pyranometers. The mean, standard deviation and standard error of the mean are shown for all measurements taken in 2008 and 2009. Calculated using the direct above canopy shortwave radiation (CNR1).

		Forest canopy transmissivity measured at each pyranometer location											
		1	2	3	4	5	6	7	8	9	10	11	12
2008	$\bar{x}$	83.95	69.41	64.26	87.23	73.26	65.28	65.06	73.07	90.37	79.37	79.71	57.48
	σ	5.80	6.77	8.52	6.92	5.18	3.90	6.73	4.42	4.85	6.42	5.39	3.92
	$\sigma_{\bar{x}}$	74.89	60.88	40.80	77.24	57.11	57.93	55.73	65.03	82.49	67.26	69.16	51.48
2009	$\bar{x}$	83.98	80.52	71.42	85.78	79.25	81.32	87.24	64.20	85.45	72.30	60.68	61.25
	σ	7.24	5.39	7.43	6.08	6.78	6.91	6.30	5.69	11.30	5.52	6.03	6.57
	$\sigma_{\bar{x}}$	62.01	66.76	49.11	66.11	54.91	62.28	62.25	51.25	51.53	54.84	41.53	39.79

The forest canopy transmissivities are shown in Figure 4.10 panel a for 2008 and Figure 4.10 panel b and c for 2009. The daily transmissivities for each of the pyranometers are shown in black and the mean transmissivity in red. Daily transmissivity for the individual pyranometers varied between 40 % and 99 % in 2008, and between 38 % and 100 % in 2009. The mean daily transmissivity for days 94 to 116 in 2008 was 73.74 %, and for the similar period (day 91 to day 116) in 2009 was 77.37 %, and the daily mean transmissivity was slightly lower at 70.19 % for days 117 to day 169. Although there is a small decrease in transmissivity in 2009, this is most likely attributable to the bud burst and leaf out commencing (pers. comm. supplementary field data on bud burst is not reported here), which would reduce the shortwave radiation penetration through the canopy. However, as the spring progresses there is a continual decrease in solar angle (increase in solar elevation) which should increase the shortwave radiation penetration therefore increasing the canopy transmissivity. As there is no trend in increasing transmissivity the largest

influence on the canopy transmissivity is from the bud burst and leaf out rather than the increasing solar elevation.

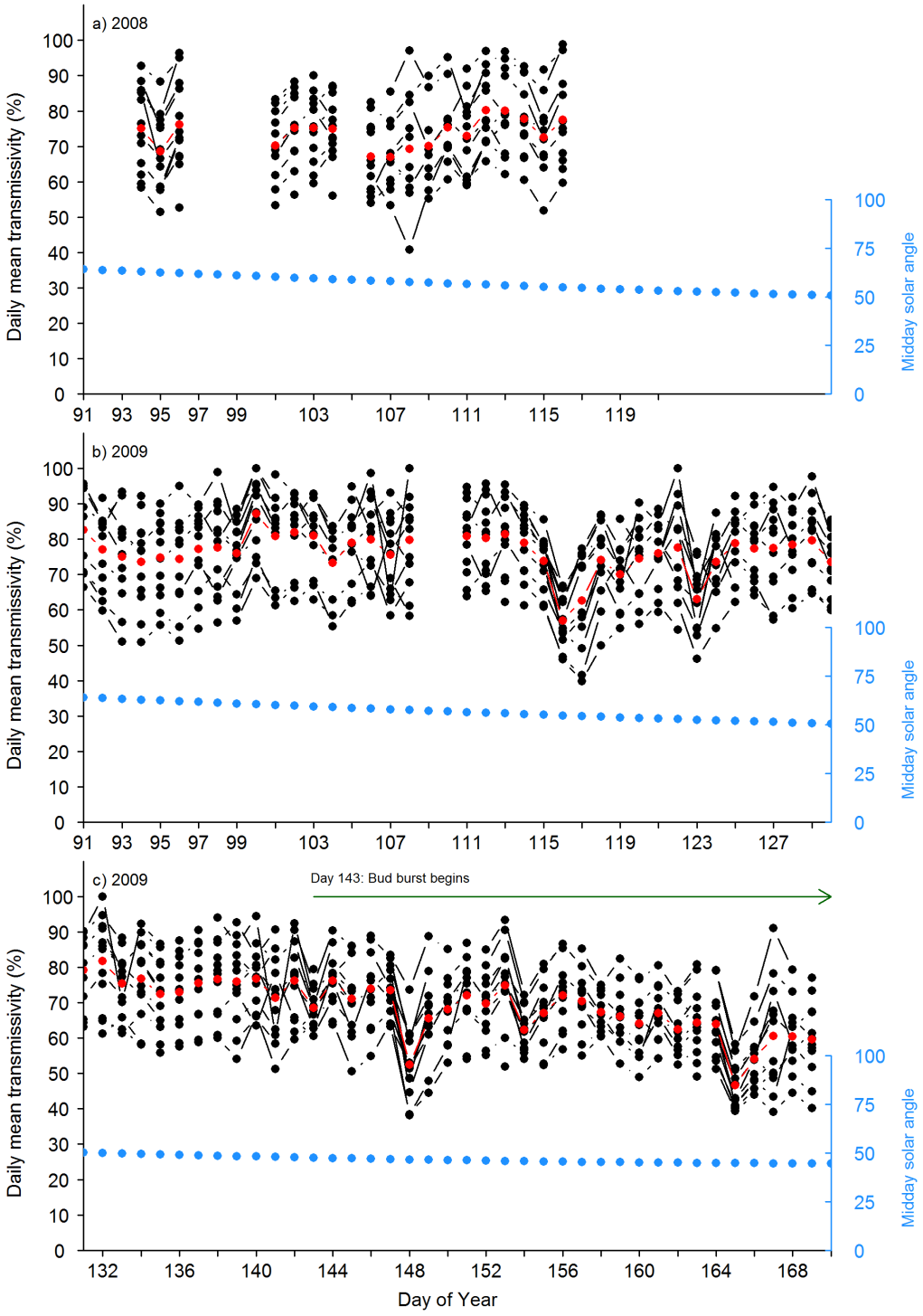

Figure 4.10: Daily mean transmissivity (%) for the pyranometers in 2008 (upper panel - a) and 2009 (lower two panels - b & c), calculated using the above canopy total shortwave radiation (CNR1) and the below canopy shortwave radiation. The black dots and lines show the 12 individual pyranometers and the red dots show the mean of the 12 pyranometers. The blue dots show the midday solar angle (from the vertical) and the green arrow indicates the bud burst.

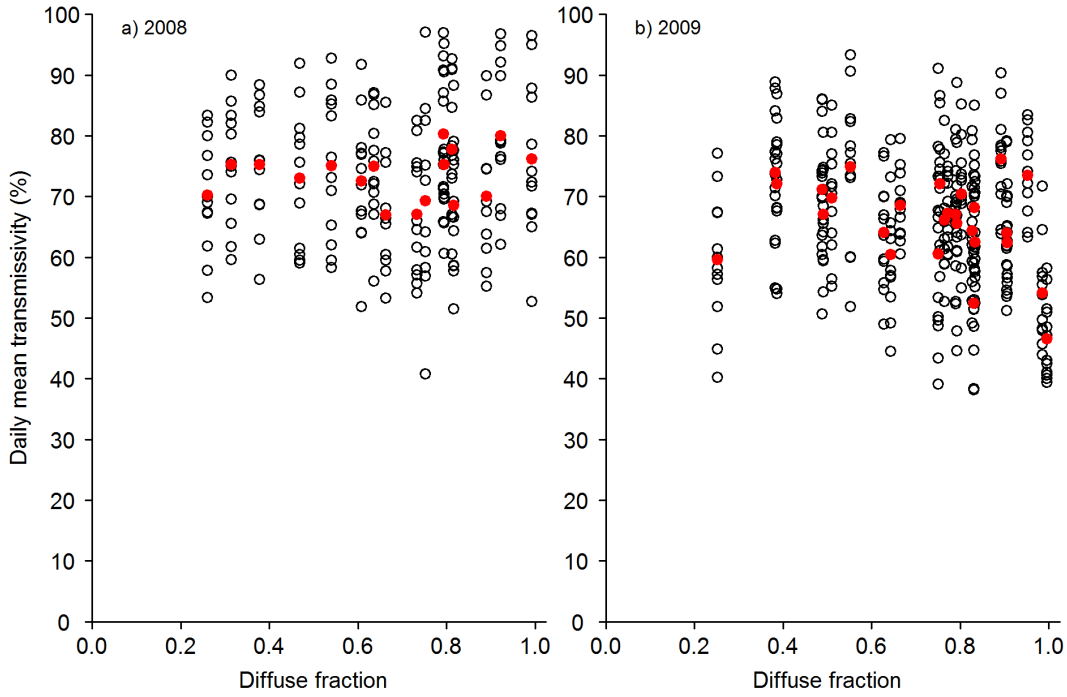

Figure 4.11: Daily mean transmissivity (%) for the pyranometers (calculated as a ratio of the below canopy shortwave radiation to above canopy total shortwave radiation (CNR1)) and the diffuse fraction (BF3) for a. 2008 (n = 17) and b. 2009 (n = 21). The black dots show the 12 individual pyranometer data and the red dots show the mean of the 12 pyranometers.

Figure 4.11 shows the daily mean forest canopy transmissivity for the 12 pyranometer locations in both years for the diffuse fraction of radiation. Irrespective of the diffuse radiation fraction the transmissivity of the canopy varies between 50 and 100 %. However, there is no clear relationship between the diffuse fraction and the canopy transmissivity for both years. This is because the canopy is very sparse, and both the direct and diffuse radiation is able to penetrate the canopy down to the pyranometers on the snow surface. Unlike dense coniferous forests which have little direct shortwave radiation penetration through the canopy, sparse deciduous forests have a distinct radiation regime which is more strongly linked to the solar elevation and the canopy structure than the fraction of diffuse radiation.

The data in 2008 (Figure 4.11) is for the snow covered period from day 94 to 115, whereas in 2009 the data is for the period day 143 to 169, after the snow covered period, once bud burst and leaf out has commenced. This change in canopy cover and solar position (increased day length and solar elevation) makes a comparison between the two years difficult. Figure 4.11 shows that there is the considerable variation in forest canopy transmissivity for the 12 pyranometers in spring and summer for both years, and that there is no relationship between canopy transmissivity and the diffuse fraction of radiation.

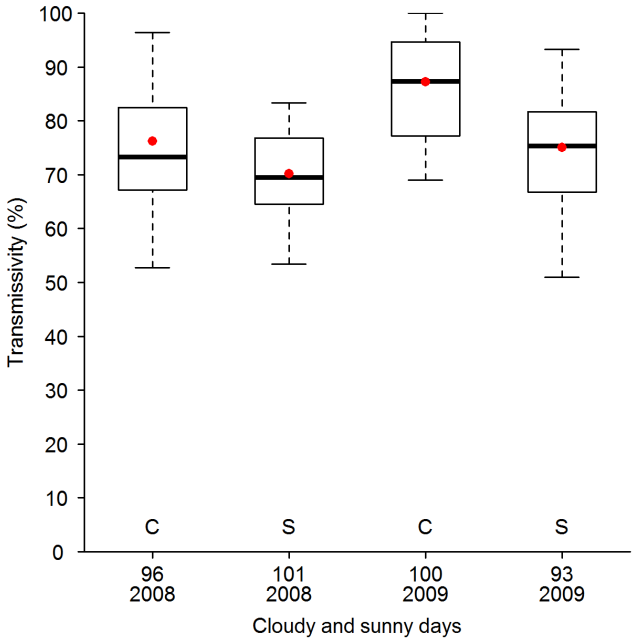

Figure 4.12: Transmissivity (%) for the pyranometers in 2008 and 2009 for uniformly sunny (S) and cloudy (C) days (calculated as a ratio of the below canopy shortwave radiation to above canopy total shortwave radiation (CNR1)). The red dots show the mean of the 12 pyranometers.

Figure 4.12 shows the changes in forest canopy transmissivity between uniformly sunny and cloudy days. In 2008 the cloudy day 96 had an average transmissivity of 76.21 % compared to the sunny day (101) which had an average transmissivity of 70.21 %. Similarly in 2009 the cloudy day 100 had an average transmissivity of 87.22 % compared to the sunny day (93) which had an average transmissivity of 75.06 %. In 2009 the sunny day 93 shows the most variability in the transmissivity, particularly compared to that of the cloudy day 100. Despite the much higher incoming shortwave radiation seen on days 101 in 2008 and day 193 in 2009 there is little difference in the transmissivity between the sunny and cloudy days. This is because the deciduous canopy is very sparse, and there is no reduction in direct shortwave radiation penetration during the spring.

4.4.1 Forest canopy transmissivity - Pyranometer and hemispherical photograph transmissivity

Figure 4.13 shows the comparison between the canopy transmissivity calculated from hemispherical photographs by GLA (Table 3.1) and the mean canopy transmissivity calculated from the shortwave radiation pyranometer data (Table 4.3).

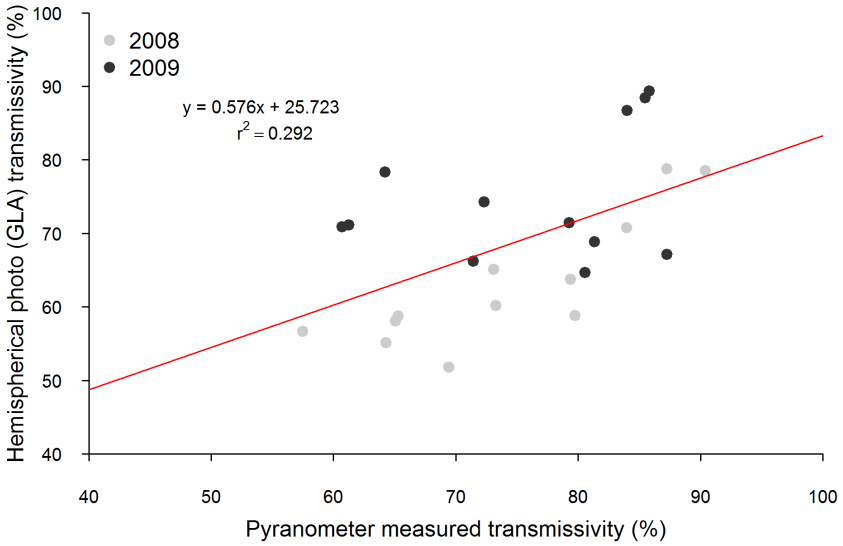

Figure 4.13: Linear regression of hemispherical photograph transmissivity (%) (calculated using GLA) and pyranometer transmissivity (%) (calculated as a ratio of the below canopy shortwave radiation to above canopy total shortwave radiation (CNR1)).

Although the correlation between the GLA calculated transmissivity and the pyranometer measured transmissivity is weak, the mean calculated transmissivity values are most relevant to the way in which these data are interpreted. The mean GLA transmissivities were 74.82 % and 73.83 % for 2008 and 2009, while the mean pyranometer measured transmissivities were 74.04 % and 76.12 % for 2008 and 2009. Therefore the two sampling methods achieve similar values when averaged over the 12 pyranometer locations, and can be used successfully to estimate average canopy cover values of transmissivity.

It is possible to scale up from the pyranometer data to the landscape scale using the hemispherical photos. The pyranometers only represent 24 locations within the forest where the pyranometers were permanently located. In order to scale up from these 24 sites to the landscape scale, the hemispherical photos taken in the survey grids and transects can be used.

4.5 Diffuse and direct radiation fractions

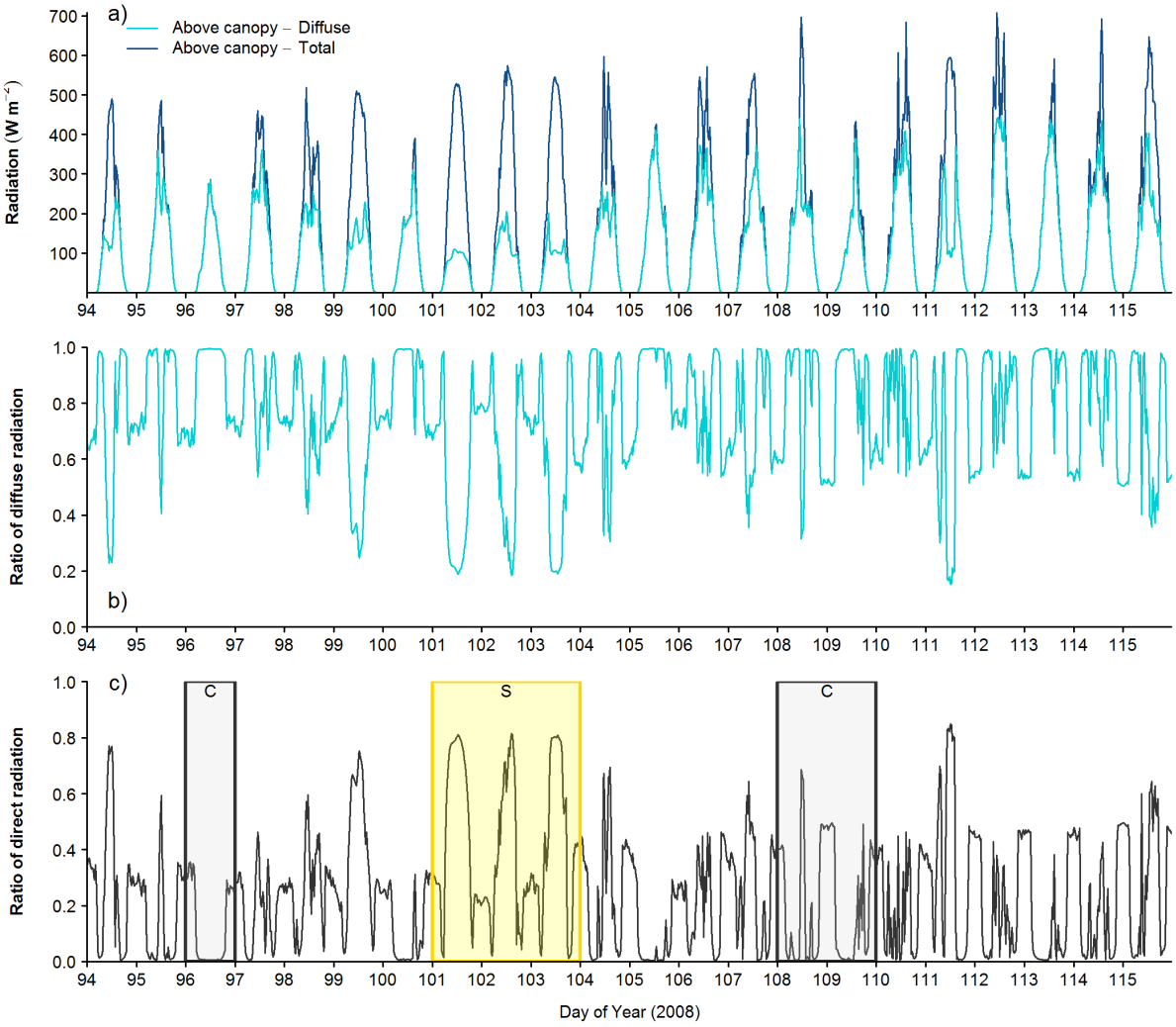

Figure 4.14: The diffuse, direct and total incoming shortwave radiation above the canopy for day 94 (3 April) to day 115 (24 April) in 2008 by a. Time series, b. Ratio of diffuse radiation and c. Ratio of direct radiation. Shaded areas and letters indicate cloudy (C - grey) and sunny (S - yellow) days.

The measurements of direct and diffuse shortwave radiation above the canopy are shown in Figure 4.14 for 2008. The data show that the fraction of diffuse radiation is very high with a mean of 0.75 for the period from day 94 to 115 in 2008 (Table 4.4). The diffuse fraction of radiation, highlights that for much of the early morning and afternoon the total radiation received above the canopy is diffuse radiation. On day 96 (the cloudy day) there is no direct radiation (as the total and diffuse radiation above the canopy are equal), whereas on the sunny days 101, 102, 103 and 111, the diffuse radiation is less than 0.3 of the total radiation received during the middle of the day.

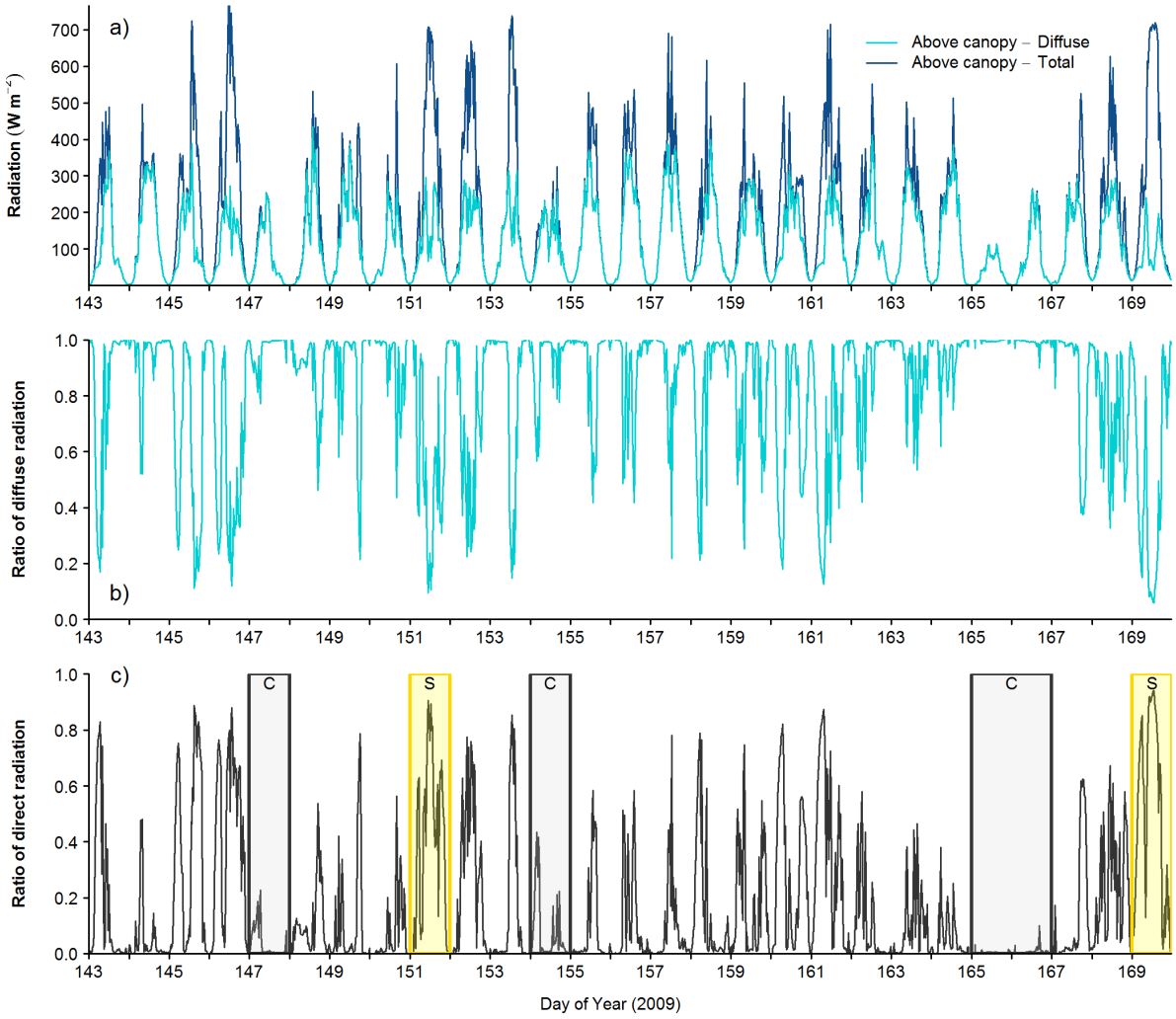

Figure 4.15: The diffuse, direct and total incoming shortwave radiation above the canopy for day 143 (23 May) to day 169 (18 June) in 2009 by a. Time series, b. Ratio of diffuse radiation and c. Ratio of direct radiation. Shaded areas and letters indicate cloudy (C - grey) and sunny (S - yellow) days.

The data in Figure 4.15 show that the fraction of diffuse radiation is very high with a mean of 0.81 for the period from day 143 to 1069 in 2009 (Table 4.4). The data from 2009 show that much of the radiation received at the Abisko field site is diffuse. The cloudy days, identified by the similar totals of diffuse and total radiation, were days 147, 154, and 165 and 166, with very little direct radiation. There was not a perfectly uniform sunny day characterised by the smooth bell shaped curve in the total above canopy radiation for the period day 143 to 169 in 2009.

As the total and diffuse above shortwave radiation were not available for the whole period of the field campaign, the data were analysed for several different periods when they were available as

summarised in Table 4.4.

Table 4.4: Direct Diffuse Fractions.

Period	Day of year in analysis	Fraction of Diffuse radiation	Fraction of Direct radiation
Spring measurements	94 - 115	0.751	0.249
When Total radiation exceeds 100 W m^{-2}	94 - 115	0.723	0.277
Fraction of day - between 0.3 (8am) - 0.7 (5pm)	94 - 115	0.713	0.287
Sunny days	101 - 103	0.582	0.418
Cloudy days	96, 100 & 109	0.856	0.144
Winter measurements	2008: 285 - 365 2009: 1 - 12	0.726	0.274
Summer measurements	2009: 143 - 243	0.805	0.195
All measurements	2008: 94 - 115, 285 - 365 2009: 1 - 12, 143 - 243	0.766	0.234

When the measurements of total and diffuse radiation are averaged for the 2008 spring period (Day 94 to 115) the diffuse fraction is 0.751. However, it is possible that these data are not representative of the Abisko site as they only represent a short period of 22 days and may be biased by comparatively small differences in diffuse and direct the early mornings and late afternoons. These data were therefore analysed for periods when the total radiation exceeded 100 W m^{-2}, which gave a diffuse fraction of 0.723, excluding bias from the small measurements at dawn and dusk. The data were also analysed using periods when the fraction of day was between 0.3 and 0.7, which gave a diffuse fraction of 0.713. This excluded more early morning and evening values and was not too dissimilar to the mean diffuse fraction for times when total radiation exceeded 100 W m^{-2}. When three sunny days and three cloudy days were analysed the diffuse fraction was 0.582 and 0.856 respectively, providing a clear indication that cloudy days are dominated by diffuse radiation. However, even the sunny days have a higher fraction of diffuse radiation than direct radiation.

The mean diffuse radiation fraction was 0.726 for all winter measurements, 0.805 for all summer measurements and 0.766 for all measurements taken at the Abisko field site. However, it is important to consider that the objective of this thesis is to model these sparse forests and the

conditions specifically in the spring period, therefore the value of 0.72 will be used as the fraction of diffuse radiation from the analysis for periods when the total radiation exceeded 100 W m^{-2} (shaded row in Table 4.4).

4.6 Discussion

4.6.1 Radiation measurements

The shortwave radiation below the sparse birch forest canopy is substantially reduced relative to that measured above the canopy. The sparse and open forest has a significant effect on the overall energy balance of the forest by reducing the incoming shortwave radiation and increasing the incoming longwave radiation. This is important for modelling snow melt as *Essery et al.* [2008a] and *Sicart et al.* [2004] found that the snow melt rate was slower in coniferous forest relative to open areas due to the reduction in shortwave radiation. The reduced incident shortwave radiation in these sparse forests may delay the onset of snow melt relative to surrounding areas of open tundra.

The below canopy shortwave radiation data set from the pyranometers highlights the variability in radiation transmission for sparse birch canopies, in particular the strong contrast between cloudy and sunny days. By separating the cloudy and sunny days it is possible to see that on the sunny days there was much greater spatial variation in radiation at the surface when the shadows are dependent on sun angle and canopy cover. In contrast, on cloudy days the radiation is diffuse and insensitive to sun angle and shadows.

Longwave radiation has received less attention than shortwave radiation [*Essery et al.*, 2008b], partly due to the scarcity and unreliability of measurements, but it may contribute as much energy as shortwave radiation on cloudy days [*Sicart et al.*, 2006]. Our results show the incoming below canopy longwave radiation was higher than the incoming shortwave radiation on cloudy days.

The objective for the field campaign was to sample the variability in the below canopy shortwave radiation regime using an array of 12 pyranometers, a firmly established method of data collection [*Hardy et al.*, 1997b, 2004; *Link et al.*, 2004; *Essery et al.*, 2008a; *Pomeroy et al.*, 2008]. The pyranometer array was designed to represent the range of canopy covers measured by the hemispherical photographs across the landscape scale. Although traditionally pyranometer arrays would be arranged randomly, or on regular grids or using a single sensor which moves along a track [*Pomeroy et al.*, 2008; *Stähli et al.*, 2009; *Webster et al.*, 2016a], those arrangements

might not have encompassed the range of canopy variation in the sparse forest for this study. By targeting sites for their distinct canopy characteristics, and confirming this with GLA we can be confident that the pyranometers encompassed the variability in below canopy shortwave radiation for the sparse birch forest.

The pyranometers, four component net radiometers, and the pyrgeometer are all standard instruments for measuring radiation in field studies [*Unwin and Corbet*, 1991]. Although alternative sensors were available, the sensors listed above were used as they were already installed at the field site. The Skye pyranometers were relatively cheap and consistent, and therefore it was possible to install an array of 12 sensors. The pyranometers required intensive maintenance to ensure the sensors were level and snow free.

Diffuse fraction

Stähli et al. [2009] found that the diffuse radiation and solar elevation were the main factors controlling shortwave radiation transmissivity. Although this was in a dense coniferous sub-alpine forest stand, the diffuse fraction of radiation is an important component to the overall radiation balance.

The measurements of the diffuse fraction of radiation show that, for Abisko, the diffuse fraction of radiation is high, varying between 0.7 in winter and spring to 0.8 in summer. Ideally there would be continuous measurements of the direct and diffuse radiation components to run the JULES model, however, these measurements are sparse. JULES is typically run with a constant value for the fraction of diffuse radiation of between 0.2 and 0.4. A diffuse fraction of 0.4 would be too low for Abisko as even on sunny days it was measured at 0.58. As the measurements of direct and diffuse radiation are difficult to gap fill, the JULES model will be run with incoming total shortwave radiation and a constant value for the diffuse fraction of 0.72, as this was a measurement taken in spring, the time of most interest in the model.
The BF3 is a sophisticated sensor for measuring the separate direct and diffuse components of radiation. This data set was limited as there was only one sunshine sensor available. Ideally a second sensor below the canopy would have provided a more comprehensive study of the below canopy shortwave radiation regime. It was also a difficult sensor to maintain, which resulted in long periods without observations. Despite this, the BF3 provided valuable measurements on the separate direct and diffuse fractions of radiation for the Abisko field site.

4.7 Summary

The radiation measurements detailed in this chapter play an important role in both model parameterisations and validation. Table 2.3 in Chapter 2 on page 50 shows a summary of the radiation measurements in both 2008 and 2009, the days when the measurements are available, and their purpose with respect to the JULES model.

Chapter 5

Fieldwork results: Snow measurements

5.1 Introduction

This chapter will outline the results of the fieldwork program which were designed to quantify the spatial and temporal variability in the properties of a seasonal snowpack in a sparse birch forest. The results of the snow surveys and snowpack temperature measurements are presented.

It is important to measure the snowpack in this complex terrain as snowfall does not equate to snow depth measured on the ground. Wind redistributes snow from areas of open tundra into the areas of forest. This redistributed snow represents a significant proportion of the snowpack within the forests. Since this thesis relates to the radiation balance of this complex ecosystem and the impact of this radiative energy during the snowmelt period, rather than snowfall or snow redistribution, the model can only be evaluated relative to the initial observed snow depth before melt, not snowfall. Therefore, it is not necessarily the snowfall period, accumulation of the snowpack or the redistribution of snow which is of interest. What the model requires is a detailed picture of the snowpack at its peak and through the snowmelt period. These measurements of the snowpack will then be used to evaluate the model representation of the radiative balance and if it can predict the snowmelt period correctly.

Snow surveys and snow courses have been used extensively to measure the properties of snowpacks. As the snow depth, density and SWE can vary immensely over short distances, the design of snow surveys must take this variability into account. Measurements of snowpack properties can then be used to assess the impact of the shortwave radiation balance within the model, and whether the model can reproduce the timing and pattern of the snowmelt.

5.2 Methodology

The study site was selected for its representation of a sparse deciduous canopy in the Arctic. The methodology for the work presented in this chapter is outlined in Chapter 2. Unless stated otherwise the same methods were employed to collect hydrological data sets for both field seasons.

5.3 Snow surveys

5.3.1 Snow surveys: Sampling strategy

The first snow survey was conducted in plot ABI3 on a 2 m by 2 m sampling frequency within a 30 m by 30 m grid (900 m^2), which gave 256 snow depth measurements. This data set was used to calculate the most efficient within grid sampling strategy for the remaining snow surveys. The most efficient sampling strategy was identified as a 5 m by 10 m grid, which required 28 snow depth measurements, (Figure 5.1). This sampling strategy had minimal difference in the mean from the highest intensity sampling strategy, while it encompassed outliers and it allowed for 4 other plots to be measured before re-sampling. The lowest (0.415 m) and the highest (0.468 m) mean depths were measured using the lowest frequency sampling for the 30 m by 30 m grid (n = 4) and 15 m by 15 m grid (n = 9) respectively. The other five sampling strategies produced mean snow depth of 0.44 m $\pm$0.01, with similar median values.

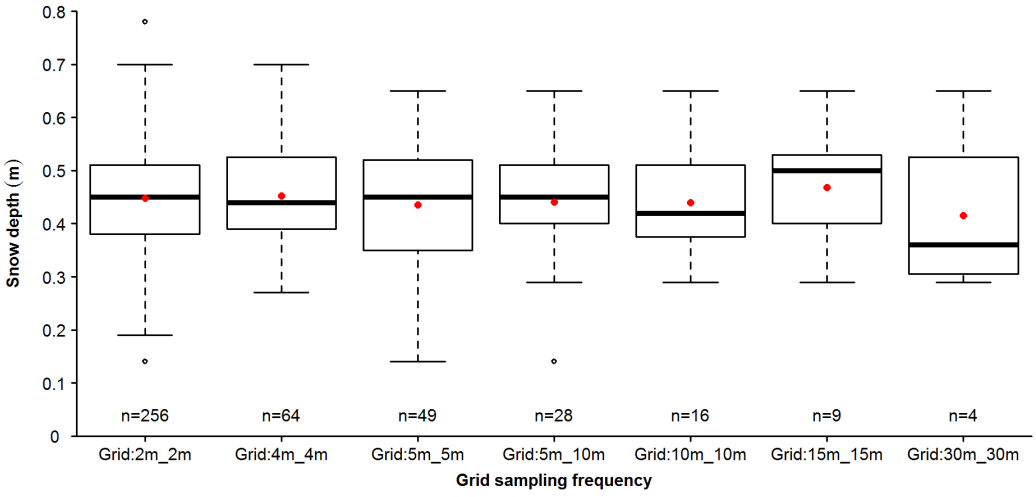

Figure 5.1: Grid snow survey sampling strategies for grid ABI3 on the 18 -19 March 2008. Red dots show the mean.

The remaining initial snow surveys in 2008 (for grids ABI2, ABI5, ABI7, ABI11) were sampled on a 5 m by 5 m grid (n = 49) within the 30 m by 30 m grid (900 m^2) and then repeat surveys were sampled every 5 m by 10 m grid (n = 28) (Figure 5.2). In 2009 all of the snow survey grids (ABI2 and ABI5) were sampled on a 5 m by 5 m grid (n = 49) within the 30 m by 30 m grid (900 m^2).

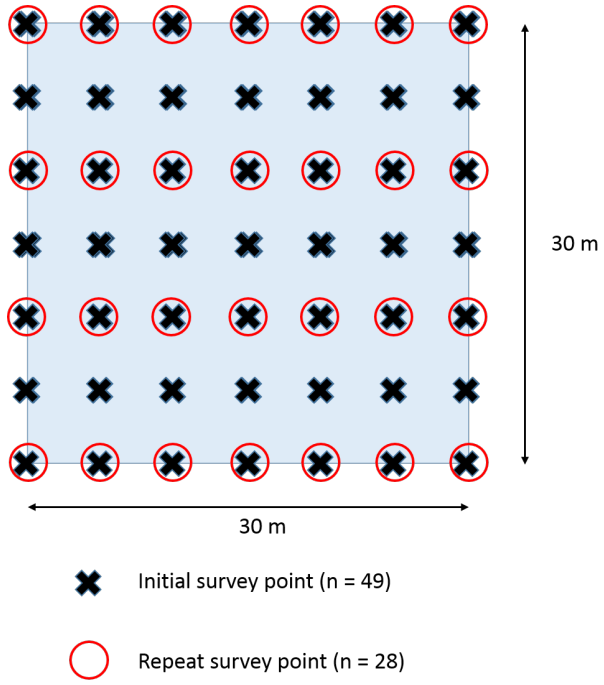

Figure 5.2: Snow survey grid sampling points for initial and repeat surveys in 2008.

5.3.2 Snow surveys: 2008

The snow depth, SWE, and density for the gridded snow surveys in 2008 measured in four forested plots (ABI2, ABI3, ABI5 and ABI7) and one open tundra plot (ABI11) are shown in Figure 5.3. It can be surmised that there was some snow compaction between day 78 and days 95 - 96 as there was not a significant increase in temperature or radiative energy, but the forest plots had a decrease in snow depth, an increase in snow density and a corresponding small increase in SWE. Snowfall during days 97 - 100 increased snow depth from the second sampling period in days 95 - 96 to the third sampling period in days 101 - 106. There was no significant period of snowmelt during the 2008 field season.

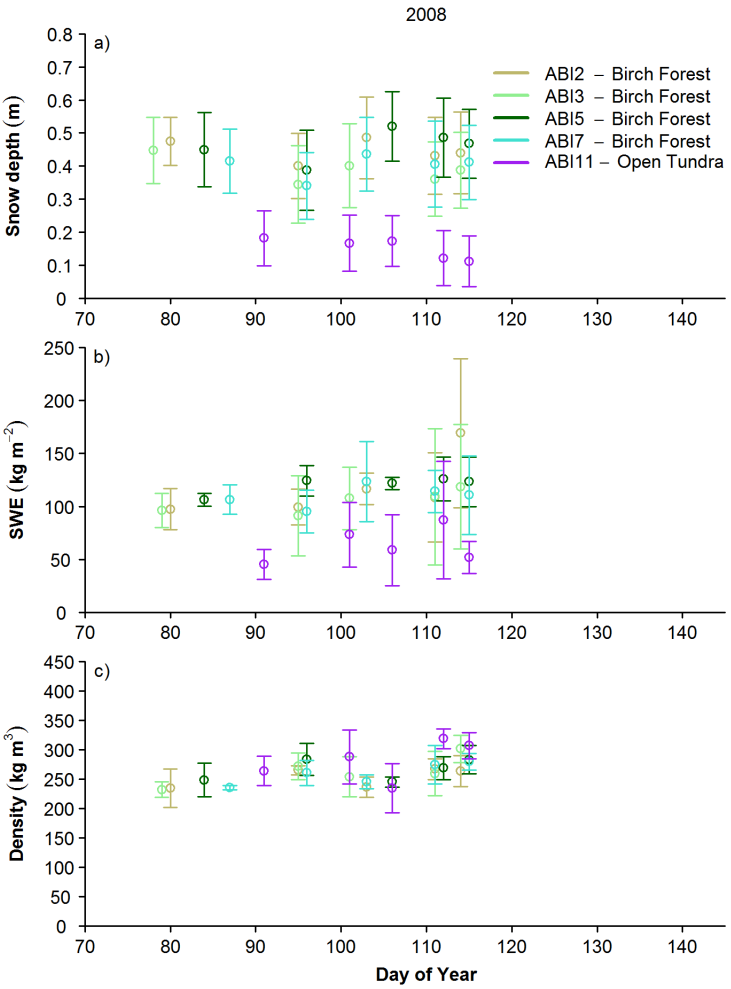

Figure 5.3: Mean snow depth (Initial n = 49, Repeat n = 38), mean SWE (n = 4) and mean density (n = 4) for 30 m by 30 m for snow surveys grids (900 m^2) in 2008. Grids ABI2, ABI3, ABI5 and ABI7 were located within the birch forest and ABI11 was located in open tundra. Bars show standard deviation.

The mean snow depth within the four forested plots were very similar, varying between 0.34 m and 0.52 m, whereas in the open tundra plot the snow depth varied between 0.12 m and 0.18 m (Figure 5.3 panel a). The snow depth data were non-normally distributed (Shapiro-Wilks, $W > 0.82$, $p > 0.05$, $n = 5$). There was no significant difference between the snow depth within the forested plots (Wilcoxon-Mann-Whitney W = 2-21, $p > 0.03$), however, there was a significant difference between the snow depth in all of the forested plots and the open tundra plot (Wilcoxon-Mann-Whitney W = 25, $p < 0.008$).

The mean SWE within the four forested plots ranged between 91.39 kg m^{-2} and 169.25 kg m^{-2}, whereas in the open tundra plot (ABI11) the mean SWE ranged between 45.26 kg m^{-2} and 87.11 kg m^{-2} (Figure 5.3 panel b). The SWE data were non-normally distributed for ABI3, ABI7

and ABI11 (Shapiro-Wilks, $W > 0.95$, $p > 0.744$, n = 3), and were normally distributed for ABI2 and ABI5 (Shapiro-Wilks, $W > 0.73$, $p < 0.044$, n = 2). There was no significant difference between the SWE within the forested plots (Wilcoxon-Mann-Whitney W = 3-19, $p > 0.05$), including between ABI5 and ABI2 (Wilcoxon-Mann-Whitney W = 7, $p > 0.309$), however there was a significant difference between the SWE in all of the forested plots and the open tundra plot (Wilcoxon-Mann-Whitney W = 25, $p < 0.008$).

The mean snow density varied between 232 kg m^{-3} and 302 kg m^{-3} within the four forested plots, and 235 kg m^{-3} and 319 kg m^{-3} in the open tundra plot (Figure 5.3 panel c). The snow density data were non-normally distributed (Shapiro-Wilks, $W > 0.76$, $p > 0.03$, n = 5), and there was no significant difference in the snow density between all of the forested plots and the open tundra plot (Wilcoxon-Mann-Whitney W = 7-15, $p > 0.05$).

5.3.3 Snow surveys: 2009

Grids

The snow survey grids in 2009 were conducted in two birch forest plots (ABI2 and ABI5). It can be surmised that there was continued snowmelt throughout the sampling period from day 110 to day 140 due to the decline in snow depth (Figure 5.4 panel a). There was no significant period of snowfall in 2009 from day 110 to 140.

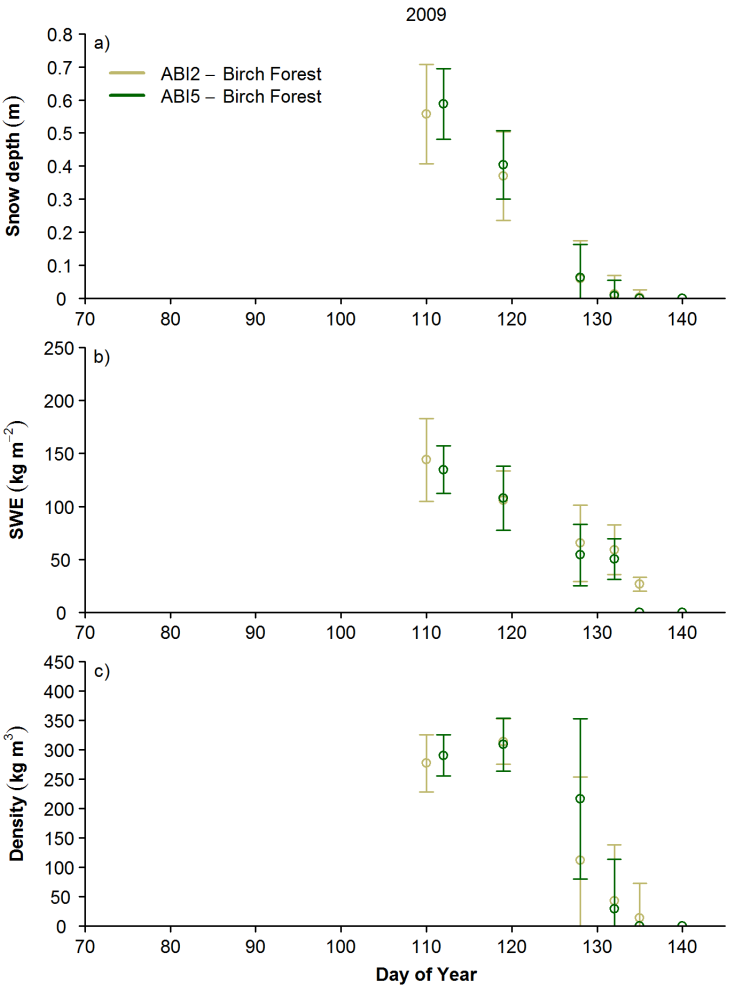

Figure 5.4: Mean snow depth (n = 49), mean SWE (n = 14 to 17) and mean density (n = 14 to 17) for 30 m by 30 m for snow surveys grids (900 m^2) in 2009. Bars show standard deviation.

On day 110 in 2009 survey grid ABI2 had a mean snow depth of 0.56 m, a mean SWE of 144 kg m^{-2}, and a mean snow density of 277 kg m^{-3}. The mean snow depth and mean SWE declined from day 110 to zero on day 140, however, the mean density increased to 314 kg m^{-3} on day 119, and then decreased to zero by day 140. On day 112 grid ABI5 had a mean snow depth of 0.59 m, a mean SWE of 135 kg m^{-2}, and a mean density of 290 kg m^{-3}. The mean snow depth and mean SWE declined from day 112 to zero on day 140, while the mean density increased to 309 kg m^{-3} on day 119, and then decreased to zero by day 140. All three snowpack properties were similar for the two grids in 2009, and also for the same grids in 2008.

Transects

The results of the north-east snow survey transect of 500 m through continuous birch forest are shown in Figure 5.5. There was a general decline in elevation away from the AWS, with a steep slope at 360 m to 500 m. On day 98 the mean snow depth was 0.55 m (Figure 5.5 panel a), mean SWE was 124 kg m^{-2} (Figure 5.5 panel b) and mean density was 245 kg m^{-3} (Figure 5.5 panel c). There was some snow redistribution and melt by day 106, which reduced the mean depth to 0.47 m, increased the mean SWE to 130 kg m^{-2} and increased the mean snow density to 295 kg m^{-3}. By day 115 the mean snow depth decreased to 0.40 m, mean SWE decreased to 104 kg m^{-2} and mean snow density decreased to 266 kg m^{-3}. There was more snowmelt, producing patchy snow cover by day 124, decreasing the mean snow depth to 0.12 m, decreasing the mean SWE to 39 kg m^{-2}, and decreasing the mean snow density to 157 kg m^{-3}. All the snow melted by day 135, however the final remaining patches of snow were associated with changes in elevation. At 165 m on the transect there was a small hollow where snow remained, also at 365 m on the leeward edge of a steep slope, and at 390 m at the base of the steep slope (Figure 5.5 panel d).

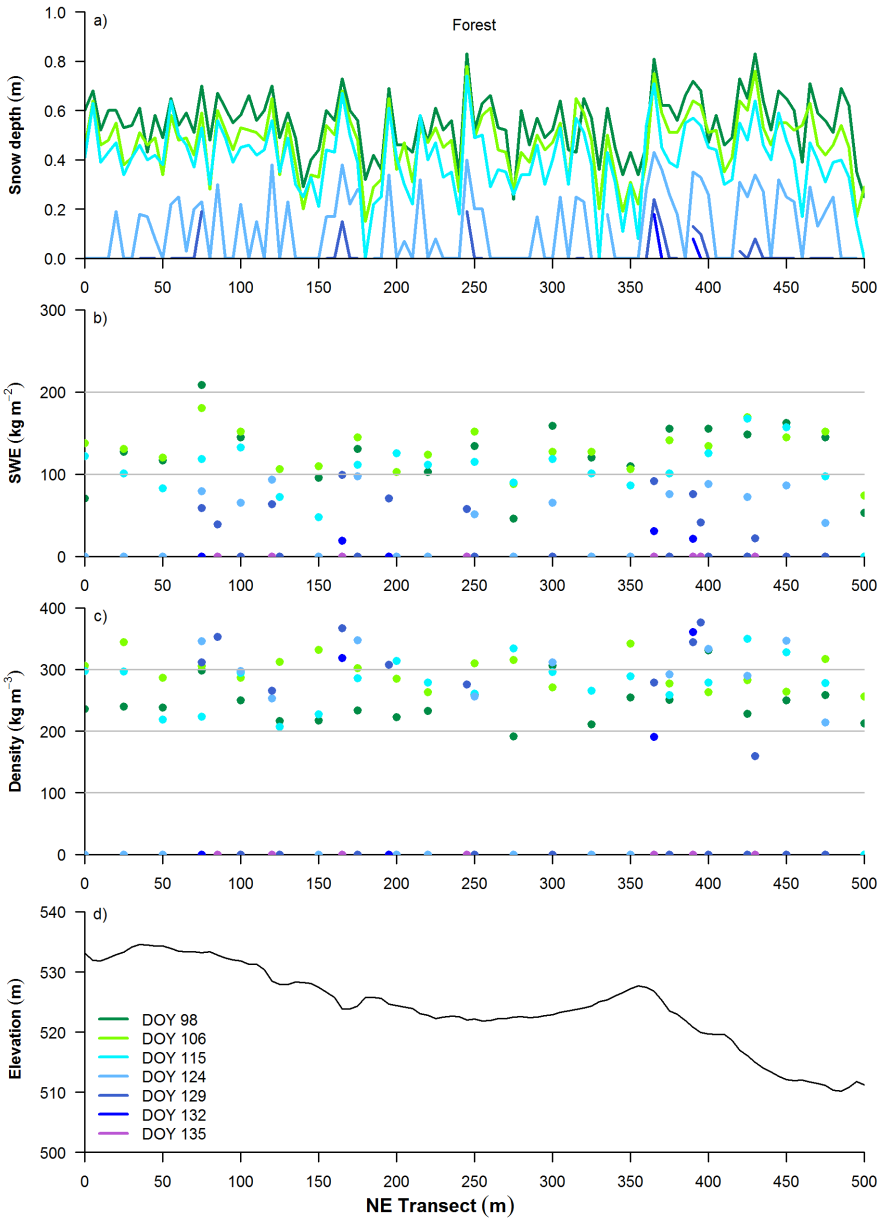

Figure 5.5: North-east snow survey transect showing observations of snow depth, SWE, snow density and elevation along a 500 m transect from the birch forest (AWS) meteorological station in 2009.

The south-east snow survey transect was 350 m in length of near uniform elevation and included a large area of open tundra between 110 m and 175 m. The mean snow depth decreased from 0.55 m on day 88, to 0.46 m on day 103. On day 112 the mean snow depth was 0.46 m again, but then decreased to 0.30 m by day 120, and 0.03 m by day 128 (Figure 5.6 panel a). The mean SWE decreased from 139 kg m^{-2} on day 88 to 115 kg m^{-2} on day 103. There was a slight increase to 123 kg m^{-2} on day 112 but then a steady decline to 93 kg m^{-2} on day 120, 27 kg m^{-2} on day 128 and 11 kg m^{-2} on day 132 (Figure 5.6 panel b). Initially there was an increase in mean snow

density from 255 kg m^{-3} on day 88, to 276 kg m^{-3} on day 103, reaching a maximum of 320 kg m^{-3} on day 112. From day 112 mean snow density declined to 278 kg m^{-3} on day 120, to 84 kg m^{-3} on day 128, 58 kg m^{-3} on day 132, and reached zero on day 135 (Figure 5.6 panel c).

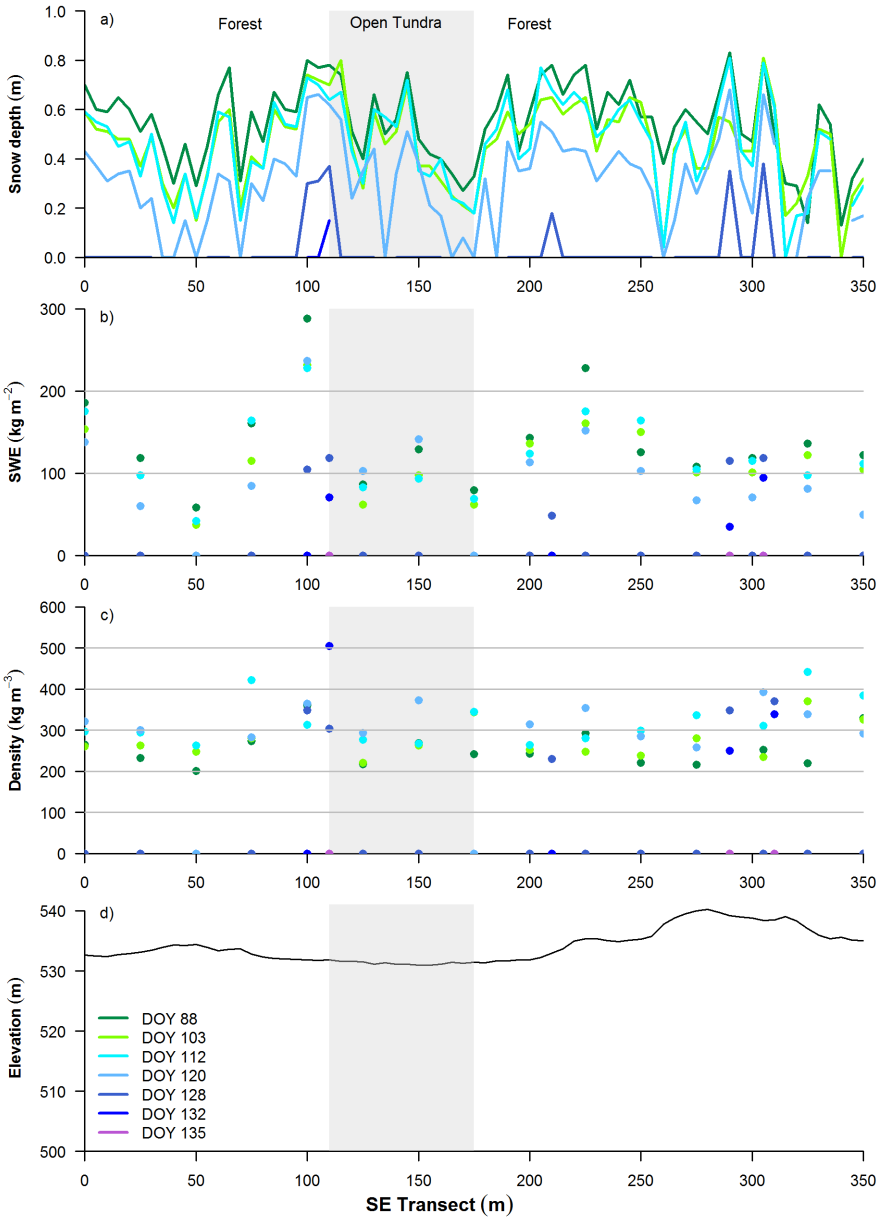

Figure 5.6: South-east snow survey transect showing observations of snow depth, SWE, snow density and elevation along a 350 m transect from the birch forest (AWS) meteorological station in 2009. Grey areas highlight areas of open tundra.

The south-west snow survey transect was 500 m in length, the first 150 m was birch forest, followed by 345 m of open tundra (Figure 5.7). There was a decline in elevation from 530 m to 515 m between 50 m and 260 m from the AWS, followed by a small but gradual increase in

elevation to 520 m from 260 m to 390 m from the AWS. There was a large snow drift in the birch forest at 90 m along the transect, which was due to wind scouring and snow redistribution from the open tundra into the windward edge of the sparse forest. The mean snow depth for the forest was much deeper than in the open tundra with a peak on day 86 at 0.53 m, decreasing to 0.45 m on day 104, 0.32 m on day 113, 0.27 m on day 120, and 0.08 m on day 128 (Figure 5.7 panel a). After this day the only snow remaining was the large drift at 90 m which was 0.18 m on day 139. The mean SWE for the forest was 128 kg m^{-2} on day 86, decreasing to 109 kg m^{-2} on day 104, 103 kg m^{-2} on day 114, and 68 kg m^{-2} on day 120 (Figure 5.7 panel b). The mean snow density in the forest increased from 269 kg m^{-3} on day 86 to 273 kg m^{-3} on day 104, from which point it then decreased to 254 kg m^{-3} on day 114, and 155 kg m^{-3} on day 120 (Figure 5.7 panel c). From day 128 onwards the only snow remaining was in a large snow drift at 90 m, which had measured SWE of more than 250 kg m^{-2} and snow density of more than 340 kg m^{-3}. There was a steady decline in mean snow depth in the open tundra from 0.21 m on day 86, to 0.17 m on day 104, to 0.13 m on day 113, 0.03 m on day 120, and completely melted away by day 128. The mean SWE for the open tundra peaked at 100 kg m^{-2} on day 86, declined to 53 kg m^{-2} on day 104, increased to 54 kg m^{-2} by day 114 and then decreased to 15 kg m^{-2} by day 120. The snow density of the open tundra was 292 kg m^{-3} on day 86, decreasing to 238 kg m^{-3} on day 104, 232 kg m^{-3} by day 114, and 66 kg m^{-3} by day 120.

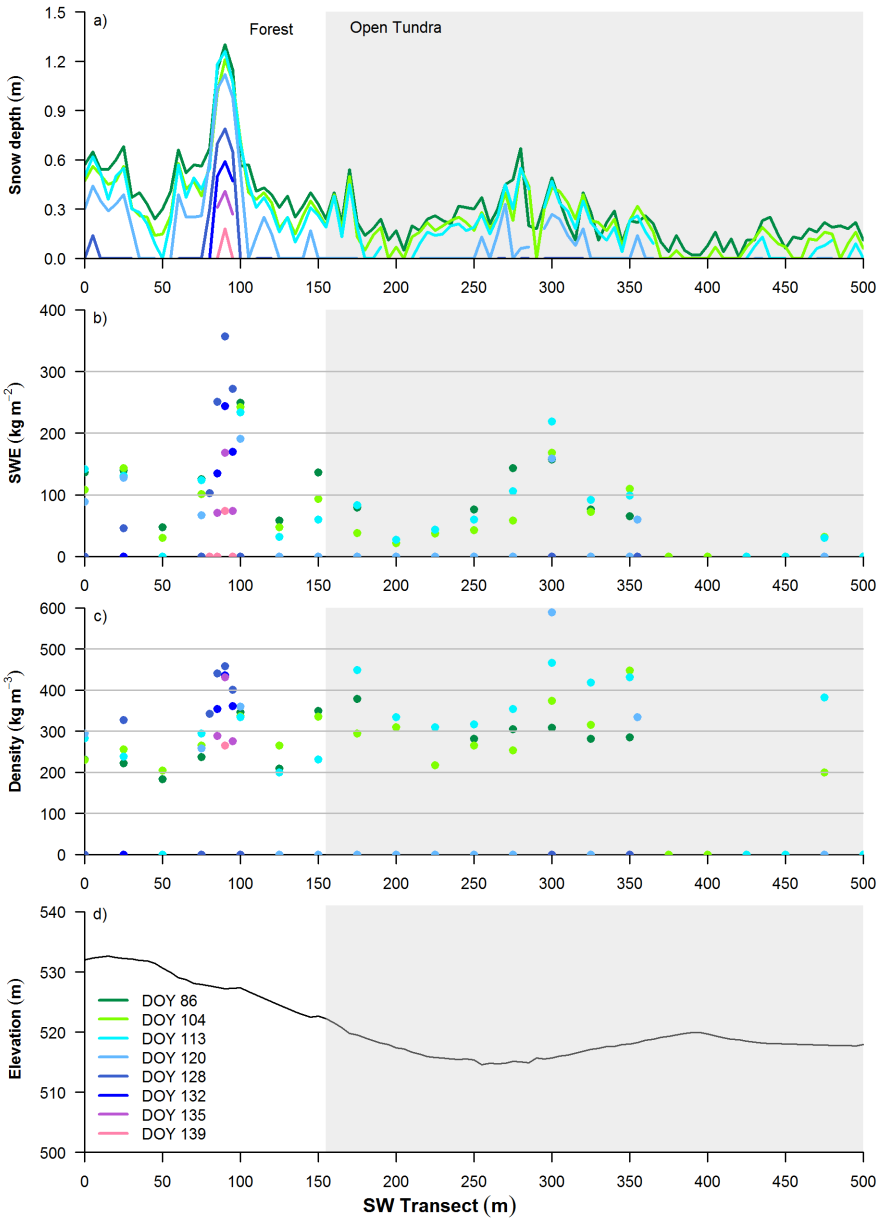

Figure 5.7: South-west snow survey transect showing observations of snow depth, SWE, snow density and elevation along a 500 m transect from the birch forest (AWS) meteorological station in 2009. Grey areas highlight areas of open tundra.

The results of the north-west snow survey transect of 500 m in length, with two areas of open tundra between 385-435 m and 480-500 m are shown in Figure 5.8. There was a decline in elevation from 533 m to 500 m from 0 m to 400 m along the transect. On day 94 the forest mean snow depth was 0.52 m, the SWE was 106 kg m^{-2} and the snow density was 242 kg m^{-3}. On the same day in the open tundra the mean snow depth was 0.30 m, the SWE was 68 kg m^{-2} and the density was 243 kg m^{-3}. By the second snow survey on day 105 the mean snow depths had decreased to 0.40 m and 0.20 m for the birch forest and open tundra respectively, the SWE had

increased in the open tundra to 73 kg m^{-2} and decreased in the forest to 103 kg m^{-2}, while both the snow densities increased to 304 kg m^{-3} and 338 kg m^{-3} for the birch forest and open tundra respectively. There was some snowmelt by the third snow survey on day 114. However, the snowmelt was more substantial between day 114 and day 124 as the mean snow depth decreased by 0.17 m to 0.01 m in the open tundra, and in the forest by 0.18 m to 0.09 m. The snow in the open tundra had melted by day 129, whereas one small patch of snow remained in the forest until day 132.

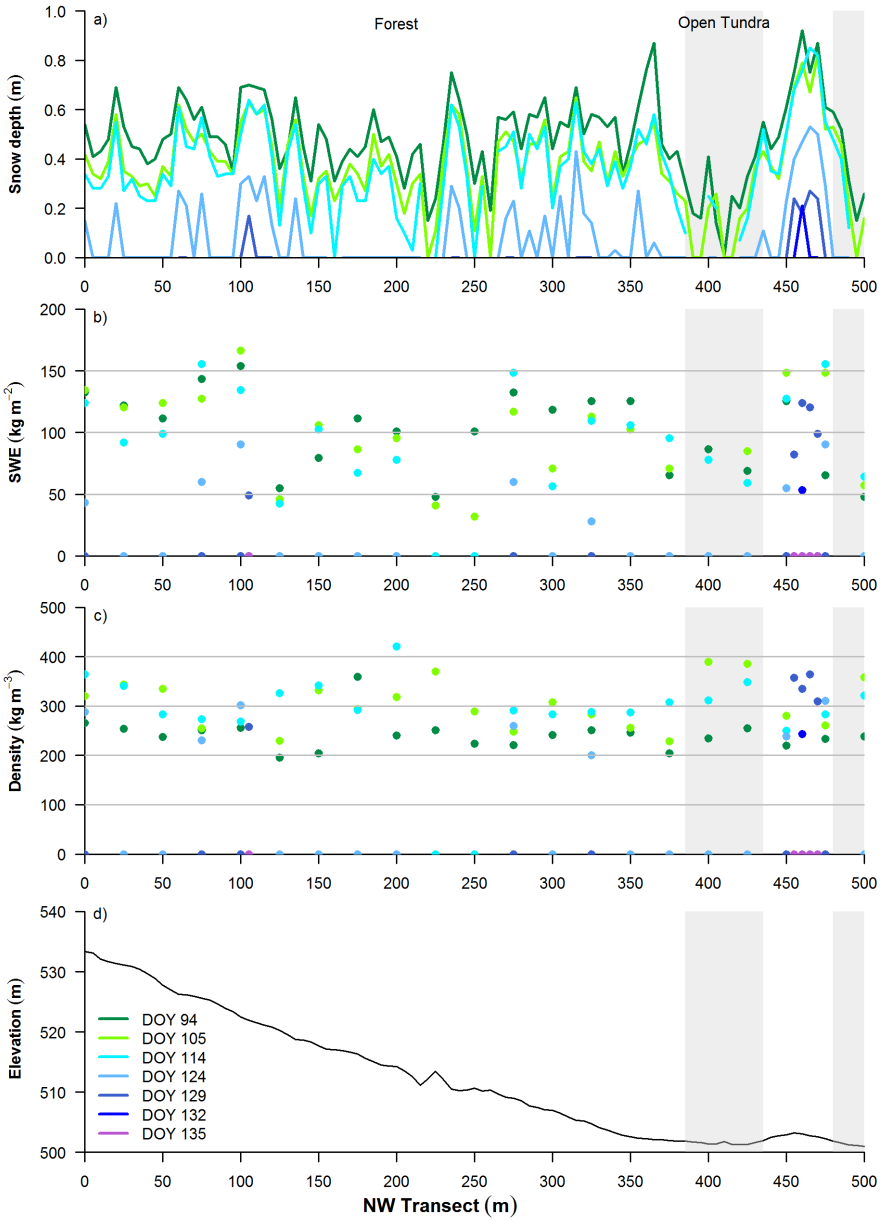

Figure 5.8: North-west snow survey transect showing observations of snow depth, SWE, snow density and elevation along a 500 m transect from the birch forest (AWS) meteorological station in 2009. Grey areas highlight areas of open tundra.

Snow Depth Continuous Measurement

Continuous snow depth measurements taken in the sparse birch forest directly west of the AWS by a Sonic Ranging SR50 sensor from day 93 to 123 in 2009 are shown in Figure 5.9. The mean snow depth was 0.385 m from days 93 to 100. Compared to the snow surveys in the grids and transects this is a shallow snowpack for the sparse birch forest. However, this data set provides a detailed pattern of both snow accumulation and snowmelt in 10 minute time steps.

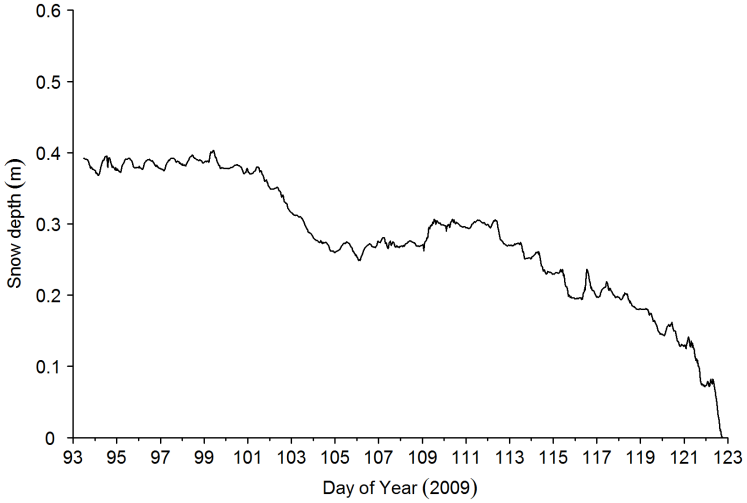

Figure 5.9: Snow depth (m) measured directly west of the AWS in 2009, data averaged to 30 minutes.

There was a period of snowmelt from day 101 to 105 which reduced the snow depth to 0.27 m. There was a small increase in snow depth overnight on day 108 and during day 109, which resulted in increased mean depth to 0.3 m. This snowfall was also seen in the radiometer data but was absent from the other snow surveys. Then there was a period of continuous snowmelt from day 112 to day 123, with the most rapid decline in snowmelt on day 121 and 122.

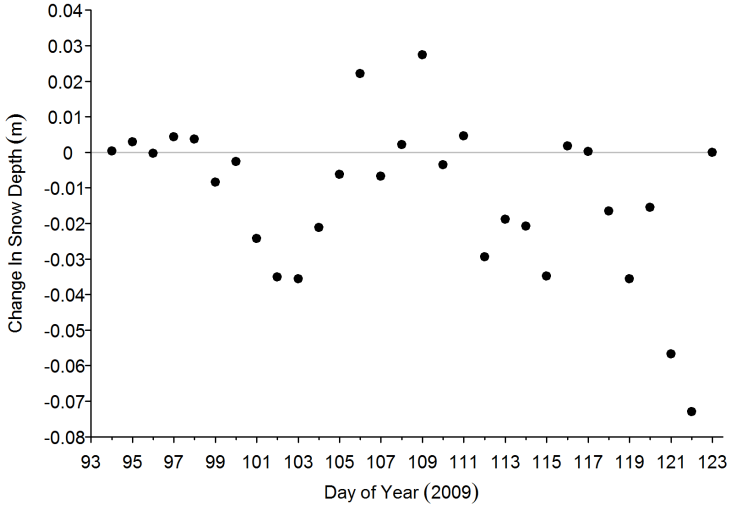

Figure 5.10: Daily Change in Snow depth (m) measured directly west of the AWS in 2009.

Figure 5.9 also shows a consistent daily variability in snow depth, which could be a side effect of the SR50 heating up during the day. The data shown in Figure 5.10 are the values of daily change in snow depth from the same site. There was a snowfall event on day 106 which accumulated 0.022 m of snow and a second period of snowfall on day 109 accumulated 0.027 m of snow. There were three distinct periods of snowmelt. The first occurred on days 101 to 104 when a total of 0.115 m of snow melted (melting of 0.024 m, 0.035 m, 0.035 m and 0.021 m of snow on days 101 to 104 respectively). The second period of snowmelt occurred on days 112 to 115 when a total of 0.102 m snow melted (melting of 0.029 m, 0.019 m, 0.020 m and 0.034 m of snow on days 112 to 115 respectively). The third and final period of snowmelt occurred on days 118 to 122 when a total of 0.194 m snow melted (melting of 0.016 m, 0.035 m, 0.015 m, 0.056 m and 0.072 m of snow on days 118 to 122 respectively). The largest loss of snow depth occurred on days 121 and 122 when 0.057 m and 0.073 m of snow melted respectively.

5.4 Snow surface and snowpack temperatures

In 2008 three infra-red thermometers (IRT) were mounted facing the snow surface. The first measured a period of 30 days from day 96 (6 April) to day 125 (4 May), a further two IRT were installed on day 106 (16 April) (Figure 5.11). For days 96 to 111 the ambient air temperature was very similar to that of the snow surface temperatures; the mean ground surface temperatures were -7.1 °C, -1.9 °C and -3.2 °C for the three IRT respectively, and the air temperature was -4.9 °C. Whereas for the period day 111 to 124, the air temperature was much warmer than the snow surface temperature but cooler than the ground surface where the snow had melted (IRT

2 and 3). The mean ground surface temperatures were -3.3 °C, 4.5 °C and 2.5 °C for the three IRTs respectively, and the air temperature was 2.0 °C. The snow at IRT 2 and 3 melted out in the morning of day 111, however the snowpack at IRT 1 did not melt until day 124. The presence of snow cover dramatically reduces the ground surface temperature relative to the air temperature but also with respect to areas of the forest floor which have already melted out. The difference in temperature of IRT above melted areas compared to the IRT still facing the snow surface on day 122, highlights that there can be large temperature variations occurring over short distances in the snowmelt period.

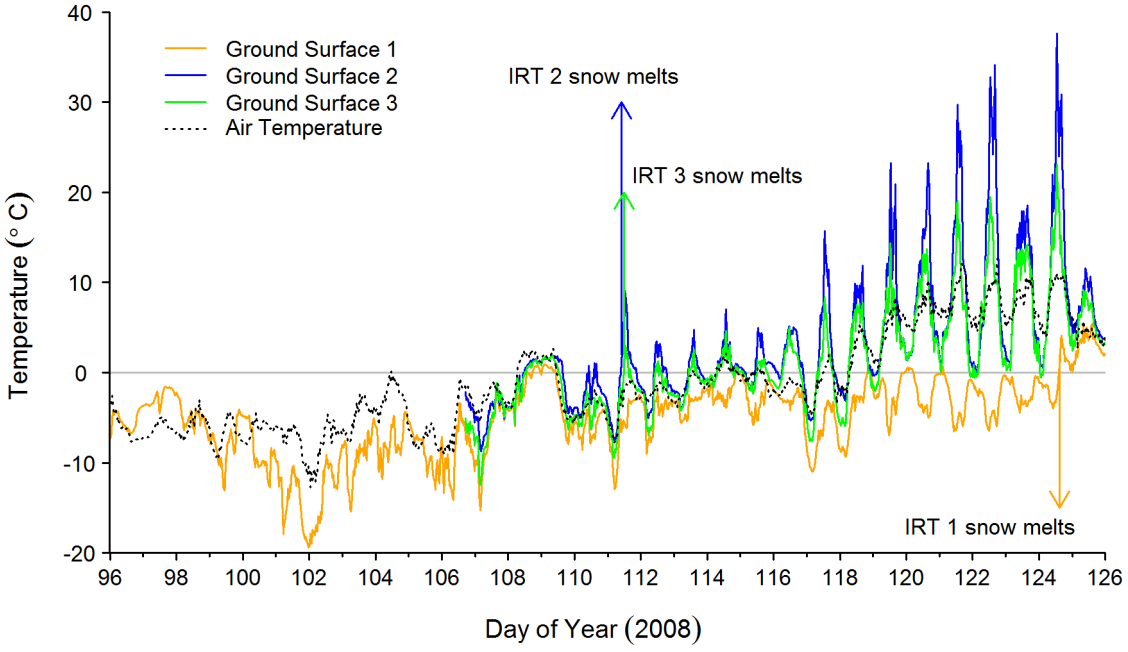

Figure 5.11: Ground surface temperatures measured with infra-red thermometers for days 96 to 125 in spring 2008 and the air temperature.

In 2009 three infra-red thermometers (IRT) were mounted facing the snow surface, measuring a period of 25 days from day 105 (15 April) to day 129 (9 May) (Figure 5.12). For days 105 to 110 the ambient air temperature was very similar to that of the snow surface temperatures; the snow surface temperatures were -5.4 °C, -4.8 °C and -5.4 °C for the three IRT respectively, and the air temperature was -4.8 °C. Whereas for the period day 111 to 122, the air temperature was warmer than the snow surface; the mean snow surface temperatures were -0.4 °C, 0.2 °C and -0.1 °C for the three IRT respectively, and the air temperature was 2.6 °C. The snow at IRT number 3 melted out in the morning on day 123, followed by IRT number 1 where the snow melted out in the afternoon on day 124, whilst the snow at IRT number 2 melted out in the morning on day 129. Over the period day 123 to 129 the IRT mean temperatures were 5.4 °C, 0.5 °C and 6.4 °C respectively and the mean air temperature was 3.7 °C. Therefore the presence of snow cover

dramatically reduces the ground surface temperature relative to the air temperature but also areas of the forest floor which have melted out are much warmer than the snow covered patches of forest floor.

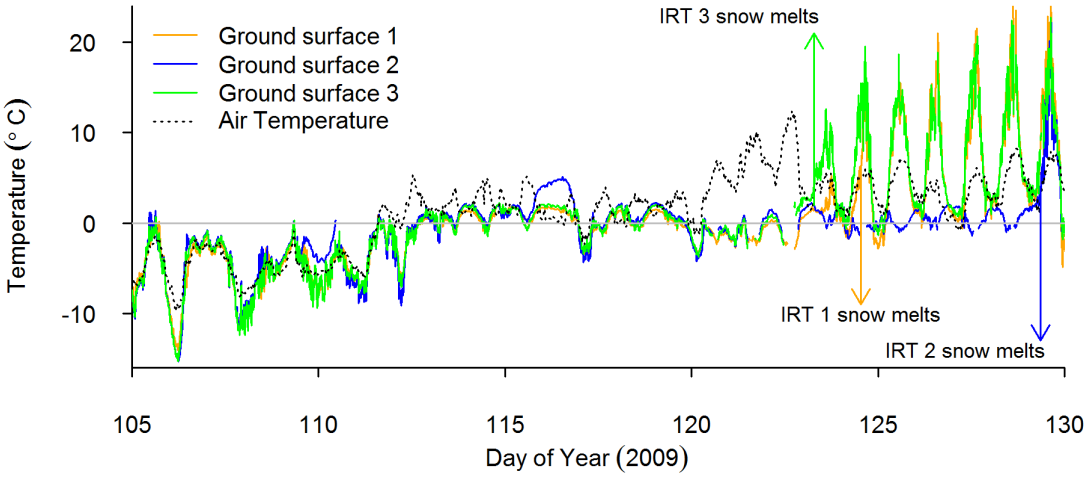

Figure 5.12: Ground surface temperatures measured with three infra-red thermometers for days 105 to 129 in spring 2009. The dotted black line indicates ambient air temperature.

The thermocouple system placed within the snowpack provides an indication of the temperatures within the snowpack and also the approximate time of the melting of snowpack by depth. Figure 5.13 shows that the mean temperature within the snowpack for the period day 96 to 101 at 5 cm, 8 cm, 14 cm and 23 cm above the ground surface were -2.7 °C, -2.9 °C, -3.3 °C and -3.8 °C respectively. There was a period of snowfall on day 97 to 100, which warmed the snowpack relative to the temperatures on day 96. During this period the warmest layer of the snowpack was the point closest to the ground, and the coldest point was closest to the snow surface. This pattern continues until day 108 when the measurement at 23 cm above the ground surface becomes the warmest part of the snowpack during the daytime, but is still the coldest part of the snowpack during the evenings. For the period day 102 to 115, the temperature in the snowpack steadily warms to around -0.5 °C. The snow at 23 cm above the ground surface melts on day 115, shortly followed by that at 14 cm on day 118 and 8 cm on day 119. Data from the lowest part of the frost gauge at 5 cm above the ground surface were problematic due to water from the melting snow getting inside the frost gauge. After the snow has melted the evening temperatures drop to -3.0 °C and -4.0 °C on days 117 and 118 highlighting that the presence of snow insulates the ground surface from the extremes of the night-time temperatures.

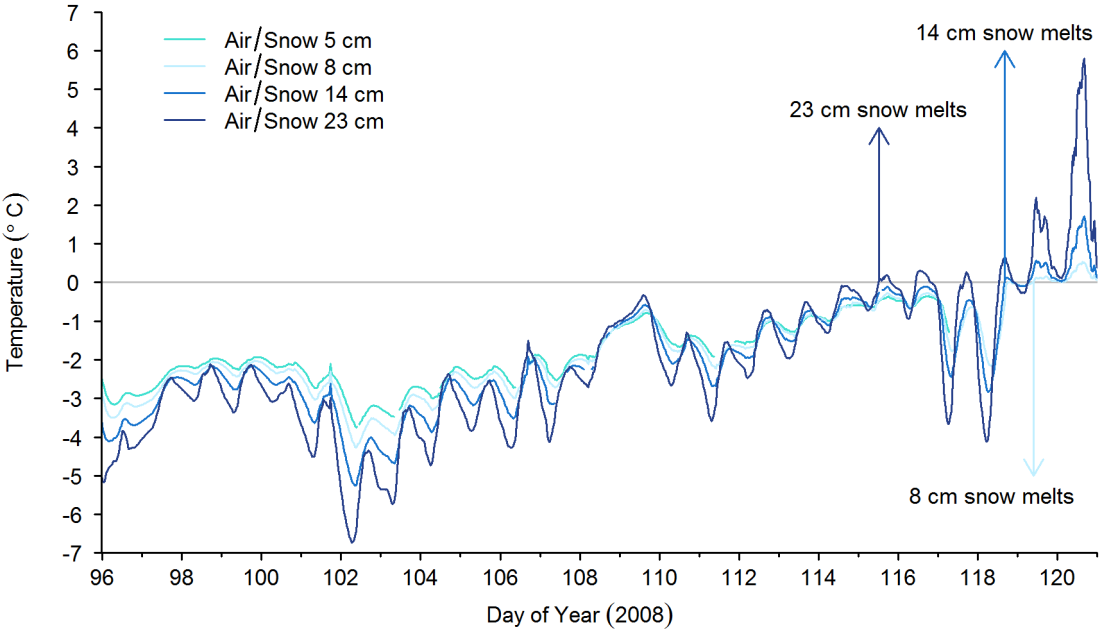

Figure 5.13: Ground surface temperatures measured with a frost gauge for days 96 to 120 in spring 2008, at 5 cm, 8 cm 14 cm and 23 cm above the ground surface.

5.5 Discussion

5.5.1 Snow surveys

Snow cover plays an important role in the surface energy balance, thermal regime, water balance, vegetation and trace gas fluxes in Arctic ecosystems [*Callaghan et al.*, 2011b]. It is therefore important to measure the properties of the snow pack to validate our land surface model. The methods employed here to gather snow depth, density and SWE data through snow surveys are firmly established in-situ measurement techniques for snow properties [*Dingman*, 2002; *Pomeroy et al.*, 1995].

The continuous snow surveys in 2008 and 2009 provide observations of snow properties in the sparse birch forest and the surrounding areas of open tundra. Snow properties were observed at peak snowmass prior to the onset of melt, and also throughout the snowmelt period. The snow survey grids measured in 2008 and repeated in 2009 show similar trends in the snow depth, density and SWE between years. Therefore, despite a lack of in-situ measurements of incoming solid or liquid precipitation, the overall snowpack depth, density and SWE have been shown to be very similar in the two consecutive years.

The snow survey results show the extent to which snow is redistributed in sparse forests. It can be assumed that the snowfall across the open tundra and sparse forests is the same. However, the snowpack depth is deeper in the areas of the sparse birch forest relative to the areas of open tundra. This is likely to be as a result of wind scour redistributing snow from the tundra to the areas of forest over the winter period. The snow survey transect observations indicated evidence for this process, typically showing an increase in snow depth at the edges of the forest. In contrast *Hardy et al.* [1997a] found that area beneath tree canopies accumulated 60 % of the snow accumulated in forest openings. The results presented here are consistent with studies of blowing snow [*Bowling et al.*, 2004; *Essery et al.*, 1999; *Essery and Pomeroy*, 2004] but snow accumulation and its redistribution by wind is not part of this thesis.

There is a marked difference between the snow properties measured in the forest and the open tundra, which is most clearly evident in the 2008 snow survey grids. The snow depth in the forest plots is deeper and has a corresponding higher SWE relative to the snow in the open tundra. The snow survey transects in 2009 included areas of open tundra, and the same pattern was observed with shallower snowpacks with a lower SWE in the areas of open tundra relative to the areas of forest. *Bewley et al.* [2010] found that an exposed plateau had lower SWE than a site at the bottom of a valley. Studies on shrub tundra ($>$ 3 m in height) showed snow accumulation in tall shrubs was 147 % greater than in sparse tundra (20 cm in height), where the snowmelt rate was 47 %

higher, resulting in a 68 % longer snowmelt duration in the shrub tundra [*Pomeroy et al.*, 2006].

The survey transect hemispherical photos showed that there was substantial within forest variability with areas of high and low canopy cover (due to canopy clumping - Figure 3.4). The snow survey transects provide a detailed spatial and temporal data set of snowpack properties, and how these change throughout the snowmelt period and with canopy cover. Overall there is considerable variability in snow depth, density and SWE within the sparse birch forest. Generally, deeper snowpacks were found at the edges of large open areas or hummocks, and shallower snowpacks were found in the most sparsely canopy covered areas of forest.

The continuous measurements of the snow depth were useful to determine the precise time and duration of snow accumulation and snowmelt, although the snowpack measured by the SR50 in 2009 was generally quite shallow compared to the mean snow depth observed in the snow survey grids and transects. This was most likely due to the proximity to the AWS tower, which may have sheltered the sensor from some snowfall. The continuous snow depth data set clearly shows periods of snowmelt from day 101 to 105 in 2009, which was also seen in the snow survey transect data. There was another period of continued snowmelt from day 112 to day 123, which was seen in both the snow survey grid and transect data. *Ryan et al.* [2008] showed that SR50 sensors underestimate the snow depth by approximately 2 cm, but despite this, they do provide useful and timely information on snow accumulation and melt.

These snowpack measurements can only be evaluated approximately with the model results of the melting rates (see Chapter 7). In addition, the precipitation data is only partially relevant and will be adjusted to enable evaluation of melting. This is discussed in detail in Chapter 6.

5.5.2 Snow temperatures

The snow surface and snowpack temperatures provide an insight into how the snowpack insulates the ground surface, how the ground surface temperature can increase with the snow melting out, and provide a precise time when the snow melts at three specific points within the forest. Although these measurements are not specifically useful for model validation, they do justify why it is important to model the timing of the snowmelt in these regions correctly as the presence of snow cover dramatically alters the ground surface temperature. These patches of melted snow are a source of energy for melt from the advection of sensible heat [*Essery et al.*, 2006; *Marsh and Pomeroy*, 1996; *Sicart et al.*, 2006]. The presence of snow cover has an important impact on the soil temperature and therefore soil fluxes of carbon and nitrogen [*Brooks et al.*, 1997].

5.6 Summary

The snowpack measurements detailed in this chapter have an important role in model validation. They will be used to initialise the snowmelt by adjusting the incoming precipitation in Chapter 6. Table 2.3 in Chapter 2 on page 50 shows a summary of the snowpack measurements in both 2008 and 2009, the days when the measurements are available, and their purpose with respect to the JULES model.

Fieldwork results: Meteorological data

6.1 Introduction

A detailed continuous set of meteorological driving data is required for using a land surface scheme. This chapter will outline the steps taken to compile a data set in order to run a land surface model for the sparse birch forest in Abisko.

6.2 Meteorological driving data

6.2.1 ABACUS meteorological data

The meteorological data required to run JULES are downward shortwave radiation (W m^{-2}), downward longwave radiation (W m^{-2}), precipitation (kg m^{-2} s^{-1}), air temperature (K), wind speed (m s^{-1}), air pressure (Pa), and specific humidity (kg kg^{-1}). The methodology for the collection of these meteorological data were outlined in Chapter 2.3.1. These 7 meteorological variables were collected from a meteorological tower established at the ABACUS birch forest site. The tower consisted of an array of sensors mounted above the height of the forest canopy.

If there were any gaps in the ABACUS above canopy driving data variables, often they could be gap filled using data from an additional array at mid-canopy height. Using relationships determined when both the mid-canopy installation and the above canopy installation were available, some periods of missing data could be gap filled. Temperature, humidity and wind speed measurements were normalised to 2 m above the ground. However, there were periods when both the above and mid-canopy sensors were not available at the ABACUS birch forest site.

A second ABACUS field site, located approximately 2 km to the southeast of the birch forest site, in an area of open continuous tundra had an established meteorological tower. Where data was

available for both the tundra and birch forest sites, a relationship based on lapse rates accounting for the elevation difference was calculated between the two sites. This relationship was used to gap fill birch site data using the ABACUS tundra site. The meteorological data presented in Figure 6.1 shows the driving data for the ABACUS birch site once it had been quality controlled and gap filled using ABACUS birch forest mid canopy data and ABACUS tundra site data.

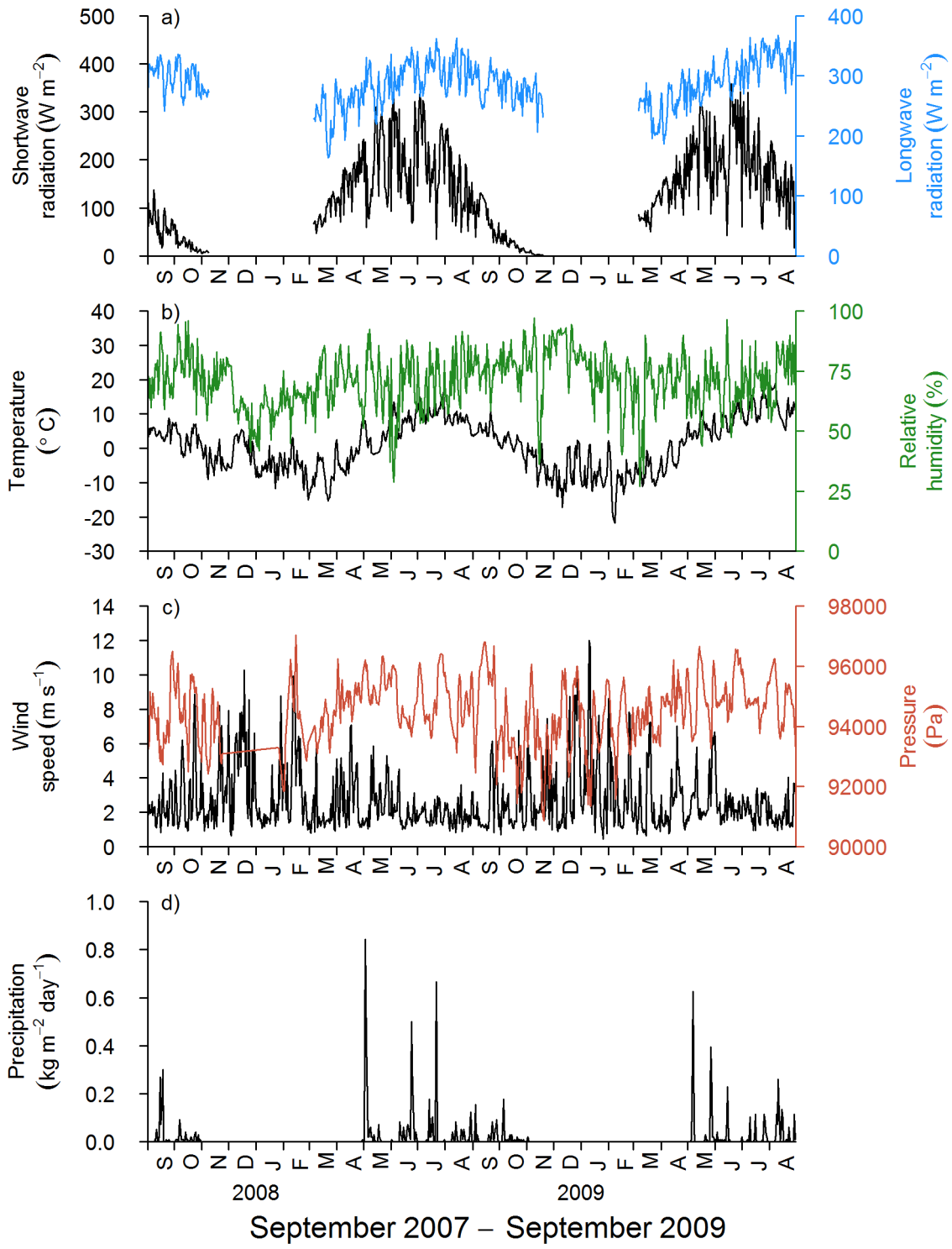

Figure 6.1: ABACUS birch forest site daily mean meteorological data, normalised for 2 m above the ground.

Figure 6.1 shows that there are still significant gaps in the shortwave radiation, longwave radiation, pressure and precipitation data. Primarily these gaps were due to power loss over the winter period.

As JULES requires a continuous set of the meteorological variables in order to run, the gaps in the meteorological driving data need to be filled.

6.2.2 Abisko Scientific Research Station meteorological data

The Abisko Scientific Research Station (ANS) is located approximately 6 km to the north of the ABACUS birch forest site (68°21 N, 18°49 E) at an altitude of 385 m a.s.l. [*Kohler et al.*, 2006] (note the ABACUS birch forest site is at 570 m a.s.l.). The meteorological data at ANS are taken using well calibrated and regularly maintained equipment. Figure 6.2 shows the daily mean meteorological data measured at ANS for the same study period.

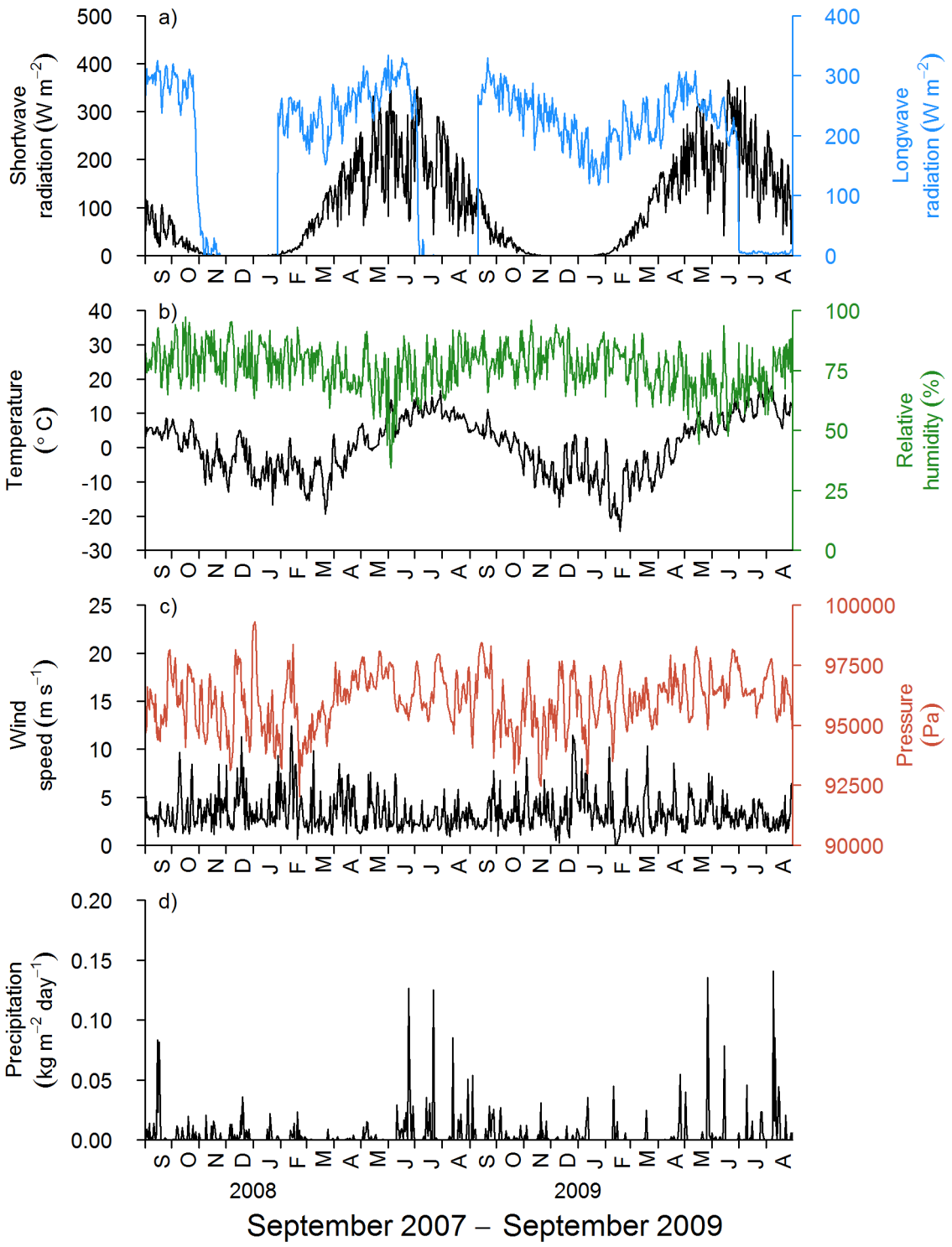

Figure 6.2: Abisko Scientific Research Station (ANS) daily mean meteorological data.

Some of the large gaps in the meteorological data for parameters of shortwave radiation, longwave radiation, pressure and precipitation at the ABACUS birch forest site, could be gap filled using the

ANS data. However, there is a gap in the longwave radiation measured at the ANS meteorology station that coincides with a gap in the ABACUS longwave radiation gap for winter 2007-2008.

6.2.3 Gap filling meteorological data

Firstly, in order to gap fill the driving data set for the ABACUS sparse birch forest, linear relationships were calculated for the shortwave radiation, longwave radiation, pressure and precipitation during periods where the meteorological variables were available at both the ABACUS and ANS sites. Secondly, these relationships was then used to adjust the ANS data to the ABACUS birch site conditions for the periods of missing data.

Therefore, in the instances where no meteorological data is available from the ABACUS birch forest site, meteorological data from ANS were used to gap-fill the data sets.

Shortwave radiation

There are two gaps for shortwave radiation in the ABACUS birch forest site meteorological driving data from November to March in both winters 2007 - 2008 and 2008 - 2009 shown by the gaps in the grey line in Figure 6.3. Data from the ANS station available for these periods are shown by the orange line in Figure 6.3.

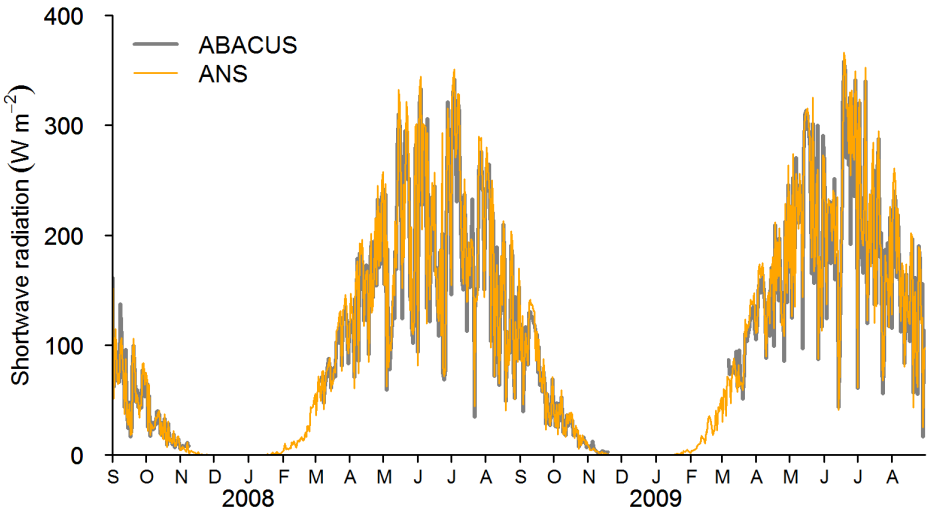

Figure 6.3: Daily mean shortwave radiation (W m^{-2}) for ANS (orange) and ABACUS (grey) sites.

A linear relationship was calculated between the data at the ABACUS birch site and ANS for periods when data were available at both sites, for a month prior to and post the winter gaps, and for ten days prior to and post the winter gaps (Figure 6.4).

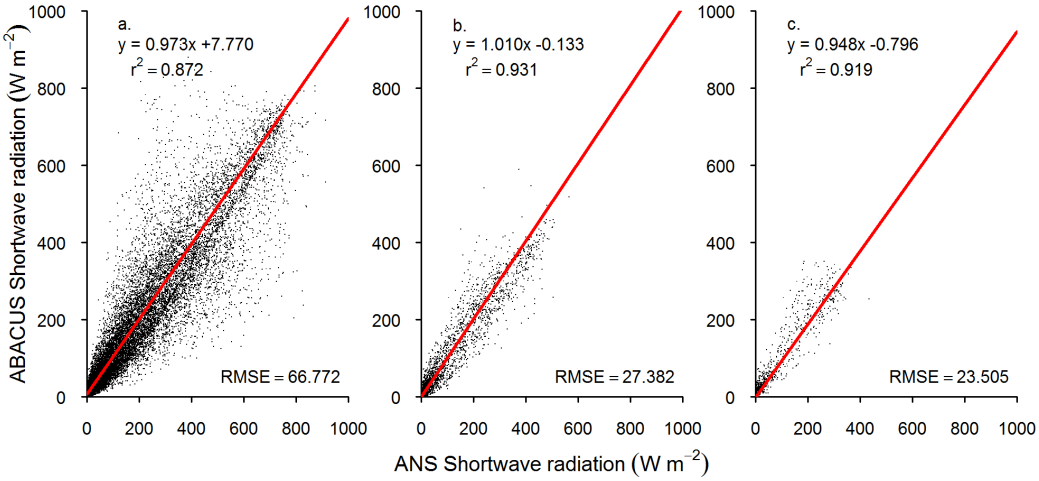

Figure 6.4: Linear regression of shortwave radiation (W m^{-2}) at the ABACUS AWS against shortwave radiation (W m^{-2}) at ANS for a) The whole period, b) A month either side of data gaps and c) 10 days either side of data gaps.

The slope and intercept from the regression based on 10 days either side of the winter gaps (Figure 6.4 panel c) were used to apply a correction to the data measured at ANS, and the night time data were truncated to zero. Using the relationship established over the 10 day period only reduced the downward shortwave radiation by a maximum of 4 W m^{-2} with respect to the ANS downward shortwave radiation. Figure 6.5 shows the shortwave radiation data gap filled using the ANS data, specifically November 2007 to March 2008 and November 2008 to March 2009.

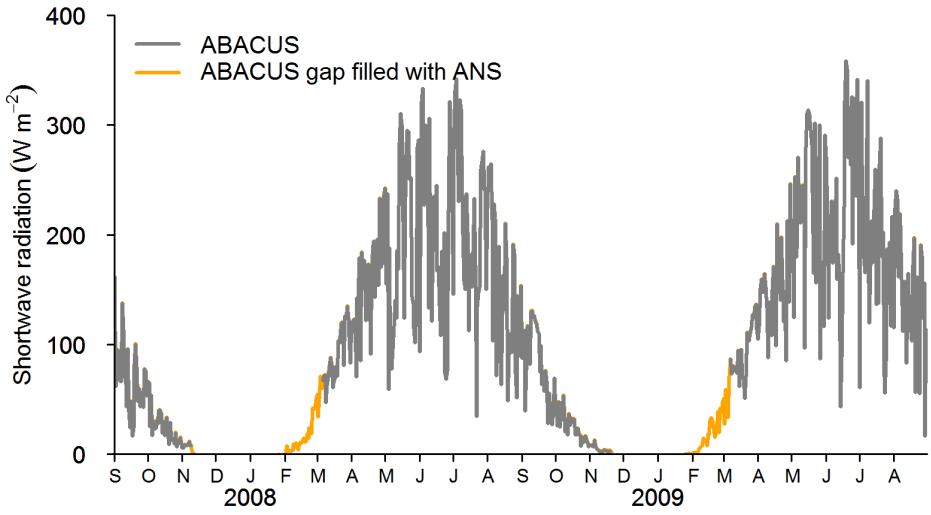

Figure 6.5: Daily mean shortwave radiation (W m^{-2}) for ABACUS data pre-gap filling (grey) and ABACUS data gap filled with ANS data (orange).

Longwave radiation

Two gaps exist for the longwave radiation in the ABACUS birch forest site driving data from November to March in both winters 2007-8008 and 2008-2009. Data from the ANS station were available for the November 2008 to March 2009 gap. However, longwave radiation at ANS were not available between November 2007 and February 2008 as shown in Figure 6.6.

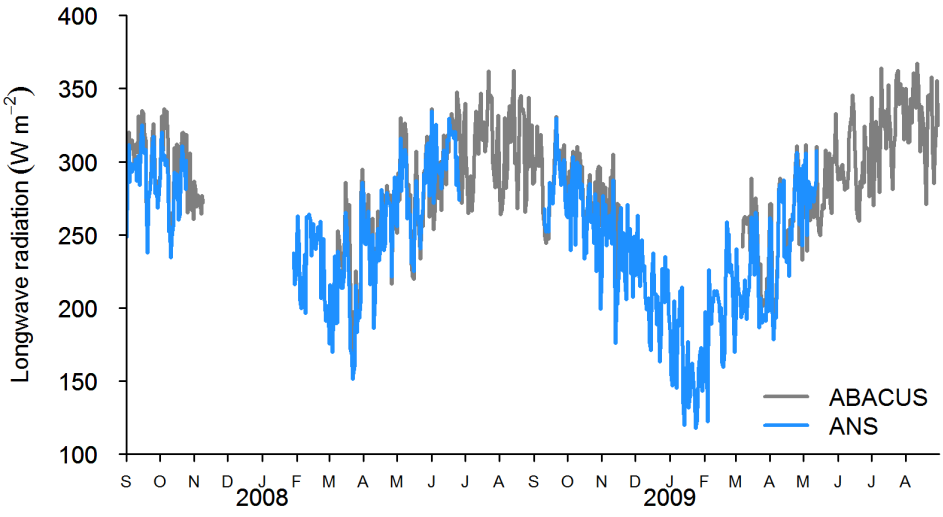

Figure 6.6: Daily mean longwave radiation (W m^{-2}) for ABACUS (grey) and ANS (blue) sites.

A linear relationship was calculated between the data at the ABACUS birch site and ANS for all data (Figure 6.7 panel a) and periods when data were available at both sites and for a month prior to and post the winter gaps (Figure 6.7 panel b).

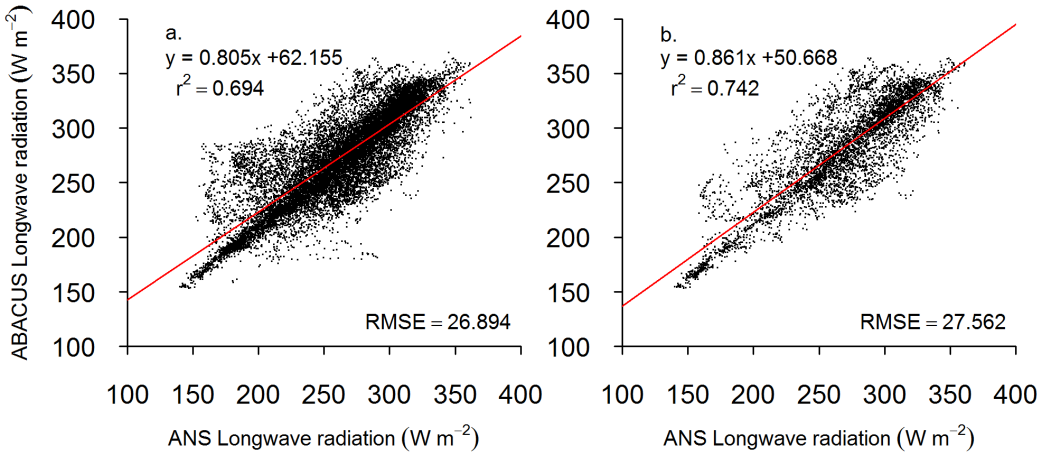

Figure 6.7: Linear regression of longwave radiation (W m^{-2}) at the ABACUS AWS against longwave radiation (W m^{-2}) at ANS for a) The whole period and b) A month either side of data gaps.

The slope and intercept from the regression based on a month either side of the winter gaps (Figure 6.7 panel b) were used to apply a correction to the data measured at ANS. When available these corrected longwave radiation data from ANS were used to gap fill the ABACUS data set for February to March 2008 and November 2008 to March 2009 (Figure 6.8). A gap in the longwave radiation data remains for the period November 2007 to February 2008.

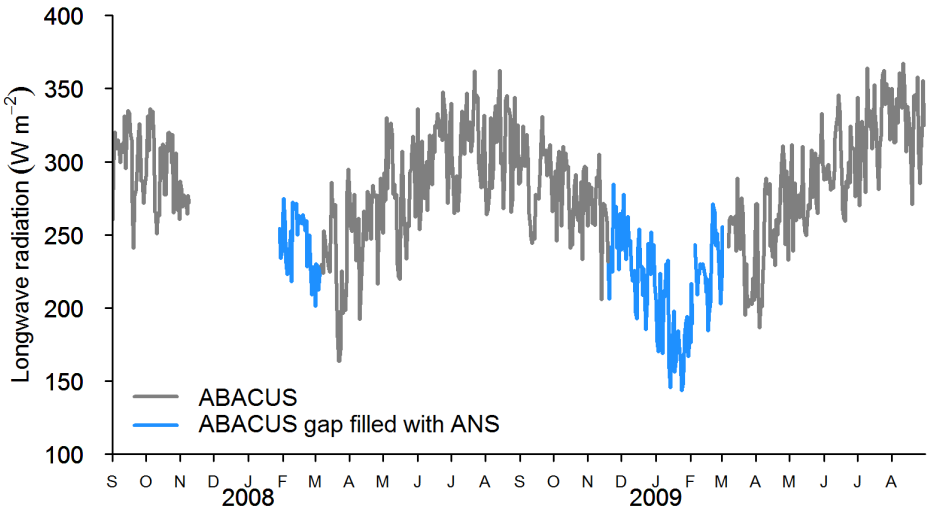

Figure 6.8: Daily mean longwave radiation (W m^{-2}) for ABACUS data pre-gap filling (grey) and ABACUS data gap filled with ANS data (blue).

Micromet model There were still gaps in the longwave radiation data over the 2007 - 2008 winter and in February 2009, which were filled using the Micromet model [*Liston and Elder*, 2006] (Figure 6.9). This very simple model only requires two meteorological variables of temperature and humidity to create a time series of data for shortwave radiation, longwave radiation, wind speed and direction pressure and precipitation, and has been shown to be robust in gap filling meteorological data sets [*Rutter et al.*, 2009; *Hoffman et al.*, 2008; *Hanna et al.*, 2013; *Essery et al.*, 2008b].

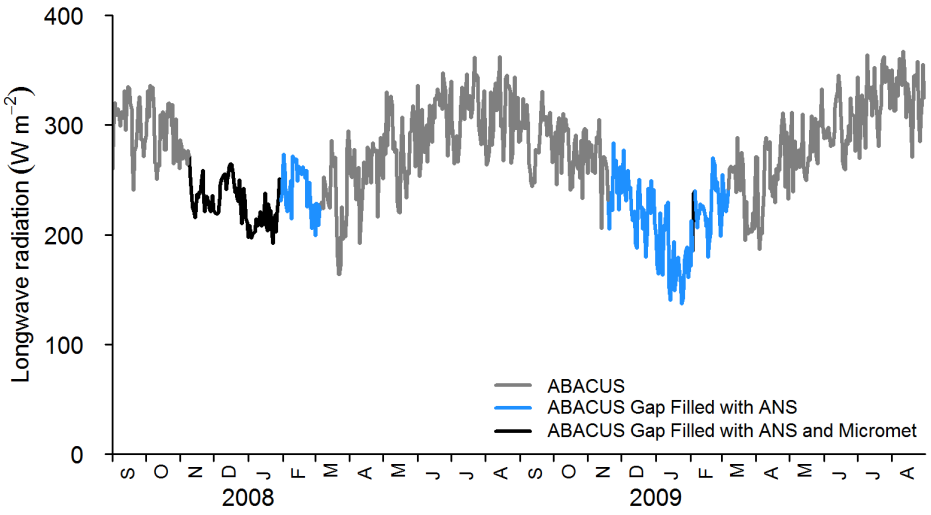

Figure 6.9: Daily mean longwave radiation (W m^{-2}) for ABACUS data pre-gap filling (grey) and ABACUS data gap filled with ANS data (blue) and Micromet modelled longwave radiation (black).

When longwave radiation estimated by the Micromet model is compared to the observations (for the periods 1 September 2007 - 10 November 2007, 5 March 2008 to 20 November 2008 and 6 March 2009 to 31 May 2009) the model mean is 294.86 W m^{-2}, whereas the observed mean at the ABACUS birch site was 279.93 W m^{-2} (Figure 6.10 and 6.11). Even though the variability in longwave radiation is not reproduced by the Micromet model, it reasonably reproduces the observed mean of longwave radiation.

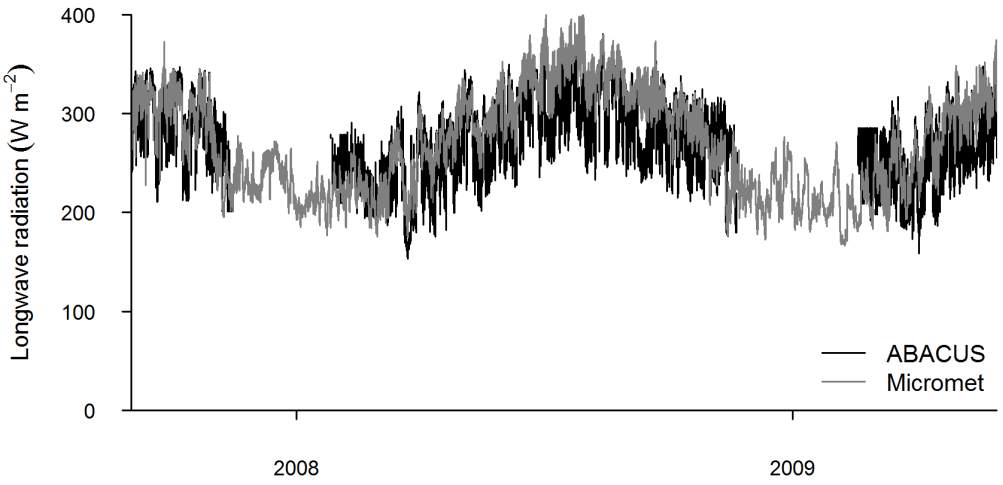

Figure 6.10: Longwave radiation (W m^{-2}) for ABACUS data pre-gap filling (black) and Micromet model (grey) in 30 minute time steps for September 2007 to May 2009.

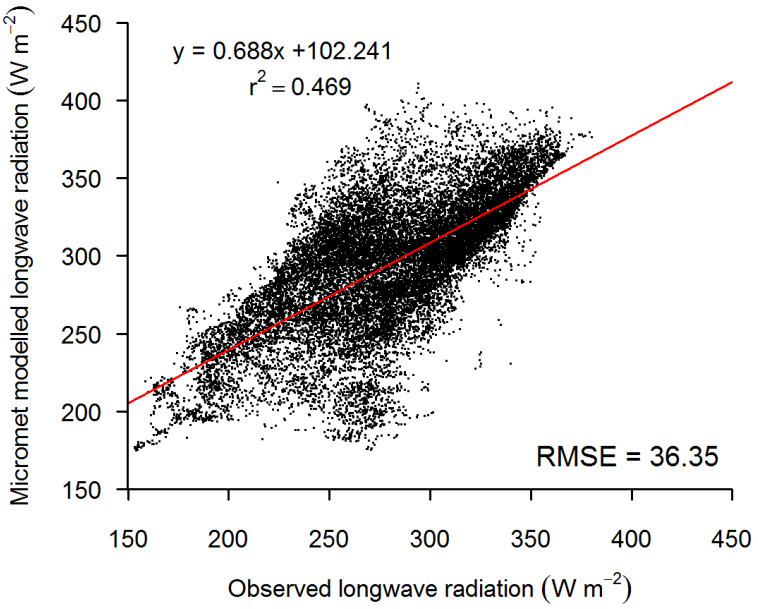

Figure 6.11: Linear regression of longwave radiation (W m^{-2}) for the Micromet model against observed longwave radiation (W m^{-2}) at the ABACUS AWS.

Tests were run to ensure that the modifications made to the longwave radiation data set were acceptable. JULES was run with longwave radiation with the Micromet gap filled data set, Micromet and ANS gap filled data set, and these data sets with additional noise to account for the

bias in the Micromet model and ANS observations. When JULES was run with all these different combinations of longwave radiation and the bias (or additional noise) no significant difference was found in the accumulation and melt of the snowpack. Therefore any differences within the surface energy balance were negligible.

Temperature and Humidity

Since the JULES model requires air temperature in Kelvins, the measured values at the ABACUS birch forest AWS were converted into Kelvins for the driving data (Figure 6.15).

As the JULES model requires specific humidity, the measured values of relative humidity were converted following the Goff Gratch equation [*WMO*, 2008] as follows:

$$Q = 0.622(e_w(\frac{U/100}{P})) \tag{6.1a}$$

$$e_w = 611.2e^{(17.62\frac{T}{T+243.12})} \tag{6.1b}$$

Where Q is the Specific humidity (kg kg^{-1}), 0.622 is the ratio of the molecular weight of water and air, e_w is the Saturation vapour pressure (hPa), U is the Relative humidity (%), P is the Pressure of moist air (hPa) and T is Temperature (^{o}C). The specific humidity data set is shown in Figure 6.15.

Pressure

One large gap exists for the pressure in the ABACUS birch forest site driving data from November 2007 to February 2008. There were also a few periods of missing data for February to March 2008. Data from the ANS station were available for the November 2007 to March 2008 gap (Figure 6.12).

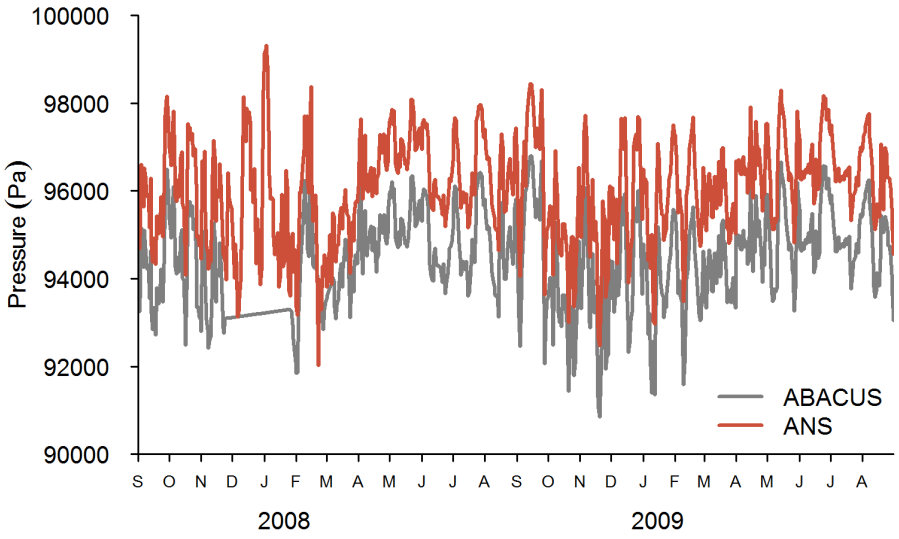

Figure 6.12: Daily mean pressure (Pa) for ABACUS (grey) and ANS (red) sites.

A linear relationship was used to represent the relationship between the pressure data observed when data were available at both sites (Figure 6.13). This simple linear relationship was used to gap fill the ABACUS data (Figure 6.14) rather than a barometric formula as the difference in elevation between the two sites was small at 180 m and this winter gap is not the period of interest for the model.

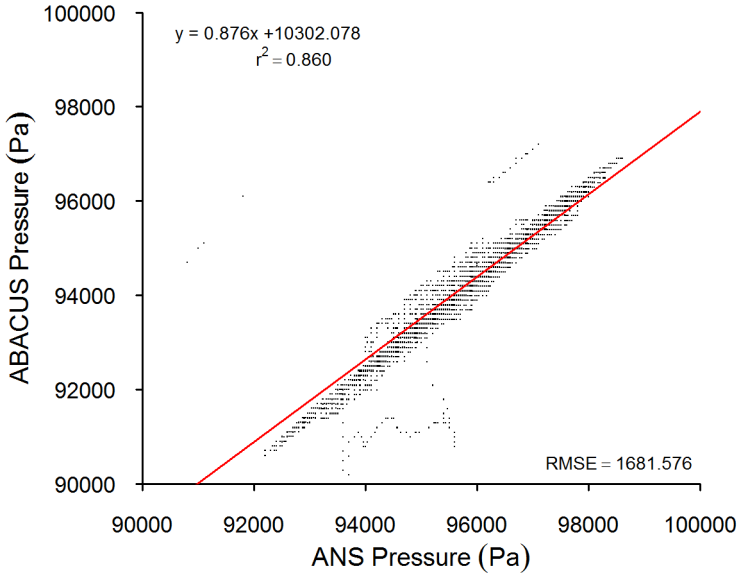

Figure 6.13: Linear regression of pressure (Pa) at the ABACUS AWS against pressure (Pa) at ANS for all data points (September 2007 to September 2009).

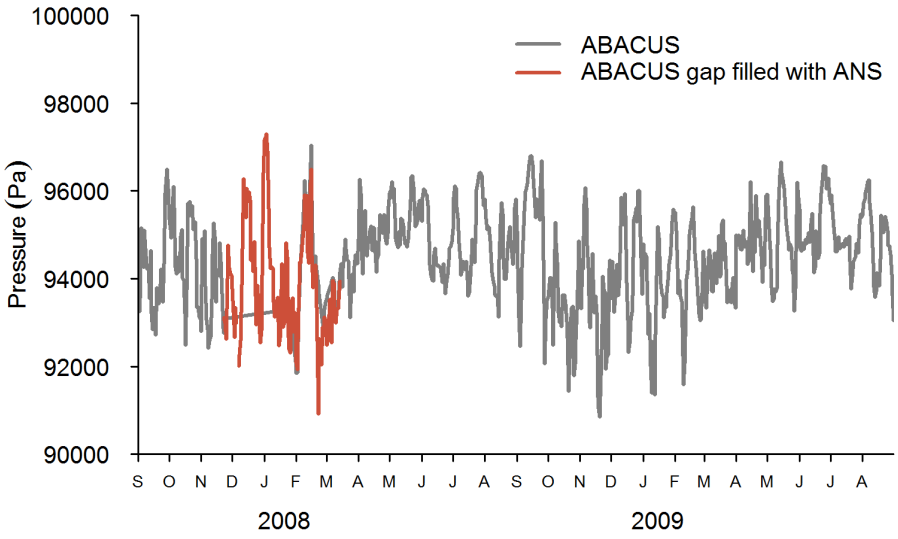

Figure 6.14: Daily mean pressure (Pa) for ABACUS data pre-gap filling (grey) and ABACUS data gap filled with ANS data (red).

Precipitation

The ABACUS birch forest site has two significant gaps in the precipitation data set from October 2007 to May 2008 and from October 2008 to May 2009. Although this is a comprehensive data set for the ABACUS birch forest site, the periods of missing precipitation in winter are key in driving the JULES model to build a snowpack. It is not possible to drive JULES using this data set.

The ANS data is a comprehensive data set, collecting both winter snowfall and summer rainfall. Gap filling the precipitation data between ANS and ABACUS presents difficulty. There is less measured precipitation at ANS than at the ABACUS birch forest site. However, the ANS meteorological station is maintained thorough the year and the rainfall gauge is emptied daily. As this represents a more detailed data set it would be better to run JULES using this data and adjust it for under-catch in the measurements.

Micromet Model Monthly Precipitation Adjustment Factors (PAF) were taken from the Micromet code [*Liston and Elder*, 2006]. Precipitation data from the ANS station were then adjusted using the PAFs and taking account of elevation.

However, when JULES was run with the Micromet adjusted ANS precipitation, it models a very shallow snowpack. This could be due to either under-catch in the observations, as the observations

at ANS of precipitation were much smaller (Figure 6.2) than the observations of precipitation at the ABACUS birch forest site (Figure 6.1). Or alternatively, it could be due to wind scour of snow which redistributes fallen snow from the areas of open tundra into the areas of sparse forests. In order for JULES to correctly model the timing of the snowpack, it must have sufficient precipitation data to model the snowpack at its peak. Therefore the precipitation data was adjusted to account for this potential under-catch and wind scour of the snow. The ANS Micromet adjusted precipitation data was multiplied by ten, which resulted in JULES producing an appropriately sized snowpack.

6.3 Discussion

Although JULES could be forced with downscaled climate data e.g. WFDEI [*Weedon et al.*, 2014] or meteorological data measured at ANS, it is preferable to use meteorological data measured in-situ at the ABACUS AWS. Measuring a set of continuous meteorological variables is challenging in high latitude environments particularly in the winter months with freezing temperatures and snowfall [*Bowling et al.*, 2003; *Essery et al.*, 2009]. The ABACUS sparse forest site was particularly challenging as it required continuous wind or solar power, regular maintenance and quality control of data. The Micromet model has been shown to be robust in gap filling meteorological data sets [*Rutter et al.*, 2009; *Hoffman et al.*, 2008; *Hanna et al.*, 2013; *Essery et al.*, 2008b]. It was used here to gap fill the longwave radiation and precipitation data when it was not possible to gap fill from the ANS data set.

The precipitation data from ANS is used to force the JULES model as it represented a more complete regularly maintained data set. Nevertheless, adjustments of the data set were necessary to account for under-catch, a common procedure for measurements of winter precipitation [*Adam and Lettenmaier*, 2003; *Bowling et al.*, 2003; *Pomeroy and Li*, 1997; *Sheffield et al.*, 2006; *Yang et al.*, 1999]. JULES was able to model an appropriately sized snowpack with the Micromet adjusted precipitation data.

6.4 Summary

The meteorological measurements detailed in this chapter have an important role in forcing the JULES model. Table 2.4 in Chapter 2 on page 51 provides a brief summary of how each of the meteorological variables were gap filled or corrected, and the dates when the measurements are available.

The final meteorological driving data for the ABACUS birch forest site with gap filled data is shown in Figure 6.15.

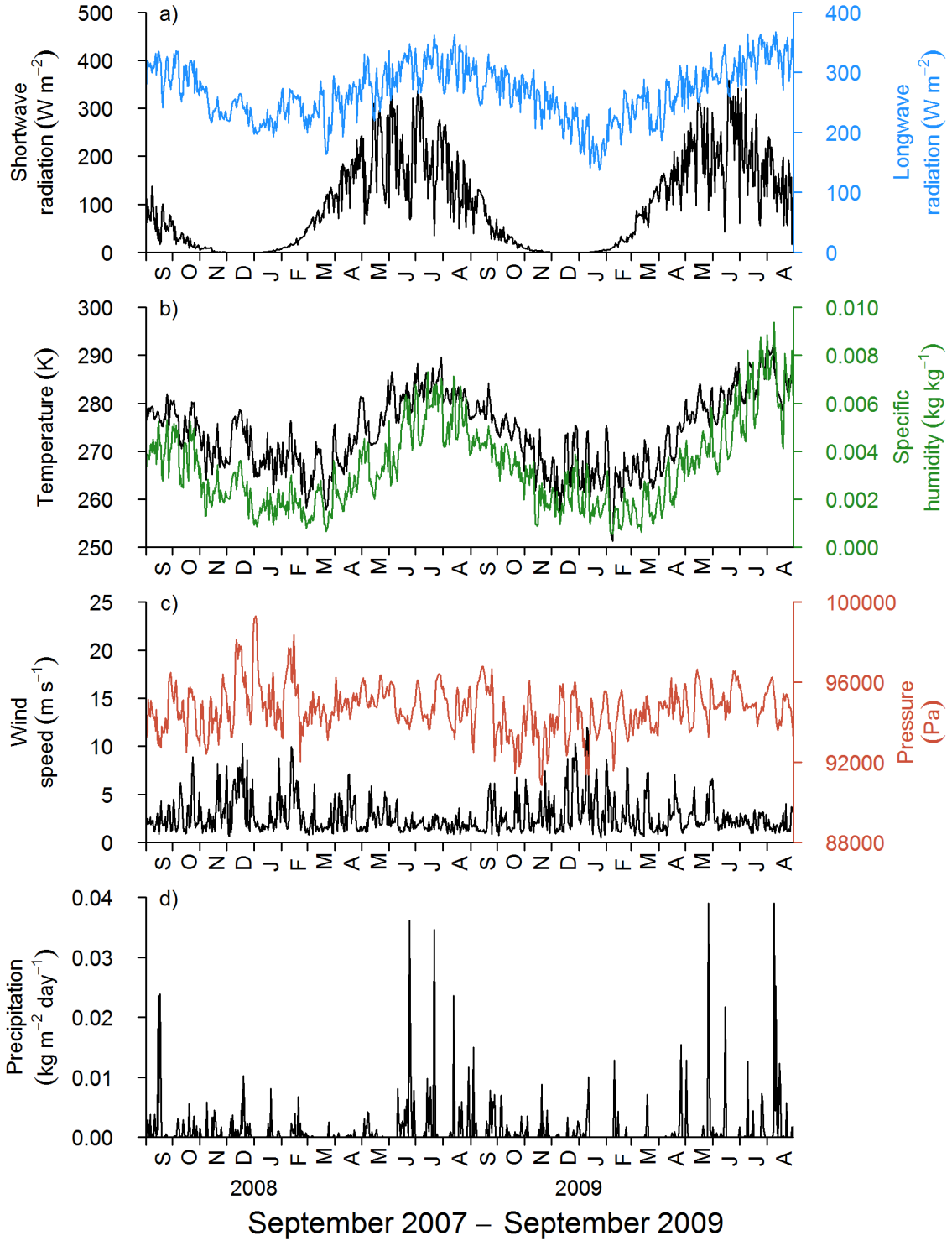

Figure 6.15: Mean daily driving (meteorological) data variables from September 2007 to September 2009.

Chapter 7

Modelling

7.1 Introduction

Land surface schemes are used within global climate models to represent land-atmosphere interactions of water, energy, and radiation. Sparse deciduous forests are poorly represented in the land-surface model JULES used in the UK Hadley Centre GCMs as it is assumed that there is a continuous thin vegetation cover above the soil surface. However, the radiation balance of high-latitude sparsely vegetated forests is highly variable both spatially and temporally. This is attributable to the highly heterogeneous distribution of trees, and specifically the gaps between trees combined with the low sun angles at these altitudes. The representation of the radiation of a sparse forest is particularly important when there is snow lying below the canopy, since the snowmelt at high latitudes is more sensitive to radiation than turbulent heat or rainfall.

The trees act on the radiation reaching the snow-pack on the forest floor in two ways. Firstly, by cutting out the incoming shortwave radiation down to the snowpack, especially during early spring when the sun is low in the sky (it has a high solar zenith angle), so that even with sparse leafless vegetation, the trees cast long shadows over the snow surface. Secondly, the low sun warms up the trees which then radiate the warmth down to the snow pack below. This is also particularly enhanced in the early spring as the low solar zenith angle means that the dark trees intercept the radiation, which is not able to penetrate down to the snow surface.

It is specifically the representation of these areas of sparse forests which need to be improved in the land surface model. The timing of the snowmelt, and release of water, is very important for other processes specifically the carbon and water balance, and therefore it is important to model this correctly.

This chapter will outline how JULES calculates the transmission of shortwave and longwave radiation through a canopy. We then assess how effectively the radiation exchanges for sparse

canopies are reproduced in the current, standard version of JULES. New equations to represent the key radiation processes will then be developed to create a Shaded gap tile within the JULES model. This new Shaded gap tile is parameterised and developed using the canopy data gathered in Abisko presented in chapter 3. The model is then run with the driving data created in Chapter 6 and the model output is validated against measurements of shortwave radiation and longwave radiation presented in Chapter 4. Finally, the resulting modelled snow mass is compared to the snow mass observations presented in Chapter 5 to explore the sensitivity of the modelled melt-date to the new Shaded gap tile.

7.2 Standard JULES

A comprehensive description of the Joint UK Land Environment Simulator (JULES) model is given by *Best et al.* [2011] and *Clark et al.* [2011]. JULES is composed of 9 surface tiles, comprising of 5 vegetation covers; Broadleaf tree, Needleleaf tree, c3 Grass, c4 Grass, and Shrub, and 4 non-vegetation covers; Urban, Water, Ice, and Bare soil as shown in Figure 7.1. For each of these tiles surface energy and mass balances are calculated for the water, heat and radiation budgets.

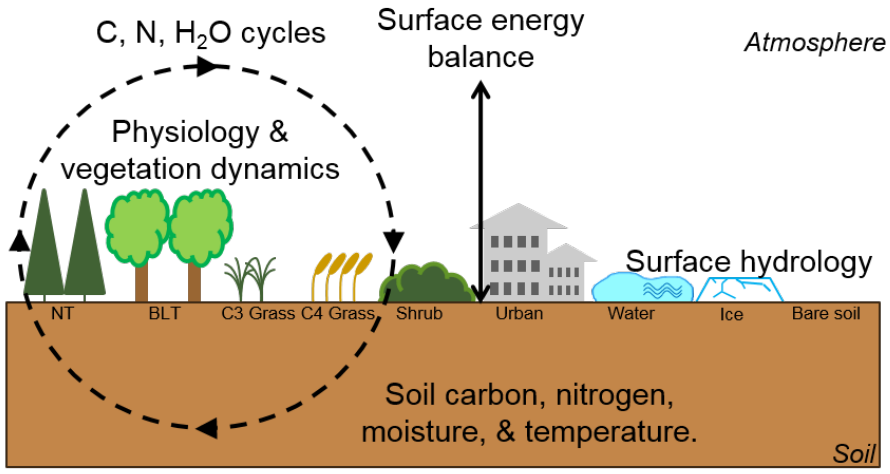

Figure 7.1: Schematic to show the nine surface tile types in the JULES model and some of the key surface processes calculated.

This study focuses on the radiation balance and how the physical and spatial structure of the sparse canopy changes the distribution of the incoming and outgoing shortwave and longwave radiation to the snowpack, and whether this has a significant effect on the longevity of the snowpack in spring. The land surface model JULES will be used to explore this.

A simple schematic of how JULES calculates the radiation balance for both tree and grass tiles is shown in Figure 7.2. The radiation balance is currently calculated using the total incoming radiation above the canopy, and does not allow shortwave radiation transmission through the canopy.

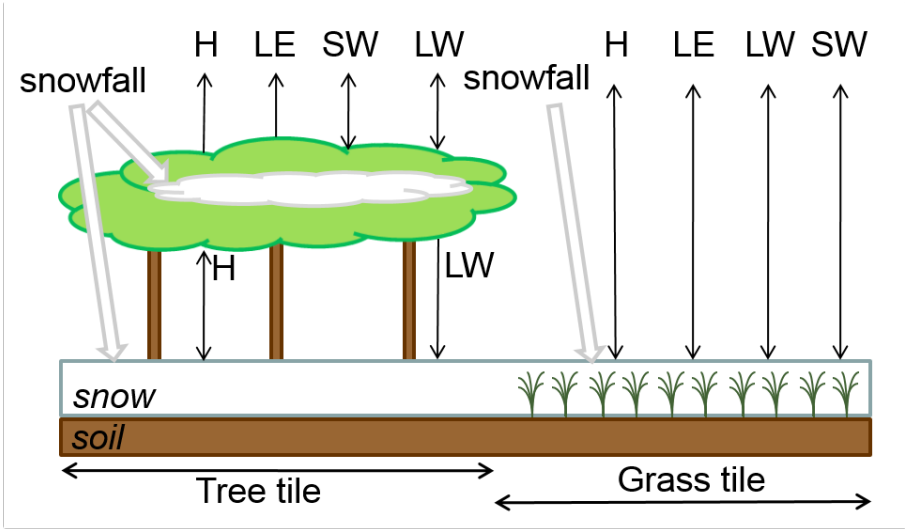

Figure 7.2: Schematic to show the current vegetation tile options for representing the sparse birch forest in JULES - A Tree and Grass tile.

7.2.1 Shortwave radiation

The current JULES model calculates the net shortwave radiation (W m^{-2}) to the surface where:

$$SW_{net} = (1 - \alpha)SW_{\downarrow} \tag{7.1}$$

Where $SW_{\downarrow}$ is the downward shortwave radiation (W m^{-2}) and α is the albedo. JULES does not allow shortwave radiation penetration under the canopy for the surface energy balance equations, therefore the canopy acts as though it is a dense impenetrable canopy.

7.2.2 Longwave radiation

The current JULES model calculates the net longwave radiation (W m^{-2}) to the surface where:

$$LW_{net} = \varepsilon LW_{\downarrow} - \varepsilon\sigma T_{*}^{4} \tag{7.2}$$

Where $LW_{\downarrow}$ is the downward longwave radiation (W m^{-2}), ε is the Emissivity, σ is the Stefan Boltzmann constant and T_* is the surface temperature (Kelvin). It is assumed that the longwave radiation has an albedo of 1 - ε .

7.2.3 Prescribed conditions and parameters

The JULES (v4.6) model requires some prescribed conditions for the sparse birch forest in Abisko. A full description of the namelist files used to run JULES for Abisko are provided in Appendix A.

Canopy radiation models 4 to 6 which include options for light limited photosynthesis and respiration, sunlit and shaded leaves, sun fleck penetration and leaf nitrogen concentrations [*Clark et al.*, 2011] could have been used, but these are calculating photosynthesis rather than fluxes of energy through the canopy. A multi-layered canopy model is not required, as canopy radiation model 4 and above would overestimate the GPP and NPP for this site as the canopy in spring is leafless branches with limited photosynthesis. As this study is focused on the radiative balance of these forests, rather than photosynthesis, canopy radiation model 1 is preferable. Canopy radiation model 1 treats the incoming radiation as a single stream and applies Beer's law to the radiation transmission through the canopy (Equation 7.3) using a light extinction coefficient of 0.50 (Table 7.1).

The canopy model options are no distinct canopy (1), a radiative canopy without a heat capacity (2), a radiative canopy with a heat capacity (3), and a radiative canopy with heat capacity which allows a snowpack to develop beneath the canopy (4). In this study the snow pack underneath the canopy is a priority therefore option 4 is used.

The snow model has two options: (1) a zero-layer scheme with a single composite layer where the snowpack develops in the top layer of the soil and (2) a multi-layered snow model which develops a snowpack above the surface of the soil. Since the latter is more comprehensive and physically realistic [*Best et al.*, 2011], the multi-layered snow scheme was used here.

Although it would be preferable to run JULES with separate direct and diffuse fractions, the in-situ measurements were only available for short periods. JULES was forced using downward shortwave radiation (rather than separate direct and diffuse fractions), and a fixed value of 0.72 for the diffuse fraction parameter (Chapter 4.5).

7.3 Canopy models

To investigate the best way to implement a radiation transfer scheme for a sparse canopy a series of canopy models were used. Firstly, a Homogeneous canopy model which treats the canopy as a single (broadleaf tree) uniformly sparse canopy with radiation transmission to the surface. The Homogeneous canopy model is based on the calculations used for photosynthesis in JULES canopy radiation model 1 implemented into the radiation fluxes. It uses a light extinction coefficient (Table 7.1) scaled with LAI, to calculate the transmission of light through the canopy (Equation 7.3). The second approach used was a Clumped canopy model which treats the canopy as two distinct areas, a denser canopy tree tile without radiation transmission to the surface and a c3 grass tile which does not have a canopy and therefore receives all the incoming shortwave radiation. The parameters for these canopy models are specified in Table 7.1.

Table 7.1: Canopy Model Parameters

	Homogeneous Canopy Model	Clumped Canopy Model	
Parameter	Sparse Tree Tile	Broadleaf Tree Tile	c3 Grass Tile
Fractional Coverage	1.00	0.25	0.75
LAI	0.25	1.00	
Area-average LAI	0.25	0.25	
Light extinction coefficient (k)	0.50		
$e^{(-k\ LAI)}$	0.882		

The fractional cover of the sparse forest canopy in Abisko can be represented in our canopy models using a sole broadleaf tree tile (Homogeneous), or a combined broadleaf tree tile (25 %) and c3 grass tile (75 %) (Clumped). Table 7.1 shows some of the fixed parameters for each of these tree and grass tiles. The fractional coverage of the Clumped canopy model is set so that the area-average LAI is the same as the Homogeneous canopy model.

7.3.1 Results - Canopy models

The following graphs show the results for the downward shortwave radiation when two canopy models ('Homogeneous' and 'Clumped' - as explained above) were designed for a sparse canopy. Figure 7.3 shows the models and the observed measurements of shortwave radiation beneath the canopy during 2008. The canopy model results and the observed measurements of shortwave radiation beneath the canopy in 2009 are shown in Figure 7.4 for day 91 to day 135, and in Figure

7.5 for day 136 to 169. Figure 7.6 shows a sunny and cloudy during 2008 and 2009. For each of these four figures the black line shows the downward shortwave radiation from the driving data, the grey area shows all the observations of below canopy shortwave radiation and the red line shows the mean of these below canopy shortwave radiation measurements. The Homogeneous canopy model is shown by the blue line, and the Clumped canopy model is shown by the purple line.

It is clear by comparing the downward shortwave radiation (black line) with the mean observations of shortwave radiation beneath the canopy (red line) on Figures 7.3, 7.4, 7.5 and 7.6 that the snow beneath the canopy is receiving less shortwave radiation on average than the radiation that is observed above the canopy of the trees.

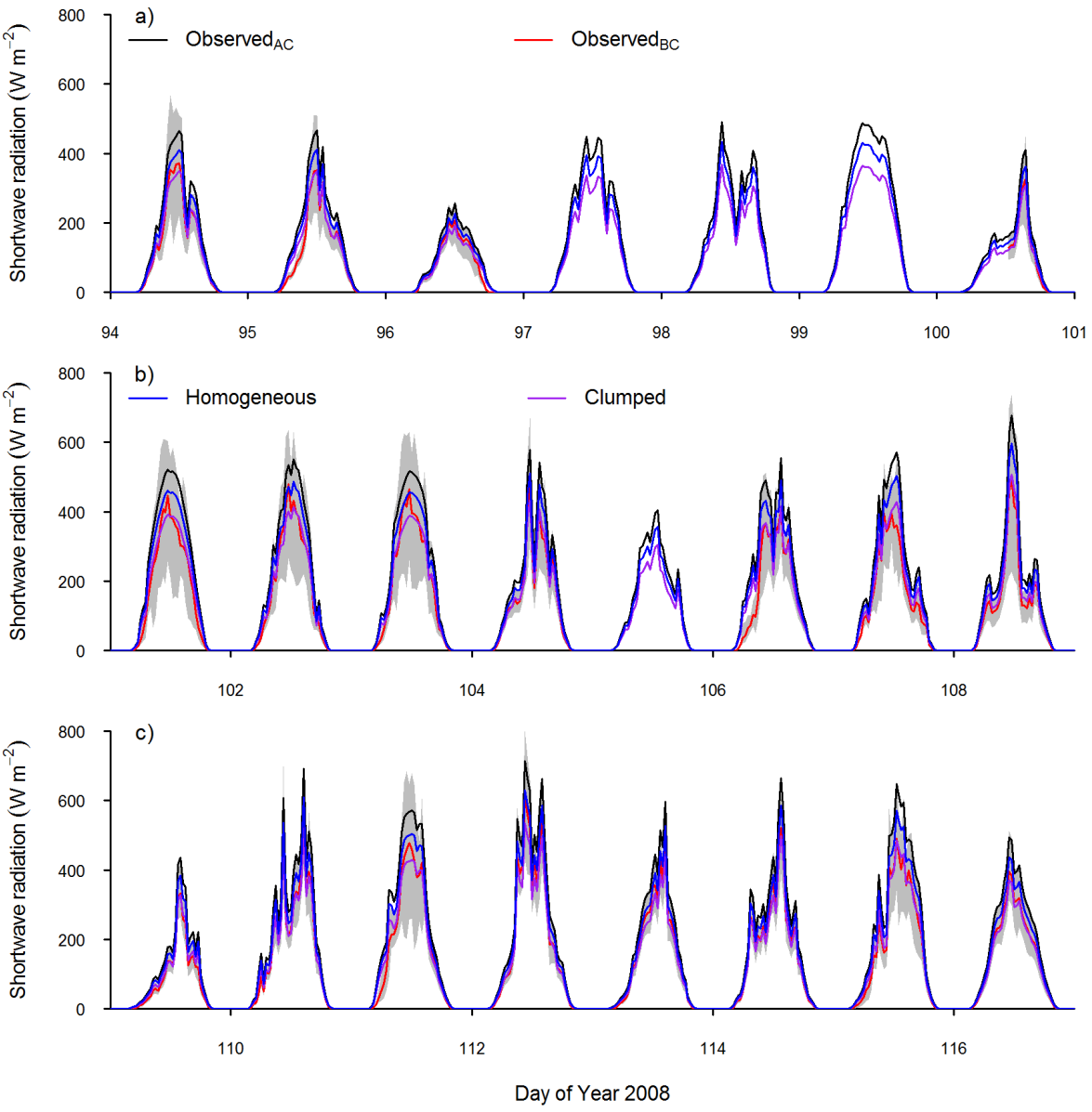

Figure 7.3: Observed and canopy modelled shortwave radiation (W m^{-2}) for day 94 (3 April) to day 116 (25 April) in 2008. The observed data comprise the observed above canopy (Observed$_{AC}$) CNR1 at the ABACUS AWS (black), the observed below canopy pyranometer data (grey) and the mean observed below canopy (Observed$_{BC}$) pyranometer data (red). The canopy models comprise Homogeneous (blue) and Clumped (purple).

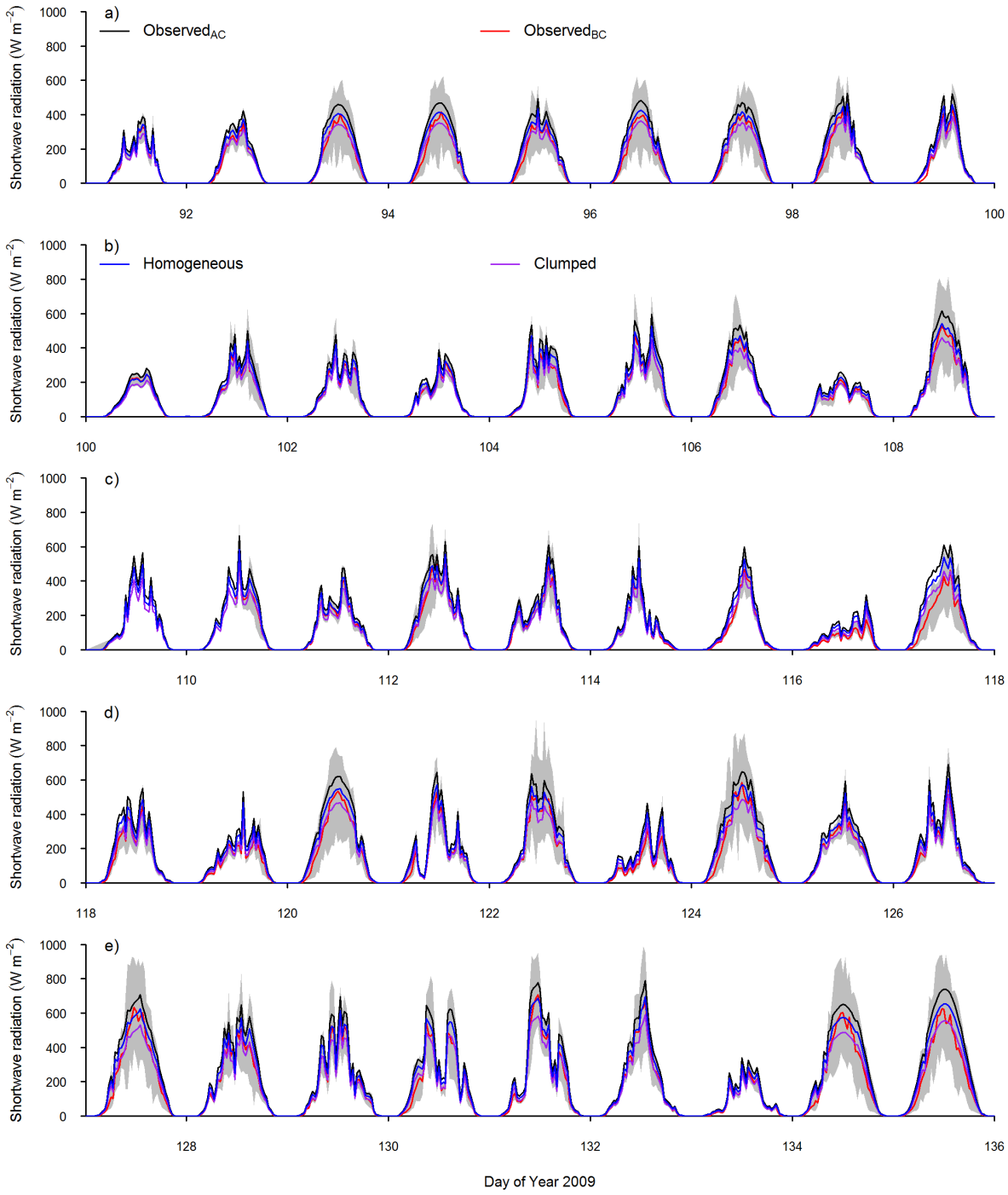

Figure 7.4: Observed and canopy modelled shortwave radiation (W m^{-2}) for day 91 (1 April) to day 135 (15 May) in 2009. The observed data comprise the observed above canopy (Observed$_{AC}$) CNR1 at the ABACUS AWS (black), the observed below canopy pyranometer data (grey) and the mean observed below canopy (Observed$_{BC}$) pyranometer data (red). The canopy models comprise Homogeneous (blue) and Clumped (purple).

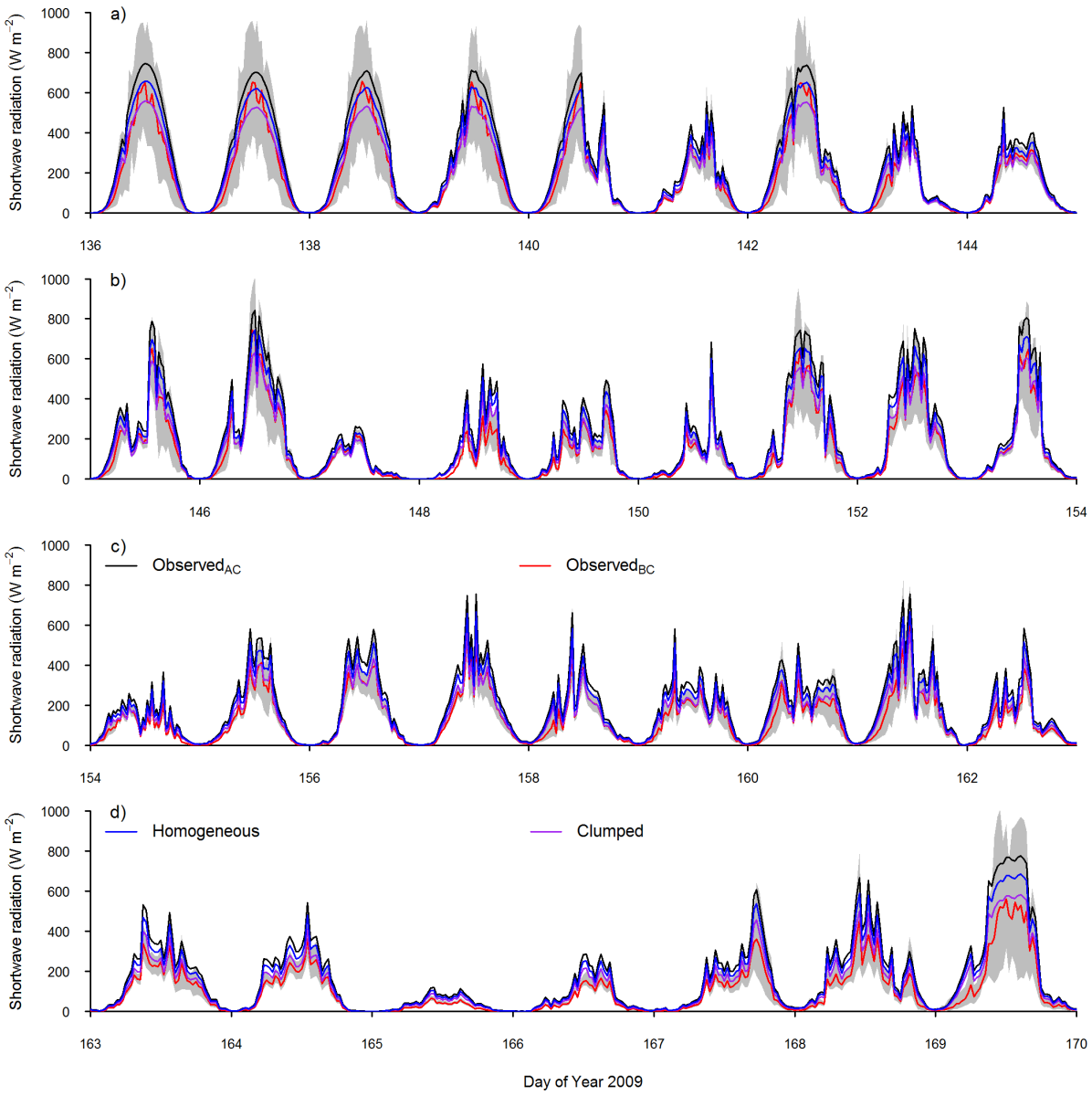

Figure 7.5: Observed and canopy modelled shortwave radiation (W m^{-2}) for day 135 (16 May) to day 169 (18 June) in 2009. The observed data comprise the observed above canopy (Observed$_{AC}$) CNR1 at the ABACUS AWS (black), the observed below canopy pyranometer data (grey) and the mean observed below canopy (Observed$_{BC}$) pyranometer data (red). The canopy models comprise Homogeneous (blue) and Clumped (purple).

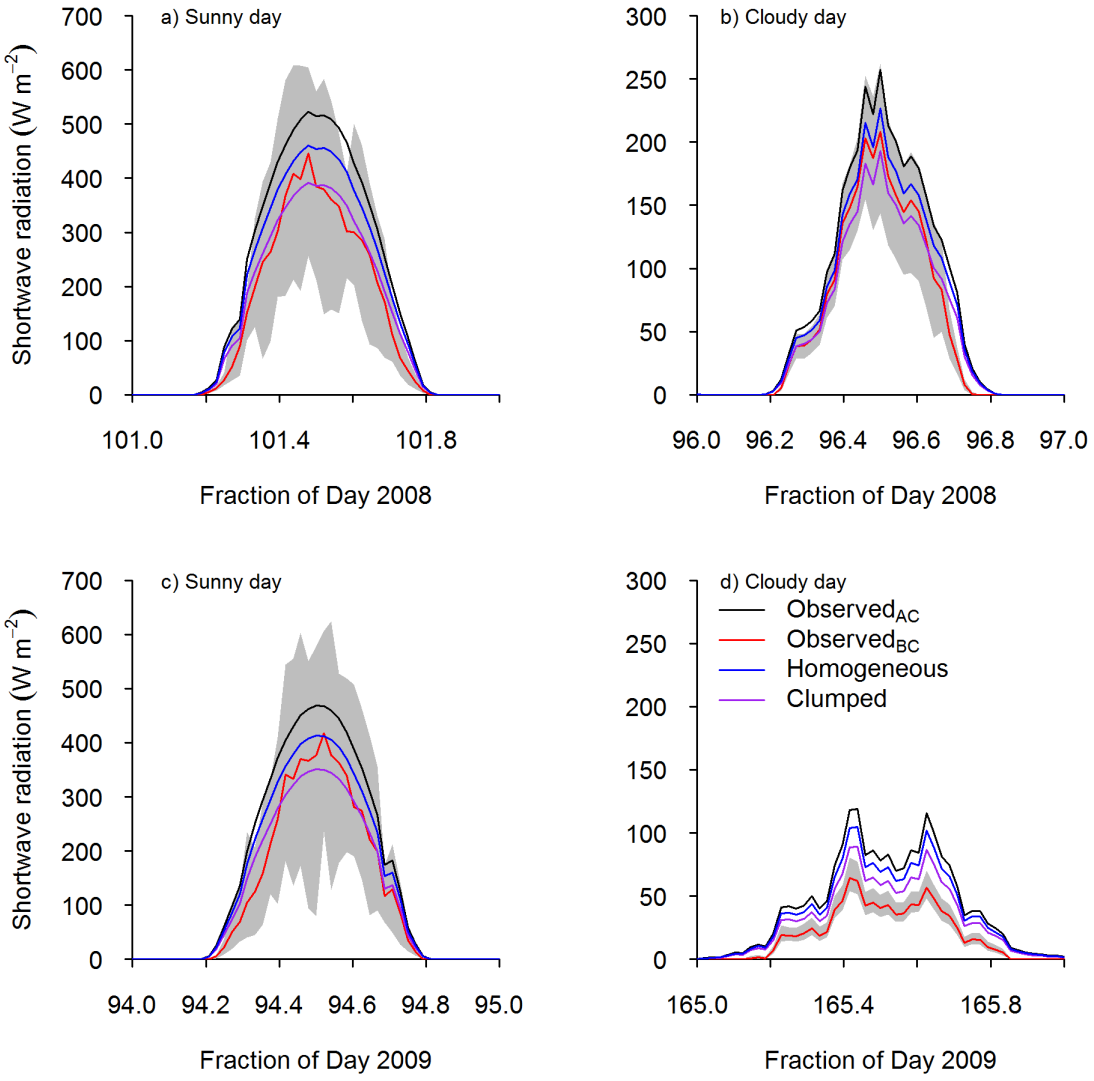

Figure 7.6: Observed and canopy modelled shortwave radiation (W m^{-2}) for a sunny day (Day 101 - 10 April) and a cloudy day (Day 96 - 5 April) in 2008 and a sunny day (Day 94 - 4 April) and a cloudy day (Day 165 - 14 June) in 2009. The observed data comprise the observed above canopy (Observed$_{AC}$) CNR1 at the ABACUS AWS (black), the observed below canopy pyranometer data (grey) and the mean observed below canopy (Observed$_{BC}$) pyranometer data (red). The canopy models comprise Homogeneous (blue) and Clumped (purple).

Homogeneous canopy model

The Homogeneous canopy model treats the incoming radiation with a Beer's law equation as follows:

$$SW_{\downarrow bc} = SW_{\downarrow ac} e^{(-k\ LAI)} \tag{7.3}$$

Where SW_{bc} is the below canopy shortwave radiation (W m^{-2}), SW_{ac} is the above canopy shortwave radiation (W m^{-2}), k is the light extinction coefficient and LAI is the leaf area index of the vegetation canopy. Equation 7.3 is applied to incoming shortwave radiation to calculate the shortwave radiation beneath the sparse forest canopy in the Homogeneous canopy model, which is shown by the blue lines in Figures 7.3, 7.4, 7.5 and 7.6.

Using the value of LAI measured in-situ of 0.25 to represent a sparse forest in the Homogeneous canopy model overestimates the shortwave radiation penetration through the canopy with respect to the observations of below canopy radiation on both sunny and cloudy days (Figure 7.6). The Homogeneous canopy model performs reasonably well at estimating the below canopy shortwave radiation on the cloudy day 96 in 2008 (Figure 7.6), yet on the sunny days like day 101 to 103, the Homogeneous canopy model overestimates the shortwave radiation measured under the canopy. Nevertheless there is reasonable agreement between the model and the observed mean shortwave radiation (Figure 7.7). The Homogeneous canopy model most notably overestimates the shortwave radiation penetrating the canopy at the start and end of the day. This can be clearly seen in Figure 7.8 which shows the ratio of observations of shortwave radiation to the Homogeneous canopy model throughout the day. The Homogeneous canopy model reasonably reproduces shortwave radiation penetration as the ratio approaches 0.8 during the middle of the day. However, the ratio at the start and the end of the day is poor as it is less than 0.4. The Homogeneous canopy model reproduces the shortwave radiation transmission through the canopy consistently in the early spring of both 2008 and 2009 (Figure 7.8), whereas by late spring (Figure 7.8 panel c) the model produces poorer results with few midday model values having a ratio of over 0.8 relative to the observations.

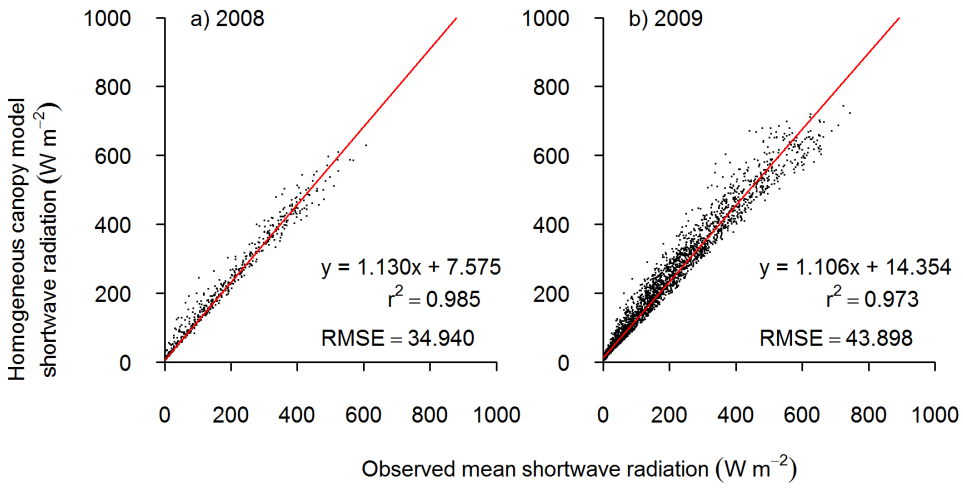

Figure 7.7: Linear regression of Homogeneous canopy modelled shortwave radiation (W m^{-2}) and observed shortwave radiation (W m^{-2}) for a. 2008 and b. 2009

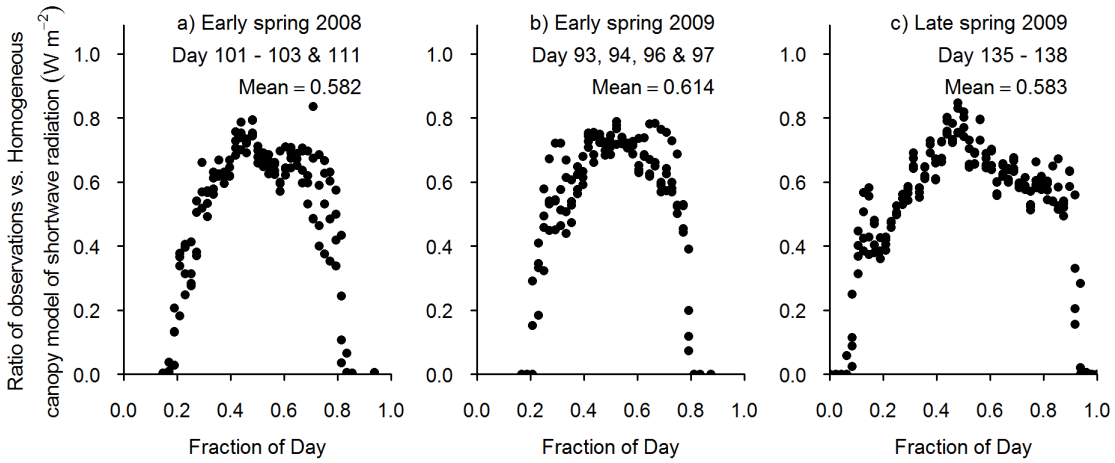

Figure 7.8: Ratio of observations to Homogeneous canopy modelled shortwave radiation (W m^{-2}) for four sunny days in a. Early spring 2008, b. Early spring 2009 and c. Late spring 2009.

Equation 7.3 is dependent upon the LAI of the tree canopy, and allows some sunlight to penetrate down through the canopy layers to the surface of the snowpack. This is because the Homogeneous canopy model treats the canopy as a thin continuous layer, or to put it another way, as though the sun were permanently overhead, even if the strength varies through the day and through the season. Therefore, the snowpack beneath the canopy receives a fixed proportion of the incoming shortwave radiation. Whereas in reality, the canopy is clumped (Figure 7.12), and the snow that lies between the clumps is only in shade when the angle of the sun is low, with this angle varying during the day and by season. The snowpack behaves as a hybrid between an open tundra snowpack and a below canopy snowpack. Therefore, modelling these sparse forests with a sole tree tile maybe not be accurately representing the canopy variability in these forests.

Clumped canopy model

To replicate the clumping of the forest canopy seen in the sparse forest canopy of Abisko and to calculate the impact of clumping on the overall shortwave radiation, we apply a different but simple model of the shortwave radiation attenuation. Assuming that the trees only cover 25 % of the area, having an LAI of 1.0, and the rest of the area is short grass vegetation with a fractional cover of 75 % and has no vegetation canopy (Table 7.1). The area-average LAI for this sparse canopy is 0.25. The Beers law Equation 7.3 is not applied to the tree tile as in the Homogeneous canopy model, and the grass tile receives all of the downward shortwave and longwave radiation. This is a Clumped canopy model and is shown by the purple lines in Figures 7.3, 7.4, 7.5 and 7.6.

These figures show that a Clumped canopy model also fails to accurately represent the shortwave radiation balance of these sparse forests as it underestimates shortwave radiation penetration through the canopy during the middle of the day. The relationship between the Clumped canopy model and observed mean shortwave radiation is shown in Figure 7.9. The ratio of the Clumped canopy model and observations for sunny days in early spring 2008, early spring 2009 and late spring 2009 is shown in Figure 7.10. This clearly shows that the Clumped canopy model underestimates the midday mean of the observations, but in general it overestimates the shortwave radiation which is able to penetrate the canopy in the early mornings and late afternoons (Figure 7.10 panel a and b). In general the relationship between Clumped canopy model and the observations does not differ between early spring and late spring.

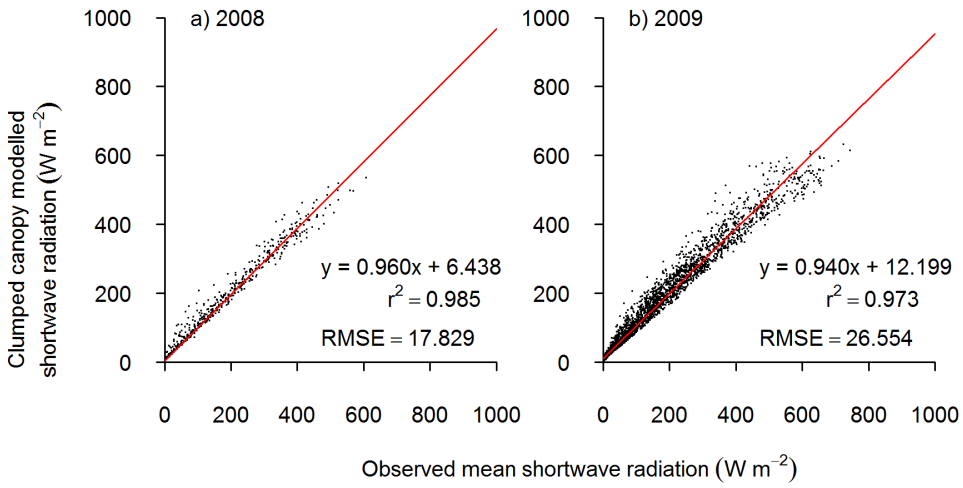

Figure 7.9: Linear regression of Clumped canopy modelled shortwave radiation (W m^{-2}) and observed shortwave radiation (W m^{-2}) for a. 2008 and b. 2009.

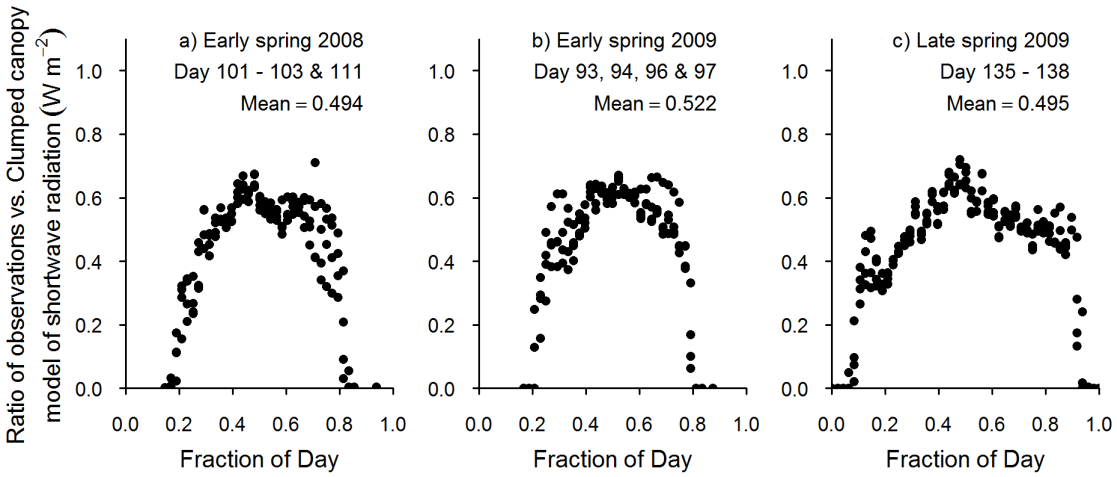

Figure 7.10: Ratio of observations to Clumped canopy modelled shortwave radiation (W m^{-2}) for four sunny days in a. Early spring 2008, b. Early spring 2009 and c. Late spring 2009.

Figures 7.3, 7.4, 7.5 and 7.6 show that both Homogeneous and Clumped canopy models fail to accurately represent the shortwave radiation balance of these sparse forests. Even though both of these solutions are able to reasonably predict the mean of the observations, they both underestimate the shortwave radiation which penetrates the canopy throughout the day, and particularly in the early morning and late afternoon.

Both the Homogeneous and Clumped canopy model have no sensitivity to azimuth, so the results are likely to be similar throughout the day (Figure 7.8 and 7.10). Crucially both of the canopy models act as if the sun were permanently overhead with no daily or season variability. Therefore both the Homogeneous and Clumped canopy models have a poor ratio of observations to modelled shortwave radiation because the model lacks this variation in the solar elevation. An alternative solution is required which accounts for this temporal variability in shortwave radiation penetration.

7.4 Development of a Shaded gap tile in JULES

The sparse birch forest in Abisko is highly heterogeneous in its characteristics. The trees are predominately polycormic (multi-stemmed) basal sprouting silver birch trees. The surface of the stems is highly heterogeneous, as the silver birch are covered in a patchwork of black lichens. The stems are on average 5 m in height, and vary from very thin ($<$ 5 cm in diameter) to the occasional monocormic (single stem) tree which can be over 30 cm in diameter and up to 6 or 7 m in height. As birch is a deciduous tree (in spring they are leafless), the canopy density is very low and the canopy architecture is dominated by thin spindly angular stems (Figure 7.11). As they are multi-stemmed the vegetation canopy is clumped around the basal stems. However, the spatial distribution of trees is highly variable. The trees themselves often clump together to create relatively dense patches of canopy, and conversely trees can also be sparsely distributed into very low density patches of vegetation canopy.

Figure 7.11: View from within the sparse birch forest near the AWS in spring 2008.

What makes modelling the shortwave radiation penetration through these sparse canopies challenging is the low solar angles in spring at high latitudes. Low solar elevation and the thin stems cast long shadows over the surface of the snow, and there is limited illumination at the surface of the snow (Figure 7.12). As spring progresses and the solar elevation increases, the shortwave radiation penetrates down through the canopy to the surface of the snowpack, and the length of the shadows cast across the surface of the snow decreases. However, due to the thin spindly

stems the shortwave radiation penetration is highly variable. As shown by the pyranometers in Chapter 4 section 4.3.2 Figure 4.2 to 4.4 individual points on the snow surface can receive all the downward shortwave radiation, and then soon afterwards (approx. 1 hour) be shaded by a tree and only receive a small proportion of the total shortwave radiation.

Figure 7.12: A sparse canopy in Abisko with shadows cast across the snowpack. Photo taken from AWS tower looking west in the afternoon (16.44 pm) of day 93 (3 April) 2009.

The hemispherical view of the sky from the surface of the snow (Figure 7.13) shows that at very low solar angles a significant proportion of vegetation would cut out the shortwave radiation penetration to the snow surface. As the solar elevation increases there is a much larger proportion of sky, and therefore more radiation reaches the surface of the snow.

Figure 7.13: Hemispherical photograph for pyranometer 6. Photo taken in the morning (approx. 10.30 am) on day 91 (1 April) in 2009.

Part of the reason why a Homogeneous canopy model fails to represent these forests is the assumption of canopy uniformity. Similarly a Clumped canopy model assumes that the forest is all clumped into one area receiving no shortwave radiation beneath the canopy and that the open area receives all the downward shortwave radiation. In reality, neither scenario is valid for these forests, as the forest is not clumped into an all shaded and all lit fraction, but a mixture of the two. Therefore, a parameter which accounts for the temporal variability in shortwave radiation penetration is needed.

This study aims to reproduce the energy balance of a sparse deciduous forest in the JULES model. The current parameterisation for a tree tile is unable to reproduce the spatial and temporal variability in shortwave radiation penetration through the forest canopy. Therefore modifications need to be made to the JULES code to allow shortwave radiation penetration down to the snowpack surface.

As noted in Chapter 4, the variation in below canopy shortwave radiation on cloudy days is caused by the canopy transmissivity or Sky view fraction. This is because diffuse radiation does not vary with time. In contrast, on sunny days the below canopy shortwave radiation varies with both diffuse and direct radiation. As with the cloudy days the canopy transmissivity reduces the diffuse fraction, but the direct radiation component varies with time of day and season due to the increasing solar elevation.

In this study modifications have been made in JULES to include a Shaded gap tile, representing shortwave radiation penetration at high latitude sites, and allowing longwave radiation from the forest to the snowpack as shown diagrammatically in Figure 7.14. This requires the introduction of several new parameters: the Sky view fraction (f_v) (%) representing the canopy transmissivity which is fixed in time; the gap size (Gap_s) which is the diameter (m) of the Shaded gap tile and is fixed in time; and the Lit fraction (f_{lit}) which is the fraction of the Shade tile which receives direct sunlight varying with hour and season. Both the parameters (f_v) and (Gap_s) were informed by the results presented in Chapters 3 and 4.

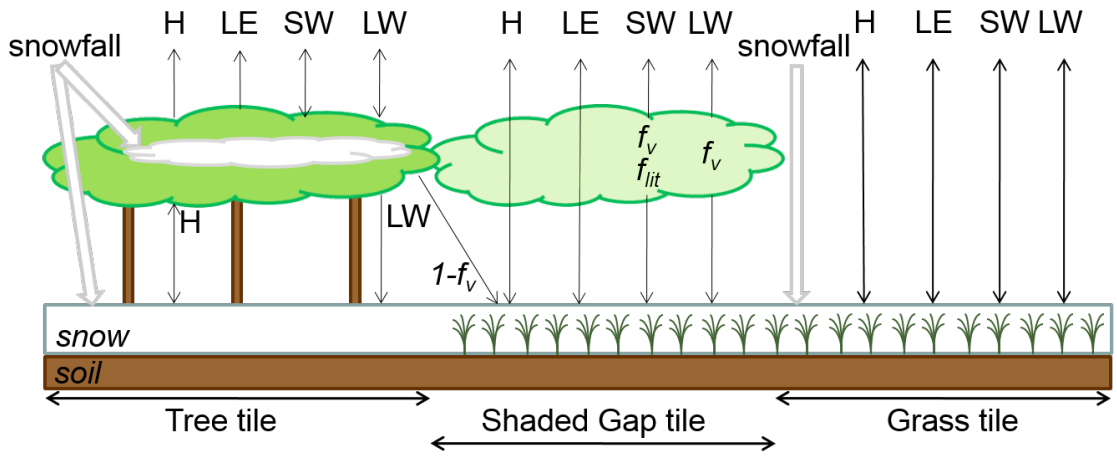

Figure 7.14: Schematic to show a Tree, Shaded gap and Grass (or tundra) tiles in JULES.

7.4.1 Parameterisations

The Lit fraction (f_{lit}) represents the fraction of a Shaded gap tile which is illuminated as illustrated in Figure 7.15. The f_{lit} parameter varies seasonally and temporally with the variability in solar elevation in spring and is calculated as a function of the azimuth angle of the sun as follows:

$$f_{lit} = 1 - \tan(Z) H_{tree} / Gap_s \tag{7.4}$$

Where H_{tree} is the tree canopy height (m), Gap_s is the diameter of the Shaded gap (m) and Z is the solar zenith angle, calculated as:

$$\cos(Z) = \sin(\frac{\pi}{180} Lat) \sin(sd) + \cos(\frac{\pi}{180} Lat) \cos(sd) \cos(hh) \tag{7.5}$$

Where $\cos(Z)$ is the cosine of the solar zenith angle, Lat is the Latitude, sd is the solar declination angle and hh is the azimuth angle of the sun relative to south, calculated as follows:

$$sd = -23.4\frac{\pi}{180}\cos(\frac{2\pi}{365}(J+10)) \tag{7.6}$$

$$hh = \pi(\frac{2T}{S} - 1) \tag{7.7}$$

Equation 7.6 is for the solar declination angle, where J is the Julian day of year and 365 is the days in year. Equation 7.7 is for the angle of the sun relative to solar noon, where T is time of day in seconds, and S is seconds in day.

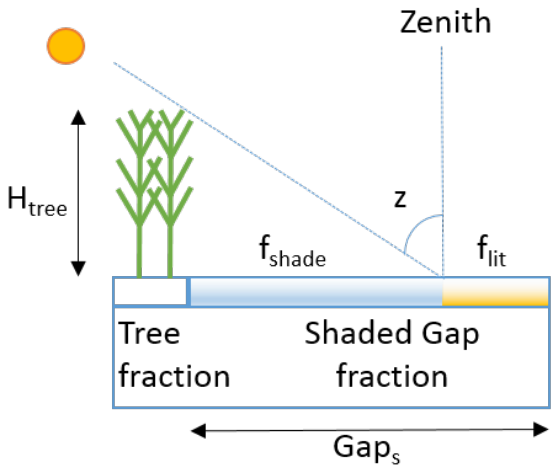

Figure 7.15: Schematic for the Lit fraction (f_{lit}) parameter in the Shaded gap tile.

By calculating f_{lit}, the transmission of downward shortwave radiation ($SW_{\downarrow}$) (W m^{-2}) through the vegetation canopy can be calculated in the Shaded gap tile as follows:

$$SW_{\downarrow} = SW_{\downarrow} f_{dif} f_v + SW_{\downarrow}(1 - f_{dif}) f_{lit} \tag{7.8}$$

Where f_{dif} is a fixed value of 0.72 for the ratio of diffuse to direct radiation (Chapter 4.5). The parameter f_v is the Sky view fraction, and the f_{lit} parameter is defined in Equation 7.4.

Lit fraction - f_{lit}

The new parameter f_{lit} varies during the course of a day, seasonally and with latitude, and is also dependent upon the tree height of the tree tile and the size of the Shaded gap. Figure 7.16 shows the daily and annual variability in the f_{lit} parameter.

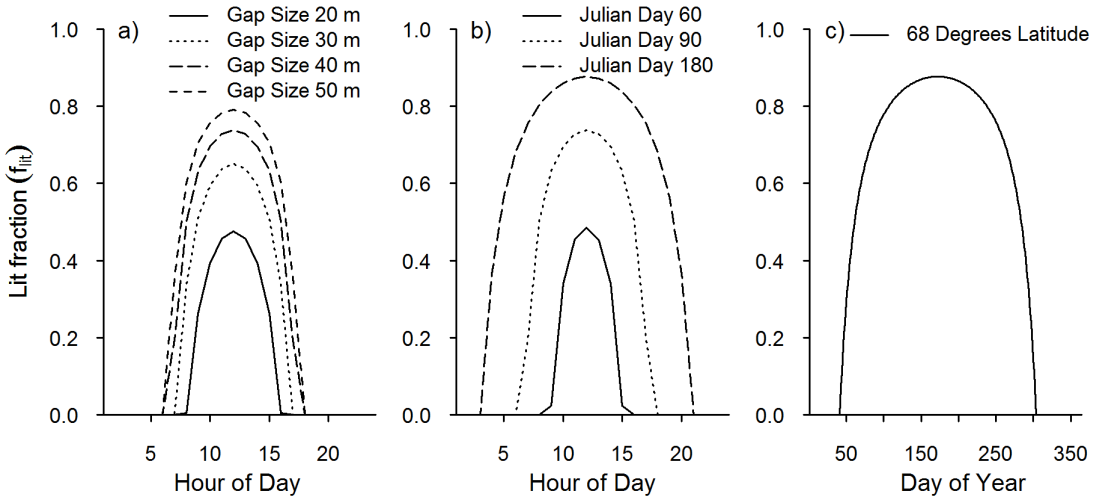

Figure 7.16: The temporal variability in the f_{lit} parameter. Panel a shows the hourly variability of f_{lit} for a fixed latitude of 68 degrees for the Gap size from 20 m to 50 m for Julian day 90. Panel b shows the hourly variability of f_{lit} for a fixed latitude of 68 degrees on Julian days 60, 90 and 180 for a Gap size of 40 m. Panel c shows the annual variability of f_{lit} at midday for a latitude of 68 degrees with a fixed Gap size of 40 m.

Figure 7.16 panel b shows how the f_{lit} parameter will impact on the incoming shortwave radiation seasonally. Julian day 60 has a mean f_{lit} of 0.088, Julian day 90 has a mean f_{lit} of 0.260, and Julian day 180 has a mean f_{lit} of 0.514. f_{lit} can be used to reproduce the temporal and seasonal variability in downward shortwave radiation for sparse forests as observed at Abisko.

Gap size - Gap_s

The survey grids were studied in detail and suggested that 30 m would be an appropriate first estimate for the Shaded gap size. However, the survey grids were necessarily limited to 30 m in diameter. The survey transects indicated that a Shaded gap size of 40 m was also appropriate (245 m to 285 m along the north-east transect (Chapter 3 section 3.3.3 Figure 3.4 panel a)) and that the maximum Gap size was 50 m (385 m to 435 m along the north-west transect (Chapter 3

section 3.3.3 Figure 3.4 panel d)).

In order to study the impact of the gap size on the model results a sensitivity study was conducted on Shaded gap sizes of 20 m, 30 m, 40 m, and 50 m in diameter. The conceptual idea that the trees of the whole area had been tightly packed into variable percentage of fractional cover leaving a shaded gap with no canopy. A Gap size diameter of 20 m and 30 m was too small irrespective of the fractional cover, as the f_{lit} parameter was too low, and too little shortwave radiation was penetrating down through to the surface of the Shaded gap (Figure 7.16 panel a). A Shaded gap size of 50 m was too large, allowing too much radiation into the Shaded gap during the early morning in spring irrespective of fractional cover, and having almost no effect during mid spring. The sensitivity study showed that multiple combinations of fractional cover would allow sufficient radiation down to a Shaded gap of 40 m in diameter.

A Gap size of 40 m was chosen to represent the sparse birch forests of Abisko, as it creates sufficient shadows to entirely shade the gap in very early spring, allows sufficient daily variability in mid spring and then has only a small effect in the early mornings by mid-summer (Table 7.3 Shaded gap size). A much smaller or larger Shaded gap size would have not represented the heterogeneity observed in the canopy cover or been representative of the sparse forest gaps in Abisko.

Sky view fraction - f_v

The parameter f_v is defined as the Sky view fraction, which is the fraction of sky viewed from the surface of the snowpack underneath the vegetation canopy. f_v was calculated using the observations of transmissivity (Chapter 3 section 3.3). Although GLA transmissivity combines direct and diffuse canopy transmissivity, it is used for f_v to infer the canopy transmission of diffuse radiation. The hemispherical photographs (n = 585) from the locations of pyranometers (n = 24), survey grids (n = 287, these contain 91 repeats from ABI2 (n = 42) and ABI5 (n = 49)) and survey transects (n = 274, areas of tundra are excluded) from both spring 2008 and 2009 were pooled and analysed with GLA to calculate a canopy transmissivity. These were used to inform the Sky view fraction parameter f_v.

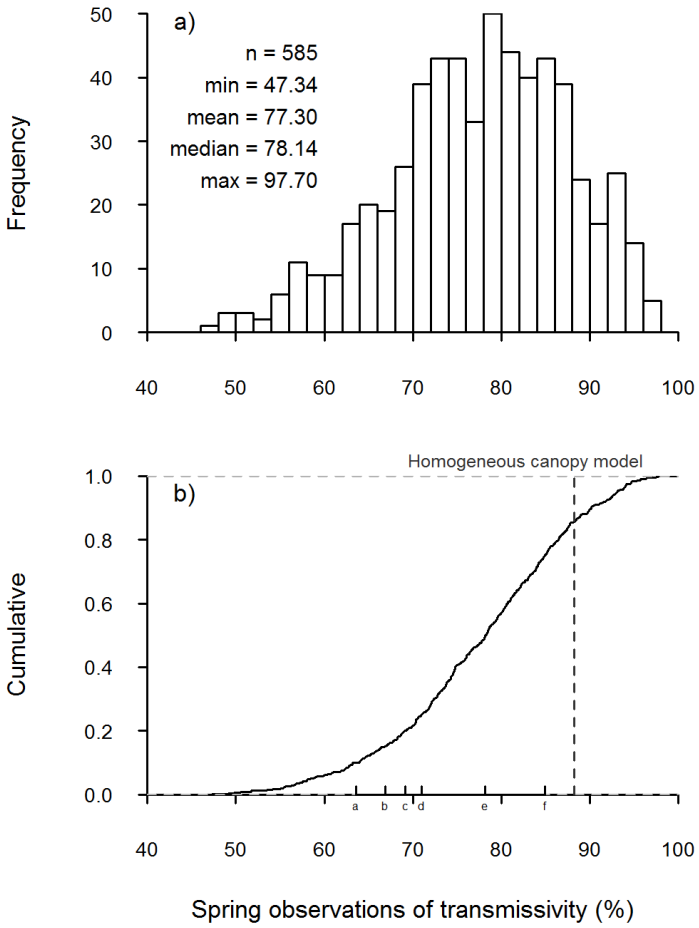

Figure 7.17: Histogram and cumulative distribution of the spring 2008 and 2009 observations of transmissivity (%). The dark grey dashed line on the cumulative curve shows the effective transmissivity when LAI is set to 0.25 in the Homogeneous canopy model from Table 7.1. Labels (a to f) refer to thresholds set for fractional cover in Table 7.2.

Figure 7.17 shows a histogram and the cumulative distribution of observed transmissivity. The mean transmissivity for all the data was 77.39 %, but there was considerable variability in transmissivity as areas with the most closed canopy had a transmissivity of 47 %, whereas areas with the most open canopy had a transmissivity of 98 %.

The cumulative distribution of this data (Figure 7.17 panel b) was used to inform the fractional cover of Tree and Shaded gap tiles, and their respective Sky view fraction. This highly heterogeneous data shows the need to rationalise the continuum of transmissivity found in the sparse forest into a simple two tiled model. Table 7.2 shows some of the possible options for fractional cover for the tree and Shaded gap (grass) tiles and their respective mean transmissivities to inform the Sky view fraction parameter.

Table 7.2: Observations of transmissivity (spring 2008 and 2009) grouped by thresholds in the cumulative distribution according to fractional cover for the tree and grass tiles. Mean transmissivity for each idealised fractional cover informs the Sky view fraction (f_v) parameter.

	Tree Tile		Shaded gap (grass) Tile	
Transmissivity threshold	Percentage cover (%)	Mean transmissivity (%)	Percentage cover (%)	Mean transmissivity (%)
a. 63.550	10	58.177	90	79.542
b. 66.828	15	60.496	85	80.378
c. 69.102	20	62.372	80	81.141
d. 70.940	25	63.962	75	81.893
e. 78.180	50	69.236	50	85.566
f. 84.880	75	73.305	25	89.661

The shaded row in Table 7.2 shows the tree tile fractional cover of 15 % with a Sky view fraction of 60.496 % and a grass tile fractional cover of 85 %, with a Sky view fraction of 80.378 %. These values were chosen to represent the parameters for the Shaded gap tile for Abisko (Table 7.3 Sky view fraction (f_v)). Increasing the LAI of the tree tile to achieve a net area averaged LAI of 0.25 is not required as the equation for the Shaded gap tile $SW_{\downarrow}$ includes some overhead LAI, unlike the default JULES grass tile.

Leaf Area Index

The LAI parameter is the Leaf Area Index of the vegetation. In sparse deciduous forest canopies in spring this would be referred to as a Stem Area Index since there are no leaves at this time. The hemispherical photographs taken in spring 2008 and 2009 (Chapter 4 section 3.3), can be analysed as observations of LAI. The hemispherical photographs (n = 585) from the locations of pyranometers (n = 24), survey grids (n = 287, these contain 91 repeats from ABI2 (n = 42) and ABI5 (n = 49)) and survey transects (n = 274, areas of tundra are excluded) from both spring 2008 and 2009 were pooled and analysed with GLA to calculate LAI.

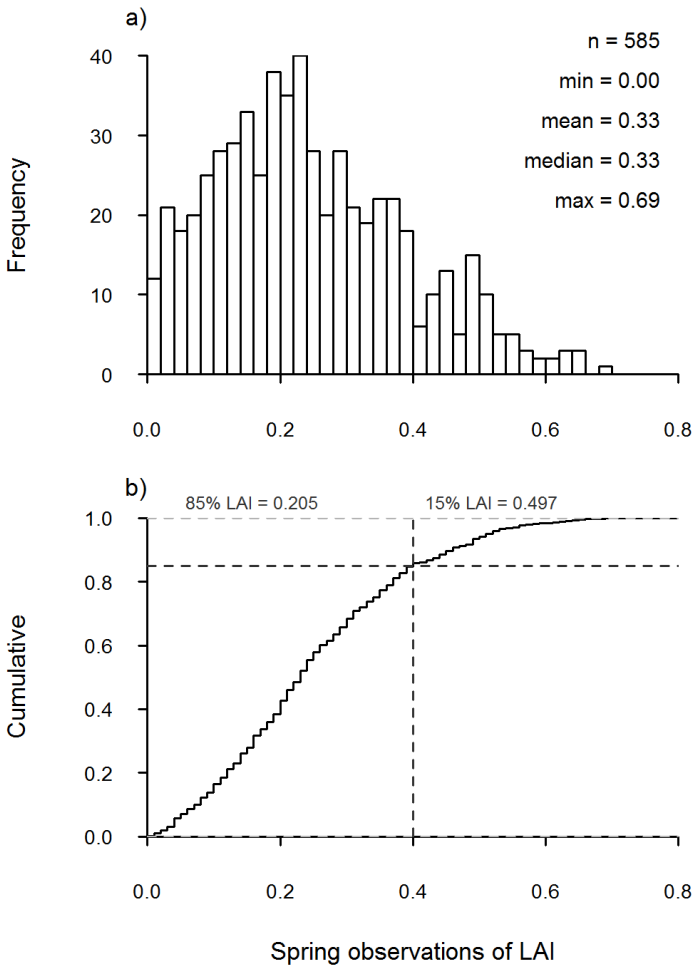

Figure 7.18: Histogram and cumulative distribution of the spring 2008 and 2009 observations of LAI. The dark grey dashed line on the cumulative curve shows the fractional cover of tree (15 %) and Shaded gap (85 %) tiles.

The mean value of all the spring observations of LAI shown in Figure 7.18 panel a was 0.25, which was used to represent the net (effective) LAI of the combined tree tile and Shaded gap tiles (Table 7.3 Area-average LAI). The lowest 85 % of the observations (n = 497) had a mean LAI of 0.205, whilst the highest 15 % (n = 88) of the data had a mean LAI of 0.497.

Assuming that as the tree tile has an LAI of 1.0 and represents 15 % of the fractional cover its area-averaged LAI is 0.15, and assuming that the new parameterisations for the Shaded gap tile are reducing the shortwave radiation penetration through the canopy to the snowpack surface of the Shaded gap, we can assume that the grass tile now has a ”canopy” with an effective LAI of 0.10.

Conceptual Shaded gap model

The new Shaded gap model was based upon an idealised version of the JULES Clumped model. It imagines that the trees of any sized area had been moved into an area covering 15 % of the tile, with the remaining 85 % of the tile area covered in grass (low level vegetation - based on the values for Abisko). The canopy of the 15 % tree covered area shades the remaining 85 % of the grass from direct shortwave radiation, according to the Sky view fraction (f_v) and sunlit fraction (f_{lit}) (Figure 7.19).

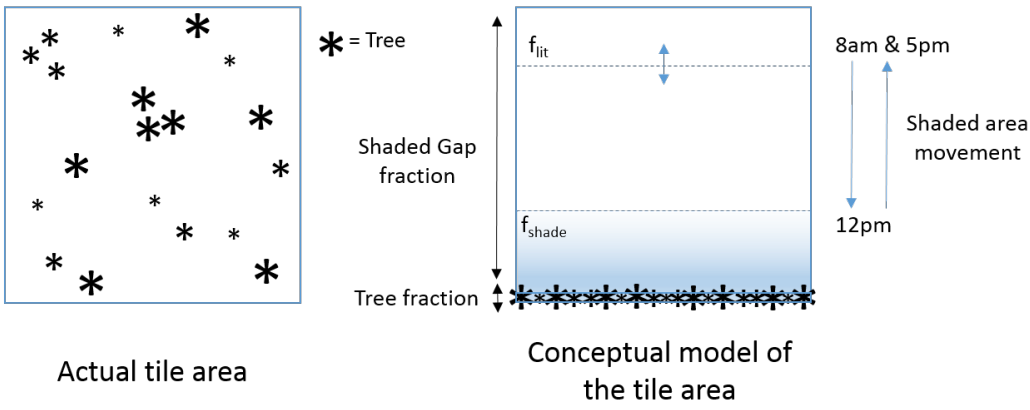

Figure 7.19: Aerial view of the actual forest and conceptual Shaded gap model.

Table 7.3 shows the parameters defined by the field observations which were used in the JULES Shaded gap model. The area averaged LAI is achieved by multiplying the LAI by the fractional cover for each tile.

Table 7.3: Actual and conceptual Shaded gap model parameters. The LAI for the Shaded gap tile is an effective LAI.

	Clumped canopy model		Conceptual Shaded gap model	
Parameter	Tree tile	Grass tile	Tree tile	Shaded gap tile
Fractional Coverage	25 %	75 %	15 %	85 %
LAI	1.00	–	1.00	**0.10
Area-average LAI	0.25		0.25 (0.15 + **0.10)	
Sky view fraction (f_v)	–	–	0.605 %	0.804 %
Shaded gap size (m)	–	–	–	40 m
Canopy height (m)	5.00	0.10	5.00	0.10

7.4.2 Results JULES Shaded gap - Shortwave radiation

The following graphs show the observed and modelled shortwave radiation for the new parameterisations of the Shaded gap tile in JULES for the sparse forest site in Abisko. The results for the Shaded gap parameterisations for 2008 are shown in Figure 7.20, early 2009 in Figure 7.21, late 2009 in Figure 7.22, and a sunny day and a cloudy day in 2008 and 2009 in Figure 7.23. For each of these four figures the black lines show the downward shortwave radiation from the driving data, the grey area shows all the observations of below canopy shortwave radiation and the red lines show the mean of the below canopy shortwave radiation measurements. The green dotted lines show the JULES Shaded gap model, and the blue dashed lines show the JULES Clumped model which uses the parameters developed in the Clumped canopy model.

Figures 7.20, 7.21, 7.22, and 7.23 show new parameterisations the JULES Shaded gap model can better reproduce the observed shortwave radiation below the sparse canopy in Abisko. The JULES Shaded gap model reproduces the diurnal pattern of very low shortwave radiation transmission in the early mornings and afternoons, and also the midday mean of the observations. This represents a substantial improvement in the representation of these forests relative to the JULES Clumped model.

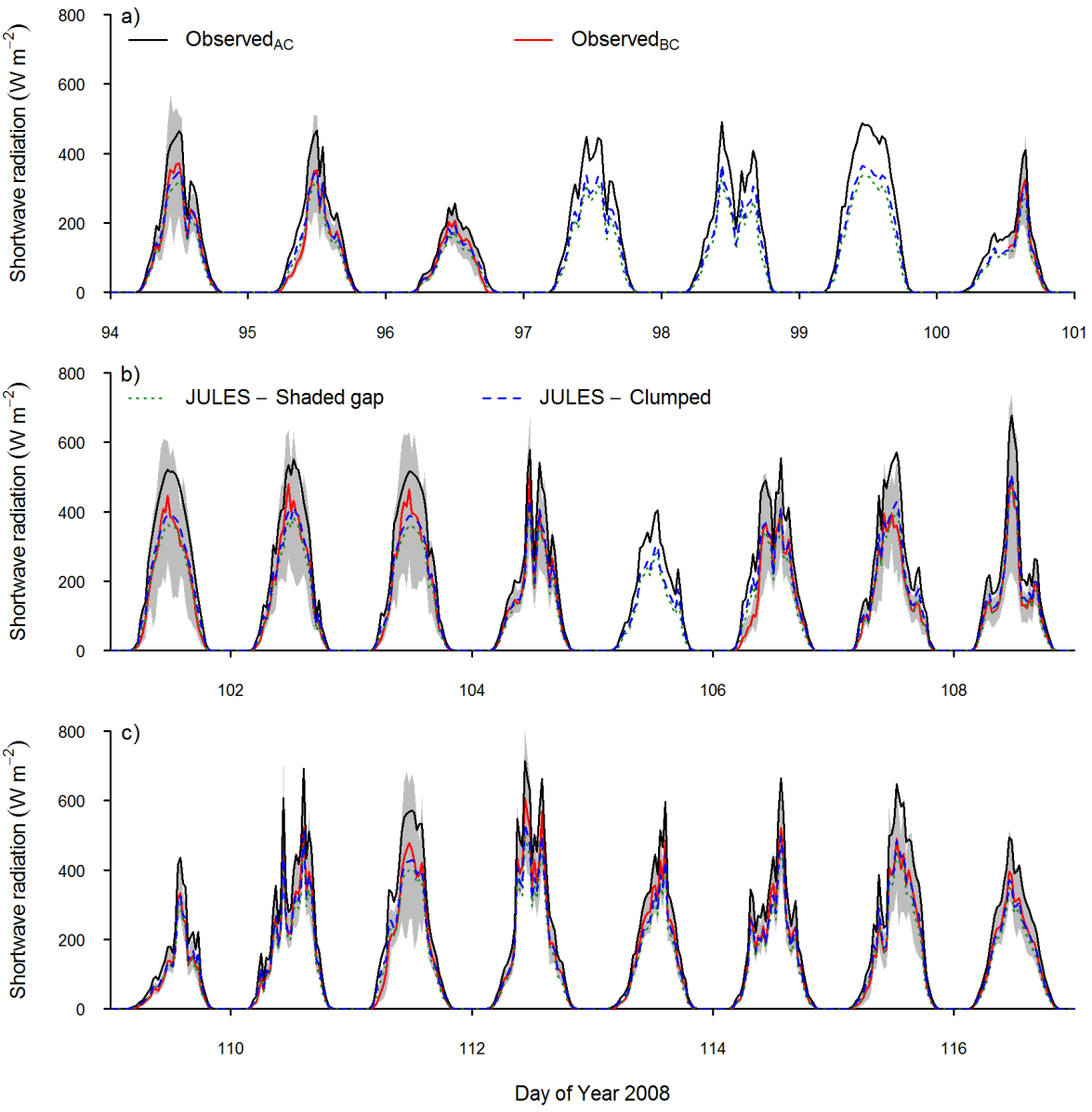

Figure 7.20: Observed and JULES modelled shortwave radiation (W m^{-2}) for day 94 (3 April) to day 116 (25 April) in 2008. The observed data comprise the observed above canopy (Observed$_{AC}$) CNR1 at the ABACUS AWS (black), the observed below canopy pyranometer data (grey) and the mean observed below canopy (Observed$_{BC}$) pyranometer data (red). The modelled data comprise JULES Shaded gap (green dotted) (JULES Tree (15 %) Shaded gap (85 %)) and JULES Clumped (blue dashed).

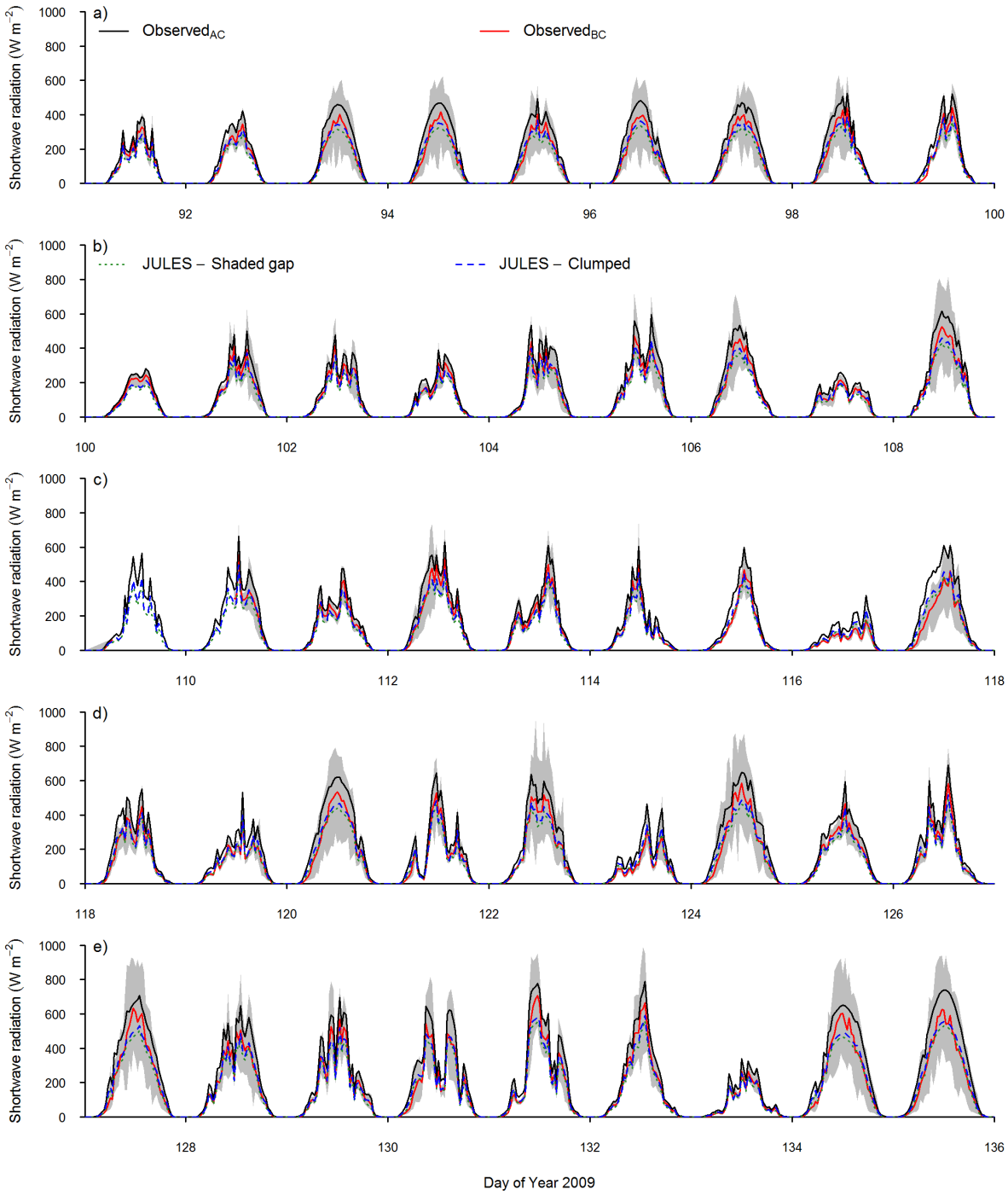

Figure 7.21: Observed and JULES modelled shortwave radiation (W m^{-2}) for day 91 (1 April) to day 135 (15 May) in 2009. The observed data comprise the observed above canopy (Observed$_{AC}$) CNR1 at the ABACUS AWS (black), the observed below canopy pyranometer data (grey) and the mean observed below canopy (Observed$_{BC}$) pyranometer data (red). The modelled data comprise JULES Shaded gap (green dotted) (JULES Tree (15 %) Shaded gap (85 %)) and JULES Clumped (blue dashed).

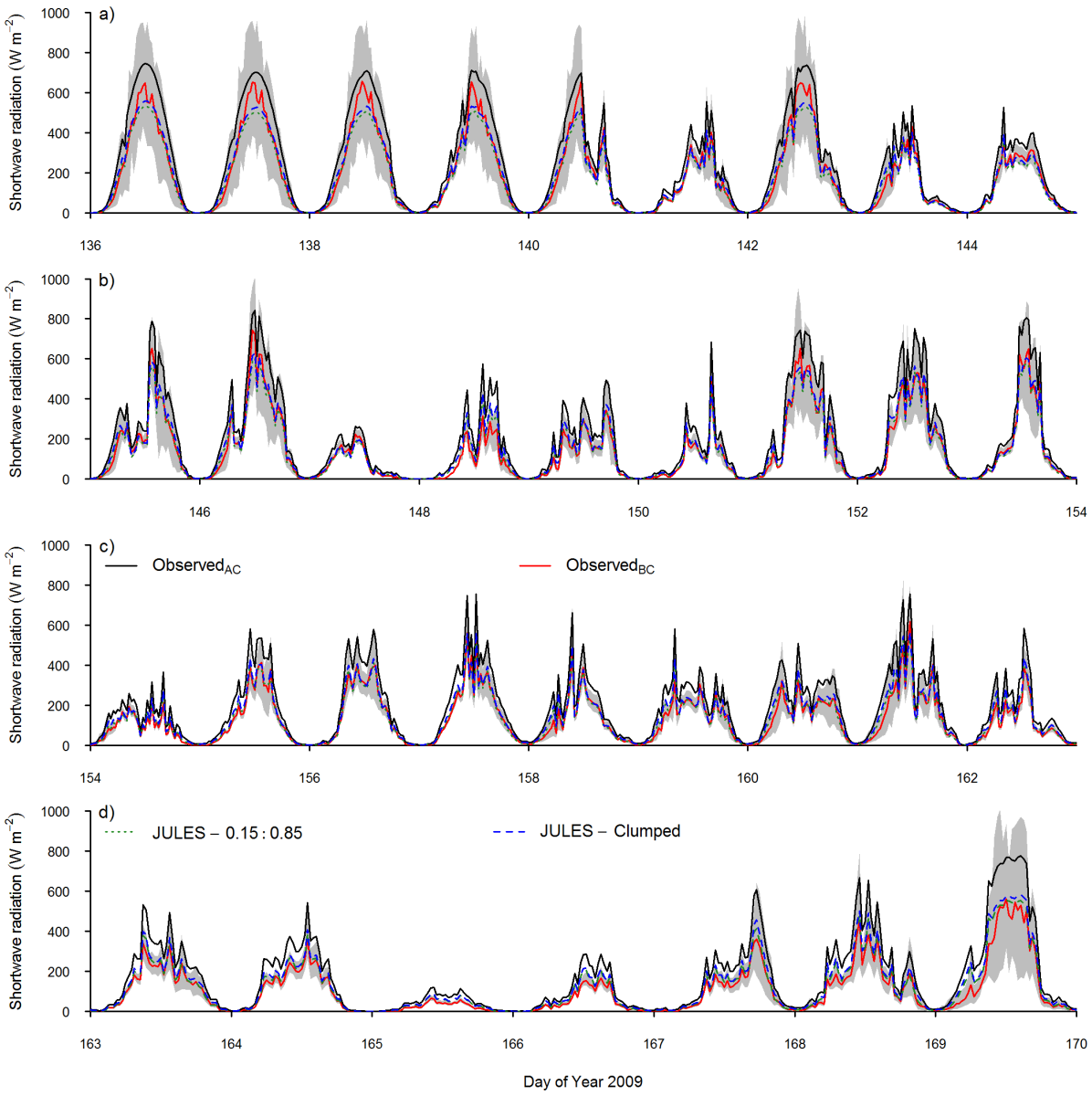

Figure 7.22: Observed and JULES modelled shortwave radiation (W m^{-2}) for day 135 (16 May) to day 169 (18 June) in 2009. The observed data comprise the observed above canopy (Observed$_{AC}$) CNR1 at the ABACUS AWS (black), the observed below canopy pyranometer data (grey) and the mean observed below canopy (Observed$_{BC}$) pyranometer data (red). The modelled data comprise JULES Shaded gap (green dotted) (JULES Tree (15 %) Shaded gap (85 %)) and JULES Clumped (blue dashed).

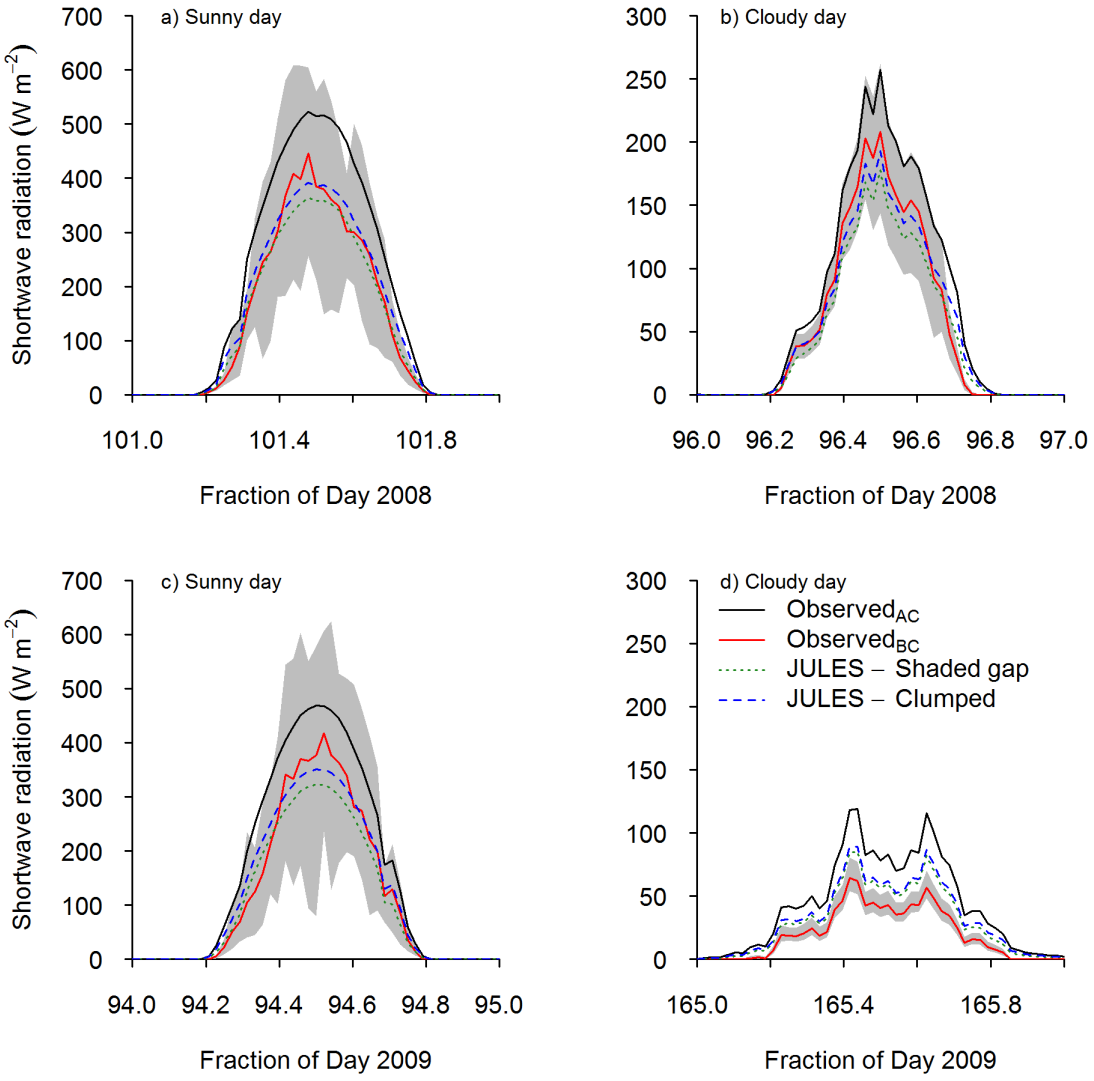

Figure 7.23: Observed and JULES modelled shortwave radiation (W m^{-2}) for a sunny day (10 April - Day 101) and a cloudy day (5 April - Day 96) in 2008 and a sunny day (4 April - Day 94) and a cloudy day (14 June - Day 165) in 2009. The observed data comprise the observed above canopy ($Observed_{AC}$) CNR1 at the ABACUS AWS (black), the observed below canopy pyranometer data (grey) and the mean observed below canopy ($Observed_{BC}$) pyranometer data (red). The modelled data comprise JULES Shaded gap (green dotted) (JULES Tree (15 %) Shaded gap (85 %)) and JULES Clumped (blue dashed).

The JULES Shaded gap model reproduces the diurnal patterns seen within the sparse forests in Abisko on both sunny and cloudy days. Figure 7.23 shows that, by introducing the f_{lit} and f_v parameters, the mean observed shortwave radiation observed under the canopy can be reproduced throughout the sunny days. This is also the case for the cloudy day 96 in 2008, as JULES Shaded gap reproduces the observed shortwave radiation observed under the canopy. JULES Shaded gap does not reasonably reproduce the observed shortwave radiation observed under the canopy on

cloudy day 165 in 2009, although it is an improvement with respect to JULES Clumped without f_{lit} and f_v. Day 165 (14 June) is in the summer and JULES Shaded gap is not running with phenology so it is likely than an LAI of 1.0 for the Tree tile is too low for this time of year. The f_{lit} parameter will also be having minimal effect at this time of year, as shown in Figure 7.16 panel b, where during Julian day 180 f_{lit} exceeds 0.6 for most of the day. The results presented in Chapter 3 also showed significant increases in the LAI and decreases in the canopy transmissivity over the summer period with respect to the spring, so it would not be expected that JULES Shaded gap would reproduce below canopy shortwave radiation during summer conditions.

Figure 7.24 shows how the f_{lit} parameter reduces the shortwave radiation penetration to the Shaded gap tile. The ratio of JULES Shaded Gap to JULES Clumped shows the fixed fraction of 0.38 for the very early and late hours of the day. When the solar zenith angle is sufficient, a proportion of the Shaded gap is illuminated and then the ratio of JULES Clumped to JULES Shaded gap modelled shortwave radiation becomes a function of the f_{lit} parameter as shown by Figure 7.16.

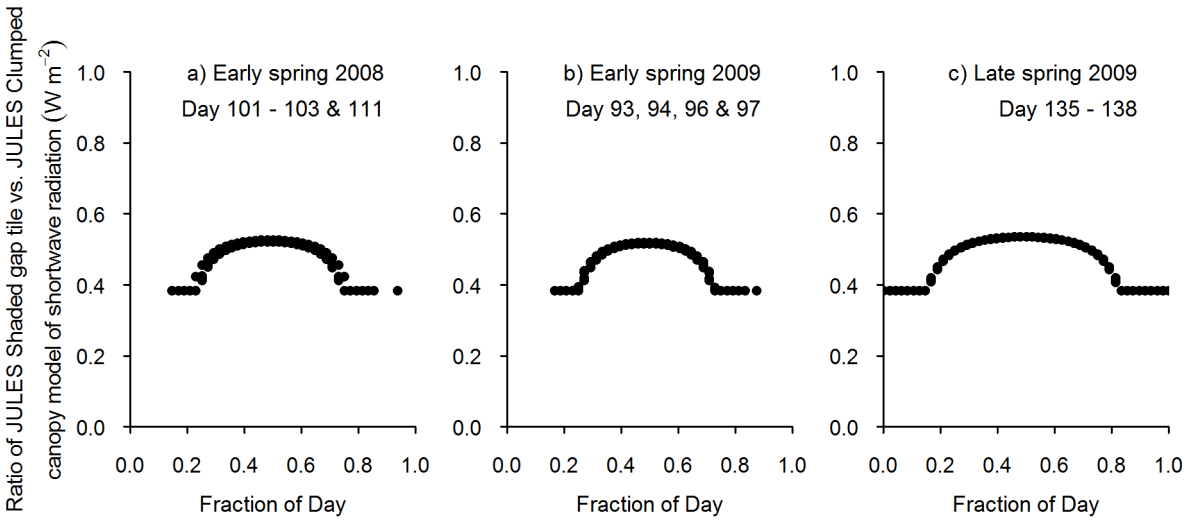

Figure 7.24: Ratio of JULES Shade Tile to JULES Clumped modelled shortwave radiation (W m^{-2}) for four sunny days in a. Early spring 2008, b. Early spring 2009 and c. Late spring 2009.

The regressions shown in Figure 7.25 between the JULES Shaded gap modelled shortwave radiation and the below canopy observed shortwave radiation show a very strong relationship.

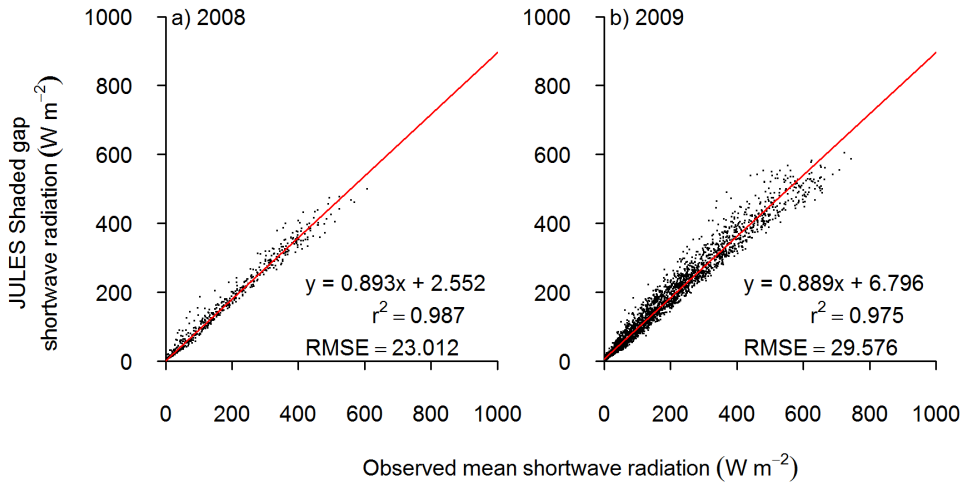

Figure 7.25: Linear regression of JULES Shaded gap modelled shortwave radiation (W m^{-2}) and observed mean shortwave radiation (W m^{-2}) for 2008 and 2009.

The regression between the JULES Shaded gap modelled shortwave radiation and the below canopy observed shortwave radiation shows a relatively small improvement with respect to the Homogeneous and Clumped canopy models (Table 7.4). For both 2008 and 2009 there is a small increase in the r^2 and decrease in the intercept. Although the RMSE was considerably better in the Clumped canopy model for both years (17.829 and 26.554) than in the Homogeneous canopy model (34.940 and 43.898), JULES Shaded Gap had slightly higher RMSE values (23.012 and 29.576) compared to the Clumped canopy model.

Table 7.4: Comparison of the regressions of the Homogeneous canopy model, Clumped canopy model, and JULES Shaded gap model and observed below canopy shortwave radiation.

		Canopy models		JULES
		Homogeneous	Clumped	Shaded gap model
Year				
2008	slope	1.130	0.960	0.893
	intercept	7.575	6.438	2.552
	r^2	0.985	0.985	0.987
	RMSE	34.940	17.829	23.012
2009	slope	1.106	0.940	0.889
	intercept	14.354	12.199	6.796
	r^2	0.973	0.973	0.975
	RMSE	43.898	26.554	29.576

Figure 7.26 shows the ratio of the JULES Shaded gap model to the below canopy observations of shortwave radiation for sunny days in early spring 2008, early spring 2009 and late spring 2009. JULES Shaded gap has a 1:1 relationship with the observations throughout the middle of the day. The relationship is weakest during the early morning and late afternoon, but JULES Shaded gap is an improvement on both the Homogeneous canopy model (Figure 7.8) and the Clumped canopy model (Figure 7.10) with longer periods of the time when the ratio is close to 1. The Shaded gap model also provides better reproduction of small measurements of shortwave radiation, in the early morning and late afternoon. JULES Shaded gap does under estimate the shortwave radiation penetration during the middle of the day, which may explain the increased RMSE with respect to the Clumped canopy model (Table 7.4).

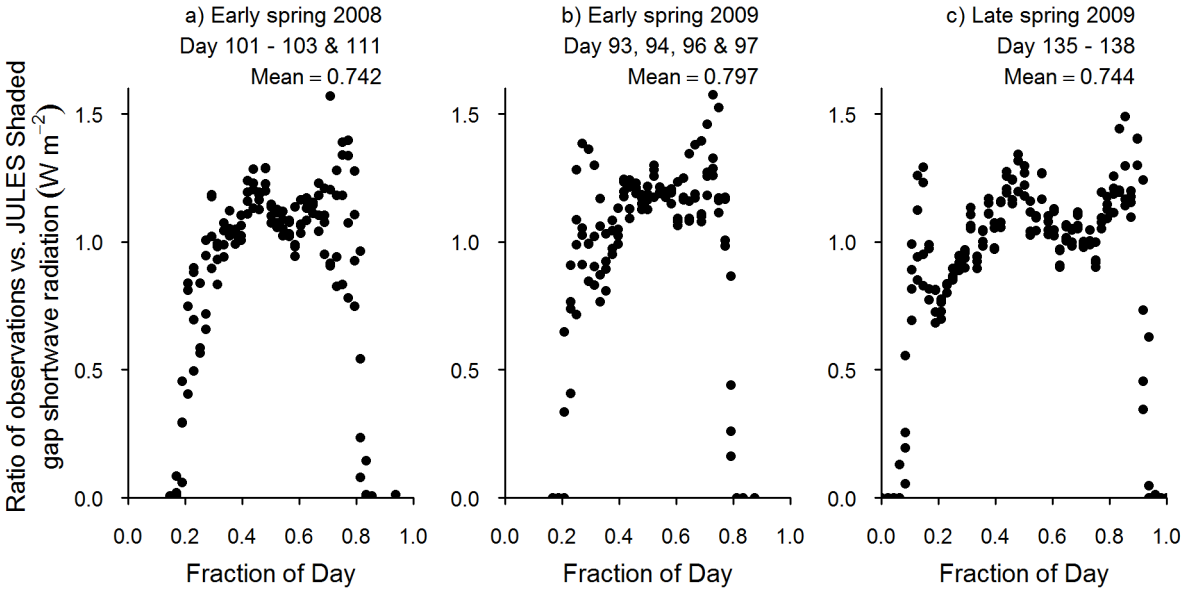

Figure 7.26: Ratio of observations to JULES Shaded gap modelled shortwave radiation (W m^{-2}) for four sunny days in a. Early spring 2008, b. Early spring 2009 and c. Late spring 2009.

The mean ratios of observed below canopy shortwave radiation to the modelled shortwave radiation show a comparatively large improvement in the JULES Shaded gap model compared to both the Homogeneous and Clumped canopy models (Table 7.5). The mean ratios increase from the Clumped canopy model to the JULES Shaded gap model from 0.494 to 0.742 in early 2008, from 0.522 to 0.797 in early spring 2009 and from 0.495 to 0.744 in late spring 2009. Although JULES Shaded gap had a higher RMSE than Clumped canopy model (Table 7.4) it produced below canopy shortwave radiation values closer to observed values during sunny spring days.

Table 7.5: Comparison of the mean ratio of observations to modelled below canopy shortwave radiation for the Homogeneous canopy model, Clumped canopy model, and JULES Shaded gap model for four sunny days in early spring 2008, early spring 2009 and late spring 2009.

		Canopy models		JULES
		Homogeneous	Clumped	Shaded gap model
Year	Days			
2008	101 to 103, & 111	0.582	0.494	0.742
2009	93, 94, 96, & 97	0.614	0.522	0.797
	135 to 138	0.583	0.495	0.744

The new parameterisations for the Shaded gap show that the shortwave radiation penetration through the canopy down to the surface of the snowpack can be accurately more reproduced using the new parameters f_{lit} and f_v.

7.4.3 Longwave radiation models

The measurements of below canopy longwave radiation show that underneath a sparse vegetation canopy there is a substantial increase in the longwave radiation with respect to the above canopy downward longwave radiation. Therefore the JULES Shaded gap model also requires modifications to the longwave radiation balance. Although JULES has longwave radiation emitted from the tree canopy to the snowpack beneath on the tree tile, what JULES Shaded gap requires is longwave radiation from the effective tree canopy to the snowpack on the Shaded gap tile.

The longwave radiation balance in sparse canopies is affected firstly by the trees which block the downward (incoming) radiation from the sky, and secondly by the incident shortwave radiation on the canopy which increases tree temperature and emits longwave radiation down to the snowpack. In the JULES Clumped model the tree tile has below canopy longwave radiation but on the grass tile all the downward longwave radiation from the sky is received. What JULES Shaded gap requires is a reduction in incoming sky longwave radiation and inclusion of the longwave radiation from the canopy to the Shaded gap acting as an effective canopy (Figure 7.14). Two solutions for the JULES Shaded Gap model below canopy longwave radiation will be presented: firstly the LW_{T_*} in the JULES Clumped model based on surface temperature and secondly the LW_{tree} in the JULES Shaded Gap model based on a new parameterisation of longwave radiation emitted from the canopy.

Longwave radiation model - JULES Clumped LW_{T_*}

As shown in Chapter 3 section 3.5 one of the simplest solutions to modelling the longwave radiation from the tree canopy to the snowpack is to use the following equation which assumes that trees emit longwave radiation according to their temperature:

$$LW_{\downarrow} = f_v LW_{\downarrow} + (1 - f_v)\varepsilon\sigma T_*^4 \tag{7.9}$$

Where $LW_{\downarrow}$ is the downward longwave radiation (W m^{-2}), ε is the Emissivity, σ is the Stefan Boltzmann constant and T_* is the tree tile surface temperature in Kelvin. As the JULES model calculates a surface temperature for the tree tile this can be used for the tree canopy temperature. This approach is used in the JULES model [*Best et al.*, 2011]. There is some debate as to whether it is the most effective way to achieve the longwave radiative component [*Webster et al.*, 2016b], especially when there is snow on the ground which is included in the value of T_* and therefore probably results in a value of longwave radiation that is too low.

7.4.4 Results JULES Clumped - Longwave radiation LW_{T*}

Figure 7.27 shows for days 103 to 116 in 2008 the longwave radiation driving data (black line), the measurements of below canopy longwave radiation (red line), and the modelled longwave radiation JULES Clumped LW_{T*} (purple line).

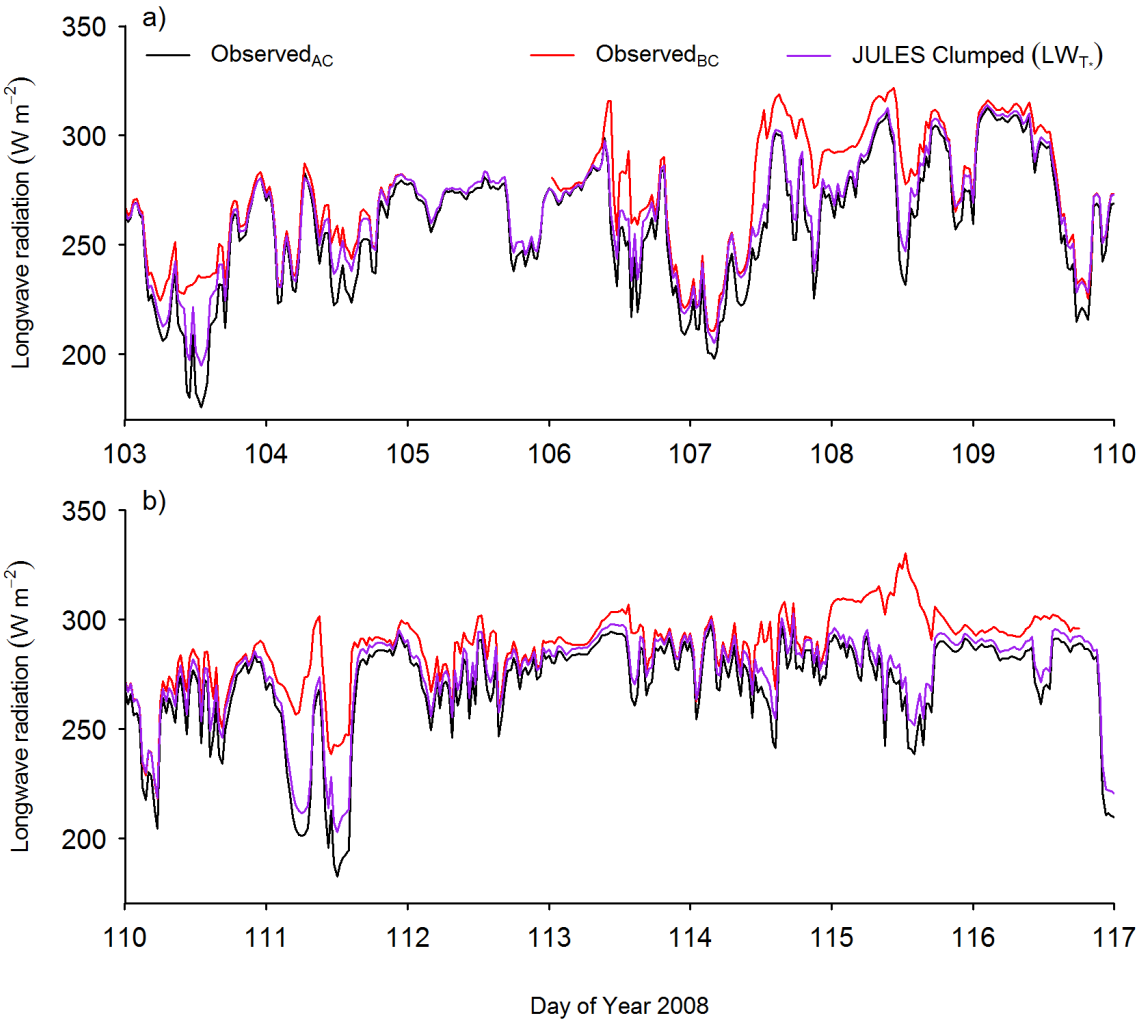

Figure 7.27: Modelled and observed below canopy longwave radiation (W m^{-2}) for day 103 (12 April) to day 116 (25 April) in 2008. The driving data is the CNR1 at the ABACUS birch tower above the canopy (black), the CGR3 is the below canopy observations (red) and the modelled longwave radiation JULES Clumped LW_{T*} (purple).

What the JULES Clumped LW_{T*} model shows is that the observations of below canopy longwave radiation can be reproduced with reasonable agreement using the tree tile surface temperature. However, the JULES Clumped LW_{T*} model does not account for the substantial fraction of observed below canopy longwave radiative energy during the middle of the day, particularly on

days 103, 107, 111, 115 and 116. The results presented in Figure 4.2 in Chapter 4 showed that these were sunny periods, dominated by shortwave radiation. The JULES Clumped LW_{T*} model performs weakest during these sunny periods and is therefore not representing the role which shortwave radiation plays in warming the tree canopy.

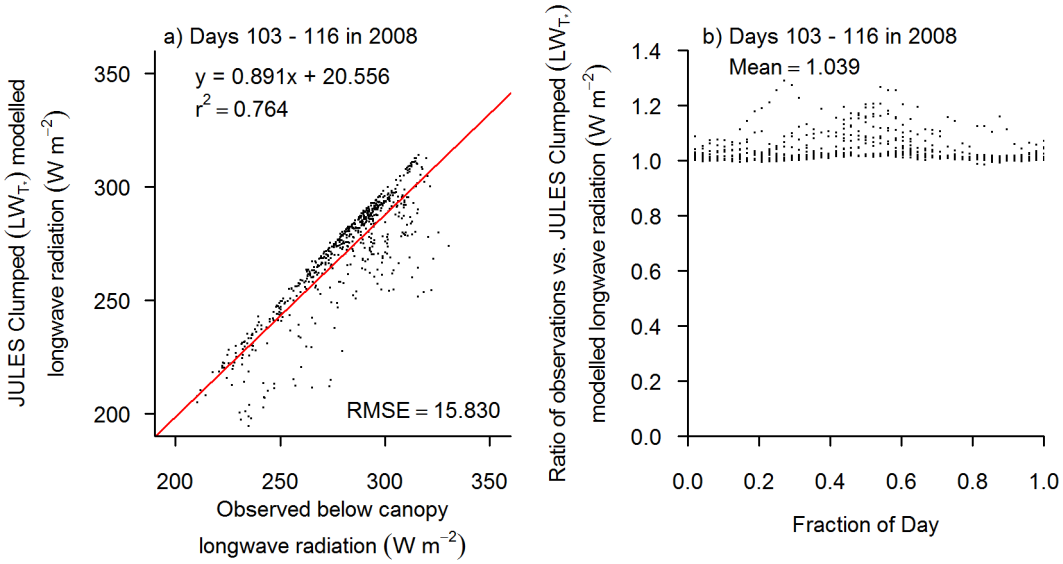

Figure 7.28: Panel a. Linear regression of JULES Clumped LW_{T*} modelled below canopy longwave radiation (W m^{-2}) and observed below canopy longwave radiation (W m^{-2}) for early spring in 2008. Panel b. Ratio of observations to JULES Clumped LW_{T*} modelled below canopy longwave radiation (W m^{-2}) for early spring in 2008.

Figure 7.28 panel a. shows the relationship between the JULES Clumped LW_{T*} modelled and observed below canopy longwave radiation, and Figure 7.28 panel b. shows the ratio of these two measurements for the measurement period day 103 to 116 in 2008. Even though there is a good 1:1 relationship between the observed and JULES Clumped LW_{T*} modelled below canopy longwave radiation, this relationship weakest during the sunniest periods on Figure 7.28, when the JULES Clumped LW_{T*} model underestimates the below canopy longwave radiation. Therefore, the JULES Clumped LW_{T*} model is not capturing the observed variability in the incident shortwave radiation warming the tree canopy. This was investigated further by comparing the tree tile surface temperature calculated by JULES (Figure 7.29) with the measured tree canopy temperatures from Chapter 3 section 3.4.

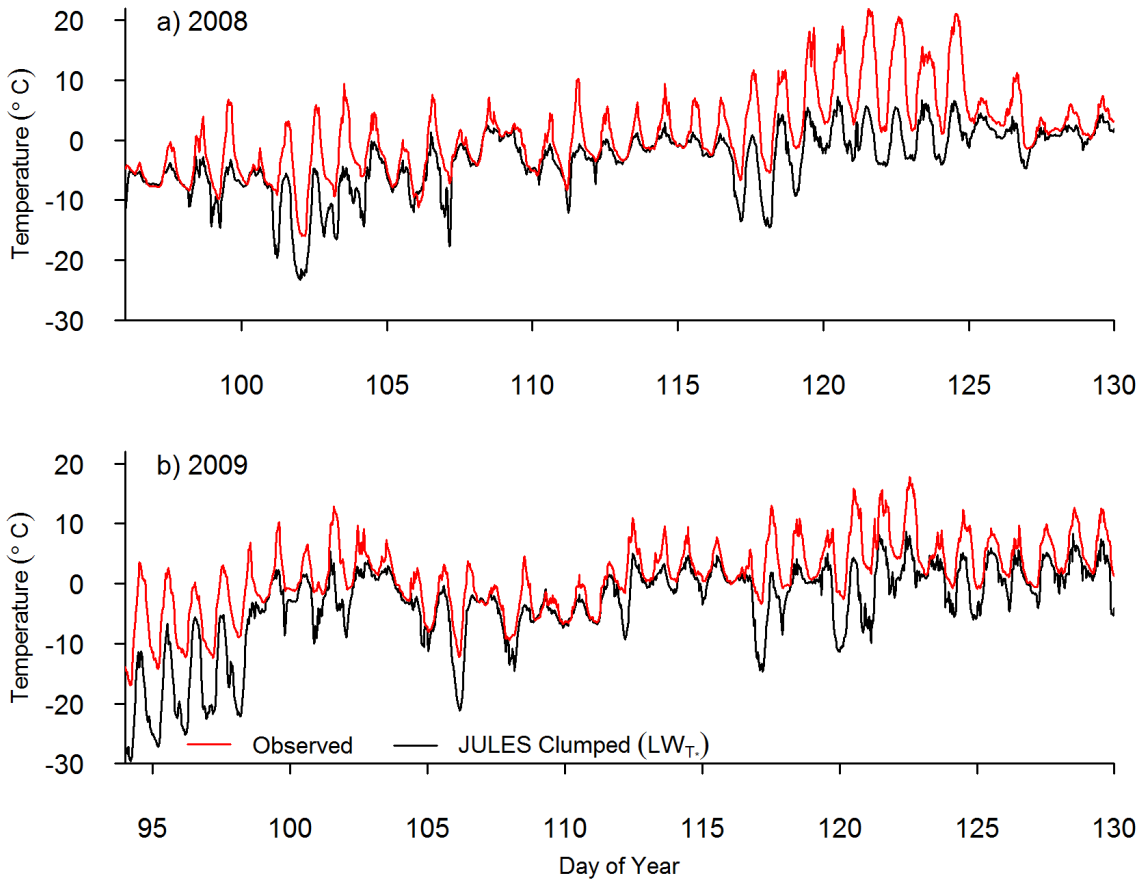

Figure 7.29: Modelled and observed tree canopy temperature for spring 2008 and 2009. The observed thermocouple canopy temperatures (red lines) and the tree tile surface temperature (LW_{T_*}) (black lines).

Figure 7.29 shows that the JULES Clumped LW_{T_*} model does not accurately reproduce the measurements of tree canopy temperature. On the sunny days, the JULES Clumped LW_{T_*} model temperatures were more than 10 °C lower than the observed mean tree temperature. Although the JULES Clumped LW_{T_*} model reproduces the diurnal variability reasonably well on days 112 to 116 in 2008 and days 109 to 111 in 2009, these days included significant periods of cloud cover or snowfall. This highlights that the JULES Clumped LW_{T_*} model is performing best during overcast conditions where shortwave radiation is low. Therefore a second solution is required which accounts for the shortwave radiation incidence on the tree canopy.

Longwave radiation model - JULES Shaded gap LW_{tree}

We decided to build a second very simple model of longwave radiation. Essentially for each time step we assume that there is no storage of energy, therefore the energy absorbed by the tree is also emitted by the tree and not held. The tree temperature measurements (see Chapter 3 section 3.4) highlighted very clearly that when the stem was no longer receiving shortwave radiation and was in shade, the branch temperature quickly fell to a few degrees above the ambient air temperature. So we can assume there is some heat held within the tree canopy, the JULES Shaded gap model will not store energy between time steps. Therefore it was assumed that the effective tree canopy above the JULES Shaded gap tile has no heat capacity and the longwave radiation from the canopy is in equilibrium over each time step.

The equation for calculating the longwave radiation contribution from the vegetation canopy (LW_{tree}) is as follows:

$$LW_{tree} = \frac{1}{2} LAI_{tree} f_v SW_{\downarrow} + LW_{\downarrow} \tag{7.10}$$

Where JULES Shaded gap LW_{tree} is the longwave radiation (W m^{-2}) from the tree canopy, LAI_{tree} is the LAI of the tree tile, f_v is the Sky view fraction, $SW_{\downarrow}$ is the downward shortwave radiation (W m^{-2}) and $LW_{\downarrow}$ is the sky downward longwave radiation (W m^{-2}). The longwave radiation from the tree canopy is a function of the total downward sky radiation and a function of the downward shortwave radiation as a function of the Sky view fraction, and half the tree tile LAI. The reason it is calculated as half the tree tile LAI is based on the tree canopy temperature measurements (see Chapter 3 section 3.4). These showed that only the side of the branch receiving the direct shortwave radiation was substantially warmer than the ambient air temperature. Therefore this fraction represents the sunlit half of the tree canopy, with any longwave radiation from the unlit side of the tree assumed to be negligible.

The equation for calculating the longwave radiation in the JULES Shaded gap tile ($LW_{\downarrow}$) (W m^{-2}) is as follows:

$$LW_{\downarrow} = f_v LW_{\downarrow} + (1 - f_v) LW_{tree} \tag{7.11}$$

This equation only allows longwave radiation from the sky to the snowpack as a function of Sky view fraction and contribution of the longwave radiation from the effective tree canopy is a function of the canopy view fraction (1 minus the Sky view fraction).

7.4.5 Results JULES Shaded gap - Longwave radiation LW_{tree}

Figure 7.30 shows for days 103 to 116 in 2008 the longwave radiation driving data (black lines), the measurements of below canopy longwave radiation (red lines), and the JULES Shaded gap tile LW_{tree} model (blue lines).

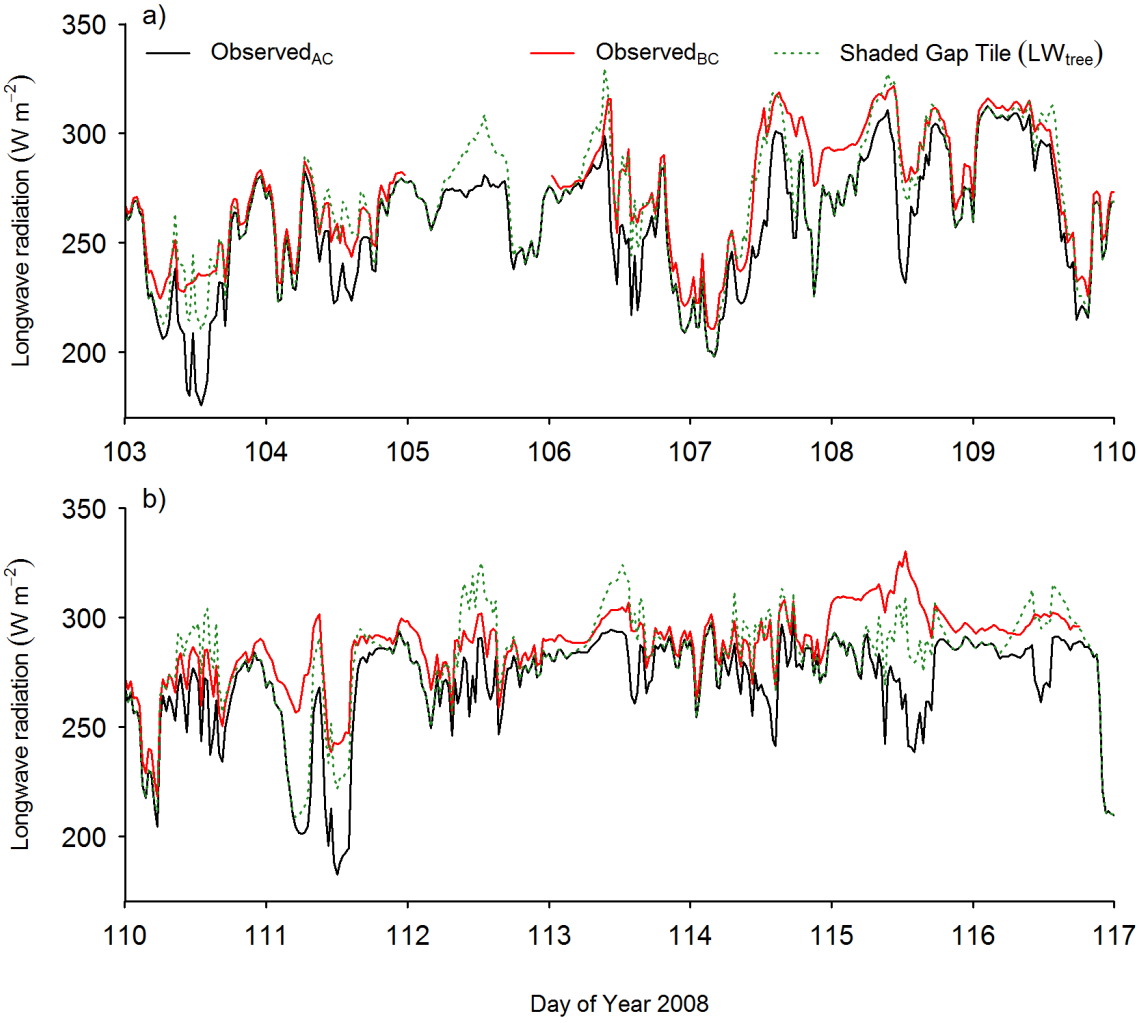

Figure 7.30: JULES Shade Tile (LW_{tree}) modelled and observed below canopy longwave radiation (W m^{-2}) for day 103 (12 April) to day 116 (25 April) in 2008. The driving data is the CNR1 at the ABACUS birch tower above the canopy (black), the CGR3 is the below canopy observations (red) and the JULES Shade Tile (blue).

The JULES Shaded gap LW_{tree} model performs very well on days 103, 104, 107, 108, 111, 114 and 115. On these days the JULES Shaded gap LW_{tree} model reproduces the below canopy observations of longwave radiation with very good agreement. Figure 4.2 in Chapter 4 showed that these were days dominated by periods of sunny conditions and therefore shortwave radiation.

The JULES Shaded gap LW_{tree} model was also much closer to the observed measurements than the JULES Clumped LW_{T_*} model during these shortwave radiation dominated periods (Figure 7.27).

The assumption of zero heat capacity in the JULES Shaded gap LW_{tree} model is not always correct. For example, on the early morning of day 111 the downward longwave radiation from the sky was comparatively low, but the below canopy measurements show that there was still a substantial longwave radiation contribution from the tree canopy, as it receives 50 W m^{-2} more than above the canopy. We can assume that as this is before the sun rises, this is longwave radiation coming from the canopy, which has been warmed during the previous day (110), and the heat has been stored for over 12 hours. Both the JULES Shaded gap LW_{tree} model and the JULES Clumped LW_{T_*} model were unable to reproduce this observed pattern in the longwave radiation in the early morning of day 111.

JULES Shaded gap was also unable to reproduce the longwave radiation observed under the canopy on day 115 for a similar reason. Even though it can match the longwave radiation contribution during the day, because the JULES Shaded gap model starts the day 25 W m^{-2} lower than is observed, the model cannot correct for this difference. However, the Shaded gap model outperformed the JULES Clumped LW_{T_*} model which could only replicate the incoming sky longwave radiation during the middle of the day and not the contribution from the canopy (Figure 7.27).

Despite the results on day 111 and 115, the simple longwave radiation model in JULES Shaded gap does reasonably well at reproducing the observed below canopy longwave radiation. Figure 7.31 shows that for both the regression and ratio, there is a stronger relationship between the observations and the JULES Shaded gap LW_{tree} model than the JULES Clumped LW_{T_*} model.

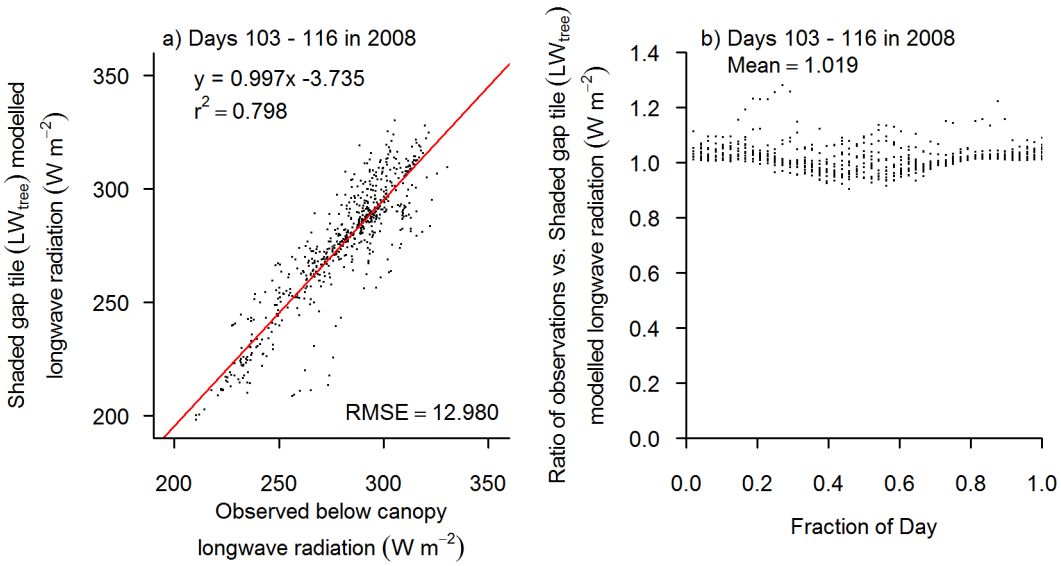

Figure 7.31: Panel a. Linear regression of JULES Shaded gap tile modelled longwave radiation (W m^{-2}) and observed below canopy longwave radiation (W m^{-2}) for early spring in 2008. Panel b. Ratio of observed below canopy longwave radiation (W m^{-2}) to JULES Shaded gap tile modelled below canopy longwave radiation (W m^{-2}) for early spring in 2008.

When the JULES Shaded gap LW_{tree} model overestimates the longwave radiation on days 112 and 113, and partially on day 116, the ratio of the relationship between the observed and modelled longwave radiation beneath the canopy drops below 1 to 0.95. Considering these are the only periods when JULES Shaded gap LW_{tree} overestimates the observed values, the JULES Shaded gap LW_{tree} model reproduces the observations with very good agreement.

Table 7.6 shows there is a stronger relationship between the JULES Shaded gap LW_{tree} model and the observations which had a higher r^2 (0.798) compared to the JULES Clumped LW_{T_*} model and the observations (r^2 = 0.764). JULES Shaded gap LW_{tree} also had a lower RMSE of 12.980 than JULES Clumped LW_{T_*} model which had an RMSE of 15.830. The slope and intercept for the regression of JULES Shaded gap LW_{tree} model against the observations were also improved (0.997 and -3.735) compared to the JULES Clumped LW_{T_*} model (0.891 and 20.556).

Table 7.6: Comparison of the regressions and ratios of the JULES Clumped LW_{T*} model, and JULES Shaded gap LW_{tree} model and observed below canopy longwave radiation for days 103 to 116 in 2008.

	Longwave radiation models	
	JULES Clumped LW_{T*}	JULES Shaded gap LW_{tree}
slope	0.891	0.997
intercept	20.556	-3.735
r^2	0.764	0.798
RMSE	15.830	12.980
Mean ratios	1.039	1.019

Verification of these parameterisations is limited by the observed data available. The only other period with measurements of the below canopy longwave radiation was in summer 2009, which represents a different canopy cover and the absence of a snowpack. Therefore the single measurement of below canopy longwave radiation for the 14 days presented here was in 2008, representing the only period when these parameterisations can be tested against observations. Despite this it is possible to compare the modelled tree temperature of the JULES Shaded gap LW_{tree} model with that of the observed tree canopy temperatures and the JULES Clumped LW_{T*} model in both 2008 and 2009 (Figure 7.32).

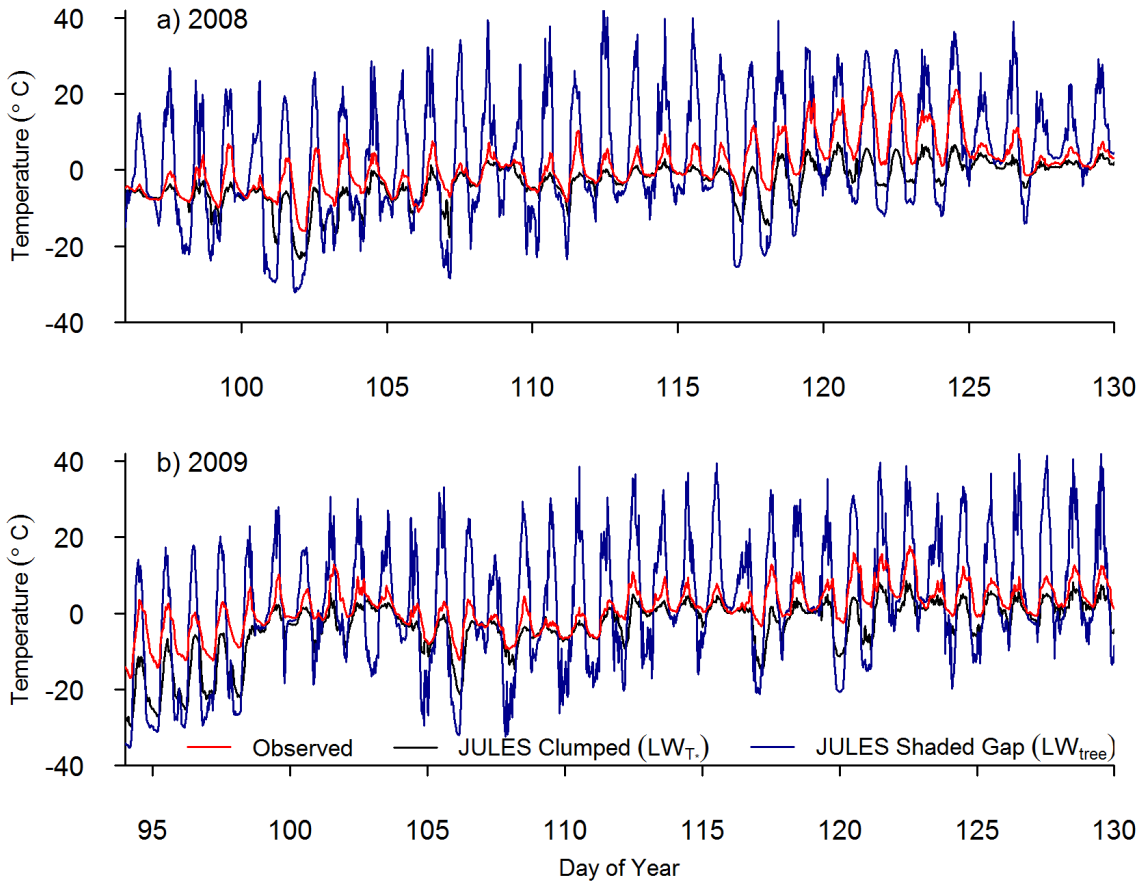

Figure 7.32: Modelled and observed tree canopy temperature for spring 2008 and 2009. The observed thermocouple canopy temperatures (red lines), the tree tile surface temperature (LW_{T*}) (black lines) and the JULES Shade Tile (LW_{tree}) tree temperature (dark blue).

Figure 7.32 shows that the modelled tree temperature of the JULES Shaded gap exceeds that of the observed tree canopy temperatures, however, unlike the tree tile surface temperature JULES Clumped LW_{T*} model, it does account for the daily variability as a result of the incoming shortwave radiation on sunny days. Although the amplitude of the modelled tree temperature exceeds that of the observations, the JULES Shaded gap LW_{tree} model reproduces the warming effect of the shortwave radiation incidence on the tree canopy which the JULES Clumped LW_{T*} model could not.

7.4.6 Results JULES Shaded gap - Snowmass

Having set up the new Shaded gap model for shortwave and longwave radiation, we ran it for the Abisko site, and diagnosed the snowmass to see if the changes in radiation would alter the snowmelt. Figure 7.33 shows the observed and modelled snowmass for both spring 2008 and 2009. The JULES BLT (a single tree tile) with an LAI of 0.25 is shown by the light grey line, JULES Clumped (a 15 % tree tile and 85 % Shaded gap tile) by the black line for a fractional cover of 25 % tree with an LAI of 1.0 and 75 % grass, and JULES Clumped by the red line for a fractional cover of 15 % tree with an LAI of 1.0 and 85 % grass.

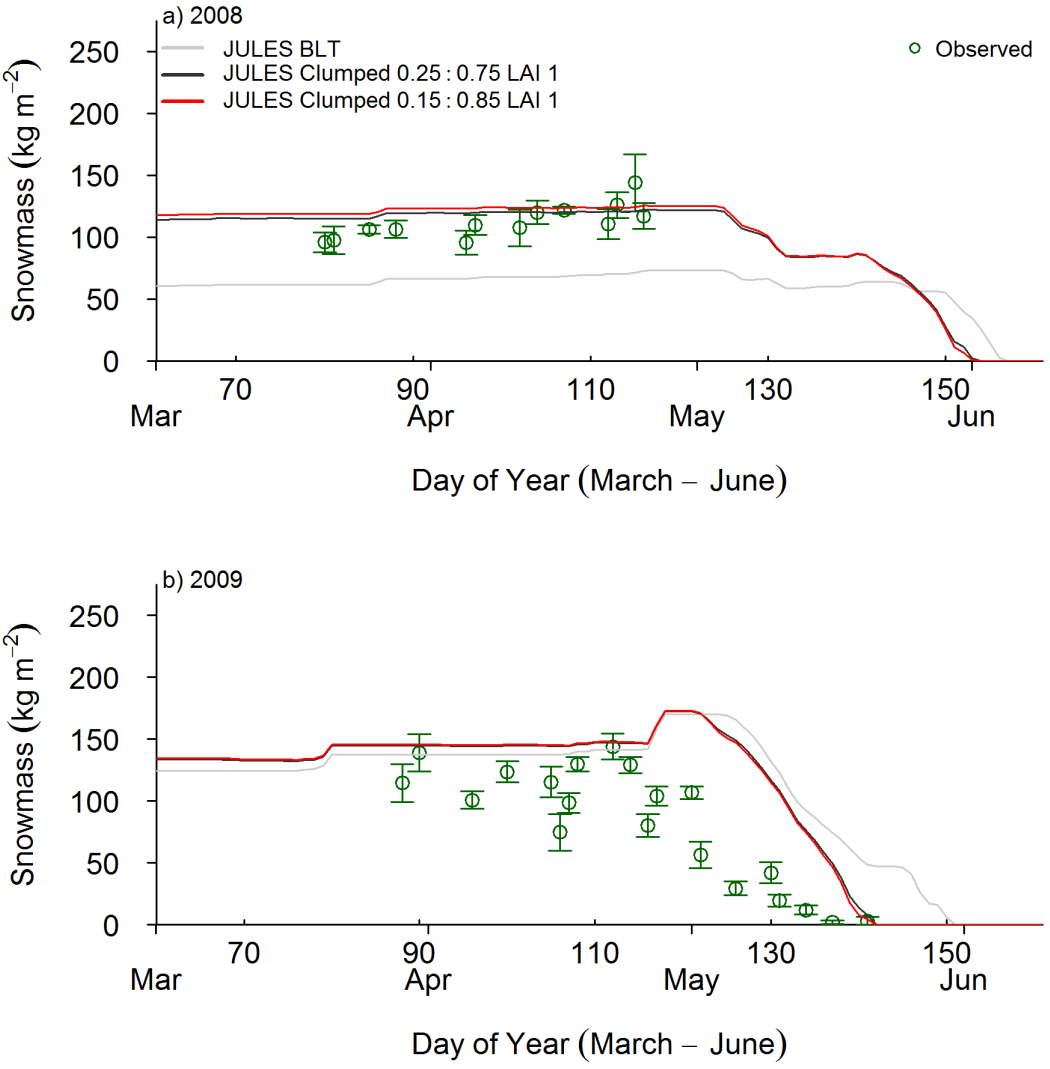

Figure 7.33: Daily mean observed and modelled snowmass for spring 2008 (a) and 2009 (b). Bars show the standard error of mean.

The JULES BLT (Broadleaf tree) shows that when a single tree tile is used to represent the sparse forests, even though there is longwave radiation from the canopy to the snowpack, the snowpack melts out later than the in-situ observations. This is most likely due to the lack of shortwave radiation transmission to the snowpack. For the winter 2007 to 2008, a winter warming event melts a substantial portion of the snowpack in JULES BLT relative to the JULES Clumped models, because this single tree tile has below canopy longwave radiation. The JULES Clumped models with 15 % and 25 % tree cover, both have snowmelt timing which is closer to the in-situ observations than JULES BLT. The only slight difference comes from the larger fractional cover of tree (25 %) having a corresponding higher longwave radiation from the canopy to the snowpack, allowing a slightly shallower snowpack to develop in winter (Black line - JULES Clumped 25 %). However, by late spring and the snowmelt period the larger area of grass in JULES Clumped 15 % has more shortwave radiation penetration than JULES Clumped 15 % and melts out slightly sooner.

Figure 7.34 shows the observed and modelled snowmass for both spring 2008 and 2009. The JULES Shaded gap modifications are shown by the yellow line for the shortwave equations only, the blue dashed line for only the longwave equations only and the green dotted line for both the shortwave and longwave equations.

Figure 7.34 shows that both the shortwave and longwave radiation modifications of the Shaded gap have a significant impact on the snowmass duration. The JULES Shaded gap shortwave only (yellow line) shaded the surface of the snow, and extends the period of snow cover substantially with respect to JULES Clumped. The JULES Shaded gap longwave only (blue dashed line), allows the longwave radiation from the tree canopy down to the surface of the snow on the Shaded gap tile, and reduces the period of snow cover substantially with respect to JULES Clumped. Of most importance is the JULES Shaded gap shortwave and longwave (green dotted line) which both shades the snow and allows longwave radiation down to the snow surface of the Shaded gap. For both years JULES Shaded gap melts the snow out two days earlier than JULES Clumped (2008: day 151 (30 May) and day 153 (1 June), 2009: day 140 (20 May) and day 142 (22 May)). Not only does JULES Shaded gap correctly model the longwave and shortwave radiation regimes but most importantly it brings the timing of the snow melt earlier which is commensurate with the observations.

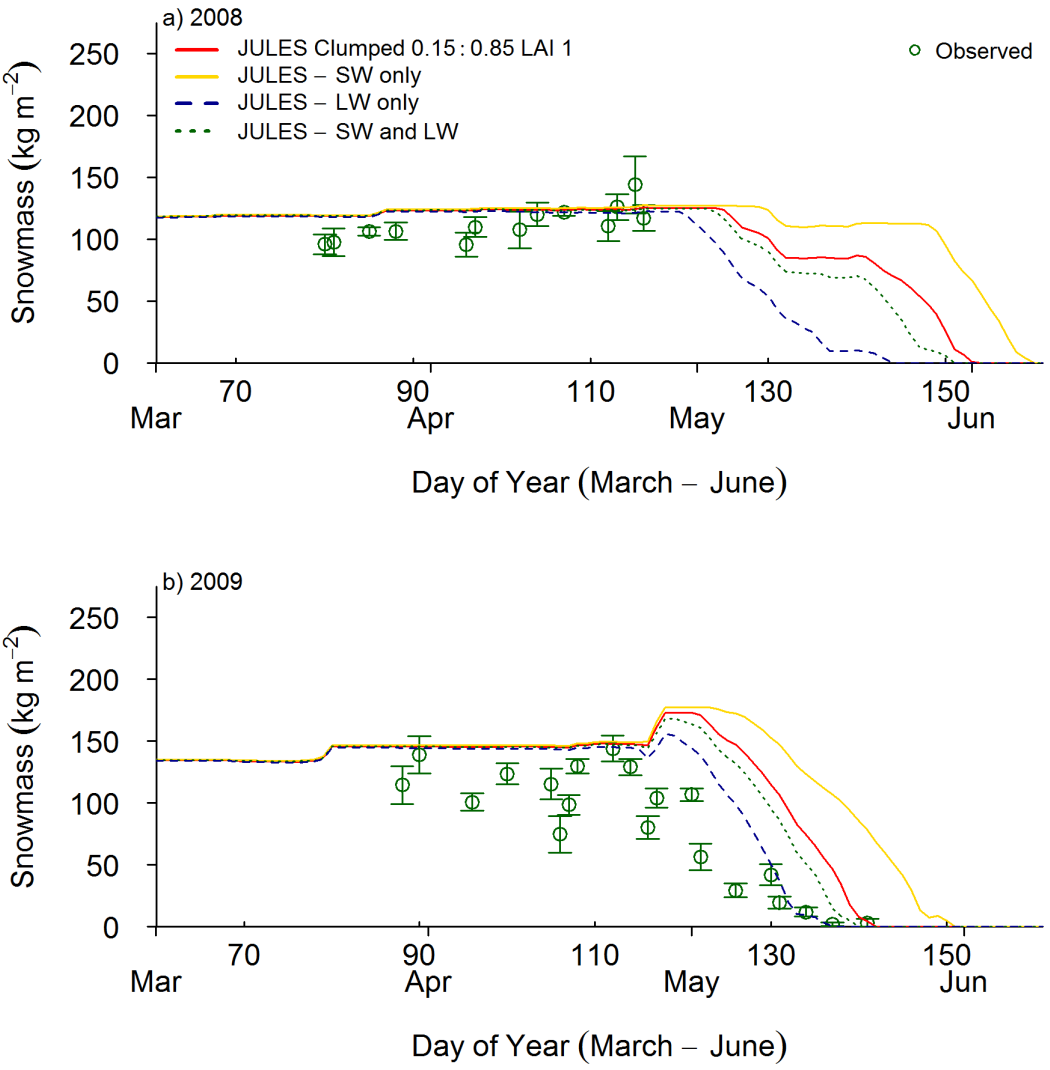

Figure 7.34: Daily mean observed and modelled snowmass for spring 2008 (a) and 2009 (b). Bars show the standard error of mean.

Figure 7.35 shows the snowmass for the tree (15 %) and grass (85 %) tile fractions for JULES Clumped (red and orange) and JULES Shaded gap (green and yellow). The JULES Shaded gap grass tile melts out earlier than the JULES Clumped grass tile by 4 days in 2008 and two days in 2009. Once the snow has melted in the Shaded gap in both years, the snowmass in the tree tile next to the Shaded gap starts to melt out earlier than the JULES Clumped tree tile, showing that once the Shaded gap is snow free, the snowmelt commences earlier in the tree tile.

Therefore JULES Shaded gap with improved representations of both the shortwave and longwave radiation balance is better able to predict the snow melt out date of sparse forests.

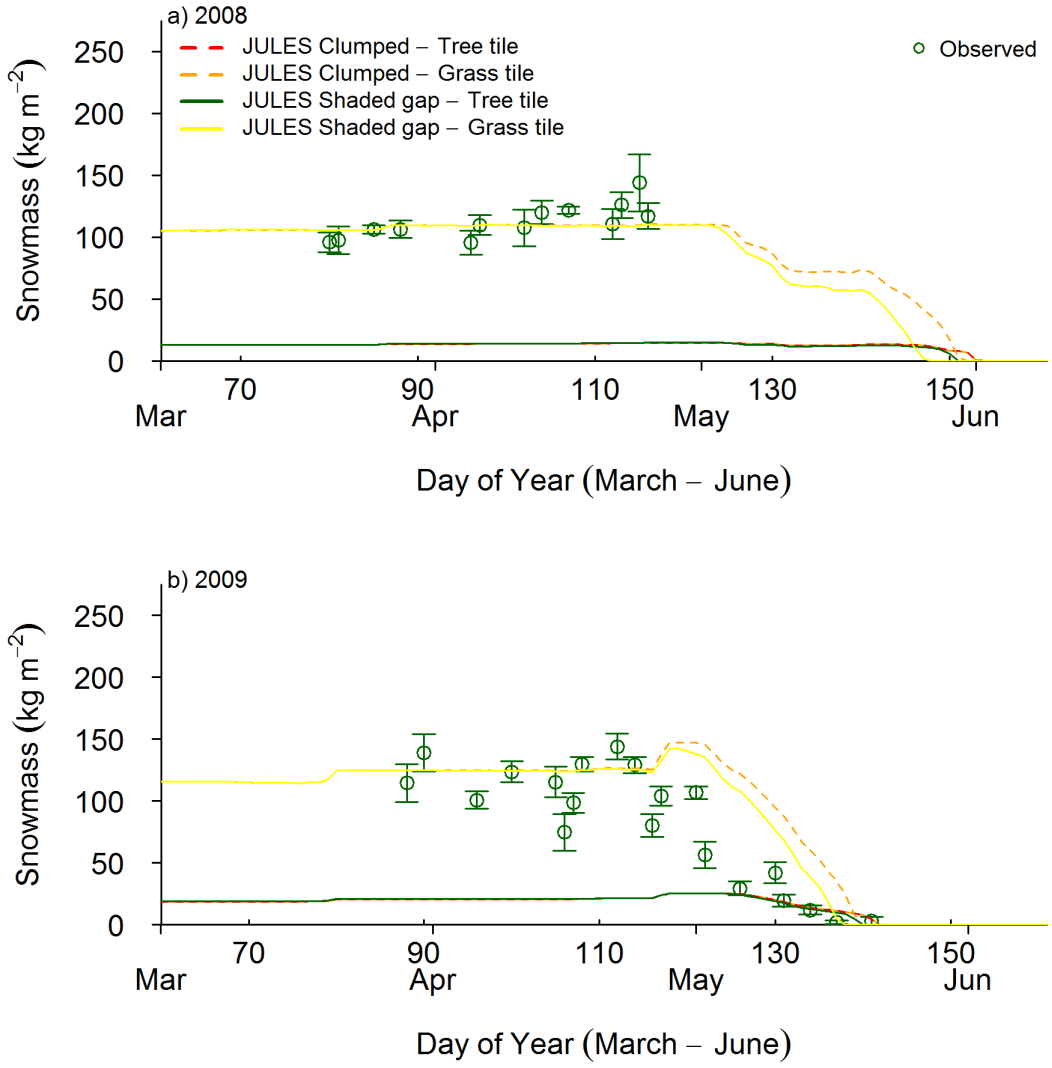

Figure 7.35: Daily mean observed and modelled snowmass for spring 2008 (a) and 2009 (b) for tree and grass tiles with JULES Clumped and JULES Shaded gap. Bars show the standard error of mean.

7.5 Discussion

There is a wealth of literature on the modelling of shortwave radiation transmission through canopies to seasonal snowpacks in snow and canopy radiation models for coniferous forests [*Ni et al.*, 1997; *Nijssen and Lettenmaier*, 1999; *Pearson et al.*, 1999; *Hardy et al.*, 2004; *Pinty et al.*, 2004; *Tribbeck et al.*, 2006; *Pomeroy et al.*, 2008; *Essery et al.*, 2008a, b; *Gouttevin et al.*, 2015], but comparatively few studies have considered sparse deciduous forests [*Link et al.*, 2004; *Lawler and Link*, 2011; *Flerchinger et al.*, 2012]. Even though the representation of these processes is a serious shortcoming of terrestrial and climate modelling [*Kattsov and Källén*, 2005; *Chapin, F. S. III et al.*, 2008; *Weller*, 2000], few studies have implemented these canopy radiation schemes into land surface models because they are computationally expensive [*Ni-Meister and Gao*, 2011] and land surface models require a simple solution.

7.5.1 Canopy models

The Homogeneous and Clumped canopy models were used to evaluate the options for representing the sparse forest canopy in a land surface model. The Homogeneous canopy model used a single tree tile and Beer's law to calculate light transmission through the canopy, which was found to underestimate the shortwave radiation penetration through the canopy on sunny days. The Clumped canopy model has two distinct tiles: a tree tile which has no transmission of shortwave radiation and is permanently in shade, and a grass tile which receives all the incoming shortwave radiation.

When comparing the relationship between the canopy models and observations, the Clumped canopy model had a lower RMSE than the Homogeneous canopy model. However, on sunny days the ratio of observations to modelled below canopy shortwave radiation was marginally better in the Homogeneous canopy model than in the Clumped canopy model. Both canopy models were particularly poor in early morning and late afternoon, as they overestimated the shortwave radiation penetration through the canopy, as they do not account for solar elevation.

The two canopy models could not represent the radiation balance of these sparse forests as they assumed canopy uniformity and no daily or seasonal variability in below canopy shortwave radiation penetration. Therefore the canopy models identified the need for a shaded gap in JULES which varies with time and season, and which accounts for low solar elevation.

7.5.2 Shortwave radiation

JULES Shaded gap was developed to incorporate several new parameters: Lit fraction (f_{lit}), Gap size (Gap_s), Sky view fraction (f_v), and canopy longwave radiation (LW_{tree}), all of which were informed by field measurements taken in 2008 and 2009.

The JULES Shaded gap model reproduces the observed mean of below canopy shortwave radiation measured by the pyranometers, as there is a strong relationship between the model and observed below canopy shortwave radiation. There is also a good ratio of observations to modelled below canopy shortwave radiation on sunny days. Therefore, the JULES Shaded gap tile is a good representation of the shortwave radiation penetration through the sparse birch canopy in Abisko. The ability of the JULES Shaded gap model to reproduce the observations is more pronounced on sunny days because, unlike the Clumped canopy model, JULES Shaded gap accounts for diurnal variability in the solar elevation.

The JULES Shaded gap model reproduced the observed shortwave radiation penetration in both sunny and cloudy conditions. Considering JULES is forced with a fixed fraction of diffuse and direct radiation, rather than separate measurements, the Shaded gap model performs well. The model could be improved for cloudy days with a higher ratio of diffuse to direct radiation, but this would compromise the model performance on sunny days. Despite this, the JULES Shaded gap model reproduces the cloudy day observations better than the JULES Clumped model.

The model relationship with the spring observations is strong, as the parameters have been informed by the fieldwork measurements taken in spring 2008 and 2009. The model fit to the summer observations in 2009 is weaker, but this study was focused on modelling the spring seasonally snow covered period pre-leaf out. The parameters used in JULES Shaded gap were informed by the fieldwork measurement campaigns which makes applying these parameterisations to other sparse canopies relatively easy, as it requires only a few specific measurements of Sky view fraction, Gap size, LAI, tree height and fractional cover which can be obtained with an array of pyranometers and hemispherical photographs.

7.5.3 Longwave radiation

The modelling of longwave radiation is as important as shortwave radiation [*Woo and Giesbrecht*, 2000; *Pomeroy et al.*, 2009] as it may contribute as much energy as shortwave radiation on cloudy days [*Sicart et al.*, 2006]. Studies have found that incorporating longwave radiation regimes improves the timing of the snowmelt, surface run-off [*Link and Marks*, 1999; *Fassnacht et al.*,

2001; *Pomeroy et al.*, 2009; *Rutter et al.*, 2009].

Incident shortwave radiation on the tree canopy warms the tree to temperatures above that of the ambient air temperature and then emits longwave radiation [*Pomeroy et al.*, 2006; *Webster et al.*, 2016b]. Since we measured canopy temperatures above that of ambient air temperature and longwave radiation higher below, than above the canopy, we can be confident that this process is observed in the sparse forests at Abisko. It is precisely this process which is included in the JULES Shaded gap LW_{tree} model. JULES does not have a canopy temperature to drive the longwave radiation emitted from the canopy to the snow surface. Instead it uses the tile temperature used in JULES Clumped LW_{T_*}, which is known to underestimate below canopy longwave radiation [*Webster et al.*, 2016b]. Despite this, observations of the Sky view fraction (f_v) parameter (hemispherical photographs) and incidence shortwave radiation to the surface (pyranometers) can be used to infer the longwave radiation emitted from the tree canopy in JULES Shaded gap LW_{tree}.

JULES Clumped neglects the below canopy contribution of longwave radiation from the tree tile to the energy balance of the grass tile. It is therefore important that JULES Shaded gap should include some parameterisations for the longwave radiation from the "effective" canopy to the snowpack of the Shaded gap. The parameterisations presented here for LW_{tree} show a reasonable correlation with the observed below canopy longwave radiation. However, it is difficult to rigorously test these parameterisations because of the lack of observed data. Despite this there is a significant period when the JULES Shaded gap model reproduces the observations with good accuracy and with the same diurnal pattern. It is worth noting that this solution is limited because it assumes with every time-step that the longwave radiation and shortwave radiation which warms up the tree canopy is radiated to the snowpack, and there is no conservation of this energy between time steps. However, the observations of tree temperature and below canopy longwave radiation show that there can be substantial longwave radiation received from the canopy overnight which must be retained as heat stored within the canopy. Despite this limitation the JULES Shaded gap model reproduces the variability of longwave radiation below the canopy.

7.5.4 Snowmelt

The energy balance of sparse forests can be improved significantly by using the JULES Shaded gap model parameterisations within land surface schemes. This study has shown how detailed measurements of the forest characteristics can be used to parameterise the vegetation canopy, shortwave and longwave radiation budgets, which allows the model to reproduce observations with good accuracy. This is of particular importance to the timing of the snowmelt and the release of water, but also for the carbon and water balance within land surface models.

Discussion

8.1 Introduction

The purpose of this thesis was to improve the representation of the radiation balance of sparse forests with a seasonal snowpack in the land surface model JULES. The current parameterisation of these sparse forests in the land surface model is basic and does not adequately represent the shortwave and longwave radiation transmission through the canopy to the snow on the forest floor. What was not clear at the start of this thesis was which component of the radiation balance was crucial to modelling these sparse forests correctly. The hypothesis is that these radiation transmissions may alter the timing of the snowmelt.

To address this hypothesis a comprehensive set of observations were carried out, designed to quantify the radiation exchanges, measure the canopy properties and determine the timing of the snowmelt. These field observations were then used to parameterise and develop a new scheme for the radiation balance of sparse forests in JULES. This chapter will discuss the steps taken to develop and test this new sparse forest scheme, and the implications of this scheme at the pan-Arctic scale.

8.2 Idealised models

In order to develop a new representation of sparse forests in JULES, we explored some simple canopy models.

One option is a very thin but continuous sparse canopy. This allows the shortwave radiation down to the surface of the snow, but it is independent of any spatial variability in the canopy cover and diurnal and seasonal changes in solar position. It does this by just using a very low value of LAI

(0.25), and was therefore called the Homogeneous canopy model in this thesis. From the field observations, it was clear that this model was not suitable as the canopy was not uniform, but highly heterogeneous, and the canopy cover could alternatively be considered as falling into two categories: denser and very sparse.

The second option developed in this thesis was to represent the sparse forest with two tiles; a clumped sparse forest and an open tundra known as the "Clumped canopy model". The Clumped canopy model does not allow any shortwave radiation transmission through the tree canopy down to the surface of the snowpack, and allows all of the shortwave radiation down to the surface of the snow on a grass tile. This second option relies upon parameterising two tiles in JULES, a clumped sparse forest and an area of open tundra.

Both of these canopy models overestimate the shortwave radiation penetration down to the snowpack during the early morning and late afternoon. The Clumped canopy model does not include any longwave radiation transmission from the tree canopy to the snow surface on the grass tile.

The third more complex but idealised model was designed in this thesis to capture the 3 dimensional nature of the sparse forests. This third idealised model known as JULES Shaded gap, represents the sparse forest with two tiles; a clumped sparse forest and an open tundra, as in the Clumped canopy model. However, in JULES Shaded gap, several new parameters were developed to better represent the shortwave and longwave radiation budget of these sparse forests. The new parameters were Gap size (Gap_s), Sky view fraction (f_v), Lit fraction (f_{lit}), and canopy longwave radiation (LW_{tree}), which were defined as follows:

- Gap size (Gap_s) - A fixed parameter which represents the diameter of the area (m) within the sparse forests which is shaded or lit, known as the Shaded gap.

- Sky view fraction (f_v) - A fixed parameter for the fraction of sky which is viewed from the snow surface. Defined by the canopy transmissivity f_v acts as an effective canopy cutting out the radiation to the snow surface for the Shaded gap tile.

- Lit fraction (f_{lit}) - A variable parameter which determines the fraction of the Shaded gap which is either shaded or lit. This parameter accounts for the diurnal and seasonal variability in solar position, and height of the tree tile canopy and Gap size (Gap_s). It effectively casts shadows across the snow surface by cutting out radiation.

- Canopy longwave radiation (LW_{tree}) - This parameter depends upon the incoming shortwave and longwave radiation as a function of Sky view fraction and LAI of the tree canopy. It radiates longwave radiation from the warmed tree canopy down to the snowpack.

8.3 Design of the field campaign

These simple idealised models need to be parameterised and tested using in-situ data. To distinguish between and parameterise the simple idealised models, we need the following:

1. Continuous measurements of shortwave radiation at a range of locations beneath the canopy to quantify the spatial and temporal variability in canopy transmissivity.
2. Detailed canopy measurements such as hemispherical photographs at multiple scales, to quantify how canopy density and transmissivity vary over large spatial scales.
3. Continuous measurements of longwave radiation beneath the canopy, to quantify its effect on the radiation balance and the snowpack.
4. Measurements of snow properties prior to and during the snow melt period, to determine the effect of the radiative fluxes on the snowpack.
5. Continuous measurements of meteorological variables to drive the model with site specific data.

8.4 Summary of field site observations for model development

The fieldwork measurement strategy for spring 2008 and 2009 set out to; define the canopy characteristics; quantify the shortwave radiation transmission through the canopy; quantify the longwave radiation transmission through the canopy; measure the snowpack properties and gather meteorological data to drive the model.

In order to assess the spatial variability in shortwave radiation transmission through the sparse canopy a set of 12 pyranometers were distributed around an area of forest approximately 30 m^2, in a range of canopy covers. These measurements were crucial for evaluating the new model parameterisations.

The land surface model requires two separate direct and diffuse incoming shortwave radiation measurements. Measurements of the diffuse and direct fraction of radiation were taken, however problems with the sensor severely restricted the periods when these measurements were available. Although it was not possible to run the model using separate diffuse and direct fractions, a constant value can be used to determine what fraction of total incoming shortwave radiation is diffuse. Therefore, the fraction of direct and diffuse shortwave radiation measurements were used to inform the model parameter for diffuse radiation. For the periods when direct and diffuse radiation measurements were available analysis showed that the fraction of diffuse radiation is very high for Abisko.

Measurements of above canopy longwave radiation were taken alongside measurements of below canopy incoming longwave radiation, although these were not continuous. These were useful in determining how the canopy cuts out incoming longwave radiation and also contributes additional longwave radiation as these dark trees are warmed up by the sun. It was not possible to study the spatial variability as only one sensor was available. Although there is only one measurement, it does give a strong indication that the longwave radiation from the canopy plays an important role in the overall radiation balance of the snowpack.

The tree canopy temperatures were measured using an array of thermocouples. The tree temperatures indicate that the shortwave radiation warmed the branches of the trees to temperatures much higher than the ambient air temperature. These were crucial in developing a simple model of the longwave radiation contribution from the canopy within the land surface model.

Measurements of the sparse forest LAI were calculated using Gap Light Analyzer (GLA) on hemispherical photographs since it was not possible to distribute pyranometers across large areas of the forest. Hemispherical photos have also been used extensively in other studies to quantify the forest structure [*Essery et al.*, 2008b; *Hardy et al.*, 2004] and have been shown to provide useful estimates of the canopy transmissivity or Sky view fraction. These photographs were analysed to give estimates of the LAI and canopy transmissivity for the survey grids and transects. In turn these photographs were analysed for spring mean LAI and transmissivity for the sparse forest, and their spatial variability. These values are important to understand that the canopy variability has been appropriately sampled and therefore justify the application of average values as model parameters.

8.5 Model development

The fieldwork data sets were then used to define and parameterise the model. The main difficulty here was incorporating the spatial and temporal variability from the field measurements into a 2 dimensional model of these ecosystems. The measurement plan of the radiation balance was designed to sample the spatial and temporal variability. However, the natural continuum of the observed parameters that exist in these sparse forests had to be rationalised. The land surface model requires a simple interpretation of the radiation balance, which can be applied globally where site specific field measurements may not be available. Therefore, the primary concern was developing a model which encompassed the 3 dimensional variability that is observed in the environment into a 2 dimensional idealised model. It should be noted that this is a conceptual model and so the in-situ observations inform the "concept", and do not need to be exact or accurate.

Each of the parameters Gap size (Gap_s), Sky view fraction (f_v), Lit fraction (f_{lit}), and canopy longwave radiation (LW_{tree}) were informed by the field observational data sets, as described below.

Sky view fraction (f_v)

The hemispherical photos were used to parameterise the Sky view fraction f_v. The hemispherical photos taken in spring had an average transmissivity of 77.39 % for the sparse birch forest in Abisko. These were separated into areas of open forest which had a transmissivity of 60.50 % and areas of Shaded gap which had a transmissivity of 80.38 %. These were then used to parameterise the canopy Sky view fraction for the tree tile and the new Shaded gap tile.

Lit fraction (f_{lit})

The need for a lit fraction was based on visual observations at the field site and a comparison from the idealised model and the observations of below canopy shortwave radiation transmission. They indicated that the model was vastly overestimating the early morning and late afternoon radiation transmission through the canopy. In reality the low solar angles meant that shortwave radiation did not penetrate through the canopy to the snow surface, and in all but the brightest sunny days, it was only the diffuse fraction which was measured in the mornings and afternoons. Therefore a new parameter was required based on the canopy height which accounted for this 3 dimensional canopy casting shadows over the snow surface, but as a function of the solar zenith angle. The lit fraction allowed incorporation of the 3 dimensional variability observed into a simple 2 dimensional model.

Gap size (Gap_s)

The Shaded gap size was required for JULES to calculate the shaded and lit fraction of the Shaded gap. This parameter is difficult to define precisely as the low solar angles and short trees create long shadows across the snow surface. If the Shaded gap size was too small the ground would almost always be shaded but if the gap size was too large the ground would receive too much shortwave radiation. On average the canopy height was 5 m, although taller in places and shorter in others. The Shaded gap was defined as 40 m, which for 68°32N creates sufficient shadows to entirely shade the gap in very early spring, allows sufficient daily variability in mid spring and then only a small effect in the early mornings by mid-summer. Based on the conceptual model 40 m was a good size as it allows for areas of sparse and dense canopy cover. A much smaller Shaded gap size would have not represented the heterogeneity observed in the canopy cover. As the f_{lit} parameter is a function of both tree height and Shaded gap size, these allow the shaded gap tile to be adjusted to other sparse forests.

LAI

The hemispherical photos were used to parameterise the LAI. The mean LAI for all the spring hemispherical photographs in Abisko was 0.25. Therefore, the net LAI of the tree tile and Shaded gap tile should equate to an area averaged LAI of 0.25. This model concept assumes all the trees from any sized area are moved into 15 % of the area, and the remaining 85 % left as Shaded gap. Therefore the tree tile LAI cannot be 0.25, but needs to be higher to account for the denser canopy from the trees being moved into a smaller area. The LAI of the tree tile was set to 1.00, which gives a net LAI of 0.15. The conceptual model of the Shaded gap includes a Sky view fraction of 0.80, which acts as an effective LAI. Although this does not behave like the canopy of the tree tile, it acts as an effective LAI of 0.10 by cutting out both the direct and diffuse shortwave radiation and the longwave radiation.

Tree canopy longwave radiation (LW_{tree})

The tree canopy longwave radiation was based on the radiation budget of the trees which was validated against the tree canopy temperature measurements. Spring tree temperatures showed that the tree canopy was warmer than the ambient air temperature, and the side of the tree receiving the shortwave radiation increased in temperature most significantly. The LW_{tree} parameter is scaled first by the Sky view fraction of shortwave radiation, then scaled by half to represent the sun lit side of the trees and finally scaled using the LAI of the tree canopy.

8.6 Shaded gap model results

Once the model was defined and parameterised, it was then run for the sparse forest in Abisko. We used in-situ, gap filled meteorological data to drive the model and the in-situ snow-surveys to validate the results. The results for the Homogeneous and Clumped canopy models were directly compared with JULES Shaded gap. It was found that the JULES Shaded gap model improved the representation of the sparse forests in the following ways.

1. The JULES Shaded gap model reproduces the observed diurnal variability in canopy transmissivity, while canopy models Homogeneous and Clumped have no diurnal variation.
2. JULES Shaded gap reproduces the below canopy observations of longwave radiation.
3. JULES Shaded gap tile improves the snow melt timing compared to JULES Clumped.

In order to quantify the relative importance of the changes to the shortwave and longwave radiation in JULES Shaded gap, the model was run with the shortwave and longwave switched on and off separately. The results showed that the changes to the shortwave radiation parameterisations alone delay the onset of snow melt. Whilst the changes to the longwave radiation parameterisations alone accelerate the snowmelt. The result that was not known before this thesis is that when both the shortwave and longwave parameterisations are introduced into the JULES Shaded gap model, it is the longwave radiation which has the largest effect on the snowpack, and therefore the snow melts out earlier than in JULES Clumped.

This thesis set out to gather data on model parameters to develop the representation of sparse forests within land surface models. Although it is easy to see that the observations of the radiation balance are not currently reproduced, what was not clear was which component of the radiation balance was crucial to modelling these sparse forests correctly. The JULES Shaded gap model developed in this thesis, shows that the longwave radiation has the most important effect on the radiation balance. The shading of the snowpack is another important process which should be included.

8.7 Implications of the Shaded gap model

These results are not only important at the local site scale for Abisko, but are of global importance as sparse forests represent a significant proportion of the northern high latitudes, which are snow covered in spring. The presence of snow has an important impact on the radiation balance, as a snow covered surface has a high albedo and reflects much of the incoming radiation. If JULES is modelling snow cover when in fact it has melted, the energy fluxes will be wrong. The next step is to assess how these new parameterisations could affect snow cover for the high latitude spring period, across the whole pan-Arctic region.

JULES (v4.7) was run in distributed mode with a grid size of 0.5° for the northern latitudes (60°N to 90°N) for 2000 to 2014, using the parameterisations specified in Appendix B, firstly for JULES and secondly for the JULES Shaded gap. The Shaded gap was introduced into the land cover map by converting all the shrub into c4 grass, and then adjusting the percentage of shrub cover to the fractional cover determined from the field observations for Abisko (see Chapter 7) with 15 % shrub, and 85 % Shaded gap (A c4 grass tile but with the parameters for a c3 grass tile). To account for the shrub vegetation clumping in the canopy from the whole fraction of shrub into the 15 %, the LAI is conserved between JULES and JULES Shaded gap from 0.25 to 1.0, with the additional 0.15 LAI included as an “effective” canopy above the Shaded gap (as in the previous JULES Shaded gap model in Chapter 7). The twelve year mean snowmass for March, April, May and June are presented in Appendix C for each of the global model runs.

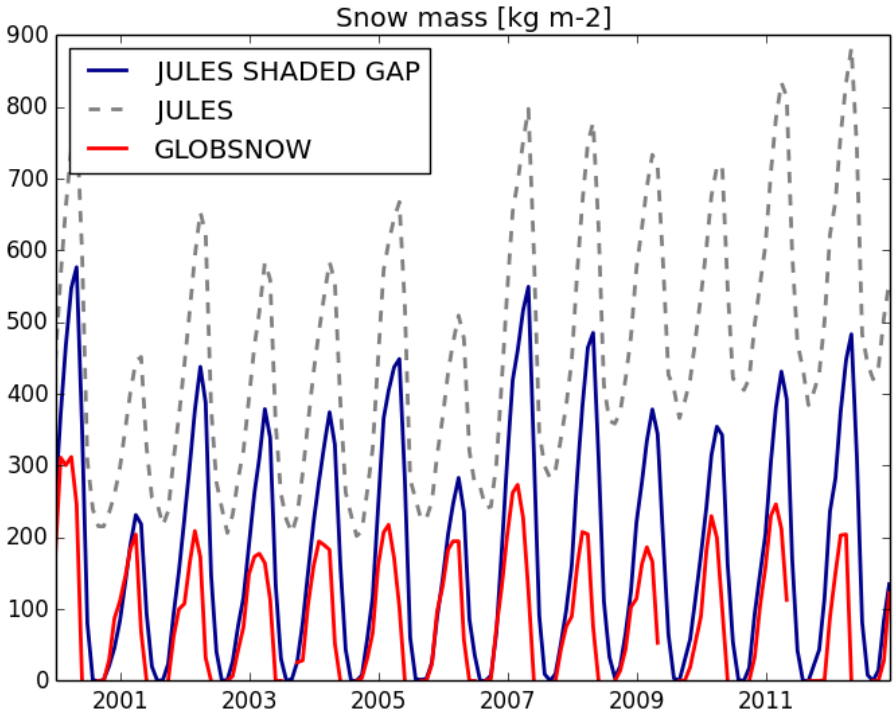

Figure 8.1: Mean snowmass (kg m^{-2}) for JULES (grey dashed) and JULES Shaded gap (dark blue) at Abisko (68.25 N and 18.75 E) for 12 years from January 2000 to December 2012. Observations from GlobSnow (red) for the nearest available pixel (67.75 N and 19.25 E). Produced in collaboration with Alberto Martinez-de la Torre, CEH.

Figure 8.1 shows the results for the grid cell within which Abisko is located, represented by JULES (dashed grey line), JULES Shaded gap (dark blue line) and GlobSnow (red line) (GlobSnow v2.0 [*Takala et al.*, 2011; *Pulliainen*, 2006]). JULES is able to reproduce some seasonal variation in snowmass, but it vastly overestimates the snowmass, with respect to both JULES Shaded gap and the observations. It is important to consider that the pixel for the Abisko site is mountainous and includes some high altitude sites which would be snow covered year round, unlike the field site in Abisko which melts out in late spring. What these results show is that with the improved parameterisations of the radiation JULES Shaded gap is able to reproduce the snowmass considerably better than JULES with respect to the observations.

Figure 8.2 shows various modelled and measured snowmass for the mean month of May over the year 2000 to 2012. Figure 8.2 panel a. shows a map of snowmass diagnosed for JULES and panel b. shows a map of snowmass diagnosed for JULES Shaded gap. The most important thing to note is that the mean May snowmass in JULES Shaded gap is considerably smaller than in JULES. JULES models snowmass for much of Alaska, northern Canada, and Siberia, while JULES Shaded gap has very little or none. This is clearly seen in Figure 8.2 panel d. depicting the difference between JULES and JULES Shaded gap. This shows that there is even

a small difference in the Scandinavian area, and a much larger difference over northern Russia, specifically Siberia and the Far East, the Yukon, North Western Territories and across to Quebec. It is these regions where the sparse deciduous forests are located and therefore crucial that the snowmass and timing of the snow melt is correctly modelled. A comparison of the model outputs with GlobSnow observations shown in Figure 8.2 panel c. indicates better agreement between the observations and the new parameterisations for JULES Shaded gap than with JULES and the observations.

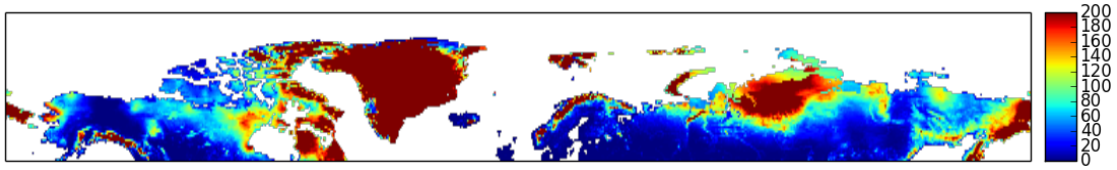

(a) JULES

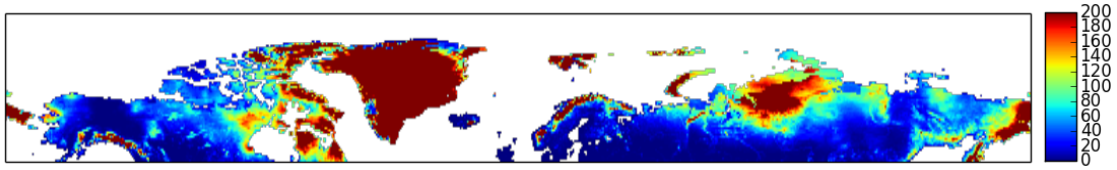

(b) JULES Shaded gap

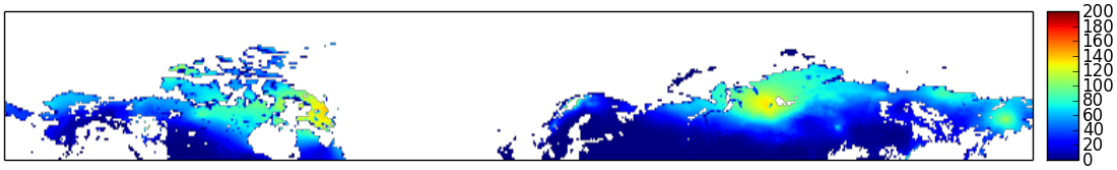

(c) GlobSnow

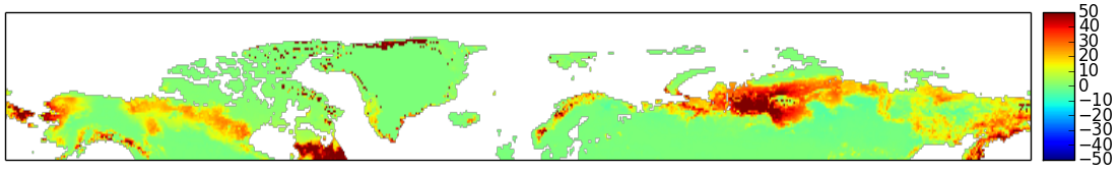

(d) JULES minus JULES Shaded gap

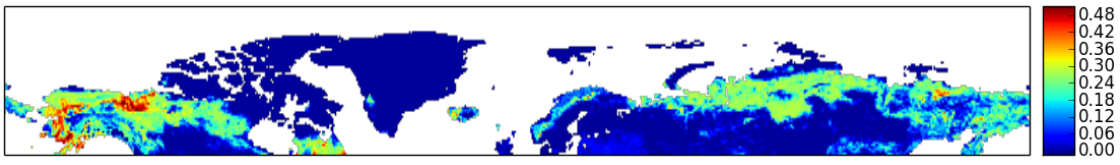

(e) Shaded gap fractional cover (JULES Shaded gap minus JULES)

Figure 8.2: Twelve year (2000 to 2012) mean May snowmass (kg m^{-2}) for panel a. JULES, panel b. JULES Shaded gap, panel c. GlobSnow, panel d. The difference between JULES and JULES Shaded gap and panel e. Shaded gap fractional cover. Produced in collaboration with Alberto Martinez-de la Torre, CEH.

8.8 Shaded gap model performance evaluation

The results of the distributed runs can be evaluated using The International Land Model Benchmarking Project (ILAMB) system. ILAMB is a comprehensive tool which allows the robust spatial and temporal analysis of model performance against a suite of observed data sets [*Luo et al.*, 2012; *Hoffman et al.*, 2017; *Schellekens et al.*, 2017]. Examining the regions where the Shaded gap fractional cover is over 0.1 in Figure 8.2 panel e, the JULES and JULES Shaded gap modelled snowmass are compared with GlobSnow observations (Table 8.1).

Table 8.1: ILAMB metrics for JULES and JULES Shaded gap models evaluated against GlobSnow for mean May snowmass (2000 to 2012). Mean snowmass, bias, RMSE and normalised (0 to 1) ILAMB scores are weighted area means over the regions with Shaded gap fractional cover greater than 0.1 (Figure 8.2 panel e). A score of zero indicates no model skill and a score of 1 indicates the model is as good as the observed data. Produced in collaboration with Alberto Martinez-de la Torre, CEH.

Model	Mean snowmass ($kg\ m^{-2}$)	Bias ($kg\ m^{-2}$)	RMSE ($kg\ m^{-2}$)	Bias Score 0 to 1	RMSE Score 0 to 1	Spatial Distribution Score 0 to 1
GlobSnow	46.25					
JULES	107.312	61.061	75.673	0.406	0.346	0.32
JULES Shaded gap	86.794	40.372	59.854	0.482	0.403	0.387

The results of the ILAMB analysis show that the mean May modelled snowmass of 86.794 $kg\ m^{-2}$ for JULES Shaded gap is improved relative to JULES 107.312 $kg\ m^{-2}$, although it is still over 40 $kg\ m^{-2}$ higher than the observed GlobSnow snowmass of 46.25 $kg\ m^{-2}$. The bias is reduced from 61.061 $kg\ m^{-2}$ for JULES to 40.372 $kg\ m^{-2}$ for JULES Shaded gap, while the bias score is improved from 0.406 in JULES to 0.482 in JULES Shaded gap.

Figure 8.3 indicates there are large areas in which JULES Shaded gap reduces the overestimation of snowmass across the pan-Arctic (areas of red in JULES Figure 8.3 panel a which are lighter red in JULES Shaded gap Figure 8.3 panel b). There are also some areas where JULES underestimates the snowcover which were exaggerated in JULES Shaded gap (areas of blue in JULES Figure 8.3 panel a which are darker blue in JULES Shaded gap Figure 8.3 panel b). In summary, JULES Shaded gap reduces the snowmass bias in northern Canada and Siberia.

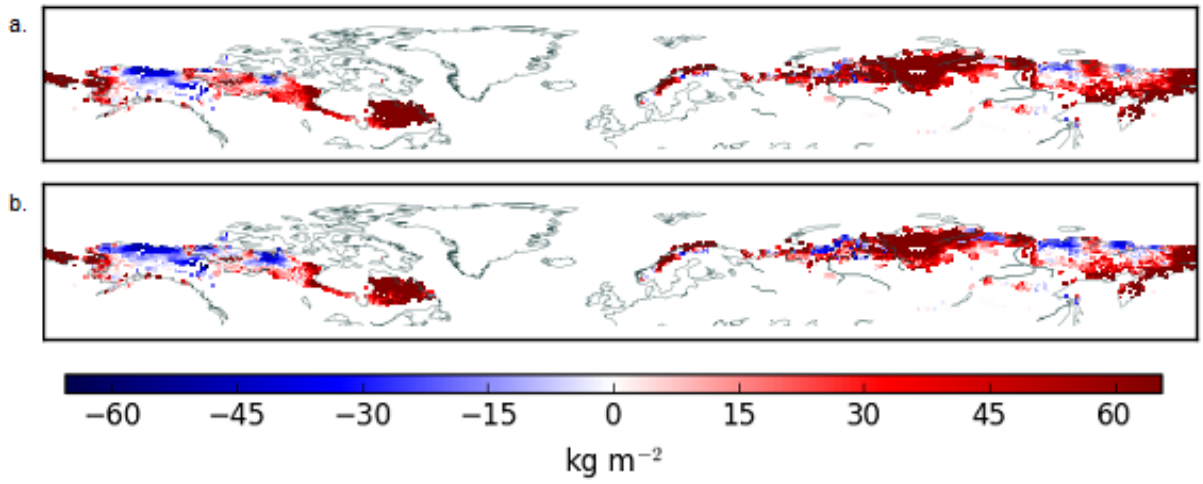

Figure 8.3: ILAMB bias of the a. JULES and b. JULES Shaded gap models evaluated against GlobSnow for mean May snowmass (2000 to 2012). Produced in collaboration with Alberto Martinez-de la Torre, CEH.

The RMSE is reduced from 75.673 kg m^{-2} for JULES to 59.854 kg m^{-2} for JULES Shaded gap, while the RMSE score improved from 0.346 in JULES to 0.403 in JULES Shaded gap (Table 8.1), with improvements in model estimated snowmass in northern Canada and Siberia (areas of blue in Figure 8.4).

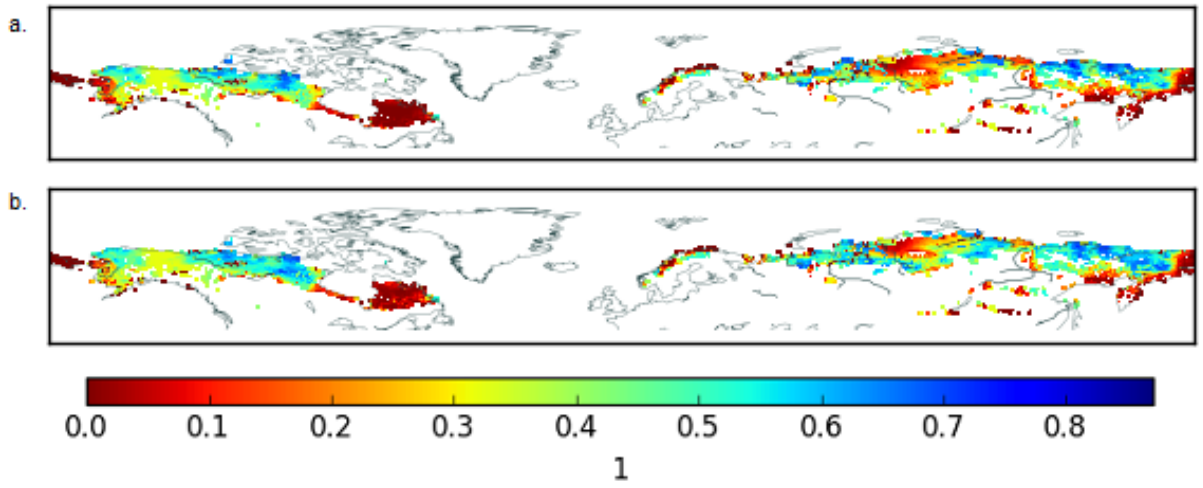

Figure 8.4: ILAMB RMSE score of the a. JULES and b. JULES Shaded gap models evaluated against GlobSnow for mean May snowmass (2000 to 2012). Produced in collaboration with Alberto Martinez-de la Torre, CEH.

The spatial distribution score of the snowmass improved from 0.320 in JULES to 0.387 in JULES Shaded gap (Table 8.1). *Taylor* [2001] describes how the metric is calculated from the spatial

correlation and normalised spatial standard deviation given in Figure 8.5. The normalised spatial standard deviation (model standard deviation over observed standard deviation) is improved from 3.1 in JULES to 2.7 in JULES Shaded gap (Figure 8.5), and there was a small decline in the spatial correlation from 0.84 to 0.82.

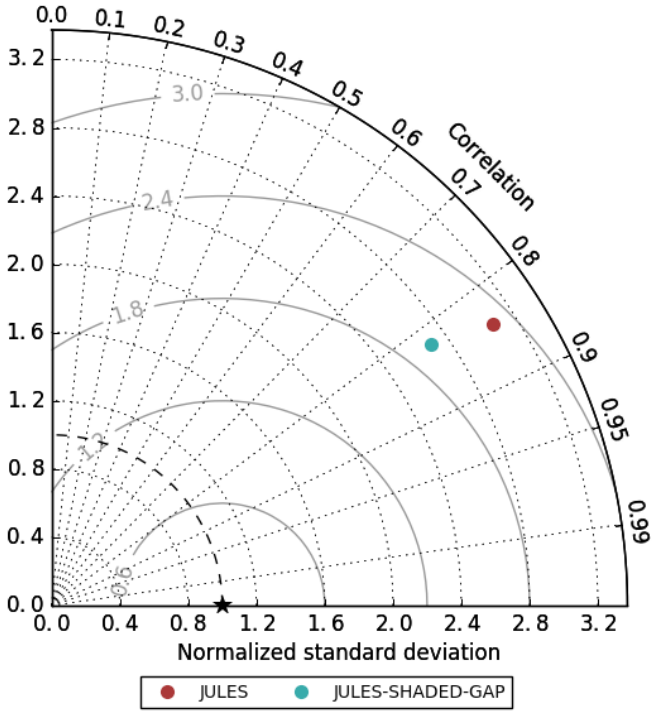

Figure 8.5: ILAMB global spatial variance of the JULES and JULES Shaded gap models evaluated against GlobSnow for mean May snowmass (2000 to 2012). Star indicates model as good as observed data (1.0). Produced in collaboration with Alberto Martinez-de la Torre, CEH.

Overall these metrics show that the Shaded gap parameterisations can improve our modelled estimate of snowmass, but there is still considerable scope for development of our representation global snowmass.

8.9 Critique of the Shaded gap model

The methods used here for defining the Shaded gap tile globally were selected in order to investigate whether the parameterisations of the Shaded gap developed for a sparse forest in Abisko had an impact on the snowmass at the global scale. Although the results show JULES Shaded gap is improving our representation of the overall snowmass, the methods used was not

the only available option. The Shaded gap fraction was introduced into a c4 grass tile, which had the parameters defined as the c3 grass tile. It was introduced by taking a proportion of the Shrub fraction and replacing it with the new Shaded gap fraction.

The fractional cover of 15 % tree (or shrub) and 85 % Shaded gap is based on the parameters validated from the Abisko field observations in Chapters 3 to 7. At this point it is important to acknowledge a more conservative approach may have considered the Shaded gap fraction to be lower than this. *Pacifico et al.* [2011] describes one way in which the vegetation fraction from the International Geosphere-Biosphere Program (IGBP) 17 land cover classes were converted into the JULES vegetation types to run JULES in distributed mode. This approach would have assumed a percentage of the grass or bare soil area in each grid cell would represent the understorey fraction in these sparse forests (Table 2 [*Pacifico et al.*, 2011]). In this sensitivity study it was assumed that the forest gaps were classified as forest and the parameters for fractional cover validated for the sparse forest in Abisko.

Another weakness of the Shaded gap global implementation is the assumed uniformity in the fractional cover of tree to Shaded gap across the pan-Arctic. From studying the sparse forest in Abisko it is clear that the canopy is clumped and size of canopy gap is not constant, as a natural mosaic exists even at the landscape scale. One next step with the Shaded gap model could include a varying fractional cover of tree to shaded gap which could be scaled with latitude and elevation or satellite derived LAI, to account for variability in sparse forest canopy cover density.

8.10 Future work on the Shaded gap model

8.10.1 In-situ sparse forest observations

The parameters developed for the Shaded Gap tile were from field observations in the sparse birch forest, Abisko, Sweden. Although, we can be confident that these data were representative of the sparse forest at the landscape scale of Abisko, the Shaded gap model is limited by parameterisation to this specific site and the field observations presented here. To develop our knowledge of how canopy transmissivity, LAI, short and longwave radiation below the canopy varies spatially, it would be necessary to measure other sparse forests across the sub-Arctic. The parameters were derived from quick and easily repeatable field measurements, so this would be feasible.

The parameters developed in the Shaded gap tile were tested (JULES (v3.1) not presented here) at two BERMS (Boreal Ecosystem Research and Monitoring Sites) Arctic forest sites with a seasonal

snow cover, in central Canada [*Hardy et al.*, 1997b; *Davis et al.*, 1998; *Ni-Meister and Gao*, 2011]. One of the sites, a needleleaf tree site, (black spruce) was used in the Snow Model Intercomparison Project (SnowMIP2) [*Essery et al.*, 2009; *Rutter et al.*, 2009], and the other was a sparse deciduous forest site (old aspen). Running the JULES Shaded gap model at these and other sites would provide information on how each of the parameters would need to be adjusted.

8.10.2 Parameter characterisation at the global scale

Lit fraction (f_{lit})

The Lit fraction was designed to vary with forest height, time of day, day in year and latitude. Ideally the other parameters of f_v, Gap_s, LAI and tree height would be adjusted in the model rather than changing the way in which this is parameterised.

Sky view fraction (f_v)

Other field studies with field observations of canopy transmissivity in sparse forests would be valuable for parameterising f_v. Field observations for other deciduous and coniferous sparse forest canopies would provide insight into the range of values suitable for the f_v parameter.

Defining f_v globally would be of significant value. *Pinty et al.* [2011] looked at the absorption of PAR from the reflected snow covered surface by boreal forests using the MODIS surface albedo product. These methods could be explored to obtain a global map of sky view fraction, as the Shaded gap model is limited by a single fixed value for sparse forests. Since there can often be disconnect between field measurements and satellite derived products, a physical theory of how the model f_v parameter varies with LAI might be an option to consider instead of having a large ancillary file.

Gap size (Gap_s)

Gap size should scale with the tree height as this would determine the shortwave radiation penetration. A Gap size of 40 m in diameter was selected from a sensitivity study for the Abisko sparse deciduous birch forest, but this not be suitable for other birch forests, other sparse forests, or sparse forests on the global scale.

Tree canopy longwave radiation (LW_{tree})

Extreme caution should be applied when taking this parameterisation to other sites and globally. LW_{tree} was validated against a single observation of below canopy shortwave radiation, and there may be substantial variability in the below canopy longwave radiation within the sparse deciduous birch forest in Abisko. Ideally, the LW_{tree} parameter would be validated with other field observations, in various forest canopy covers. Further field observations might necessitate further development of the longwave radiation model.

8.10.3 Multi-layer energy balance in land surface models

The JULES Shaded gap model can now be used as a research tool in sensitivity studies, however this may not be the optimum operational development moving forward. The land surface fluxes represent a priority area for development in the land surface modelling community [*Pitman et al.*, 2009; *Jimenez et al.*, 2011; *de Noblet-Ducoudre et al.*, 2012]. The Organising Carbon and Hydrology In Dynamic Ecosystems-CANopy model (ORCHIDEE-CAN) contains a multi-layered energy budget scheme [*Naudts et al.*, 2015; *Chen et al.*, 2016; *Ryder et al.*, 2016], and also in the interactions between soil-biosphere-atmosphere (ISBA) land surface model which includes parameterisation for a multi-energy balance (ISBA-MEB) [*Boone et al.*, 2017]. The introduction of a multi-layered energy balance as in ORCHIDEE and ISBA would not only improve the short and longwave radiation balance in JULES but also calculations of the sensible and latent heat fluxes, canopy turbulence, canopy resistance, and evapotranspiration [*Pitman et al.*, 2009; *Jimenez et al.*, 2011; *de Noblet-Ducoudre et al.*, 2012; *Ryder et al.*, 2016; *Boone et al.*, 2017].

8.11 Summary

JULES Shaded gap has been shown to improve the representation of both the shortwave and longwave radiation in sparse forests and brings the snowmelt timing more aligned with in-situ observational data. When JULES Shaded gap is evaluated on the global scale, it vastly improves the modelled snowmass, across large areas of sparse forest in northern Canada, Scandinavia and Northern Russia with respect to both satellite observations and standard JULES. The performance of the land surface-snow-vegetation interactions of JULES is improved by using this novel approach to the radiation balance of sparse forests in climate-sensitive Arctic regions. This shortening of the modelled snow-season directly impacts on the simulated carbon and water balance regionally and has wider relevance at the pan-Arctic scale. The timing of the snowmelt has been shown to be an important factor in controlling the soil temperature, length of the growing season and tree growth [*Vaganov et al.*, 1999; *Neilson et al.*, 2001; *Hardy et al.*, 2001; *Tanja et al.*, 2003; *Steinweg et al.*, 2008; *Jahn et al.*, 2010; *Hartley et al.*, 2010] it is difficult to define if this

would result in a net sink or source of carbon as they are finely balanced ecosystems [*Serreze et al.*, 2000; *Sitch et al.*, 2007; *Serreze and Barry*, 2011]. The release of snow as melt water can be the single largest input of freshwater to many northern latitude catchments, and correctly timing this has many useful applications in river flow and flood hydrology [*Shook et al.*, 1993; *Janowicz et al.*, 1997; *Nijssen et al.*, 2003; *Niu and Yang*, 2006; *Essery et al.*, 2009; *Clow*, 2010]. Furthermore these observational data can be used to develop and evaluate high latitude land-surface processes and biogeochemical feedbacks in other earth system models.

References

Adam, J. C., and D. P. Lettenmaier, Adjustment of global gridded precipitation for systematic bias, *Journal of Geophysical Research-Atmospheres*, *108*(D9), 4257, doi:10.1029/2002JD002499, 2003.

AMAP, Snow, Water, Ice and Permafrost in the Arctic (SWIPA): Climate Change and the Cryosphere, *Tech. rep.*, Arctic Monitoring and Assessment Programme (AMAP), Oslo, Norway, 2011.

Anderson, M., Studies of the woodland light climate: I. The photographic computation of light conditions, *Journal of Ecology*, *52*(1), 27–41, 1964.

Andersson, N. A., T. V. Callaghan, and P. S. Karlsson, The Abisko Scientific Research Station, *Ecological Bulletins; Plant ecology in the subarctic Swedish Lapland*, *45*, 11–14, 1996.

Ayers, M., *Biotic interactions and global change*, chap. Plant defence, herbivory, and climate change, pp. 75–94, Sinauer Associates Inc., Sunderland, Massachusetts, 1993.

Barnekow, L., Holocene tree-line dynamics and inferred climatic changes in the Abisko area, northern Sweden, based on macrofossil and pollen records, *Holocene*, *9*(3), 253–265, doi: 10.1191/095968399676322637, 1999.

Best, M. J., et al., The Joint UK Land Environment Simulator (JULES), model description - Part 1: Energy and water fluxes, *Geoscientific Model Development*, *4*(3), 677–699, doi: 10.5194/gmd-4-677-2011, 2011.

Betts, R. A., Offset of the potential carbon sink from boreal forestation by decreases in surface albedo, *Nature*, *408*(6809), 187–190, doi:10.1038/35041545, 2000.

Bewley, D., J. W. Pomeroy, and R. L. H. Essery, Solar radiation transfer through a subarctic shrub canopy, *Arctic Antarctic and Alpine Research*, *39*(3), 365–374, doi:10.1657/1523-0430(06-023) [BEWLEY]2.0.CO;2, 2007.

Bewley, D., R. Essery, J. Pomeroy, and C. Menard, Measurements and modelling of snowmelt and turbulent heat fluxes over shrub tundra, *Hydrology and Earth System Sciences*, *14*(7), 1331–1340, doi:10.5194/hess-14-1331-2010, 2010.

Blyth, E., D. B. Clark, R. Ellis, C. Huntingford, S. Los, M. Pryor, M. Best, and S. Sitch, A comprehensive set of benchmark tests for a land surface model of simultaneous fluxes of water and carbon at both the global and seasonal scale, *Geoscientific Model Development*, *4*(2), 255–269, doi:10.5194/gmd-4-255-2011, 2011.

Bonan, G., *Ecological Climatology; concepts and applications*, chap. Surface energy fluxes, pp. 209–247, Cambridge Press, Cambridge, 2002.

Bonan, G. B., and H. H. Shugart, Environmental factors and ecological processes in boreal forests, *Annual Review of Ecology and Systematics*, *20*, 1–28, 1989.

Bonan, G. B., D. Pollard, and S. L. Thompson, Effects of boreal forest vegetation on global climate, *Nature*, *359*(6397), 716–718, doi:10.1038/359716a0, 1992.

Boone, A., P. Samuelsson, S. Gollvik, A. Napoly, L. Jarlan, E. Brun, and B. Decharme, The interactions between soil–biosphere–atmosphere land surface model with a multi-energy balance (ISBA-MEB) option in SURFEXv8 – Part 1: Model description, *Geoscientific Model Development*, *10*(2), 843–872, doi:10.5194/gmd-10-843-2017, 2017.

Boone, A., et al., The AMMA land surface model intercomparison project (ALMIP), *Bulletin of the American Meteorological Society*, *90*(12), 1865–1880, doi:10.1175/2009BAMS2786.1, 2009.

Bowling, L. C., J. W. Pomeroy, and D. P. Lettenmaier, Parameterization of blowing-snow sublimation in a macroscale hydrology model, *Journal of Hydrometeorology*, *5*(5), Int Assoc Hydrol Sci; Int Assoc Meteorol & Atmospher Sci, doi:10.1175/1525-7541(2004)005⟨0745:POBSIA⟩2.0.CO;2, 2004.

Bowling, L. C., et al., Simulation of high-latitude hydrological processes in the Torne-Kalix basin: PILPS phase 2(e) - 1: Experiment description and summary intercomparisons, *Global and Planetary Change*, *38*(1-2), 1–30, doi:10.1016/S0921-8181(03)00003-1, 2003.

Brooks, P. D., S. K. Schmidt, and M. W. Williams, Winter production of CO_2 and N_2O from Alpine tundra: Environmental controls and relationship to inter-system C and N fluxes, *Oecologia*, *110*(3), 403–413, doi:10.1007/PL00008814, 1997.

Brotzge, J. A., and C. E. Duchon, A field comparison among a domeless net radiometer, two four-component net radiometers, and a domed net radiometer, *Journal of Atmospheric and Oceanic Technology*, *17*(12), 1569–1582, doi:10.1175/1520-0426(2000)017⟨1569:AFCAAD⟩2.0.CO;2, 2000.

Callaghan, T., *Arctic Climate Impact Assessment*, chap. Arctic Tundra and Polar Desert Ecosystems, pp. 244–352, Cambridge University Press, 2005.

Callaghan, T. V., M. Johansson, J. Key, T. Prowse, M. Ananicheva, and A. Klepikov, Feedbacks and Interactions: From the Arctic Cryosphere to the Climate System, *Ambio*, *40*((Suppl 1)), 75–86, doi:10.1007/s13280-011-0215-8, 2011a.

Callaghan, T. V., et al., Multiple Effects of Changes in Arctic Snow Cover, *Ambio*, *40*(1), 32–45, doi:10.1007/s13280-011-0213-x, 2011b.

Carlsson, B., P. Karlsson, and B. Svensson, *Swedish Plant Geography*, chap. Alpine and subalpine vegetation, Opulus Press, Uppsala, 1999.

Chang, A. T. C., J. L. Foster, and D. K. Hall, Effects of forest on the snow parameters derived from microwave measurements during the BOREAS Winter Field Campaign, *Hydrological Processes*, *10*(12), 1565–1574, doi:10.1002/(SICI)1099-1085(199612)10:12⟨1565, 1996.

Chapin, F. S. III, J. T. Randerson, A. D. McGuire, J. A. Foley, and C. B. Field, Changing feedbacks in the climate-biosphere system, *Frontiers In Ecology and the Environment*, *6*(6), 313–320, doi:10.1890/080005, 2008.

Chen, J. M., Optically-based methods for measuring seasonal variation of leaf area index in boreal conifer stands, *Agricultural and Forest Meteorology*, *80*(2-4), 135–163, doi:10.1016/0168-1923(95)02291-0, 1996.

Chen, J. M., and T. A. Black, Measuring leaf-area index of plant canopies with branch architecture, *Agricultural and Forest Meteorology*, *57*(1-3), 1–12, doi:10.1016/0168-1923(91)90074-Z, 1991.

Chen, J. M., and T. A. Black, Defining leaf-area index for non-flat leaves, *Plant Cell and Environment*, *15*(4), 421–429, doi:10.1111/j.1365-3040.1992.tb00992.x, 1992.

Chen, J. M., T. A. Black, and R. Adams, Evaluation of hemispherical photography for determining plant area index and geometry of a forest stand, *Agricultural and Forest Meteorology*, *56*(12), 129–143, doi:10.1016/0168-1923(91)90108-3, 1991.

Chen, J. M., P. D. Blanken, T. A. Blank, M. Guilbeault, and S. Chen, Radiation regime and canopy architecture in a boreal aspen forest, *Agricultural and Forest Meteorology*, *86*(1-2), 107–125, doi:10.1016/S0168-1923(96)02402-1, 1997a.

Chen, J. M., P. M. Rich, S. T. Gower, J. M. Norman, and S. Plummer, Leaf area index of boreal forests: Theory, techniques, and measurements, *Journal of Geophysical Research-Atmospheres*, *102*(D24), 29,429–29,443, doi:10.1029/97JD01107, 1997b.

Chen, Y., et al., Evaluating the performance of land surface model ORCHIDEE-CAN v1.0 on water and energy flux estimation with a single- and multi-layer energy budget scheme, *Geoscientific Model Development*, *9*(9), 2951–2972, doi:10.5194/gmd-9-2951-2016, 2016.

Clark, D. B., et al., The Joint UK Land Environment Simulator (JULES), model description - Part 2: Carbon fluxes and vegetation dynamics, *Geoscientific Model Development*, *4*(3), 701–722, doi:10.5194/gmd-4-701-2011, 2011.

Clark, M. P., M. C. Serreze, and D. A. Robinson, Atmospheric controls on Eurasian snow extent, *International Journal of Climatology*, *19*(1), 27–40, doi:10.1002/(SICI)1097-0088(199901)19:1⟨27, 1999.

Clow, D., Changes in the timing of snowmelt and streamflow in Colorado: A response to recent warming, *Journal of Climate*, *23*(9), 2293–2306, doi:10.1175/2009JCLI2951.1, 2010.

Collins, M., et al., *Climate Change 2013: The Physical Science Basis. Contribution of Working Group I to the Fifth Assessment Report of the Intergovernmental Panel on Climate Change*, chap. Long-term Climate Change: Projections, Commitments and Irreversibility, 12, Cambridge University Press, Cambridge, United Kingdom and New York, NY, USA, 2013.

Cox, P., R. Betts, C. Jones, S. Spall, and I. Totterdell, Acceleration of global warming due to carbon-cycle feedbacks in a coupled climate model, *Nature*, *408*, 184–187, doi:10.1038/35047138, 2000.

Cox, P. M., R. A. Betts, C. B. Bunton, R. L. H. Essery, P. R. Rowntree, and J. Smith, The impact of new land surface physics on the GCM simulation of climate and climate sensitivity, *Climate Dynamics*, *15*(3), 183–203, doi:10.1007/s003820050276, 1999.

Cullather, R. I., Y. Lim, L. N. Boisvert, L. Brucker, J. N. Lee, and S. M. J. Nowicki, Analysis of the warmest Arctic winter, 20152016, *Geophysical Research Letters*, *43*(20), 10,808–10,816, doi:10.1002/2016GL071228, 2016.

Dai, Y. J., R. E. Dickinson, and Y. P. Wang, A two-big-leaf model for canopy temperature, photosynthesis, and stomatal conductance, *Journal of Climate*, *17*(12), 2281–2299, doi:10.1175/1520-0442(2004)017⟨2281:ATMFCT⟩2.0.CO;2, 2004.

Dai, Y. J., et al., The Common Land Model, *Bulletin of the American Meteorological Society*, *84*(8), 1013–1023, doi:10.1175/BAMS-84-8-1013, 2003.

Dankers, R., E. J. Burke, and J. Price, Simulation of permafrost and seasonal thaw depth in the JULES land surface scheme, *Cryosphere*, *5*(3), 773–790, doi:10.5194/tc-5-773-2011, 2011.

Davis, R. E., J. P. Hardy, W. Ni, C. Woodcock, J. C. McKenzie, R. Jordan, and X. Li, Variation of snow cover ablation in the boreal forest: A sensitivity study on the effects of conifer canopy, *Journal of Geophysical Research-Atmospheres*, *102*(D24), 29,389–29,395, doi:10.1029/97JD01335, 1997.

Davis, R. E., J. R. Metcalfe, J. P. Hardy, and B. Goodison, Variations in snow accumulation in the southern boreal forest - Preliminary analysis of 1993-1994 and 1994-1995 snow measurements, *Proceedings of the Fifty-fifth Annual Eastern Snow Conference*, pp. Amer Geophys Union; Amer Water Resources Assoc; State Univ New York,EOLEOLOswego Campus, 1998.

de Noblet-Ducoudre, N., et al., Determining Robust Impacts of Land-Use-Induced Land Cover Changes on Surface Climate over North America and Eurasia: Results from the First Set of LUCID Experiments, *Journal of Climate*, *25*(9), 3261–3281, doi:10.1175/JCLI-D-11-00338.1, 2012.

Derksen, C., and R. Brown, Spring snow cover extent reductions in the 2008-2012 period exceeding climate model projections, *Geophysical Research Letters*, *39*, L19,504, doi:10.1029/2012GL053387, 2012.

Dickinson, R. E., M. Shaikh, R. Bryant, and L. Graumlich, Interactive canopies for a climate model, *Journal of Climate*, *11*(11), 2823–2836, doi:10.1175/1520-0442(1998)011⟨2823:ICFACM⟩2.0.CO;2, 1998.

Dingman, S., *Physical hydrology*, chap. Snow and Snowmelt, pp. 166–219, Waveland Press, 2002.

Dirmeyer, P. A., X. Gao, M. Zhao, Z. Guo, T. Oki, and N. Hanasaki, GSWP-2 - Multimodel analysis and implications for our perception of the land surface, *Bulletin of the American Meteorological Society*, *87*(10), 1381–1397, doi:10.1175/BAMS-87-10-1381, 2006.

Dye, D. G., Variability and trends in the annual snow-cover cycle in Northern Hemisphere land areas, 1972-2000, *Hydrological Processes*, *16*(15), 3065–3077, doi:10.1002/hyp.1089, 2002.

Ellis, C. R., and J. W. Pomeroy, Estimating sub-canopy shortwave irradiance to melting snow on forested slopes, *Hydrological Processes*, *21*(19), Canadian Geophys Union, Hydrol Sect; Canadian Soc Soil Sci, doi:10.1002/hyp.6794, 2007.

Ellis, C. R., J. W. Pomeroy, T. Brown, and J. MacDonald, Simulation of snow accumulation and melt in needleleaf forest environments, *Hydrology and Earth System Sciences*, *14*(6), 925–940, doi:10.5194/hess-14-925-2010, 2010.

Ellis, C. R., J. W. Pomeroy, R. L. H. Essery, and T. E. Link, Effects of needleleaf forest cover on radiation and snowmelt dynamics in the Canadian Rocky Mountains, *Canadian Journal of Forest Research-revue Canadienne De Recherche Forestiere*, *41*(3), 608–620, doi:10.1139/X10-227, 2011.

Englund, S., J. O'Brien, and D. Clark, Evaluation of digital and film hemispherical photography and spherical densitometry for measuring forest light environments, *Canadian Journal of Forest Research-revue Canadienne De Recherche Forestiere*, *30*, 1999–2005, 2000.

Esseen, P.-A., B. Ehnstrom, L. Ericson, and K. Sjoberg, Boreal forests, *Ecological Bulletins; Boreal ecosystems and landscapes: Structures, processes and conservation of biodiversity*, *46*, 16–47, 1997.

Essery, R., and J. Pomeroy, Sublimation of snow intercepted by coniferous forest canopies in a climate model, in *Soil-Vegetation-Atmosphere Transfer schemes and large-scale hydrological models*, no. 270 in IAHS Publication, pp. 343–347, 2001.

Essery, R., and J. Pomeroy, Vegetation and topographic control of wind-blown snow distributions in distributed and aggregated simulations for an Arctic tundra basin, *Journal of Hydrometeorology*, *5*(5), Int Assoc Hydrol Sci; Int Assoc Meteorol & Atmospher Sci, doi:10.1175/1525-7541(2004)005⟨0735:VATCOW⟩2.0.CO;2, 2004.

Essery, R., L. Li, and J. Pomeroy, A distributed model of blowing snow over complex terrain, *Hydrological Processes*, *13*(14-15), 2423–2438, doi:10.1002/(SICI)1099-1085(199910)13:14/15⟨2423, 1999.

Essery, R., M. Best, R. Betts, and P. Cox, Explicit Representation of Subgrid Heterogeneity in a GCM Land Surface Scheme, *Journal of Hydrometeorology*, *4*, 530–543, 2002.

Essery, R., J. Pomeroy, J. Parviainen, and P. Storck, Sublimation of snow from coniferous forests in a climate model, *Journal of Climate*, *16*(11), 1855–1864, doi:10.1175/1520-0442(2003)016⟨1855:SOSFCF⟩2.0.CO;2, 2003.

Essery, R., R. Granger, and J. Pomeroy, Boundary-layer growth and advection of heat over snow and soil patches: Modelling and parameterization, *Hydrological Processes*, *20*(4), 953–967, doi:10.1002/hyp.6122, 2006.

Essery, R., P. Bunting, J. Hardy, T. Link, D. Marks, R. Melloh, J. Pomeroy, A. Rowlands, and N. Rutter, Radiative transfer modeling of a coniferous canopy characterized by airborne remote sensing, *Journal of Hydrometeorology*, *9*(2), 228–241, doi:10.1175/2007JHM870.1, 2008a.

Essery, R., J. Pomeroy, C. Ellis, and T. Link, Modelling longwave radiation to snow beneath forest canopies using hemispherical photography or linear regression, *Hydrological Processes*, *22*(15), 2788–2800, doi:10.1002/hyp.6930, 2008b.

Essery, R., N. Rutter, J. Pomeroy, R. Baxter, M. Stahli, D. Gustafsson, A. Barr, P. Bartlett, and K. Elder, SnowMIP2 An Evaluation of Forest Snow Process Simulations, *Bulletin of the American Meteorological Society*, *90*(8), 1120–1135, doi:10.1175/2009BAMS2629.1, 2009.

Fassnacht, S., K. Snelgrove, and E. Soulis, Daytime longwave radiation approximation for physical hydrological modelling of Snowmelt: a case study of southwestern Ontario, in *Proceedings Sixth IAHS Scientific Assembly Symposium*, vol. 270, pp. 279–286, IAHS: Maastricht, 2001.

Flannigan, M., and C. Wagner, Climate change and wildfire in Canada, *Canadian Journal of Forest Research*, *21(1)*, 66–72, 1991.

Flannigan, M., Y. Bergeron, O. Engelmark, and B. Wotton, Future wildfire in circumboreal forests in relation to global warming, *Journal of Vegetation Science*, *9(4)*, 469–476, 1998.

Flerchinger, G. N., M. L. Reba, and D. Marks, Measurement of surface energy fluxes from two rangeland sites and comparison with a multilayer canopy model, *Journal of Hydrometeorology*, *13*(3), 1038–1051, doi:10.1175/JHM-D-11-093.1, 2012.

Foppa, N., A. Hauser, D. Oesch, S. Wunderle, and R. Meister, Validation of operational AVHRR subpixel snow retrievals over the European Alps based on ASTER data, *International Journal of Remote Sensing*, *28*(21), 4841–4865, doi:10.1080/01431160701253287, 2007.

Frazer, G., C. Canham, and K. Lertzman, *Gap Light Analyzer (GLA), Version 2.0: Imaging software to extract canopy structure and gap light transmission indices from true-colour fisheye photographs, users manual and program documentation*, 1999.

Frazer, G. W., R. A. Fournier, J. A. Trofymow, and R. J. Hall, A comparison of digital and film fisheye photography for analysis of forest canopy structure and gap light transmission,

Agricultural and Forest Meteorology, *109*(4), 249–263, doi:10.1016/S0168-1923(01)00274-X, 2001.

Garriques, S., N. V. Shabanov, K. Swanson, J. T. Morisette, F. Baret, and R. B. Myneni, Intercomparison and sensitivity analysis of Leaf Area Index retrievals from LAI-2000, accuPAR, and digital hemispherical photography over croplands, *Agricultural and Forest Meteorology*, *148*(8-9), 1193–1209, doi:10.1016/j.agrformet.2008.02.014, 2008.

Gedney, N., P. Cox, R. Betts, O. Boucher, C. Huntingford, and P. Stott, Detection of a direct carbon dioxide effect in continental river runoff records, *Nature*, *439*, 835–838, doi:10.1038/nature04504, 2006.

Gonsamo, A., J.-M. N. Walter, and P. Pellikka, CIMES: A package of programs for determining canopy geometry and solar radiation regimes through hemispherical photographs, *Computers and Electronics in Agriculture*, *79*(2), 207–215, doi:10.1016/j.compag.2011.10.001, 2011.

Goodison, B., H. Ferguson, and G. McKay, *Handbook of Snow: Principles, Processes, Management and Use*, chap. Measurement and data analysis, pp. 191–274, Pergamon Press, Toronto, 1981.

Goodison, B., P. Louie, and D. D. Yang, WMO Instruments and Observing Methods Report No. 67 Solid Precipitation Measurement Intercomparison, *Tech. rep.*, World Meteorological Organization, 1998.

Gouttevin, I., M. Lehning, T. Jonas, D. Gustafsson, and M. Molder, A two-layer canopy model with thermal inertia for an improved snowpack energy balance below needleleaf forest (model SNOWPACK, version 3.2.1, revision 741), *Geoscientific Model Development*, *8*(8), 2379–2398, doi:10.5194/gmd-8-2379-2015, 2015.

Gower, S. T., O. Krankina, R. Olson, M. Apps, S. Linder, and C. Wang, Net primary production and Carbon allocation patterns of boreal forest ecosystems, *Ecological Applications*, *11*, 1395–1411, 2001.

Groisman, P. Y., T. R. Karl, and R. W. Knight, Observed impact of snow cover on the heat-balance and the rise of continental spring temperatures, *Science*, *263*(5144), 198–200, doi:10.1126/science.263.5144.198, 1994.

Gryning, S. E., E. Batchvarova, and H. A. R. De Bruin, Energy balance of a sparse coniferous high-latitude forest under winter conditions, *Boundary-layer Meteorology*, *99*(3), 465–488, doi:10.1023/A:1018939329915, 2001.

Halldin, S., *Vegetation, Water, Humans and the Climate: A New Perspective on an Interactive System*, *Global Change The IGBP Series*, vol. Part B, chap. Radiation Measurements in Integrated Terrestrial Experiments, pp. 167–171, Springer-Berlin Heidelberg, doi:10.1007/978-3-642-18948-7_14, 2004.

Hanna, E., J. M. Jones, J. Cappelen, S. H. Mernild, L. Wood, K. Steffen, and P. Huybrechts, The influence of North Atlantic atmospheric and oceanic forcing effects on 1900-2010 Greenland summer climate and ice melt/runoff, *International Journal of Climatology*, *33*(4), 862–880, doi:10.1002/joc.3475, 2013.

Harding, R. J., and J. W. Pomeroy, Energy balance of the winter boreal landscape, *Journal of Climate*, *9*(11), 2778–2787, doi:10.1175/1520-0442(1996)009⟨2778:TEBOTW⟩2.0.CO;2, 1996.

Harding, R. J., S. E. Gryning, S. Halldin, and C. R. Lloyd, Progress in understanding of land surface/atmosphere exchanges at high latitudes, *Theoretical and Applied Climatology*, *70*(1-4), 5–18, doi:10.1007/s007040170002, 2001.

Hardy, J. P., R. E. Davis, R. Jordan, X. Li, C. Woodcock, W. Ni, and J. C. McKenzie, Snow ablation modeling at the stand scale in a boreal jack pine forest, *Journal of Geophysical Research-Atmospheres*, *102*(D24), 29,397–29,405, doi:10.1029/96JD03096, 1997a.

Hardy, J. P., R. E. Davis, R. Jordan, W. Ni, and C. Woodcock, Snow ablation modeling in conifer and deciduous stands of the boreal forest, *Eastern Snow Conference 1997, Proceedings*, pp. Canadian Geophys Union; Environ Canada–Natl hyrol Res Inst; US Army ColdEOLEOLRegions Res & Engn Lab, 1997b.

Hardy, J. P., R. E. Davis, R. Jordan, W. Ni, and C. E. Woodcock, Snow ablation modelling in a mature aspen stand of the boreal forest, *Hydrological Processes*, *12*(10-11), 1763–1778, doi:10.1002/(SICI)1099-1085(199808/09)12:10/11⟨1763, 1998.

Hardy, J. P., R. Melloh, G. Koenig, D. Marks, A. Winstral, J. W. Pomeroy, and T. Link, Solar radiation transmission through conifer canopies, *Agricultural and Forest Meteorology*, *126*(3-4), 257–270, doi:10.1016/j.agrformet.2004.06.012, 2004.

Hardy, J. P., et al., Snow depth manipulation and its influence on soil frost and water dynamics in a northern hardwood forest, *Biogeochemistry*, *56*(2), 151–174, doi:10.1023/A:1013036803050, 2001.

Hartley, I. P., D. W. Hopkins, M. Sommerkorn, and P. A. Wookey, The response of organic matter mineralisation to nutrient and substrate additions in sub-arctic soils, *Soil Biology and Biochemistry*, *42*(1), 92–100, doi:10.1016/j.soilbio.2009.10.004, 2010.

Henderson-Sellers, A., A. J. Pitman, P. K. Love, P. Irannejad, and T. H. Chen, The Project for Intercomparison of Land-surface Parameterization Schemes (PILPS) - Phase-2 and Phase-3, *Bulletin of the American Meteorological Society*, *76*(4), 489–503, doi:10.1175/1520-0477(1995)076⟨0489:TPFIOL⟩2.0.CO;2, 1995.

Hoffman, F. M., et al., International Land Model Benchmarking (ILAMB) 2016 Workshop Report, DOE/SC-0186, *Tech. rep.*, U.S. Department of Energy, Office of Science, Germantown, Maryland, USA, doi:10.2172/1330803, 2017.

Hoffman, M. J., A. G. Fountain, and G. E. Liston, Surface energy balance and melt thresholds over 11 years at Taylor Glacier, Antarctica, *Journal of Geophysical Research - Earth Surface*, *113*(F4), doi:10.1029/2008JF001029, 2008.

Huntington, H., and G. Weller, *Arctic Climate Impact Assessment*, chap. An Introduction to the Arctic Climate Impact Assessment, pp. 1–20, Cambridge University Press, 2005.

Inoue, A., K. Yamamoto, and N. Mizoue, Comparison of automatic and interactive thresholding of hemispherical photography, *Journal of Forest Science (Prague)*, *57*(2), 78–87, 2011.

IPCC, *Climate Change 2014: Synthesis Report Contribution of Working Groups I, II and III to the Fifth Assessment Report of the Intergovernmental Panel on Climate Change*, 151 pp., Geneva, Switzerland, 2014.

Jahn, M., T. Sachs, T. Mansfeldt, and M. Overesch, Global climate change and its impacts on the terrestrial arctic carbon cycle with special regards to ecosystem components and the greenhouse-gas balance, *Journal of Plant Nutrition and Soil Science*, *173*(5), 627–643, doi: 10.1002/jpln.200900331, 2010.

Janowicz, J. R., D. M. Gray, and J. W. Pomeroy, Snowmelt and runoff in a subarctic mountain basin, *Proceedings of the Hydro-ecology Workshop On the Arctic Environmental Strategy Action On Water*, (16), Canadian Geophys Union; Hydrol CGU; Natl Hydrol Res Inst, 1997.

Jarcuska, B., S. Kucbel, and P. Jaloviar, Comparison of output results from two programmes for hemispherical image analysis: Gap Light Analyser and WinScanopy, *Journal of Forest Science (Prague)*, *56*(4), 147–153, 2010.

Jennings, S., N. Brown, and D. Sheil, Assessing forest canopies and understorey illumination: canopy closure, canopy cover and other measures, *Forestry*, *71*, 59–73, 1999.

Jimenez, C., et al., Global intercomparison of 12 land surface heat flux estimates, *Journal of Geophysical Research-atmospheres*, *116*, D02,102, doi:10.1029/2010JD014545, 2011.

Jiménez Cisneros, B., T. Oki, N. Arnell, G. Benito, J. Cogley, P. Dll, T. Jiang, and S. Mwakalila, *Climate Change 2014: Impacts, Adaptation, and Vulnerability. Part A: Global and Sectoral Aspects. Contribution of Working Group II to the Fifth Assessment Report of the Intergovernmental Panel on Climate Change*, chap. Freshwater resources, pp. 229–269, Cambridge University Press, Cambridge, United Kingdom and New York, NY, USA, 2014.

Jin, M., and S. Liang, An improved land surface emissivity parameter for land surface models using global remote sensing observations, *Journal of Climate*, *19*(12), 2867–2881, doi:10.1175/JCLI3720.1, 2006.

Jonckheere, I., S. Fleck, K. Nackaerts, B. Muys, P. Coppin, M. Weiss, and F. Baret, Review of methods for in situ leaf area index determination - Part I. Theories, sensors and hemispherical photography, *Agricultural and Forest Meteorology*, *121*(1-2), 19–35, doi:10.1016/j.agrformet.2003.08.027, 2004.

Jonckheere, I., K. Nackaerts, B. Muys, and P. Coppin, Assessment of automatic gap fraction estimation of forests from digital hemispherical photography, *Agricultural and Forest Meteorology*, *132*(1-2), 96–114, doi:10.1016/j.agrformet.2005.06.003, 2005.

Juday, G., *Arctic Climate Impact Assessment*, chap. Forests, Land Management, and Agriculture, pp. 782–854, Cambridge University Press, 2005.

Kaplan, J. O., et al., Climate change and Arctic ecosystems: 2. Modeling, paleodata-model comparisons, and future projections, *Journal of Geophysical Research-Atmospheres*, *108*(D19), 8171, doi:10.1029/2002JD002559, 2003.

Kattsov, V., and E. Källén, *Arctic Climate Impact Assessment*, chap. Future Climate Change: Modelling and Scenarios for the Arctic, pp. 100–144, Cambridge University Press, 2005.

Kimball, B. A., and S. B. Idso, A model of thermal radiation from partly cloudy and overcast skies, *Water Resources Research*, *18*(4), 931–936, 1982.

King, J., J. Pomeroy, D. Gray, C. Fierz, P. Föhn, R. Harding, R. Jordan, E. Martin, and C. Plüss, *Snow and Climate: Physical processes, surface energy exchange and modelling*, chap. Snow-atmosphere energy and mass balance, Cambridge University Press, Cambridge, 2008.

Klein, A. G., D. K. Hall, and G. A. Riggs, Improving snow cover mapping in forests through the use of a canopy reflectance model, *Hydrological Processes*, *12*(10-11), 1723–1744, doi:10.1002/(SICI)1099-1085(199808/09)12:10/11⟨1723, 1998.

Kohler, J., O. Brandt, M. Johansson, and T. Callaghan, A long-term arctic snow depth record from Abisko, northern Sweden, 1913-2004, *Polar Research*, *25*(2), 91 – 113, 2006.

Kohsiek, W., C. Liebethal, T. Foken, R. Vogt, S. P. Oncley, C. Bernhofer, and H. A. R. Debruin, The energy balance experiment EBEX-2000. part III: Behaviour and quality of the radiation measurements, *Boundary-layer Meteorology*, *123*(1), 55–75, doi:10.1007/s10546-006-9135-8, 2007.

Larsen, J., O. Anisimov, A. Constable, A. Hollowed, N. Maynard, P. Prestrud, T. Prowse, and J. Stone, *Climate Change 2014: Impacts, Adaptation, and Vulnerability. Part B: Regional Aspects. Contribution of Working Group II to the Fifth Assessment Report of the Intergovernmental Panel on Climate Change*, vol. 28, chap. Polar regions, pp. 1567–1612, Cambridge University Press, Cambridge, United Kingdom and New York, NY, USA, 2014.

Lawler, R. R., and T. E. Link, Quantification of incoming all-wave radiation in discontinuous forest canopies with application to snowmelt prediction, *Hydrological Processes*, *25*(21), 3322–3331, doi:10.1002/hyp.8150, 2011.

Leblanc, S. G., J. M. Chen, R. Fernandes, D. W. Deering, and A. Conley, Methodology comparison for canopy structure parameters extraction from digital hemispherical photography in boreal forests, *Agricultural and Forest Meteorology*, *129*(3-4), 187–207, doi:10.1016/j.agrformet.2004.09.006, 2005.

Lemke, P., et al., *Climate Change 2007: The Physical Science Basis. Contribution of Working Group I to the Fourth Assessment Report of the Intergovernmental Panel on Climate Change*, chap. Observations: Changes in Snow, Ice and Frozen Ground, pp. 337–383, Cambridge University Press, Cambridge, United Kingdom and New York, NY, USA., 2007.

Li, X. W., L., A. H. Strahler, and C. E. Woodcock, A hybrid geometric optical-radiative transfer approach for modeling albedo and directional reflectance of discontinuous canopies, *Transactions On Geoscience and Remote Sensing*, *33*(2), 466–480, 1995.

Lieffers, V. J., C. Messier, K. J. Stadt, F. Gendron, and P. G. Comeau, Predicting and managing light in the understory of boreal forests, *Canadian Journal of Forest Research-revue Canadienne De Recherche Forestiere*, *29*(6), 796–811, doi:10.1139/cjfr-29-6-796, 1999.

Link, T. E., and D. Marks, Point simulation of seasonal snow cover dynamics beneath boreal forest canopies, *Journal of Geophysical Research: Atmospheres*, *104*(D22), 27,841–27,857, doi:10.1029/1998JD200121, 1999.

Link, T. E., D. Marks, and J. P. Hardy, A deterministic method to characterize canopy radiative transfer properties, *Hydrological Processes*, *18*(18), 3583–3594, doi:10.1002/hyp.5793, 2004.

Liston, G. E., and K. Elder, A meteorological distribution system for high-resolution terrestrial modeling (MicroMet), *Journal of Hydrometeorology*, *7*(2), 217–234, doi:10.1175/JHM486.1, 2006.

Luo, Y. Q., et al., A framework for benchmarking land models, *Biogeosciences*, *9*(10), 3857–3874, doi:10.5194/bg-9-3857-2012, 2012.

Macfarlane, C., A. Grigg, and C. Evangelista, Estimating forest leaf area using cover and fullframe fisheye photography: Thinking inside the circle, *Agricultural and Forest Meteorology*, *146*(1-2), 1–12, doi:10.1016/j.agrformet.2007.05.001, 2007.

Maisongrande, P., B. Duchemin, and G. Dedieu, VEGETATION/SPOT: an operational mission for the Earth monitoring; presentation of new standard products, *International Journal of Remote Sensing*, *25*(1), 9–14, doi:10.1080/0143116031000115265, 2004.

Marsh, P., and J. W. Pomeroy, Meltwater fluxes at an arctic forest-tundra site, *Hydrological Processes*, *10*(10), 1383–1400, doi:10.1002/(SICI)1099-1085(199610)10:10⟨1383, 1996.

McBean, G., *Arctic Climate Impact Assessment*, chap. Arctic Climate: Past and Present, pp. 21–60, Cambridge University Press, 2005.

Melloh, R. A., J. P. Hardy, R. N. Bailey, and T. J. Hall, An efficient snow albedo model for the open and sub-canopy, *Hydrological Processes*, *16*(18), 3571–3584, doi:10.1002/hyp.1229, 2002.

Michel, D., R. Philipona, C. Ruckstuhl, R. Vogt, and L. Vuilleumier, Performance and uncertainty of cnr1 net radiometers during a one-year field comparison, *Journal of Atmospheric and Oceanic Technology*, *25*(3), 442–451, doi:10.1175/2007JTECHA973.1, 2008.

Moeser, D., J. Roubinek, P. Schleppi, F. Morsdorf, and T. Jonas, Canopy closure, LAI and radiation transfer from airborne LiDAR synthetic images, *Agricultural and Forest Meteorology*, *197*, 158–168, doi:10.1016/j.agrformet.2014.06.008, 2014.

Moeser, D., F. Morsdorf, and T. Jonas, Novel forest structure metrics from airborne LiDAR data for improved snow interception estimation, *Agricultural and Forest Meteorology*, *208*, 40–49, doi:10.1016/j.agrformet.2015.04.013, 2015.

Naudts, K., et al., A vertically discretised canopy description for ORCHIDEE (SVN r2290) and the modifications to the energy, water and carbon fluxes, *Geoscientific Model Development*, *8*(7), 2035–2065, doi:10.5194/gmd-8-2035-2015, 2015.

Neilson, C. B., P. M. Groffman, S. P. Hamburg, C. T. Driscoll, T. J. Fahey, and J. P. Hardy, Freezing effects on carbon and nitrogen cycling in northern hardwood forest soils, *Soil Science Society of America Journal*, *65*(6), 1723–1730, 2001.

Ni, W., X. Li, C. E. Woodcock, J.-L. Roujean, and R. E. Davis, Transmission of solar radiation in boreal conifer forests: Measurements and models, *Journal of Geophysical Research*, *102*(D24), 29,555–29,566, 1997.

Ni-Meister, W., and H. Gao, Assessing the impacts of vegetation heterogeneity on energy fluxes and snowmelt in boreal forests, *Journal of Plant Ecology*, *4*(1-2), 37–47, doi:10.1093/jpe/rtr004, 2011.

Nijssen, B., and D. P. Lettenmaier, A simplified approach for predicting shortwave radiation transfer through boreal forest canopies, *Journal of Geophysical Research*, *104*, 859–868, doi:10.1029/1999JD900377, 1999.

Nijssen, B., et al., Simulation of high latitude hydrological processes in the torne-kalix basin: PILPS phase 2(e) - 2: Comparison of model results with observations, *Global and Planetary Change*, *38*(1-2), 31–53, doi:10.1016/S0921-8181(03)00004-3, 2003.

Niu, G.-Y., and Z.-L. Yang, Effects of frozen soil on snowmelt runoff and soil water storage at a continental scale, *Journal of Hydrometeorology*, *7*(5), 937–952, doi:10.1175/JHM538.1, 2006.

Nobis, M., *SideLook 1.1 - Imaging software for the analysis of vegetation structure with true-colour photographs; http://www.appleco.ch.*, 2005.

Nobis, M., and U. Hunziker, Automatic thresholding for hemispherical canopy photographs based on edge detection, *Agricultural and Forest Meteorology*, *128*(3-4), 243 – 250, doi:10.1016/j.agrformet.2004.10.002, 2005.

Nolin, A. W., Towards retrieval of forest cover density over snow from the multi-angle imaging spectroradiometer (MISR), *Hydrological Processes*, *18*(18), 3623–3636, doi:10.1002/hyp.5803, 2004.

Ohmura, A., Physical basis for the temperature-based melt-index method, *Journal of Applied Meteorology*, *40*(4), 753–761, doi:10.1175/1520-0450(2001)040⟨0753:PBFTTB⟩2.0.CO;2, 2001.

Oleson, K. W., et al., *Technical Description of version 4.0 of the Community Land Model (CLM)*, 2010.

Pacifico, F., et al., Evaluation of a photosynthesis-based biogenic isoprene emission scheme in JULES and simulation of isoprene emissions under present-day climate conditions, *Atmospheric Chemistry and Physics*, *11*(9), 4371–4389, doi:10.5194/acp-11-4371-2011, 2011.

Parajka, J., S. Dadson, T. Lafon, and R. Essery, Evaluation of snow cover and depth simulated by a land surface model using detailed regional snow observations from Austria, *Journal of Geophysical Research-Atmospheres*, *115*, D24,117, doi:10.1029/2010JD014086, 2010.

Pearson, D. W. C., C. C. Daamen, R. J. Gurney, and L. P. Simmonds, Combined modelling of shortwave and thermal radiation for one-dimensional SVATs, *Hydrology and Earth System Sciences*, *3*, 15–30, 1999.

Pearson, R. G., S. J. Phillips, M. M. Loranty, P. S. A. Beck, T. Damoulas, S. J. Knight, and S. J. Goetz, Shifts in Arctic vegetation and associated feedbacks under climate change, *Nature Climate Change*, *3*(7), 673–677, 2013.

Peterson, T., and R. Vose, An overview of the Global Historical Climatology Network temperature database, *Bulletin of the American Meteorological Society*, *78*, 2837–2849, 1997.

Pinty, B., J. . L. Widlowski, M. Verstraete, I. Andredakis, O. Arino, M. Clerici, T. Kaminski, and M. Taberner, Snowy backgrounds enhance the absorption of visible light in forest canopies, *Geophysical Research Letters*, *38*, L06,404, doi:10.1029/2010GL046417, 2011.

Pinty, B., et al., Radiation transfer model intercomparison (RAMI) exercise, *Journal of Geophysical Research-Atmospheres*, *106*(D11), 11,937–11,956, doi:10.1029/2000JD900493, 2001.

Pinty, B., et al., Radiation transfer model intercomparison (RAMI) exercise: Results from the second phase, *Journal of Geophysical Research-Atmospheres*, *109*(D6), D06,210, doi:10.1029/2003JD004252, 2004.

Pitman, A. J., et al., Uncertainties in climate responses to past land cover change: First results from the LUCID intercomparison study, *Geophysical Research Letters*, *36*, L14,814, doi:10.1029/2009GL039076, 2009.

Pomeroy, J., A. Rowlands, J. Hardy, T. Link, D. Marks, R. Essery, J. E. Sicart, and C. Ellis, Spatial variability of shortwave irradiance for snowmelt in forests, *Journal of Hydrometeorology*, *9*(6), 1482–1490, doi:10.1175/2008JHM867.1, 2008.

Pomeroy, J. W., and K. Dion, Winter radiation extinction and reflection in a boreal pine canopy: Measurements and modelling, *Hydrological Processes*, *10*(12), 1591–1608, doi:10.1002/(SICI)1099-1085(199612)10:12⟨1591, 1996.

Pomeroy, J. W., and L. Li, Development of the prairie blowing snow model for application in climatological and hydrological models, *Eastern Snow Conference 1997, Proceedings*, pp. Canadian Geophys Union; Environ Canada–Natl hyrol Res Inst; US Army ColdEOLEOLRegions Res & Engn Lab, 1997.

Pomeroy, J. W., P. Marsh, H. G. Jones, and T. D. Davies, Spatial distribution of snow chemical load at the tundra taiga transition, in *Biogeochemistry of seasonally snow-covered catchments*, no. 228 in IAHS Publication, pp. 191–203, 1995.

Pomeroy, J. W., D. M. Gray, K. R. Shook, B. Toth, R. L. H. Essery, A. Pietroniro, and N. Hedstrom, An evaluation of snow accumulation and ablation processes for land surface modelling, *Hydrological Processes*, *12*(15), 2339–2367, doi:10.1002/(SICI)1099-1085(199812)12:15⟨2339, 1998.

Pomeroy, J. W., D. M. Gray, N. R. Hedstrom, and J. R. Janowicz, Prediction of seasonal snow accumulation in cold climate forests, *Hydrological Processes*, *16*(18), 3543–3558, doi:10.1002/hyp.1228, 2002.

Pomeroy, J. W., D. S. Bewley, R. L. H. Essery, N. R. Hedstrom, T. Link, R. J. Granger, J. E. Sicart, C. R. Ellis, and J. R. Janowicz, Shrub tundra snowmelt, *Hydrological Processes*, *20*(4), 923–941, doi:10.1002/hyp.6124, 2006.

Pomeroy, J. W., D. Marks, T. Link, C. Ellis, J. Hardy, A. Rowlands, and R. Granger, The impact of coniferous forest temperature on incoming longwave radiation to melting snow, *Hydrological Processes*, *23*(17), 2513–2525, doi:10.1002/hyp.7325, 2009.

Press, M. C., T. V. Callaghan, and J. A. Lee, How will European Arctic ecosystems respond to projected global environmental change?, *Ambio*, *27*(4), 306–311, 1998.

Pulliainen, J., Mapping of snow water equivalent and snow depth in boreal and sub-arctic zones by assimilating space-borne microwave radiometer data and ground-based observations, *Remote Sensing of Environment*, *101*(2), 257–269, doi:10.1016/j.rse.2006.01.002, 2006.

Qu, X., and A. Hall, On the persistent spread in snow-albedo feedback, *Climate Dynamics*, *42*, 69–81, 2014.

Rhoads, A. G., S. P. Hamburg, T. J. Fahey, T. G. Siccama, and R. Kobe, Comparing direct and indirect methods of assessing canopy structure in a northern hardwood forest, *Canadian Journal of Forest Research-revue Canadienne De Recherche Forestiere*, *34*(3), 584–591, doi:10.1139/x03-231, 2004.

Rich, P. M., J. Wood, D. Vieglais, K. Burek, and N. Webb, *Hemiview User Manual*, 1999.

Robinson, D. A., K. F. Dewey, and R. R. Heim, Global snow cover monitoring - An update, *Bulletin of the American Meteorological Society*, *74*(9), 1689–1696, doi:10.1175/1520-0477(1993)074⟨1689:GSCMAU⟩2.0.CO;2, 1993.

Rowlands, A., J. Pomeroy, J. Hardy, D. Marks, K. Elder, and R. Melloh, Small-scale spatial variability of radiant energy for snowmelt in a mid-latitude sub-alpine forest, in *59th Eastern Snow Conference, Stowe, Vermont, USA.*, 2002.

Rupp, T., Chapin, F. S. III, and A. Starfield, Response of subarctic vegetation to transient climatic change on the Seward Peninsula in northwest Alaska, *Global Change Biology*, *6*, 541–555., 2000a.

Rupp, T., A. Starfield, and Chapin, F. S. III, A frame-based spatially explicit model of subarctic vegetation response to climatic change: comparison with a point model, *Landscape Ecology*, *15*, 383–400, 2000b.

Rupp, T., Chapin, F. S. III, A. Starfield, and P. Duffy, Modeling boreal forest dynamics in interior Alaska, *Climatic Change*, *55*, 213–233, 2002.

Rutter, N., et al., Evaluation of forest snow processes models (SnowMIP2), *Journal of Geophysical Research-Atmospheres*, *114*, D06,111, doi:10.1029/2008JD011063, 2009.

Ryan, W. A., N. J. Doesken, and S. R. Fassnacht, Evaluation of ultrasonic snow depth sensors for U.S. snow measurements, *Journal of Atmospheric and Oceanic Technology*, *25*(5), 667–684, doi:10.1175/2007JTECHA947.1, 2008.

Ryder, J., et al., A multi-layer land surface energy budget model for implicit coupling with global atmospheric simulations, *Geoscientific Model Development*, *9*(1), 223–245, doi:10.5194/gmd-9-223-2016, 2016.

Schellekens, J., et al., A global water resources ensemble of hydrological models: the eartH_2Observe Tier-1 dataset, *Earth System Science Data*, *9*, 389–413, doi:10.5194/essd-9-389-2017, 2017.

Sellers, P. J., Canopy reflectance, photosynthesis and transpiration, *International Journal of Remote Sensing*, *6*(8), 1335–1372, 1985.

Sellers, P. J., J. A. Berry, G. J. Collatz, C. B. Field, and F. G. Hall, Canopy reflectance, photosynthesis, and transpiration 3. A Reanalysis using improved leaf models and a new canopy integration scheme, *Remote Sensing of Environment*, *42*(3), 187–216, doi:10.1016/0034-4257(92)90102-P, 1992.

Sellers, P. J., et al., BOREAS in 1997: Experiment overview, scientific results, and future directions, *Journal of Geophysical Research*, *102*(D24), 28,731–28,769, 1997.

Serreze, M. C., and R. G. Barry, Processes and impacts of arctic amplification: A research synthesis, *Global and Planetary Change*, *77*(12), 85–96, doi:http://dx.doi.org/10.1016/j.gloplacha.2011.03.004, 2011.

Serreze, M. C., et al., Observational evidence of recent change in the northern high-latitude environment, *Climatic Change*, *46*(1-2), 159–207, doi:10.1023/A:1005504031923, 2000.

Sheffield, J., G. Goteti, and E. F. Wood, Development of a 50-year high-resolution global dataset of meteorological forcings for land surface modeling, *Journal of Climate*, *19*(13), 3088–3111, doi:10.1175/JCLI3790.1, 2006.

Shook, K., D. Gray, and J. W. Pomeroy, Temporal variation in snowcover area during melt in prairie and alpine environments, *Nordic Hydrology*, *24*(2-3), 183–198, 1993.

Sicart, J. E., J. W. Pomeroy, R. L. H. Essery, J. Hardy, T. Link, and D. Marks, A sensitivity study of daytime net radiation during snowmelt to forest canopy and atmospheric conditions, *Journal of Hydrometeorology*, *5*, 774–784, doi:10.1175/1525-7541(2004)005⟨0774:ASSODN⟩2.0.CO;2, 2004.

Sicart, J. E., J. W. Pomeroy, R. L. H. Essery, and D. Bewley, Incoming longwave radiation to melting snow: observations, sensitivity and estimation in northern environments, *Hydrological Processes*, *20*(17), 3697–3708, doi:10.1002/hyp.6383, 2006.

Sitch, S., et al., Assessing the carbon balance of circumpolar Arctic tundra using remote sensing and process modeling, *Ecological Applications*, *17*(1), 213–234, doi:10.1890/1051-0761(2007)017[0213:ATCBOC]2.0.CO;2, 2007.

Slater, A. G., et al., The representation of snow in land surface schemes: Results from PILPS 2(d), *Journal of Hydrometeorology*, *2*(1), 7–25, doi:10.1175/1525-7541(2001)002⟨0007:TROSIL⟩2.0.CO;2, 2001.

Stähli, M., T. Jonas, and D. Gustafsson, The role of snow interception in winter-time radiation processes of a coniferous sub-alpine forest, *Hydrological Processes*, *23*(17), 2498–2512, 2009.

Steinweg, J. M., M. C. Fisk, B. McAlexander, P. M. Groffman, and J. P. Hardy, Experimental snowpack reduction alters organic matter and net N mineralization potential of soil macroaggregates in a northern hardwood forest, *Biology and Fertility of Soils*, *45*(1), 1–10, doi:10.1007/s00374-008-0305-3, 2008.

Takala, M., K. Luojus, J. Pulliainen, C. Derksen, J. Lemmetyinen, J.-P. Karna, J. Koskinen, and B. Bojkov, Estimating northern hemisphere snow water equivalent for climate research through assimilation of space-borne radiometer data and ground-based measurements, *Remote Sensing of Environment*, *115*(12), 3517–3529, doi:10.1016/j.rse.2011.08.014, 2011.

Tanja, S., et al., Air temperature triggers the recovery of evergreen boreal forest photosynthesis in spring, *Global Change Biology*, *9*(10), 1410–1426, doi:10.1046/j.1365-2486.2003.00597.x, 2003.

Taylor, K. E., Summarizing multiple aspects of model performance in a single diagram, *Journal of Geophysical Research-atmospheres*, *106*(D7), 7183–7192, doi:10.1029/2000JD900719, 2001.

Tenow, O., Hazards to a mountain birch forest: Abisko in perspective, *Ecological Bulletins; Plant ecology in the subarctic Swedish Lapland*, *45*, 104–114, 1996.

Tenow, O., H. Bylund, P. S. Karlsson, and J. Hoogesteger, Rejuvenation of a mountain birch forest by an Epirrita autumnata (Lepidoptera : Geometridae) outbreak, *Acta Oecologica-international Journal of Ecology*, *25*(1-2), 43–52, doi:10.1016/j.actao.2003.10.006, 2004.

Thompson, C., J. Beringer, F. S. Chapin, and A. D. McGuire, Structural complexity and land-surface energy exchange along a gradient from arctic tundra to boreal forest, *Journal of Vegetation Science*, *15*(3), 397–406, doi:10.1658/1100-9233(2004)015[0397:SCALEE]2.0.CO;2, 2004.

Trenberth, K. E., et al., *Climate Change 2007: The Physical Science Basis. Contribution of Working Group I to the Fourth Assessment Report of the Intergovernmental Panel on Climate Change*, chap. Observations: Surface and Atmospheric Climate Change, Cambridge University Press, Cambridge, United Kingdom and New York, NY, USA., 2007.

Tribbeck, M. J., R. J. Gurney, and E. M. Morris, The radiative effect of a fir canopy on a snowpack, *J. Hydrometeor*, *7*(5), 880–895, doi:10.1175/JHM528.1, 2006.

Turner, M., S. Collins, A. Lugo, J. Magnuson, R. T.S., and F. Swanson, Disturbance dynamics and ecological response: The contribution of long-term ecological research, *BioScience*, *53(1)*, 46–56, 2003.

Unwin, D., and S. Corbet, *Insects, plants and microclimate*, vol. 15, chap. The climatic environment near the ground, pp. 4–11, naturalists' handbooks ed., The Richmond Publishing Co. Ltd., Slough, 1991.

Usher, M., *Arctic Climate Impact Assessment*, chap. Principles of Conserving the Arctics Biodiversity, pp. 539–596, Cambridge University Press, 2005.

Vaganov, E. A., M. K. Hughes, A. V. Kirdyanov, F. H. Schweingruber, and P. P. Silkin, Influence of snowfall and melt timing on tree growth in subarctic Eurasia, *Nature*, *400*(6740), 149–151, 1999.

Vaughan, D., et al., *Climate Change 2013: The Physical Science Basis. Contribution of Working Group I to the Fifth Assessment Report of the Intergovernmental Panel on Climate Change*, chap. Observations: Cryosphere, 4, Cambridge University Press, Cambridge, United Kingdom and New York, NY, USA, 2013.

Verseghy, D. L., N. A. McFarlane, and M. Lazare, CLASS - A Canadian Land-Surface Scheme for GCMs 2. Vegetation Model and Coupled Runs, *International Journal of Climatology*, *13*(4), 347–370, doi:10.1002/joc.3370130402, 1993.

Virtanen, T., and S. Neuvonen, Performance of moth larvae on birch in relation to altitude, climate, host quality and parasitoids, *Oecologia*, *120*(1), 92–101, doi:10.1007/s004420050837, 1999.

Virtanen, T., S. Neuvonen, and A. Nikula, Modelling topoclimatic patterns of egg mortality of Epirrita autumnata (Lepidoptera : Geometridae) with a geographical information system:

predictions for current climate and warmer climate scenarios, *Journal of Applied Ecology*, *35*(2), 311–322, doi:10.1046/j.1365-2664.1998.00299.x, 1998.

Viterbo, P., and A. C. M. Beljaars, An improved land-surface parameterization scheme in the ECMWF model and its validation, *Journal of Climate*, *8*(11), 2716–2748, doi:10.1175/1520-0442(1995)008⟨2716:AILSPS⟩2.0.CO;2, 1995.

Walsh, J., *Arctic Climate Impact Assessment*, chap. Cryosphere and Hydrology, pp. 184–236, Cambridge University Press, 2005.

Webster, C., N. Rutter, F. Zahner, and T. Jonas, Measurement of incoming radiation below forest canopies: A comparison of different radiometer configurations, *Journal of Hydrometeorology*, *17*(3), 853–864, doi:10.1175/JHM-D-15-0125.1, 2016a.

Webster, C., N. Rutter, F. Zahner, and T. Jonas, Modeling subcanopy incoming longwave radiation to seasonal snow using air and tree trunk temperatures, *Journal of Geophysical Research-Atmospheres*, *121*(3), 1220–1235, doi:10.1002/2015JD024099, 2016b.

Weedon, G. P., G. Balsamo, N. Bellouin, S. Gomes, M. J. Best, and P. Viterbo, The WFDEI meteorological forcing data set: WATCH Forcing Data methodology applied to ERA-Interim reanalysis data, *Water Resources Research*, *50*(9), 7505–7514, doi:10.1002/2014WR015638, 2014.

Weiss, M., and F. Baret, *CAN-EYE User Manual*, French National Institute of Agricultural Research (INRA), v6.1 ed., 2010.

Weiss, M., F. Baret, G. J. Smith, I. Jonckheere, and P. Coppin, Review of methods for in situ leaf area index (LAI) determination Part II. Estimation of LAI, errors and sampling, *Agricultural and Forest Meteorology*, *121*(1-2), 37–53, doi:10.1016/j.agrformet.2003.08.001, 2004.

Weller, G., Arctic climate impact assessment (ACIA), *Arctic Science Conference Abstracts*, *51*, American Association for the Advancement of Science (AAAS), 2000.

Welles, J. M., and J. M. Norman, Instrument for indirect measurement of canopy architecture, *Agronomy Journal*, *83*(5), 818–825, 1991.

Whittaker, R., and G. Likins, *Primary production of the Biosphere*, Springer-Verlag, New York, 1975.

Widlowski, J., et al., Third radiation transfer model intercomparison (RAMI) exercise: Documenting progress in canopy reflectance models, *Journal of Geophysical Research-Atmospheres*, *112*(D9), D09,111, doi:10.1029/2006JD007821, 2007.

Widlowski, J., et al., RAMI4PILPS: An intercomparison of formulations for the partitioning of solar radiation in land surface models, *Journal of Geophysical Research-Biogeosciences*, *116*, G02,019, doi:10.1029/2010JG001511, 2011.

Williams, D. W., and A. M. Liebhold, Forest defoliators and climatic-change - potential changes in spatial-distribution of outbreaks of western spruce budworm (lepidoptera, Tortricidae) and gypsy-moth (lepidoptera, Lymantriidae), *Environmental Entomology*, *24*(1), 1–9, 1995.

WMO, Guide to Meteorological Instruments and Methods of Observation (CIMO Guide no. 8) Appendix 4b, *Tech. rep.*, World Meteorological Organization, Geneva, 2008.

Woo, M.-K., and M. A. Giesbrecht, Simulation of snowmelt in a subarctic spruce woodland: 1. Tree model, *Water Resources Research*, *36*, 2275–2285, doi:10.1029/2000WR900094, 2000.

Work, R., H. Stockwell, T. Freeman, and R. Beaumont, Accuracy of field snow surveys western United States, including Alaska., *Tech. rep.*, US Army Cold Regions Research and Engineering Laboratory. Technical report 163, Hanover, NH, 1965.

Yang, D. Q., et al., Quantification of precipitation measurement discontinuity induced by wind shields on national gauges, *Water Resources Research*, *35*(2), 491–508, doi:10.1029/1998WR900042, 1999.

Appendices

A

Appendix A - JULES Abisko runs namelist files

The JULES model (v4.6) requires a series of namelist files which specify the parameters required to run the model. The parameters of note to run for the Abisko site are listed in Table 1.

JULES can spin up for a maximum of 10 cycles, but runs after spinning up for 2 years (repeating September 2007 to September 2008 twice).

Table 1: Abisko runs namelist parameters

drive.nml		
	Fraction of diffuse Radiation	diff_frac_const=0.72
	Temperature for snow	t_for_snow=274
jules_radiation.nml		
	Switch for prognostic snow properties in model albedo	l_snow_albedo=.true
	Switch for albedo model	l_spec_alb_bs=.true
	Switch for albedo model	l_spec_albedo=.true
	Albedo weights	wght_alb=0.25,0.25,0.25,0.25,
jules_snow.nml		
	Canopy Snowfall Interception Factor	snowinterceptfact 0.0,
	Snowmass held under the Canopy	cansnowpft= T T F F F
	Maximum Number of Snow Layers	nsmax = 3,
	Thickness of each Snow layer (m)	dzsnow = 0.1 0.2 0.4
jules_vegetation.nml		
	Canopy Model	can_model=4,
	Canopy Radiation Model	can_rad_mod=1,
Pft_params.nml		BLT, NLT, C3, C4, Shrub
	Canopy Height (m)	canht_ft_io=5.00,16.38,0.10,1.26,1.0,
	LAI	lai_io=1.0,4.0,2.0,4.0,1.0,
	Light extinction coefficient	kext_io=0.5,0.5,0.5,0.5,0.5,
model_grid.nml		
	Latitude	68.32
	Longitude	18.83
timesteps.nml		
	Run start	main_run_start='2007-08-31 23:00:00',
	Run end	main_run_end='2009-08-31 23:00:00',
	Spin up	max_spinup_cycles=10,
	Spin up start	spinup_start="2007-09-01 00:00:00"
	Spin up end	spinup_end="2008-09-01 00:00:00"
tile_fractions.nml		BLT, NLT, C3, C4, Shrub, Urban, Water, Bare soil, Ice
	Fractional Cover	0.15 0.0 0.85 0.0 0.0 0.0 0.0 0.0 0.0

B

Appendix B - JULES global runs namelist files

The JULES (v4.7) global model runs required a series of namelist files which specify the parameters required to run the model. The parameters specific in Table 1 were used in addition to the parameters defined in Table 2 and 3. The parameters of note to run for the Abisko site are listed in Table 2 and then JULES Shaded gap parameters are defined in Table 3.

Table 2: Global runs namelist parameters

jules_snow.nml		
	Snowmass held under the Canopy	cansnowpft= T T F F T
Pft_params.nml		
	Canopy Height (m)	canht_ft_io=19.01,16.38,0.10,0.79,5.0,
	LAI	lai_io=5.0,4.0,2.0,2.0,0.25,
timesteps.nml		
	Time steps	1 hour
	Run start	main_run_start='1990-01-01 00:00:00',
	Run end	main_run_end='2013-01-01 00:00:00',
	Spin up	max_spinup_cycles=1,
	Spin up start	spinup_start="1990-01-01 00:00:00"
	Spin up end	spinup_end="1999-12-31 23:30:00"
Driving Data		
	WFDEI [*Weedon et al.*, 2014]	0.5 degrees
Rose suite		
	https://code.metoffice.gov.uk/trac/roses-u/browser/a/i/4/1/5/trunk@26912	u-ai415

Table 3: Shaded gap global runs namelist parameters

Pft_params.nml		
	LAI	lai_io=5.0,4.0,2.0,2.0,1.0,

C

Appendix C - JULES global runs results

The snowmass diagnostics from the pan-Arctic runs are shown in Figure 1, Figure 2, Figure 4, and Figure 5. Figure 1 shows the snowmass for JULES, Figure 2 shows the snowmass for JULES Shaded gap, Figure 3 shows the observations from GlobSnow, Figure 4 shows the difference between JULES and JULES Shaded gap, and Figure 5 shows the normalised difference between JULES and JULES Shaded gap.

The Figure 6 shows the fractional cover for C4 grass in JULES, JULES Shaded gap and the difference in fractional cover.

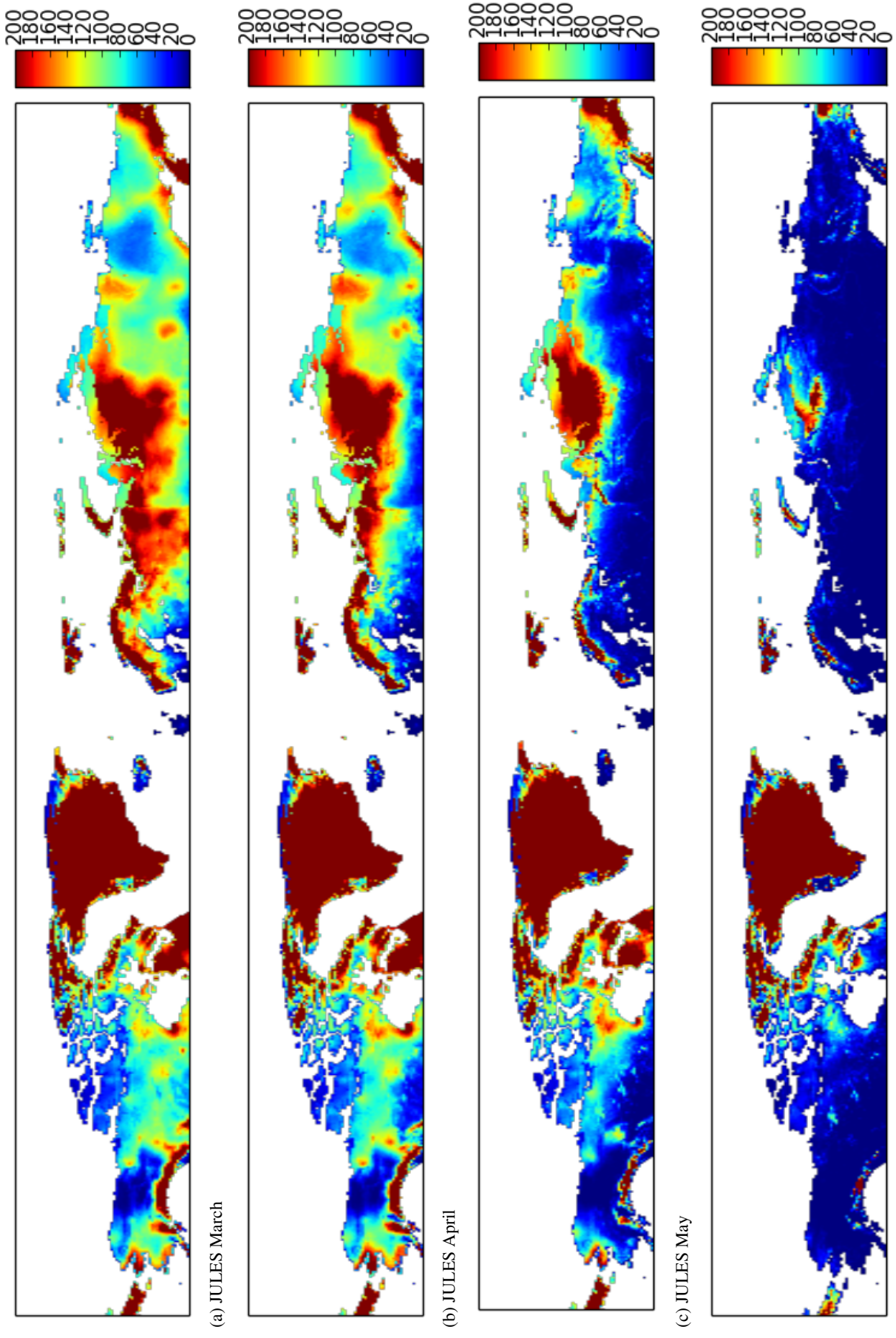

Figure 1: JULES twelve year (2000 to 2012) mean snowmass (kg m^{-2}) for a) March, b) April, c) May and d) June.

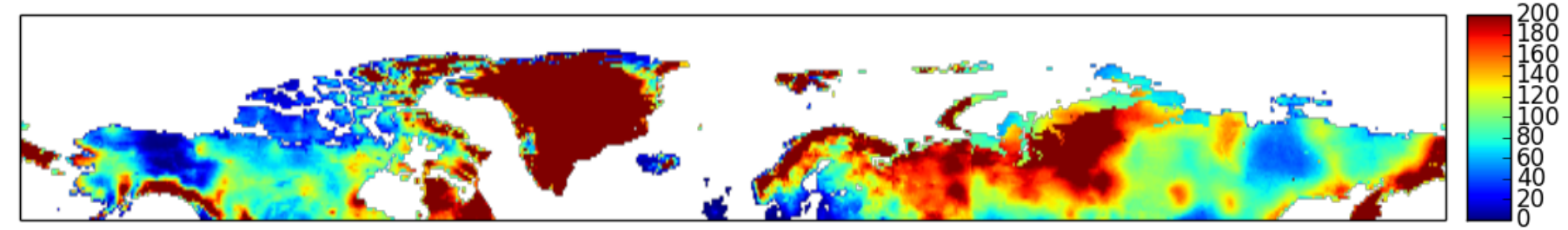

(a) JULES Shaded gap March

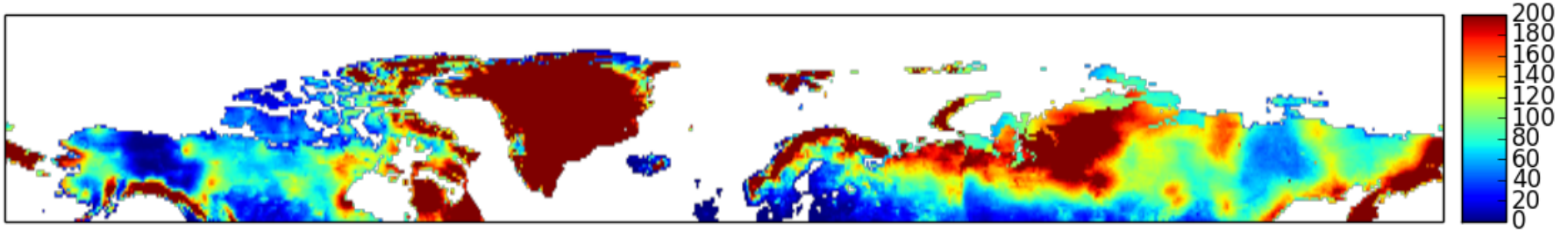

(b) JULES Shaded gap April

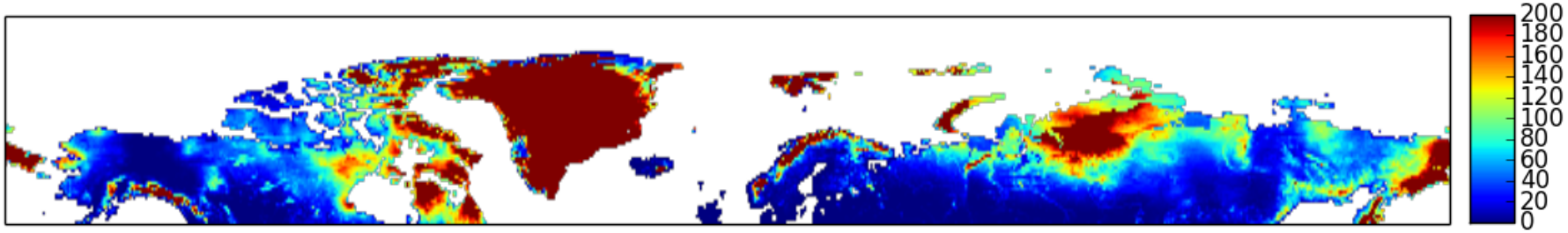

(c) JULES Shaded gap May

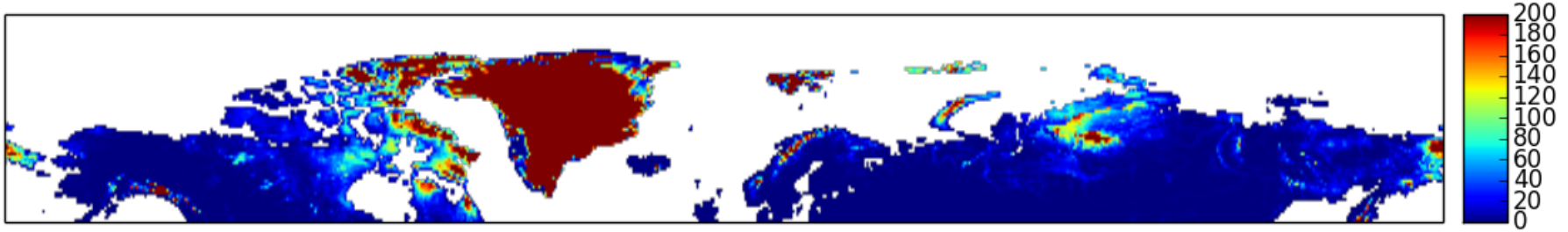

(d) JULES Shaded gap June

Figure 2: JULES Shaded gap twelve year (2000 to 2012) mean snowmass (kg m^{-2}) for a) March, b) April, c) May and d) June.

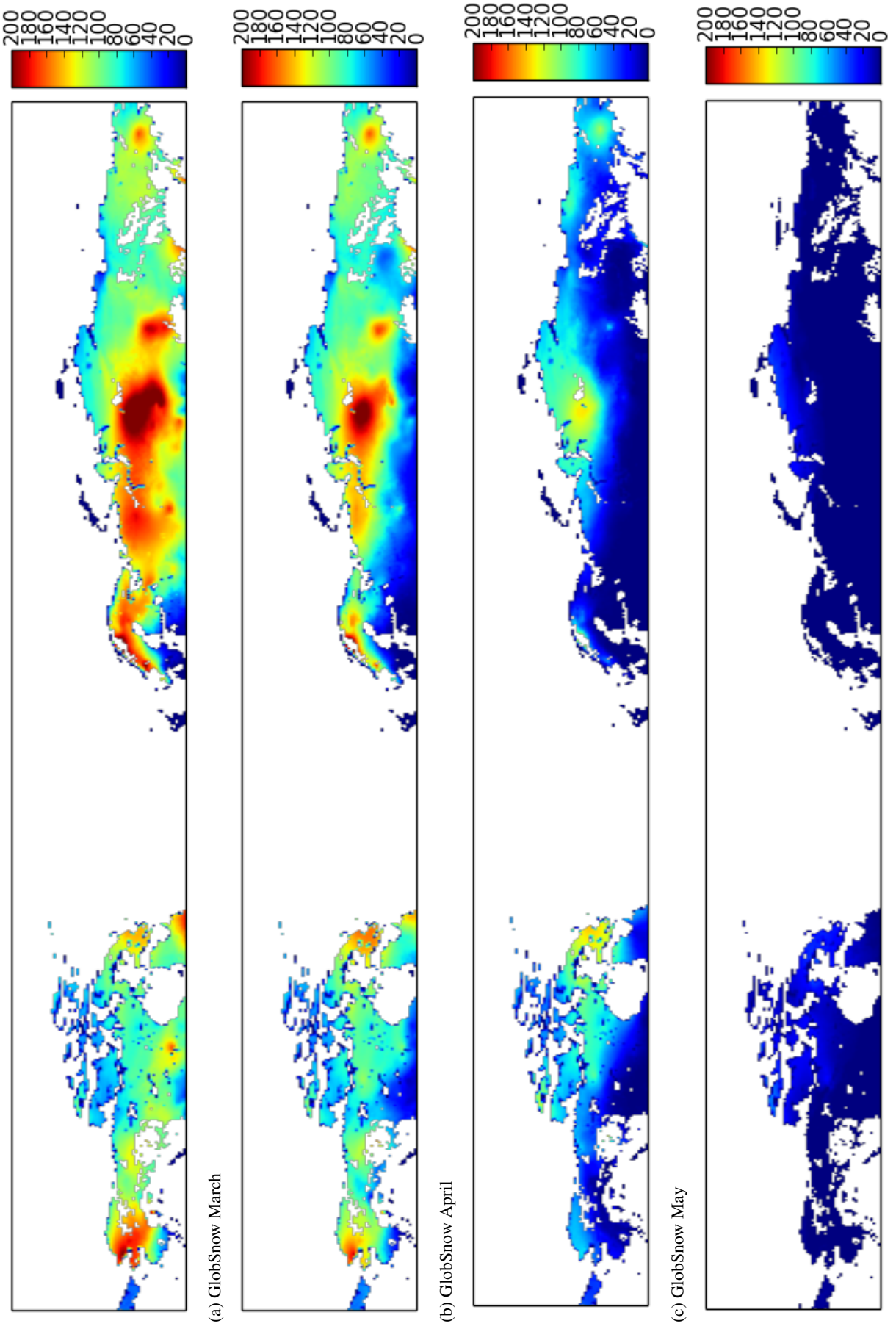

Figure 3: GlobSnow twelve year (2000 to 2012) mean snowmass (kg m^{-2}) for a) March, b) April, c) May and d) June.

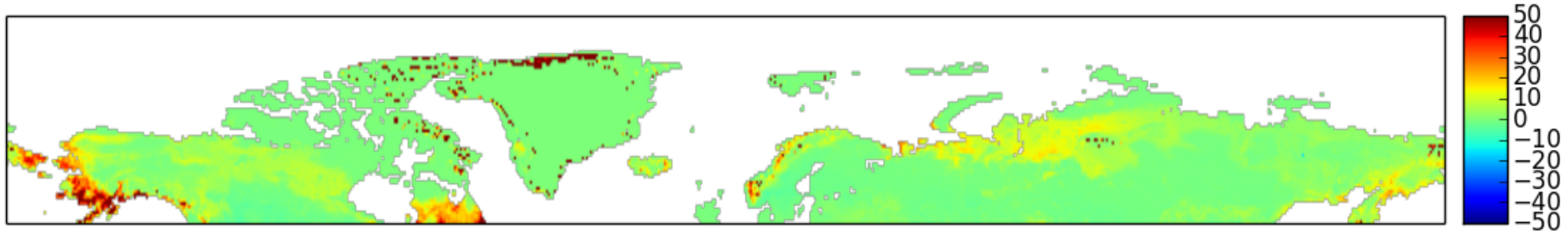

(a) JULES minus JULES Shaded gap March

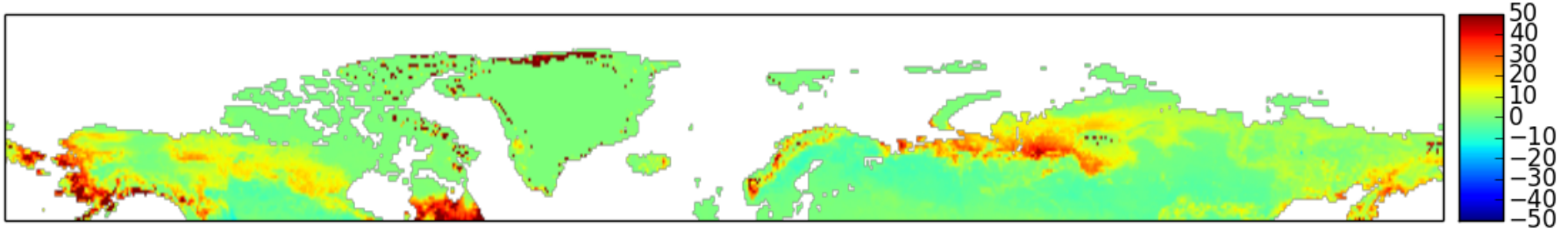

(b) JULES minus JULES Shaded gap April

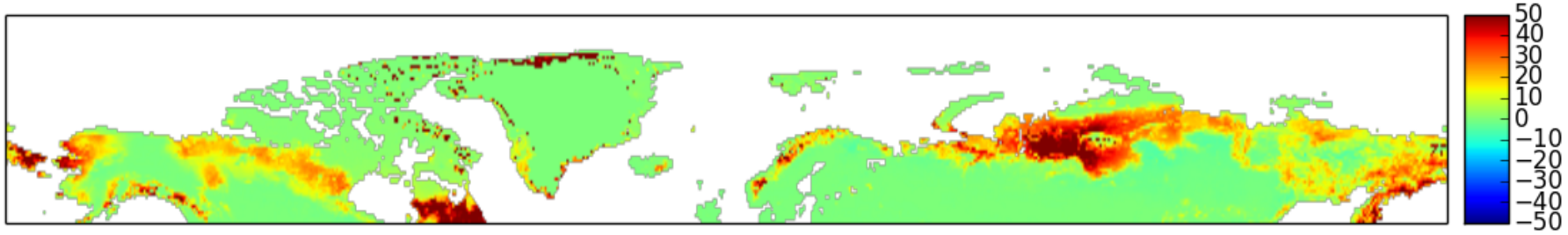

(c) JULES minus JULES Shaded gap May

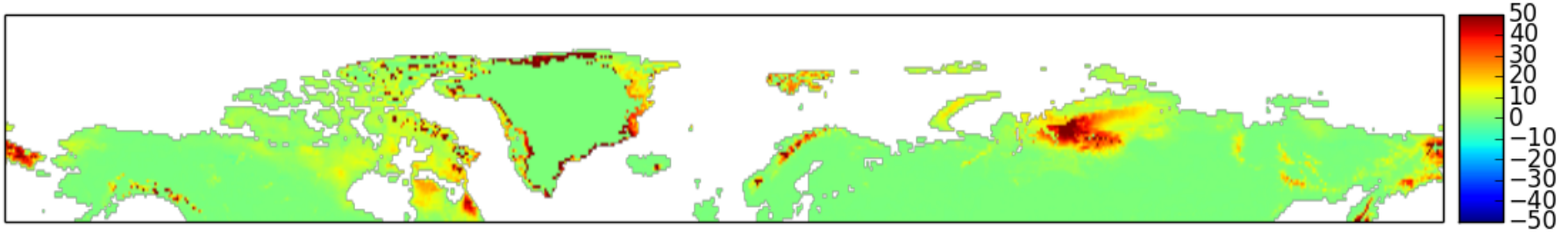

(d) JULES minus JULES Shaded gap June

Figure 4: The difference between JULES and JULES Shaded gap twelve year (2000 to 2012) mean snowmass (kg m^{-2}) for a) March, b) April, c) May and d) June.

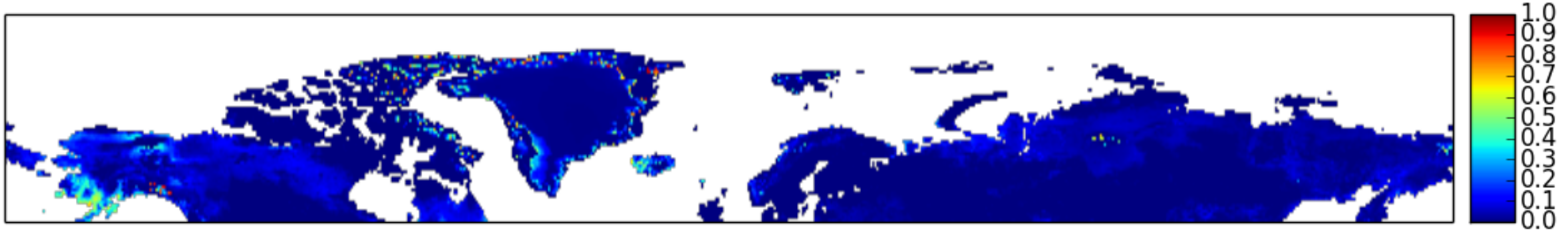

(a) JULES minus JULES Shaded gap (normalised) March

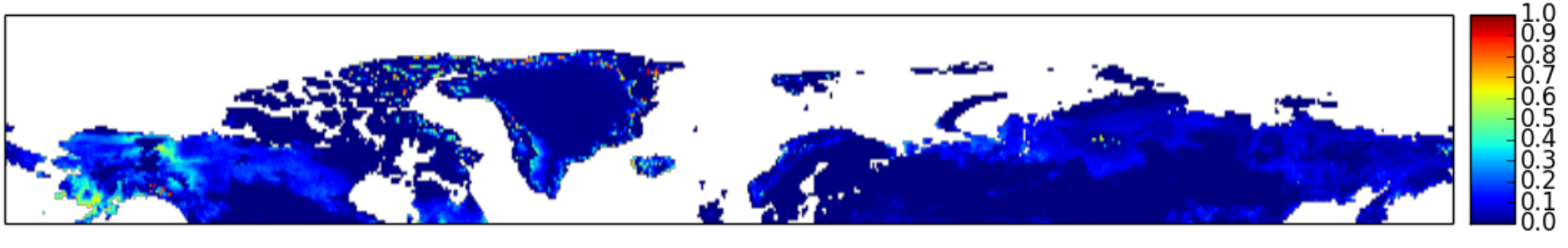

(b) JULES minus JULES Shaded gap (normalised) April

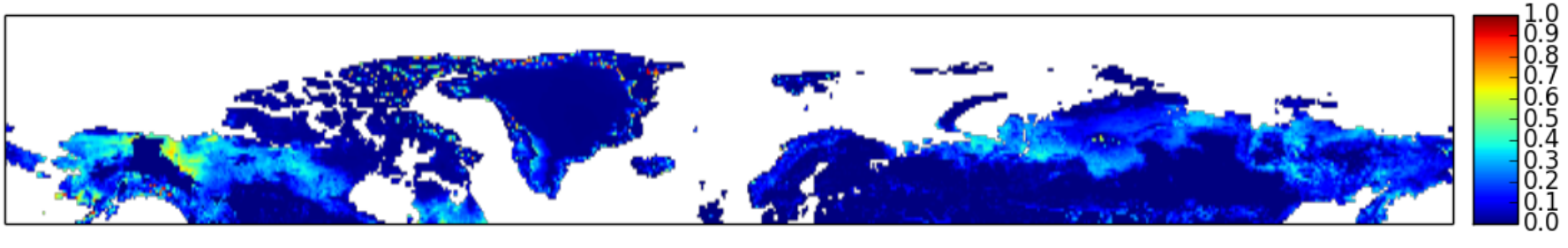

(c) JULES minus JULES Shaded gap (normalised) May

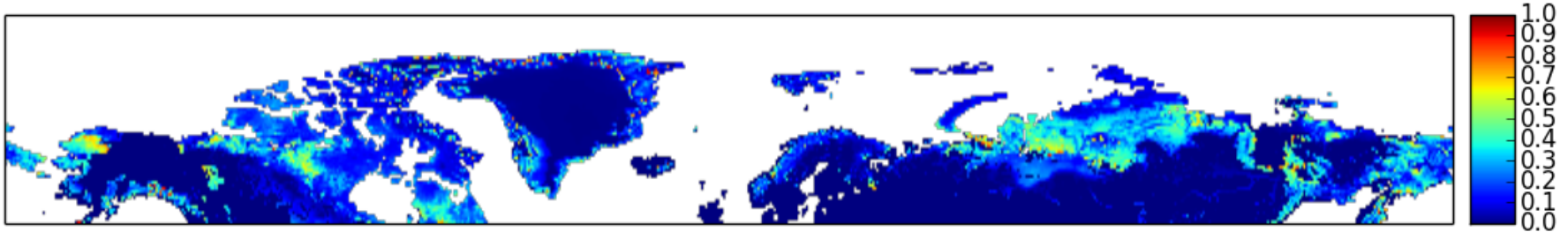

(d) JULES minus JULES Shaded gap (normalised) June

Figure 5: The normalised difference between JULES and JULES Shaded gap twelve year (2000 to 2012) mean snowmass (kg m^{-2}) for a) March, b) April, c) May and d) June.

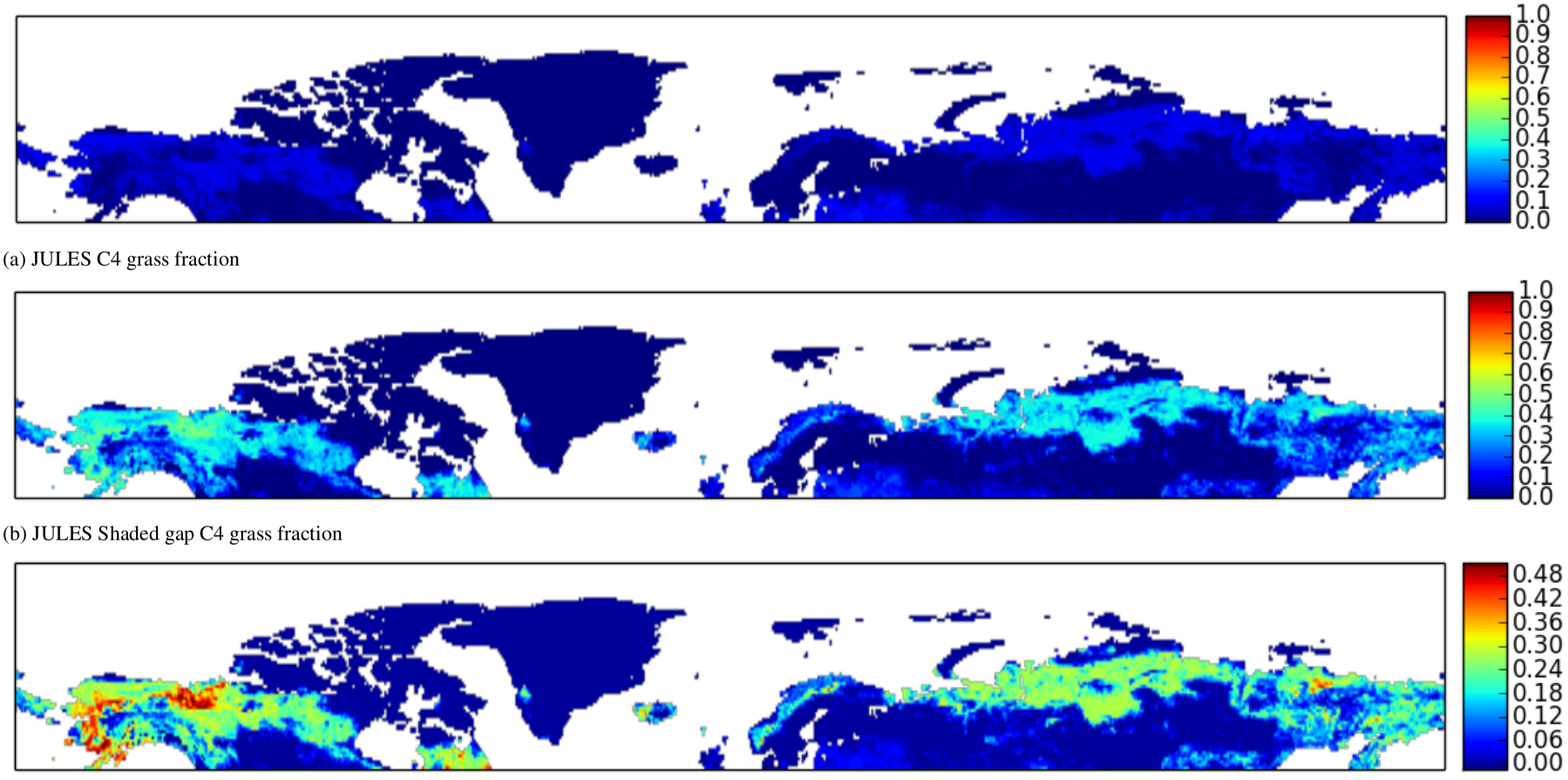

(a) JULES C4 grass fraction

(b) JULES Shaded gap C4 grass fraction

(c) JULES Shaded gap minus JULES C4 grass fraction difference

Figure 6: C4 Grass fractional cover for a) JULES, b) JULES Shaded gap and c) the difference between JULES and JULES Shaded gap.